METALS. SUPERCONDUCTORS

An asymptotic approximation of multiple-scattering theory in very-low-energy electron diffraction from a metal surface

G. V. Vol'f, Yu. P. Chuburin, and D. V. Fedorov

Physicotechnical Institute, Ural Division, Russian Academy of Sciences, 426001 Izhevsk, Russia

V. N. Strocov*)

Department of Physics, Chalmers University of Technology and Göteborg University, S-41296 Göteborg, Sweden

(Submitted December 4, 1998; resubmitted April 1, 1999)
Fiz. Tverd. Tela (St. Petersburg) **41**, 2105–2108 (December 1999)

An asymptotic approximation of multiple-scattering theory has been used to analyze the intensity of very-low-energy-electron diffraction (VLEED). An analytic expression relating the amplitudes of the Bloch waves excited in a crystal (and, hence, the VLEED intensities) to the critical zone points of an infinite crystal has been obtained. The possibilities of the new approach are compared with a calculation of partial electron-transmission coefficients made by the matching method employed conventionally in interpretation of VLEED data. While providing a comparable accuracy, the proposed approach is fairly simple and free of the instabilities inherent in matching-method calculations. The explicit connection of the quantities obtained by this method with the electron dispersion relation for an infinite crystal makes it promising for analysis of band-structure effects in VLEED and photoemission experiments.
 [S1063-7834(99)00112-4]

The interest in VLEED experiments performed in the energy range of $\sim 0-40$ eV is largely accounted for by the possibility of their use in determination of the electronic band structure of high-lying excited states.[1–4]

The corresponding analysis of the VLEED intensity is connected intimately with the computational methods permitting one to classify its structure and establish reference points for experimental bulk-band mapping. Interpretation of VLEED experiments for this purpose involves decomposition of the wave function of the scattered electron in Bloch waves of the bulk crystal, which permits determination of the contribution due to the jth band $E_j(\mathbf{k})$.[2,5] One employs for this purpose, as a rule, the matching method.[6,7] The main problem with this method consists in that even without taking into account absorption, which is usually low for the energies of interest, the Bloch waves have to be determined by solving a secular equation including complex $k_\perp$,[7,8] which presents considerably more serious difficulties than the standard problem of finding the dispersion relation $E_j(\mathbf{k})$ with real $k_\perp$. Additional problems arise in connection with the instability of the computational procedure.[9] Therefore experimental VLEED data are presently interpreted primarily using qualitative semiempirical methods.[5,9]

Another approach to the solution of this problem, which is used in dynamic LEED theory, is offered by the multiple scattering theory.[10] When employed in its standard form, however, the multiple scattering theory is inconvenient to analyze bulk band-structure effects; indeed, it yields the total wave function in a crystal without decomposing it in Bloch waves, and, thus, with no explicit relation to $D_j(\mathbf{k})$.

We are presenting here a new approximate approach within the multiple-scattering theory formalism, an asymptotic multiple-scattering (AMS) method, where the emphasis is placed on scattering in the bulk of the crystal. This method establishes a connection between VLEED spectra and an asymptotic presentation of the wave function inside a crystal, which is expressed through the characteristics of the Bloch electron in a bulk crystal. In particular, when neglecting inelastic processes, it offers a direct relation of the bulk-band critical points to the VLEED structure, which underlies experimental mapping of final-state bands in photoemission.

1. FORMULATION OF THE AMS APPROACH

Neglecting inelastic processes, which are insignificant for VLEED energies,[1–3] the AMS approach is based on two physically straightforward and reasonable approximations.

(1) Within the unit cell of a semi-infinite crystal, including the surface transition region where the potential differs noticeably from the bulk and vacuum limits, the wave function is approximated by its asymptotic bulk (on the side of the crystal) and vacuum (on the side of free space) forms.

(2) One neglects the contributions to the wave function of the scattering electron which decay exponentially away from the crystal surface. (This approximation is not fundamentally necessary and is introduced only for the sake of physical clarity and simplification of expressions.)

It can be shown that in the case of electron scattering from metal surfaces and at energies typical of VLEED experiments the above approximations cause only a small error in the intensity of that part of the VLEED structure which is due to the nature of bulk-band dispersion.[6,7,9]

The meaning of these approximations consists essentially in separating the contribution due to the bulk band structure $E_j(\mathbf{k})$ to the scattering process.

Strictly speaking, the characteristics of the electronic structure of an infinite crystal can enter multiple-scattering theory in the case of a bounded crystal of a large size only asymptotically, through the behavior of the wave function of the scattering electron $\Psi(\mathbf{r})$ deep inside the crystal. Therefore in order to separate the bulk contribution to partial transmission coefficients in the model of a semi-infinite crystal, we neglect, in accordance with the above approximations, the structure of the surface potential barrier and set the potential $V_+(\mathbf{r})$ of a semi-infinite crystal occupying a half-space $x_\perp \geqslant 0$ to

$$V_+(\mathbf{r}) = V(\mathbf{r})\Theta(x_\perp), \tag{1}$$

where $V(\mathbf{r})$ is the potential of an infinite crystal, and $\Theta(x)$ is the Heaviside function.

If all electrons in an incident beam have an energy E and a wave-vector component parallel to the surface $\mathbf{K}_\parallel$, then in the bulk of the crystal ($x_\perp \gg 0$) we have[11]

$$\Psi(\mathbf{K}_\parallel, E; \mathbf{r}) = \sum_{j=1}^{N(E,\mathbf{K}_\parallel)} T_j \Phi_j(\mathbf{k}_\parallel, k_\perp^{(j)}(E); \mathbf{r}), \tag{2}$$

where $\mathbf{k}_\parallel = \mathbf{K}_\parallel - \mathbf{g}_\nu$ is the reduced quasimomentum, $\mathbf{g}_\mu$ are reciprocal-lattice vectors of a semi-infinite crystal, $N(E,\mathbf{K}_\parallel)$ is the number of energy bands of an infinite crystal satisfying the energy conservation relation

$$E_j(\mathbf{k}_\parallel, k_\perp^{(j)}) = E \tag{3}$$

and the condition of the absence of electron sources in the crystal bulk $\partial E_j(\mathbf{k}_\parallel, k_\perp^{(j)}(E))/\partial k_\perp > 0$, and $E_j(\mathbf{k}_\parallel, k_\perp^{(j)})$ is the dispersion relation for the Bloch electron in the jth band of an infinite crystal with a wave function $\Phi_j(\mathbf{k}_\parallel, k_\perp^{(j)}(E); \mathbf{r})$.

The partial transmission coefficients T_j entering Eq. (2) are of considerable interest and represent the subject of this investigation. The contribution of the corresponding band to VLEED (partial absorbed current) and to photoemission (partial photocurrent) was shown[2,5] to be proportional to $|T_j|^2$.

The wave function of a scattering electron satisfies the equation

$$\Psi(\mathbf{K}_\parallel, E; \mathbf{r}) = \exp\{i(\mathbf{K}_\parallel, \sqrt{E - \mathbf{K}_\parallel^2})\mathbf{r}\} - \int_\Omega G_{\mathbf{k}}(\mathbf{r}, \mathbf{r}'; E + i0) V_+(\mathbf{r}') \Psi(\mathbf{K}_\parallel, E, \mathbf{r}') d\mathbf{r}' \tag{4}$$

with the free-electron Green's function[12,13] defined in the cell Ω ($-\infty < x_\perp < \infty$) of a semi-infinite crystal.

Following this model, we replace the function $\Psi(\mathbf{r}')$ in the region Ω_+ ($x'_\perp \geqslant 0$) with its asymptotic expression (2). Then in the vacuum region and for $x_\perp \leqslant 0$ we obtain, to within terms decaying exponentially in $|x_\perp|$,[14]

$$\Psi(\mathbf{K}_\parallel, E; \mathbf{r}) = \exp\{i(\mathbf{K}_\parallel, \sqrt{E - \mathbf{K}_\parallel^2})\mathbf{r}\} - \sum_{\mathbf{g}_\mu = 0}^{\mathbf{g}_\mu^{\max}} \frac{i \exp\{i(\mathbf{k}_\parallel + \mathbf{g}_\mu, -\sqrt{E - (\mathbf{k}_\parallel + \mathbf{g}_\mu)^2})\mathbf{r}\}}{2S\sqrt{E - (\mathbf{k}_\parallel + \mathbf{g}_\mu)^2}} \times \sum_{j=1}^{N(E,\mathbf{K}_\parallel)} T_j a_j^-(\mathbf{k}_\parallel + \mathbf{g}_\mu, E), \tag{5}$$

where S is the area of the section of the Ω cell by the surface plane, and

$$a_j^-(\mathbf{k}_\parallel + \mathbf{g}_\mu, E) = \int_{\Omega_+} \exp\{i(\mathbf{k}_\parallel + \mathbf{g}_\mu, -\sqrt{E - (\mathbf{k}_\parallel + \mathbf{g}_\mu)^2})\mathbf{r}\} \times V(\mathbf{r}) \Phi_j(\mathbf{k}_\parallel, k_\perp^{(j)}(E); \mathbf{r}) d\mathbf{r}. \tag{6}$$

All nondecaying terms, for which $(\mathbf{k}_\parallel + \mathbf{g}_\mu)^2 \leqslant E$, are retained in the sum over $\mathbf{g}_\mu$ in (5).

Consider now a semi-infinite crystal with a Hamiltonian $\hat{H}^+ = -\Delta + V_+(\mathbf{r})$ as an infinite crystal but with the $x_\perp < 0$ layers removed, i.e., we set

$$\hat{H}^+ = \hat{H}^\infty - V(\mathbf{r})\Theta(-x_\perp). \tag{7}$$

If $G_{\mathbf{k}}^{(\infty)}(\mathbf{r}, \mathbf{r}'; E)$ is Green's function of the $\hat{H}^\infty$ operator defined in the Ω cell, then it can be shown that

$$\Psi(\mathbf{K}_\parallel, E; \mathbf{r}) = \int_{\Omega_-} G_{\mathbf{k}}^{(\infty)}(\mathbf{r}, \mathbf{r}'; E) V(\mathbf{r}') \Psi(\mathbf{K}_\parallel, E; \mathbf{r}') d\mathbf{r}', \tag{8}$$

where Ω_- is the $x_\perp < 0$ region of the Ω cell.

For $x_\perp > x'_\perp$ one obtains,[15] to within terms decaying exponentially for $|x_\perp - x'_\perp| \to \infty$,

$$G_{\mathbf{k}}^{(\infty)}(\mathbf{r}, \mathbf{r}'; E) = id \sum_{j=1}^{N(E,\mathbf{K}_\parallel)} \frac{\Phi_j(\mathbf{r}; \mathbf{k}_\parallel, k_\perp^{(j)}) \Phi_j^*(\mathbf{r}'; \mathbf{k}_\parallel, k_\perp^{(j)})}{\partial E_j(\mathbf{k}_\parallel, k_\perp^{(j)})/\partial k_\perp}, \tag{9}$$

where d is the interplanar distance.

As before, we set $\Psi(\mathbf{r}')$ in Ω_- equal to its asymptotic expression (5) to obtain for $x_\perp \gg 0$, with due account of Eqs. (8), (9), and (2),

$$\sum_{j=1}^{N(E,\mathbf{K}_\parallel)} T_j \Phi_j(\mathbf{r}; \mathbf{k}_\parallel, k_\perp^{(j)}(E)) = id \sum_{j=1}^{N(E,\mathbf{K}_\parallel)} \frac{\Phi_j(\mathbf{r}; \mathbf{k}_\parallel, k_\perp^{(j)})}{\partial E_j(\mathbf{k}_\parallel, k_\perp^{(j)})/\partial k_\perp} \left[b_j^+(\mathbf{K}_\parallel, E) - \sum_{\mathbf{g}_\mu = 0}^{\mathbf{g}_\mu^{\max}} \frac{i b_j^-(\mathbf{k}_\parallel + \mathbf{g}_\mu, E)}{2S\sqrt{E - (\mathbf{k}_\parallel + \mathbf{g}_\mu)^2}} \times \sum_{j=1}^{N(E,\mathbf{K}_\parallel)} T_i a_i^-(\mathbf{k}_\parallel + \mathbf{g}_\mu, E) \right], \tag{10}$$

where

$$b_j^{\pm}(\mathbf{k}_\parallel+\mathbf{g}_\mu,E)=\int_{\Omega_-}\Phi_j^*(\mathbf{r};\mathbf{k}_\parallel,k_\perp^{(j)}(E))V(\mathbf{r})\times\exp\{i(\mathbf{k}_\parallel+\mathbf{g}_\mu,\pm\sqrt{E-(\mathbf{k}_\parallel+\mathbf{g}_\mu)^2})\}d\mathbf{r}. \quad (11)$$

Averaging (11) over an arbitrarily small but finite primary-beam energy interval yields

$$b_j^{\pm}(\mathbf{k}_\parallel+\mathbf{g}_\mu,E)=\int_S\exp\{i(\mathbf{k}_\parallel+\mathbf{g}_\mu)\mathbf{r}_\parallel\}\times\left\{\frac{\partial}{\partial x_\perp}\Phi_j^*(\mathbf{r}_\parallel,0;\mathbf{k}_\parallel,k_\perp^{(j)}(E))\mp i\sqrt{E-(\mathbf{k}_\parallel+\mathbf{g}_\mu)^2}\Phi_j^*(\mathbf{r}_\parallel,0;\mathbf{k}_\parallel,k_\perp^{(j)}(E))\right\}d\mathbf{r}_\parallel \quad (12)$$

and

$$a_j^-(\mathbf{k}_\parallel+\mathbf{g}_\mu,E)=-b_j^{-*}(\mathbf{k}_\parallel+\mathbf{g}_\mu,E). \quad (13)$$

In view of Eq. (10), the partial transmission coefficients T_j satisfy the coupled equations

$$\sum_{i=1}^{N(E,\mathbf{K}_\parallel)}\left[\delta_{ij}\frac{\partial E_j(\mathbf{k}_\parallel,k_\perp^{(j)})}{\partial k_\perp}+\frac{d}{2S}\sum_{\mathbf{g}_\mu=0}^{\mathbf{g}_\mu^{\max}}\frac{b_j^-(\mathbf{k}_\parallel+\mathbf{g}_\mu,E)b_i^{-*}(\mathbf{k}_\parallel+\mathbf{g}_\mu,E)}{\sqrt{E-(\mathbf{k}_\parallel+\mathbf{g}_\mu)^2}}\right]T_i=idb_j^+(\mathbf{K}_\parallel,E). \quad (14)$$

2. EFFICIENCY OF THE AMS APPROACH: ACCURACY AND PRACTICAL REALIZATION

The possibilities of the AMS approach were tested by comparing it with the results obtained[2,5] by the matching method on a model cubic (100) crystal. This model is very close to the Cu(111) case. We chose it because by varying properly the model crystal-field potential $V(\mathbf{r})$ one could obtain various band configurations $E_j(\mathbf{k})$ similar to the real ones, and study in detail the properties of the AMS approach. A typical situation is displayed in Fig. 1. The results obtained are presented in the form of partial absorbed currents $I_j=|T_j|^2v_{g\perp}$ ($v_{g\perp}$ is the electron group-velocity component normal to the surface).

The AMS approach demonstrated a good accuracy throughout the range of reasonable variation of $V(\mathbf{r})$; indeed, the singularities in the energy dependence of T_j obtained in the two calculations practically coincide. This aspect is crucial for an analysis of VLEED data. The agreement is clearly better than that obtained using semiempirical methods.[5] It becomes still better if the fraction of Fourier components of the type of decaying plane waves in Bloch states increases (see Fig. 1), although the AMS approach does not make use of the free-electron approximation. The slightly larger discrepancy seen far from the free-electron parts of the bands is caused by the limited basis set employed in the matching method. Remarkably, the agreement remains good even under strong scattering, i.e., for potentials $V(\mathbf{r})$ which yield dispersion relations $E_j(\mathbf{k})$ differing considerably from the free-electron one.

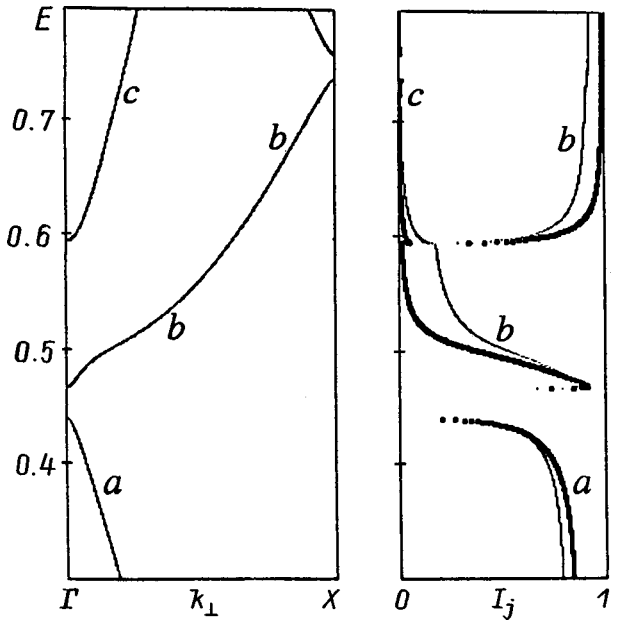

FIG. 1. A typical VLEED-spectrum calculation for normal incidence of electrons on a cubic (100) crystal. Left: $E_j(k_\perp)$, right: partial Bloch-wave absorbed currents $I_j=|T_j|^2v_{g\perp}$: thin lines — matching procedure, solid lines — AMS approach. Energy in $4|\Gamma X|^2$ units. In this calculation, the $V(\mathbf{r})$ Fourier components were $V_0=-0.5$, $V_4=0.01$, $V_8=0.02$, $V_{16}=0.06$, and the others are zero.

It should be noted that in the $V(\mathbf{r})=-V_0\Theta(x_\perp)$ case (the jellium model with a stepped surface barrier) the AMS approach does not involve any approximations, because the wave function in a crystal coincides with its asymptotic form even in the near-surface region. In this case the problem of T_j determination allows an analytic solution, and the results obtained coincide completely with those of AMS.

The AMS approach is fairly straightforward. The quantities of interest can be derived using standard computational programs developed for bulk band structure calculations (see Ref. 5 for practical aspects). Because of the equation system obtained being low order and of the absence of instability effects, the method permits one to operate with crystals having many atoms in the unit cell, which are still not amenable to numerical calculation by the exact matching procedure. It should be pointed out that Eq. (14) acquires the simplest and most revealing form when the unit cell of a semi-infinite crystal is set perpendicular to its surface. For real crystals this can require introduction of a large bulk unit cell,[16] which contains a greater number of atoms than the standard one. In band structure calculations this is simply equivalent to increasing the basis set.

Thus the AMS approach to analyzing VLEED data outlined above is based primarily on the fact that because of weak absorption the structure of VLEED spectra is dominated by the behavior of the wave function in the bulk of a crystal. This becomes manifest in a direct relation between the VLEED intensity and the volume dispersion relation $E_j(\mathbf{k})$, which has been expressed for the first time in the

form of an analytic expression connecting the Bloch wave amplitudes with the critical points ($\partial E_j/\partial k_\perp = 0$) in the $E_j(\mathbf{k})$ relationship. The two approaches exhibit a remarkably good agreement over a broad range of $E_j(\mathbf{k})$ configurations, including bands differing strongly from the free-electron ones. The approach is straightforward and computationally efficient. It is promising for wherever one has to analyze band aspects of VLEED, in particular, in experimental band-structure mapping by the VLEED method.

*)Permanent address: Institute of High-Speed Computations and Databases, Russian Academy of Sciences, 194291 St. Petersburg, Russia.

[1] V. N. Strocov, Int. J. Mod. Phys. B **9**, 1755 (1995).
[2] V. N. Strocov, H. Starnberg, and P. O. Nilsson, J. Phys.: Condens. Matter **8**, 7539 (1996); Phys. Rev. B **56**, 1717 (1997).
[3] V. N. Strocov, H. Starnberg, P. O. Nilsson, H. E. Brauer, and L. J. Holleboom, Phys. Rev. Lett. **79**, 467 (1997).
[4] V. N. Strocov, R. Claessen, G. Nicolay, S. Hüfner, A. Kimura, A. Harasawa, S. Shin, A. Kakizaki, P. O. Nillson, H. I. Starnberg, and P. Blaha, Phys. Rev. Lett. **81**, 4943 (1998).
[5] V. N. Strocov, Solid State Commun. **106**, 101 (1998).
[6] G. Capart, Surf. Sci. **13**, 361 (1969).
[7] J. B. Pendry, J. Phys. C **2**, 2273 (1969).
[8] D. L. Smith and C. Mailhiot, Rev. Mod. Phys. **62**, 173 (1990).
[9] E. E. Krasovskii and W. Schattke, Phys. Rev. B **56**, 12874 (1997).
[10] J. B. Pendry, *Low-Energy Electron Diffraction* (Academic, London, 1974); M. A. van Hove and S. Y. Tong, *Surface Crystallography by LEED* (Springer, Berlin, 1979).
[11] Yu. P. Chuburin, Teor. Mat. Fiz. **77**, 472 (1988).
[12] N. Kar and P. Soven, Phys. Rev. B **11**, 3761 (1975).
[13] W. Kohn, Phys. Rev. B **11**, 3756 (1975).
[14] Yu. P. Chuburin, Teor. Mat. Fiz. **72**, 120 (1987).
[15] Yu. P. Chuburin, Teor. Mat. Fiz. **98**, 38 (1994).
[16] R. A. Evarestov, M. I. Petrashen, and E. M. Ledovskaya, Phys. Status Solidi B **68**, 453 (1975).

Translated by G. Skrebtsov

Influence of interatomic correlation effects on short-range order in hexagonal close-packed polycrystalline alloys

V. M. Silonov

M. V. Lomonosov Moscow State University, 119899 Moscow, Russia

E. V. Evlyukhina, O. V. Kris'ko, and A. B. Evlyukhin

Vladimir State University, 600026 Vladimir, Russia

(Submitted December 21, 1998; resubmitted April 12, 1999)
Fiz. Tverd. Tela (St. Petersburg) **41**, 2109–2115 (December 1999)

The first x-ray diffraction procedure suitable for the investigation of short-range order in polycrystalline alloys having a hexagonal close-packed (hcp) lattice is developed on the basis of the theory proposed by M. A. Krivoglaz for diffuse x-ray scattering by hcp single-crystal alloys. This procedure takes into account specific details of the crystal structure of the hcp lattice, in particular, the presence of two atoms in the unit cell and the close radii of the individual coordination spheres. The realistic character of the procedure is demonstrated experimentally in the example of hcp Mg–Dy and Mg–Tb alloys. The new procedure is used to calculate, for the first time, the modulating functions of linear and quadratic size effects in Mg–Dy and Mg–Tb alloys. It is shown that the size-effect modulating functions for coordination spheres with close radii have different characters, and their inclusion in diffuse scattering sets the stage for solving the problem of calculating the short-range order parameters on these spheres.
 [S1063-7834(99)00212-9]

Atomic ordering in alloys having body-centered cubic and face-centered cubic structures have now been studied to a satisfactory degree. Up to now, however, there has been a lack of correct experimental methods for investigating the short-range order of polycrystalline hexagonal close-packed (hcp) alloys. The main reason for this deficit is the complexity of the calculations required by the presence of two atoms in the unit cell, a condition that severely limits the applicability of the scattering theory for crystals with an hcp lattice, developed by M. A. Krivoglaz back in the 1960s,[1] to experimental studies of polycrystalline structures. In the past the standard procedure developed for alloys containing one atom in the unit cell has been used to investigate short-range order in polycrystalline alloys having an hcp lattice.[2–5] This approach ignores the fact that the hcp lattice is not a Bravais lattice, and its unit cell contains two atoms. In polycrystalline alloys having an hcp lattice the individual coordination spheres have close radii, compounding the difficulties of determining the short-range order parameters on these spheres. In the standard procedure such spheres are conjoined, and effective short-range order parameters are estimated for them.[2–6] However, this approach can yield incorrect results.

It is a well-known fact (see, e.g., Refs. 1 and 2) that in the scattering of x-rays by solid solutions the intensity distribution is governed both by factors characterizing specific details of the internal structure of an alloy and by factors associated with the general phenomena of x-ray scattering by crystal structures. Among the factors identified with internal structure are short-range order, static lattice distortions, the concentration and atomic factors of the alloy components, etc. The specific features imparted to x-ray scattering by differences in the atomic factors of the components and static lattice distortions are called size effects. They can be both linear and quadratic.

The objective of the present study is to develop an x-ray structural procedure for the investigation of short-range order in hcp polycrystalline alloys, taking into account the distinctive features of the crystal lattice, and to test the procedure in application to magnesium alloys doped with rare-earth metals. The proposed procedure permits the presence of two atoms in the unit cell of alloys having an hcp structure to be taken into account in the investigation of short-range order, along with the influence of interatomic correlation (size) effects on short-range order.

1. PROCEDURE FOR THE INVESTIGATION OF SHORT-RANGE ORDER IN HCP POLYCRYSTALLINE ALLOYS

An expression for the intensity of diffuse x-ray scattering by a single crystal having an hcp lattice has been derived by Krivoglaz and Tyu Khao,[1] who interpreted the lattice as two intermeshed primitive lattices (Fig. 1). By virtue of the equivalence of the sublattices γ and γ' ($\gamma,\gamma'=1,2$) the vectors $\boldsymbol{\rho}_{\gamma\gamma'}$ connecting the sublattice sites and the correlation parameters $\varepsilon(\boldsymbol{\rho}_{\gamma\gamma'})$:

$$\boldsymbol{\rho}_{11}=\boldsymbol{\rho}_{22}, \quad \boldsymbol{\rho}_{12}=-\boldsymbol{\rho}_{21},$$
$$\varepsilon(\boldsymbol{\rho}_{12})=\varepsilon(\boldsymbol{\rho}_{21}), \quad \varepsilon(\boldsymbol{\rho}_{11})=\varepsilon(\boldsymbol{\rho}_{22}). \tag{1}$$

Taking Eqs. (1) into account, we expand the equation for the diffuse x-ray scattering intensity[1] into two parts:

$$I(\mathbf{q})=I_0(\mathbf{q})+I_1(\mathbf{q}), \tag{2}$$

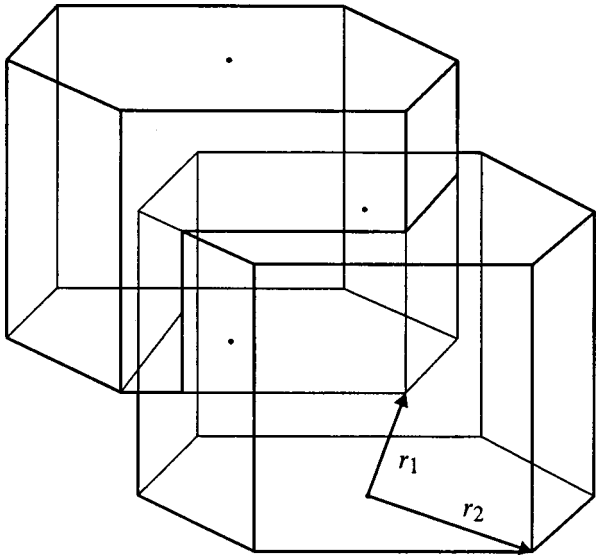

FIG. 1. Lattice having an hcp structure: $\mathbf{r}_1$ and $\mathbf{r}_2$ are the radius vectors of the first and second coordination spheres.

where $I_0(\mathbf{q})$ is a term that does not depend on the correlation parameters,

$$I_0(\mathbf{q}) = 2Nc(1-c)[f^2\{(\mathbf{q}\cdot\mathbf{A_{Q11}})(\mathbf{q}\cdot\mathbf{A^*_{Q11}}) + (\mathbf{q}\cdot\mathbf{A_{Q21}}) \times(\mathbf{q}\cdot\mathbf{A^*_{Q21}}) + 2\,\mathrm{Re}\,((\mathbf{q}\cdot\mathbf{A_{Q11}})(\mathbf{q}\cdot\mathbf{A^*_{Q21}}) \times\exp[i\mathbf{G}\cdot(\mathbf{R}_1-\mathbf{R}_2)])\} - f\Delta f\{\,\mathrm{Re}\,(\mathbf{q}\cdot\mathbf{A_{Q11}} \times\exp[i\mathbf{G}\cdot\mathbf{R}_1]) + \mathrm{Re}\,(\mathbf{q}\cdot\mathbf{A_{Q21}}\exp[i\mathbf{G}\cdot\mathbf{R}_2]) + \mathrm{Re}(\mathbf{q}\cdot\mathbf{A_{Q12}}\exp[i\mathbf{G}\cdot\mathbf{R}_1]) + \mathrm{Re}\,(\mathbf{q}\cdot\mathbf{A_{Q22}}\exp[i\mathbf{G}\cdot\mathbf{R}_2])\} + \Delta f^2], \tag{3}$$

and $I_1(\mathbf{q})$ is a term associated with the correlation parameters,

$$I_1(\mathbf{q}) = N\Bigg[2\sum_{\boldsymbol{\rho}_{11}}\varepsilon(\boldsymbol{\rho}_{11})\exp(i\mathbf{Q}\cdot\boldsymbol{\rho}_{11})(f^2\{(\mathbf{q}\cdot\mathbf{A_{Q11}})(\mathbf{q}\cdot\mathbf{A^*_{Q11}}) + (\mathbf{q}\cdot\mathbf{A_{Q21}})(\mathbf{q}\cdot\mathbf{A^*_{Q21}}) + 2\,\mathrm{Re}\,((\mathbf{q}\cdot\mathbf{A_{Q11}})(\mathbf{q}\cdot\mathbf{A^*_{Q21}}) \times\exp[i\mathbf{G}\cdot(\mathbf{R}_1-\mathbf{R}_2)])\} - f\Delta f\{2\,\mathrm{Re}\,((\mathbf{q}\cdot\mathbf{A_{Q11}}) \times\exp[i\mathbf{G}\cdot\mathbf{R}_1]) + 2\,\mathrm{Re}\,((\mathbf{q}\cdot\mathbf{A_{Q21}})\exp[i\mathbf{G}\cdot\mathbf{R}_2])\} + \Delta f^2) + 2\sum_{\boldsymbol{\rho}_{12}}\varepsilon(\boldsymbol{\rho}_{12})\cos(\mathbf{Q}\boldsymbol{\rho}_{12})(f^2\{2\,\mathrm{Re}\,((\mathbf{q}\cdot\mathbf{A_{Q11}}) \times(\mathbf{q}\cdot\mathbf{A^*_{Q12}})) + \mathrm{Re}\,((\mathbf{q}\cdot\mathbf{A_{Q11}})^2\exp[i\mathbf{G}\cdot(\mathbf{R_1}-\mathbf{R}_2)] + (\mathbf{q}\cdot\mathbf{A^*_{Q21}})^2\exp[i\mathbf{G}\cdot(\mathbf{R}_2-\mathbf{R}_1)])\} - f\Delta f\{\mathrm{Re}\,((\mathbf{q}\cdot\mathbf{A_{Q11}})[\exp[i\mathbf{G}\cdot\mathbf{R}_1]+\exp[-i\mathbf{G}\cdot\mathbf{R}_2]] + (\mathbf{q}\cdot\mathbf{A_{Q21}})[\exp[i\mathbf{G}\cdot\mathbf{R}_2]+\exp[-i\mathbf{G}\cdot\mathbf{R}_1]])\} + \Delta f^2)\Bigg]. \tag{4}$$

Here N is the number of unit cells, $\mathbf{q}$ is the scattering vector, $\mathbf{G}$ is the reciprocal lattice vector, $\mathbf{Q}$ is the scattering vector normalized to the first Brillouin zone ($\mathbf{Q}=\mathbf{q}-\mathbf{G}$), c is the concentration, $\Delta f = f_A - f_B$, $f = c_A f_A + c_B f_B$, c_A and c_B are the concentrations of the components, f_A and f_B are their atomic factors, $\mathbf{A}_{\mathbf{Q}\gamma\gamma'}$ are the proportionality factors between Fourier components of the static displacements and concentrations, and $\mathbf{R}_1$ and $\mathbf{R}_2$ are the radius vectors of atoms in the unit cell; the first of these radius vectors is conveniently placed at the origin of a Cartesian coordinate system $\mathbf{R}_1=(0,0,0)$, so that when the basis vectors $\mathbf{a}_1=(\alpha/2,\sqrt{3}\alpha/2,0)$, $\mathbf{a}_2=\alpha/2,-\sqrt{3}\alpha/2,0)$, $\mathbf{a}_3=(0,0,c)$ are taken into account, the coordinates of the second atom are $\mathbf{R}_2=(0,\alpha/\sqrt{3},c/2)$; here α and c are the lattice constants.

The intensities $I_1(\mathbf{q})$ in Eq. (4) can be expanded into six terms:

$$I_1(\mathbf{q}) = I_\alpha^{(1)}(\mathbf{q}) + I_L^{(1)}(\mathbf{q}) + I_{\mathrm{sq}}^{(1)}(\mathbf{q}) + I_\alpha^{(2)}(\mathbf{q}) + I_L^{(2)}(\mathbf{q}) + I_{\mathrm{sq}}^{(2)}(\mathbf{q}). \tag{5}$$

By way of comparison, the expression for the diffuse scattering intensity (I_D), in which only one atom is contained in the unit cell,[6] has the form

$$I_D = I_\alpha + I_L + I_{\mathrm{sq}}.$$

Here I_α, I_L, and I_{sq} are the intensities associated with short-range order and with linear and quadratic size effects, respectively.[2]

The superscript (1) attached to the intensities in Eq. (5) indicates that correlations between atoms within each sublattice are taken into account in the expressions for $I_\alpha^{(1)}(\mathbf{q})$, $I_L^{(1)}(\mathbf{q})$, and $I_{\mathrm{sq}}^{(1)}(\mathbf{q})$. The superscript (2) indicates that correlations between atoms of different sublattices are taken into account in the expressions for $I_\alpha^{(2)}(\mathbf{q})$, $I_L^{(2)}(\mathbf{q})$, and $I_{\mathrm{sq}}^{(2)}(\mathbf{q})$.

Thus, allowing for interactions within each sublattice and making use of the relation between the correlation parameters and short-range order parameters $[\Sigma_{\boldsymbol{\rho}_{\gamma\gamma'}}\varepsilon(\boldsymbol{\rho}_{\gamma\gamma'}) = c(1-c)\Sigma_{\boldsymbol{\rho}_{\gamma\gamma'}}\alpha(\boldsymbol{\rho}_{\gamma\gamma'})]$, we have

$$I_\alpha^{(1)}(\mathbf{q}) = 2Nc(1-c)\Delta f^2\sum_{\boldsymbol{\rho}_{11}}\alpha(\boldsymbol{\rho}_{11})\exp(i\mathbf{Q}\cdot\boldsymbol{\rho}_{11}), \tag{6}$$

$$I_L^{(1)}(\mathbf{q}) = -4Nc(1-c)f\Delta f\sum_{\boldsymbol{\rho}_{11}}\alpha(\boldsymbol{\rho}_{11})\exp(i\mathbf{Q}\cdot\boldsymbol{\rho}_{11}) \times[\mathrm{Re}\,(\mathbf{q}\cdot\mathbf{A_{Q11}}) + \mathrm{Re}\,(\mathbf{q}\cdot\mathbf{A_{Q21}}\exp[i\mathbf{G}\cdot\mathbf{R}_2])], \tag{7}$$

$$I_{\mathrm{sq}}^{(1)}(\mathbf{q}) = 2Nc(1-c)f^2\sum_{\boldsymbol{\rho}_{11}}\alpha(\boldsymbol{\rho}_{11})\exp(i\mathbf{Q}\cdot\boldsymbol{\rho}_{11})\{(\mathbf{q}\cdot\mathbf{A_{Q11}}) \times(\mathbf{q}\cdot\mathbf{A^*_{Q11}}) + (\mathbf{q}\cdot\mathbf{A_{Q21}})(\mathbf{q}\cdot\mathbf{A^*_{Q21}}) + 2\,\mathrm{Re}\,((\mathbf{q}\cdot\mathbf{A_{Q11}}) \times(\mathbf{q}\cdot\mathbf{A^*_{Q21}})\exp[-i\mathbf{G}\cdot\mathbf{R}_2])\}. \tag{8}$$

Taking into account interactions between atoms of different sublattices, we obtain

$$I_\alpha^{(2)}(\mathbf{q}) = 2Nc(1-c)\Delta f^2\sum_{\boldsymbol{\rho}_{12}}\alpha(\boldsymbol{\rho}_{12})\cos(\mathbf{Q}\cdot\boldsymbol{\rho}_{12}), \tag{9}$$

$$I_L^{(2)}(\mathbf{q}) = -2Nc(1-c)f\Delta f\sum_{\boldsymbol{\rho}_{12}} \alpha(\boldsymbol{\rho}_{12})\cos(\mathbf{Q}\cdot\boldsymbol{\rho}_{12}) \times[\mathrm{Re}\,((\mathbf{q}\cdot\mathbf{A}_{\mathbf{Q11}})(1+\exp[-i\mathbf{G}\cdot\mathbf{R}_2])) + \mathrm{Re}\,(\mathbf{q}\cdot\mathbf{A}_{\mathbf{Q12}}(1+\exp[i\mathbf{G}\cdot\mathbf{R}_2]))], \quad (10)$$

$$I_{\mathrm{sq}}^{(2)}(\mathbf{q}) = 2Nc(1-c)f^2\sum_{\boldsymbol{\rho}_{12}} \alpha(\boldsymbol{\rho}_{12})\cos(\mathbf{Q}\cdot\boldsymbol{\rho}_{12}) \times\{2\,\mathrm{Re}\,((\mathbf{q}\cdot\mathbf{A}_{\mathbf{Q11}})(\mathbf{q}\cdot\mathbf{A}^*_{\mathbf{Q12}})) + \mathrm{Re}\,((\mathbf{q}\cdot\mathbf{A}_{\mathbf{Q11}})^2\exp[-i\mathbf{G}\cdot\mathbf{R}_2] + (\mathbf{q}\cdot\mathbf{A}^*_{\mathbf{Q21}})^2\exp[i\mathbf{G}\cdot\mathbf{R}_2])\}. \quad (11)$$

Although the most accurate short-range order values can be obtained from measurements of the intensity of diffuse scattering by a single crystal, in practice it is customary to work with polycrystalline objects. We must therefore transform from the expressions for the single-crystal scattering intensities $I_\alpha^{(j)}$, $I_L^{(j)}$, and $I_{\mathrm{sq}}^{(j)}$ to expressions for the intensities $I_{\alpha,p}^{(j)}$, $I_{L,p}^{(j)}$, and $I_{\mathrm{sq},p}^{(j)}$ in the case of polycrystals. Such a transformation requires that we average Eqs. (6)–(11) over all orientations of the scattering vector.

The averaging operation can be performed analytically only for Eqs. (6) and (9):

$$I_{\alpha,p}^{(j)}(q) = 2Nc(1-c)\Delta f^2\sum_i \alpha_i C_i\frac{\sin(qR_i)}{(qR_i)}, \quad (12)$$

where $j=1,2$, C_i and α_i are the coordination number and the short-range order parameter for the ith coordination sphere, and R_i is the radius of the ith coordination sphere.

All other terms can be averaged numerically by integrating in spherical coordinates over the angles γ and ϕ. Inasmuch as the first Brillouin zone has translational symmetry, the integration can be performed within the limits of the irreducible part, which occupies 1/24 of the volume of the first zone. As a result, the averaging is carried out over ϕ in the limits from 0 to $\pi/6$ and over the angle γ in the limits from 0 to $\pi/2$.

The expression for $I_0(\mathbf{q})$ is conveniently expanded into two parts, one that takes linear effects into account, and the other for quadratic effects:

$$I_{L,p}(q) = \frac{6}{\pi}\int_0^{\frac{\pi}{6}} d\phi\int_0^{\frac{\pi}{2}} \{\mathrm{Re}\,(\mathbf{q}\cdot\mathbf{A}_{\mathbf{Q11}}) + \mathrm{Re}(\mathbf{q}\cdot\mathbf{A}_{\mathbf{Q12}}) + \mathrm{Re}\,(\mathbf{q}\cdot\mathbf{A}_{\mathbf{Q21}}\exp[i\mathbf{G}\cdot\mathbf{R}_2]) + \mathrm{Re}\,(\mathbf{q}\cdot\mathbf{A}_{\mathbf{Q22}}\exp[i\mathbf{G}\cdot\mathbf{R}_2])\}\sin\gamma d\gamma, \quad (13)$$

$$I_{\mathrm{sq},p}(q) = \frac{6}{\pi}\int_0^{\frac{\pi}{6}} d\phi\int_0^{\frac{\pi}{2}} \{(\mathbf{q}\cdot\mathbf{A}_{\mathbf{Q11}})(\mathbf{q}\cdot\mathbf{A}^*_{\mathbf{Q11}}) + (\mathbf{q}\cdot\mathbf{A}_{\mathbf{Q21}})\times(\mathbf{q}\cdot\mathbf{A}^*_{\mathbf{Q21}}) + 2\,\mathrm{Re}\,((\mathbf{q}\cdot\mathbf{A}_{\mathbf{Q11}})(\mathbf{q}\cdot\mathbf{A}^*_{\mathbf{Q21}})\times\exp[-i\mathbf{G}\cdot\mathbf{R}_2])\}\sin\gamma d\gamma. \quad (14)$$

The intensities due to size effects with allowance for intrasublattice interactions can be written in the form

$$I_{L,p}^{(1)}(q) = \frac{6}{\pi}\int_0^{\frac{\pi}{6}} d\phi\int_0^{\frac{\pi}{2}} \sum_{\boldsymbol{\rho}_{11}} \alpha(\boldsymbol{\rho}_{11})\exp(i\mathbf{q}\boldsymbol{\rho}_{11}) \times[2\,\mathrm{Re}\,(\mathbf{q}\cdot\mathbf{A}_{\mathbf{Q11}}) + 2\,\mathrm{Re}\,(\mathbf{q}\cdot\mathbf{A}_{\mathbf{Q21}}\exp[i\mathbf{G}\cdot\mathbf{R}_2])]\sin\gamma d\gamma, \quad (15)$$

$$I_{\mathrm{sq},p}^{(1)}(q) = \frac{6}{\pi}\int_0^{\frac{\pi}{6}} d\phi\int_0^{\frac{\pi}{2}} \sum_{\boldsymbol{\rho}_{11}} \alpha(\boldsymbol{\rho}_{11})\exp(i\mathbf{q}\boldsymbol{\rho}_{11})\{(\mathbf{q}\cdot\mathbf{A}_{\mathbf{Q11}}) \times(\mathbf{q}\cdot\mathbf{A}^*_{\mathbf{Q11}}) + (\mathbf{q}\cdot\mathbf{A}_{\mathbf{Q21}})(\mathbf{q}\cdot\mathbf{A}^*_{\mathbf{Q21}}) + 2\,\mathrm{Re}\,((\mathbf{q}\cdot\mathbf{A}_{\mathbf{Q11}})(\mathbf{q}\cdot\mathbf{A}^*_{\mathbf{Q21}})\exp \times[-i\mathbf{G}\cdot\mathbf{R}_2])\}\sin\gamma d\gamma. \quad (16)$$

Analogous expressions can be written with allowance for interactions between sublattices:

$$I_{L,p}^{(2)}(q) = \frac{6}{\pi}\int_0^{\frac{\pi}{6}} d\phi\int_0^{\frac{\pi}{2}} \sum_{\boldsymbol{\rho}_{12}} \alpha(\boldsymbol{\rho}_{12})\cos(\mathbf{q}\boldsymbol{\rho}_{12}) \times[\mathrm{Re}\,(\mathbf{q}\cdot\mathbf{A}_{\mathbf{Q11}}(1+\exp[-i\mathbf{G}\cdot\mathbf{R}_2])) + \mathrm{Re}\,(\mathbf{q}\cdot\mathbf{A}_{\mathbf{Q21}}(1+\exp[i\mathbf{G}\cdot\mathbf{R}_2]))]\sin\gamma d\gamma, \quad (17)$$

$$I_{\mathrm{sq},p}^{2}(q) = \frac{6}{\pi}\int_0^{\frac{\pi}{6}} d\phi\int_0^{\frac{\pi}{2}} \sum_{\boldsymbol{\rho}_{12}} \alpha(\boldsymbol{\rho}_{12})\cos(\mathbf{q}\boldsymbol{\rho}_{12}) \times\{2\,\mathrm{Re}\,((\mathbf{q}\cdot\mathbf{A}_{\mathbf{Q11}})(\mathbf{q}\mathbf{A}^*_{\mathbf{Q12}})) + \mathrm{Re}\,((\mathbf{q}\cdot\mathbf{A}_{\mathbf{Q11}})^2\exp[-i\mathbf{G}\cdot\mathbf{R}_2] + (\mathbf{q}\cdot\mathbf{A}^*_{\mathbf{Q21}})^2\exp[i\mathbf{G}\cdot\mathbf{R}_2])\}\sin\gamma d\gamma. \quad (18)$$

We now write the sums

$$\sum_{\boldsymbol{\rho}_{11}} \alpha(\boldsymbol{\rho}_{11})\exp(i\mathbf{q}\boldsymbol{\rho}_{11}) \quad \text{and} \quad \sum_{\boldsymbol{\rho}_{12}} \alpha(\boldsymbol{\rho}_{12})\cos(\mathbf{q}\boldsymbol{\rho}_{12})$$

in explicit form for the first six coordination spheres.

We enumerate the radii of the coordinations spheres $\mathbf{r}_1, \mathbf{r}_2, \ldots, \mathbf{r}_6$ in order of increasing distance from the atom designated as the origin. The first sublattice then contains the vectors $\mathbf{r}_2$, $\mathbf{r}_4$, and $\mathbf{r}_6$, and between the sublattices are the vectors $\mathbf{r}_1$, $\mathbf{r}_3$, and $\mathbf{r}_5$ (Fig. 1), so that we can write

$$\sum_{\boldsymbol{\rho}_{11}} \alpha(\boldsymbol{\rho}_{11})\exp(i\mathbf{q}\boldsymbol{\rho}_{11}) = \alpha_2\sum_{N=1}^{6}\exp(i\mathbf{q}\mathbf{r}_2) + \alpha_4\sum_{N=1}^{2}\exp(i\mathbf{q}\mathbf{r}_4) + \alpha_6\sum_{N=1}^{6}\exp(i\mathbf{q}\mathbf{r}_6), \quad (19)$$

where $\alpha_2=\alpha(\mathbf{r}_2)$, $\alpha_4=\alpha(\mathbf{r}_4)$, $\alpha_6=\alpha(\mathbf{r}_6)$, $\boldsymbol{\rho}_{11}$ denotes the radius vectors connecting the atom designated as the origin with all atoms in the first sublattice, and N is the number of atoms on the corresponding coordination spheres.

Analogously, for the second sum we have

$$\sum_{\boldsymbol{\rho}_{12}} \alpha(\boldsymbol{\rho}_{12})\cos(\mathbf{q}\boldsymbol{\rho}_{12}) = \alpha_1 \sum_{N=1}^{6} \cos(\mathbf{q}\mathbf{r}_1) + \alpha_3 \sum_{N=1}^{6} \cos(\mathbf{q}\mathbf{r}_3) + \alpha_5 \sum_{N=1}^{12} \cos(\mathbf{q}\mathbf{r}_5), \tag{20}$$

where $\alpha_1=\alpha(\mathbf{r}_1)$, $\alpha_3=\alpha(\mathbf{r}_3)$, $\alpha_5=\alpha(\mathbf{r}_5)$, and $\boldsymbol{\rho}_{12}$ denotes the set of vectors connecting the initial atom, located in the first sublattice, with atoms of the second lattice.

The Cartesian coordinates of atoms situated on the corresponding coordination spheres are readily calculated from the lattice geometry. The coordinates of the vector $\mathbf{q}$ are: $(2\pi/\alpha)q_x$, $(2\pi/\alpha)q_y$, $(2\pi/c)q_z$.

Doing the calculations, we obtain

$$\begin{aligned}\sum_{\boldsymbol{\rho}_{11}} \alpha(\boldsymbol{\rho}_{11})\exp(i\mathbf{q}\boldsymbol{\rho}_{11}) = \alpha_2[&2\cos(2\pi q_y) \\ &+ 2\cos\pi(\sqrt{3}q_x+q_y) \\ &+ 2\cos\pi(\sqrt{3}q_x-q_y)] \\ &+ \alpha_4[2\cos(2\pi q_z)] \\ &+ \alpha_6[2\cos(2\pi\sqrt{3}q_x) \\ &+ 2\cos\pi(\sqrt{3}q_x+3q_y) \\ &+ 2\cos\pi(\sqrt{3}q_x-3q_y)].\end{aligned} \tag{21}$$

For the next sum we have

$$\begin{aligned}\sum_{\boldsymbol{\rho}_{12}} \alpha(\boldsymbol{\rho}_{12})\cos(\mathbf{q}\boldsymbol{\rho}_{12}) = \alpha_1\Bigg[&2\cos\pi\left(-\frac{2}{\sqrt{3}}q_x+q_z\right) \\ &+ 2\cos\pi\left(\frac{1}{\sqrt{3}}q_x-q_y-q_z\right) \\ &+ 2\cos\pi\left(\frac{1}{\sqrt{3}}q_x+q_y+q_z\right)\Bigg] \\ &+ \alpha_3\Bigg[2\cos\pi\left(\frac{2}{\sqrt{3}}q_x+2q_y+q_z\right) \\ &+ 2\cos\pi\left(\frac{4}{\sqrt{3}}q_x-q_z\right) \\ &+ 2\cos\pi\left(-\frac{2}{\sqrt{3}}q_x+2q_y-q_z\right)\Bigg] \\ &+ \alpha_5\Bigg[2\cos\pi\left(\sqrt{7}q_x+\frac{\sqrt{7}}{\sqrt{3}}q_y+q_z\right) \\ &+ 2\cos\pi\left(\sqrt{7}q_x-\frac{\sqrt{7}}{\sqrt{3}}q_y+q_z\right) \\ &+ 4\cos\pi\left(-\sqrt{7}q_x-\frac{\sqrt{7}}{\sqrt{3}}q_y+q_z\right) \\ &+ 4\cos\left(2\pi\frac{\sqrt{7}}{\sqrt{3}}q_y\right)\cos\pi q_z\Bigg].\end{aligned} \tag{22}$$

Substituting Eq. (21) into (15) and (16) and substituting Eq. (22) into (17) and (18), we can then take into account the influence of size effects in the diffuse x-rayscattering intensity out to the sixth coordination sphere.

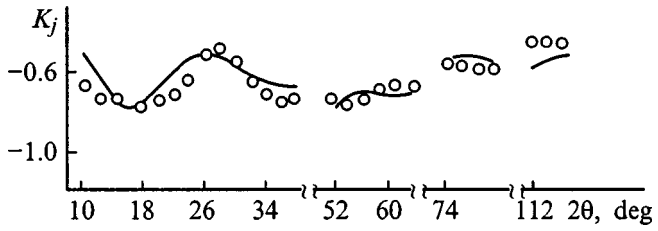

FIG. 2. Diffuse x-ray scattering intensity in the alloy Mg–3.4 at.% Dy, experimental (circles) and synthesized (solid curve); K_j is the diffuse x-ray scattering intensity normalized to Laue scattering.

The general expression for the intensity of diffuse x-ray scattering by a polycrystalline structure has the form

$$\begin{aligned}I_{D,p}(q) = AI_{L,p}(q) + BI_{\mathrm{sq},p}(q) + I^{(1)}_{\alpha,p}(q) + AI^{(1)}_{L,p}(q) \\ + BI^{(1)}_{\mathrm{sq},p}(q) + I^{(2)}_{\alpha,p}(q) + AI^{(2)}_{L,p}(q) + BI^{(2)}_{\mathrm{sq},p}(q),\end{aligned} \tag{23}$$

where $A=-2Nc(1-c)f\Delta f$, and $B=2Nc(1-c)f^2$. It is customary to facilitate the calculations by replacing expression (23) with the function

$$K(q)=I_{D,p}(q)/I_{LR}, \tag{24}$$

where $I_{LR}=Nc(1-c)\Delta f^2$ is the Laue scattering intensity. The short-range order parameters can be determined from the experimentally measured values of $K(q)$ by, for example, the least-squares method.[2]

2. SAMPLES AND EXPERIMENTAL PROCEDURE

The alloys chosen for the investigation were Mg-3.4 at.% Dy and Mg–2.9 at.% Tb, which were prepared at the A. A. Baĭkov Institute of Metallurgy. The raw materials had the following purities: magnesium 99.95%; rare-earth metals at least 99.82% with impurities mostly (0.10–0.13%) of other rare-earth metals. The alloys were melted in steel crucibles under flux VI2, which consists of a mixture of chlorides with a CaF_2 additive.[7,8] After ingots of the alloys had been cast, they were hot-pressed into rods of diameter 17 mm with an approximately 90% compression ratio. The rods were cut into blanks in the form of wafers having dimensions $3\times17\times20$ mm. The samples were then ground and polished with diamond pastes.

The diffuse x-ray scattering intensities were measured on an x-ray diffractometer of the DRON series using FeK_α radiation. Monochromatization was achieved on a flat silicon single crystal [(111) reflecting plane]. The scattered radiation was recorded by means of a BDS-6-05 scintillation counter.

The atomic factors and Compton scattering intensities of the components were taken from Ref. 9, and dispersion corrections were taken from Ref. 10. Thermal scattering was calculated from theory.[11]

The measurement results are shown in Figs. 2 and 3. It is evident from the figures that diffuse maxima typical of short-range order exist in the range of angles up to the first struc-

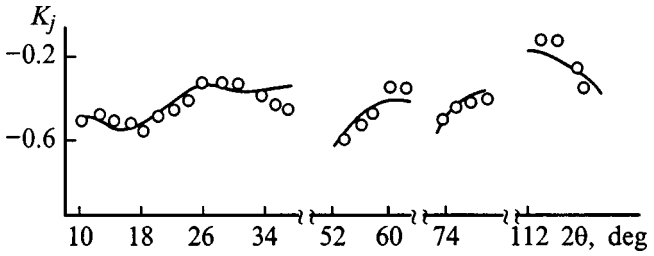

FIG. 3. Diffuse x-ray scattering intensity in the alloy Mg–2.9 at.% Tb, experimental (circles) and synthesized (solid curve); K_j is the diffuse x-ray scattering intensity normalized to Laue scattering.

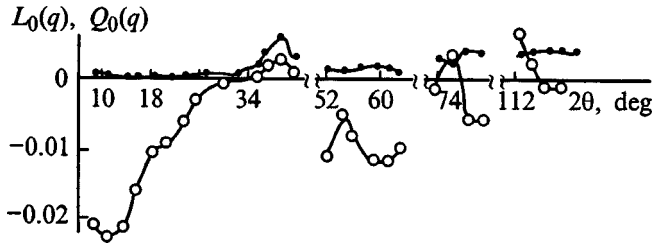

FIG. 4. Modulating functions of linear $[L_0(q)$, circles] and quadratic $[Q_0(q)$, dots] size effects on the zeroth coordination sphere for the alloy Mg-3.4 at.% Dy.

tural reflection, which is located in the scale-break interval along the 2Θ axis: $36-52°$. The curves are situated below the Laue background level, possibly because the actual concentration of rare-earth metals is lower in the subsurface layer. This condition could very likely be fostered by the sample preparation technology.

3. CALCULATION OF THE SIZE-EFFECT MODULATING FUNCTIONS

To facilitate the calculations, as mentioned, the diffuse x-rayscattering intensity is normalized to Laue scattering (24); in this case the size-effect terms occurring in the diffuse x-ray scattering intensity are called modulating functions of the size effects. Accordingly, the size-effect modulating functions characterize structural features associated with static lattice distortions, differences in the atomic factors of the alloy components, and the concentration of the latter.

Equations (13)–(18) have been used to calculate the modulating functions of linear and quadratic size effects on the zeroth and first two coordination spheres for polycrystalline alloys Mg–3.4 at.% Dy and Mg–2.9 at.% Tb.

The coefficients $\mathbf{A}_{\mathbf{Q}\gamma\gamma'}$ are calculated by the method of Krivoglaz and Tyu Khao, which is based on a simplified Born–Bagby model taking the lattice symmetry into account.[1]

Since the functions represented in Eqs. (13)–(18) are normalized, they must be multiplied by the characteristics of the alloy and divided by the Laue scattering intensity I_{LR}. We then have

$$L_i^{(j)}(q) = -2Nc(1-c)f\Delta f I_{L,p}^{(j)}/I_{LR}, \tag{25}$$

$$Q_i^{(j)}(q) = 2Nc(1-c)f^2 I_{\mathrm{sq},p}^{(j)}/I_{LR}, \tag{26}$$

where $L_i^{(j)}$ and $Q_i^{(j)}$ are the modulating functions of linear and quadratic size effects, respectively, $i=0,1,2$ enumerates the coordination spheres, and $j=1,2$ enumerates intrasublattice interactions $(j=1)$ and interactions between sublattices $(j=2)$. Atoms of different sublattices are situated on the first sphere: $L_1^{(2)}(q)$, $Q_1^{(2)}(q)$, and atoms of one sublattice are found on the second sphere: $L_2^{(1)}(q)$, $Q_2^{(1)}(q)$.

Figure 4 shows graphs of the size-effect modulating functions on the zeroth coordination sphere for the Mg–Dy alloy. The curves calculated for the Mg–Tb alloy have a similar form. Their similarity is attributable to the insignificant difference in the alloy characteristics by which the normalized functions are multiplied, owing to the close atomic numbers of terbium and dysprosium (66 and 65). It is evident from the figure that the main contribution to the diffuse x-ray scattering intensity in the first interval of angles is from the modulating functions of linear size effects, whereas those of quadratic effects are very close to zero in the range of angles from 10° to 32°, and only in the intervals from the second to the last do they have nonzero values and tend to increase as the scattering angle increases.

Figure 5 shows graphs of modulating functions of linear size effects, calculated by means of Eq. (25) for the Mg–Dy alloy. The character of the modulations is similar for the second alloy. On the other hand, the graphs of the functions on the first coordination sphere and on the second sphere have different forms for each individual alloy.

Figure 6 shows graphs of the modulating functions for quadratic size effects, calculated according to Eq. (26) for the Mg–Dy alloy. As in the case of the linear size effects, the character of the modulations is similar for the two investigated alloys. It is evident from the figure that their contribution to the total intensity is not very large in comparison with the contribution of the functions for linear size effects.

It is obvious from the figure that the functions for quadratic size effects, calculated for Mg–Dy and Mg–Tb alloys, which have an hcp lattice, differ significantly from the analogous functions for alloys having fcc and bcc structures. In the latter case the modulating functions for quadratic size

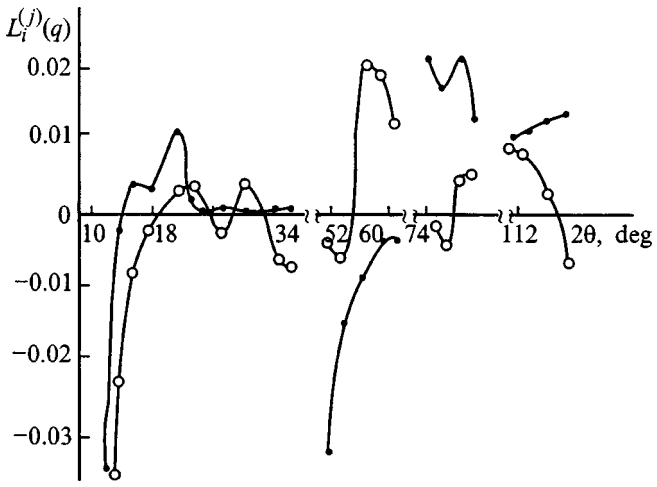

FIG. 5. Modulating functions of the linear size effect on the first $(L_1^{(2)}$, dots) and second $(L_2^{(1)}$, circles) coordination spheres for the alloy Mg–3.4 at.% Dy.

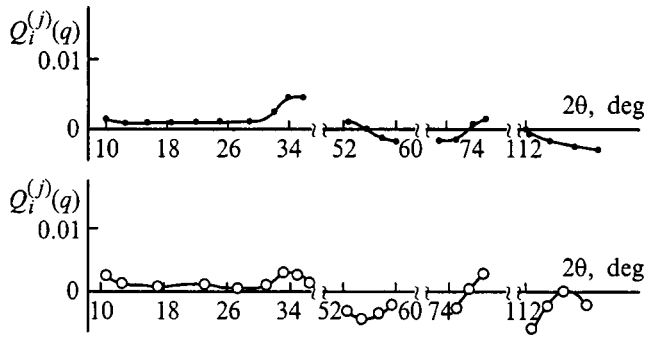

FIG. 6. Modulating functions of the quadratic size effect on the first ($Q_1^{(2)}$, dots) and second ($Q_2^{(1)}$, circles) coordination spheres for the alloy Mg–3.4 at.% Dy.

effects oscillate about a curve that slowly increases with the scattering angle according to the law $(1-e^{-2M})$, where $2M$ is a temperature factor[2]; the oscillations of the functions are reminiscent of the thermal diffuse scattering curve. The form of the functions for quadratic size effects differs for alloys of magnesium with rare-earth metals. For example, whereas the functions increase only slightly on the zeroth sphere as the scattering angle increases, the same trend is not observed on the first and second coordination spheres. Moreover, the functions calculated according to Eq. (24) for Mg–Dy and Mg–Tb alloys are found to be small. To a certain degree this result is attributable to the fact that the difference in the atomic factors (Δf) of magnesium and the rare-earth metals dysprosium and terbium is appreciable (54, 53), while the average atomic factor $(f=c_A f_A+c_B f_B)$ is approximately equal to the atomic factor of magnesium $(c_A f_A \approx f_A=12)$, owing to the low concentration of the second components. The end result of all this is that the factor $f^2/\Delta f^2$ in Eq. (24) is found to be of the order of 10^{-2}, the quadratic-size-effect functions multiplied with it are small, and their contribution to the total intensity becomes insignificant. In contrast, the quadratic size effect strongly significantly influences the total intensity in alloys whose components have close atomic factors.

Consequently, for alloys of magnesium with rare-earth metals the modulating functions of the size effects on the first and second coordination spheres differ in character, the main contribution to the total intensity coming from the functions for linear size effects. Quadratic size effects, in which interactions of atoms between sublattices are taken into account (first sphere), are small and do not increase with the scattering angle as in the case of fcc and bcc alloys.

TABLE I. Short-range order parameters for the alloy Mg–3.4 at.% Dy (dimensionless units).

α_1	α_2	α_3	α_4	α_{5-6}	α_0
−0.018	0.017	0.04	1.25	−0.12	−0.42

TABLE II. Short-range order parameters for the alloy Mg-2.9 at.% Dy (dimensionless units).

α_1	α_2	α_3	α_4	α_{5-6}	α_0
−0.011	0.018	0.05	0.84	−0.13	−0.40

4. CALCULATION OF THE SHORT-RANGE ORDER PARAMETERS

We have calculated the short-range order parameters from diffuse x-ray scattering data, taking into account the modulating functions of size effects on the zeroth and first two coordination spheres. The results of the calculations are shown in Tables I and II.

It is evident from the tables that the short-range order parameters on the first coordination sphere are less than zero, and those on the second sphere are greater than zero. It should also be noted that despite the extreme closeness of the radii of the first two spheres (3.20 Å and 3.22 Å for Mg–Dy; 3.21 Å and 3.22 Å for Mg–Tb), the allowance for size effects on these spheres permits them to be treated separately, and the short-range order parameters to be determined for them. The separation of the two closely similar coordination spheres is made possible by virtue of the difference in the size-effect modulating functions on the first and second spheres.

From the calculated short-range order parameters we have plotted the synthesized curves shown in Figs. 2 and 3. It is clear from the figures that the experimental and synthesized intensities come acceptably close to one another.

We have thus developed an x-ray procedure for the investigation of short-range order in polycrystalline alloys having an hcp lattice, based on an analysis of the influence of correlations on size effects. In the example of the hcp alloys Mg-3.4 at.% Dy and Mg-2.9 at.% Tb we have proved experimentally that the proposed model is realistic.

On the basis of the new procedure we have calculated for the first time the modulating functions of linear and quadratic size effects for hcp alloys. We have shown that for alloys of magnesium with rare-earth metals the size-effect modulating functions on the first and second coordination spheres differ in character, where the functions for linear size effects contribute predominantly to the total intensity.

Allowance for the size-effect modulating functions on the first two coordination spheres, which have close radii, has enabled us to solve the problem of calculating the short-range order parameters on these spheres.

[1] M. A. Krivoglaz and Tyu Khao, Metallofizika (Kiev) **24**, 63 (1968).
[2] V. I. Iveronova and A. A. Katsnel'son, *Short-Range Order in Solid Solutions* (Nauka, Moscow, 1977), p. 256.
[3] S. A. Veremchuk, A. A. Katsnel'son, V. M. Avdyukhina, and S. V. Sveshnikov, Fiz. Met. Metalloved. **39**, 1324 (1975).
[4] L. A. Safronova, A. A. Katsnel'son, S. V. Sveshnikov, and Yu. M. L'vov, Fiz. Met. Metalloved. **43**, 76 (1977).

[5] D. S. Gencheva, A. A. Katsnel'son, and L. L. Rokhlin, Fiz. Met. Metalloved. **51**, 788 (1981).
[6] V. M. Silonov, E. V. Evlyukhina, and L. L. Rokhlin, Vestn. Mosk. Univ., Fiz., Astron. **36**(5), 93 (1995).
[7] L. L. Rokhlin, Fiz. Met. Metalloved. **56**, 733 (1983).
[8] L. L. Rokhlin and I. E. Tarygina, Fiz. Met. Metalloved. **59**, 1188 (1985).
[9] J. H. Hubbel, W. J. Veigele, and E. A. Brigges, J. Phys. Chem. Ref. Data **4**, 471 (1975).
[10] T. Cromer and D. Liberman, J. Chem. Phys. **53**, 1891 (1970).
[11] A. A. Katsnel'son and I. I. Popova, Izv. Vyssh. Uchebn. Zaved. Fiz. **5**, 132 (1974).

Translated by James S. Wood

Isotope effect in manganites and hydrogenated palladium

É. L. Nagaev

L. F. Vereshchagin Institute of High-Pressure Physics, Russian Academy of Sciences, 14092 Troitsk, Moscow District, Russia

(Submitted April 14, 1999)
Fiz. Tverd. Tela (St. Petersburg) **41**, 2116–2120 (December 1999)

A theory of the isotopic dependence of the hydrogen content in palladium and the excess oxygen content in manganites is formulated. The theoretical results for the first system are obtained without any fitting parameters and reproduce the experimental data within 2–3% error limits in the temperature range from 170 K to 1450 K. An exact expression for the magnitude of the effect is also obtained for the second system, but owing to the lack of necessary experimental data, it can only be estimated in order of magnitude. © *1999 American Institute of Physics.* [S1063-7834(99)00312-3]

There are two physical solid-state systems in which the isotope effect is very pronounced and can be of utmost importance in practical applications. The two systems are hydrogenated palladium, which is used to separate hydrogen isotopes, and the manganites, which have applications as materials exhibiting colossal magnetoresistance. The isotope effect in Pd:H has been known for a very long time and has been thoroughly investigated (see, e.g., Refs. 1 and 2). It is manifested by a difference in the concentrations of hydrogen and deuterium absorbed by the metal at a given pressure and temperature of the gas in which it occurs. Oddly enough, however, so far no one has succeeded in deriving *ab initio* expressions for the ratio of these concentrations without recourse to fitting parameters.

Only very recently has the isotope effect been discovered in manganites, where it is manifested by substantial changes in their electrical and magnetic properties when light oxygen ^{16}O is replaced by heavy oxygen ^{18}O (Ref. 3). According to Zhao *et al.*,[3] for example, this substitution lowers the Curie point T_C of the ferromagnetic compound $La_{1-x}Ca_xMnO_3$ with $x=0.2$ by 20 K, i.e., by 10%. Since then a great many papers have been published, reporting the discovery of other manifestations of a giant isotope effect (the papers are cited in Ref. 4).

By analogy with the isotope effect in BCS superconductors, Zhao *et al.*[3] have attributed the effect here to electron–phonon interaction. However, the new effect is at least an order of magnitude greater than should be expected from the dependence of the exchange integrals on lattice vibrations. For electron–phonon interaction to produce such strong isotope effects, it would have to be anomalously strong itself. However, the giant isotope effect is observed only in certain compositions and not in others. For example, in the same compound $La_{1-x}Ca_xMnO_3$ as discussed in Ref. 3, but with $x>0.4$, the isotropic shift of T_C is only 2%, which corresponds to the normal magnitude of electron–phonon interaction.[5] This conclusion compels us to assume that the giant isotope effect is in fact associated with some kind of chemical factors. Accordingly, the hypothesis of anomalously strong electron–phonon interaction,[3] which is not corroborated in other properties of manganites, is superfluous.

It has been suggested previously[4] that the giant isotope effect in manganites is attributable to an oxygen excess relative to the stoichiometric composition. The manganites have *p*-type conductivity as a result of their doping with bivalent ions of the Ca type. Excess oxygen also functions as an acceptor and, in sufficiently large quantities, can significantly increase the density of holes in samples and, hence, their magnetization as well if their ferromagnetic properties are entirely the result of indirect exchange mediated by holes. At the same time, excess oxygen creates a ''chemical pressure'' in manganites, altering their lattice constant. Judging from the fact that an insulator–metal transition in manganites is sometimes possible at very low external pressures,[6] the transition can indeed be instigated by ''chemical pressure.''

Of course, trivial factors can also be cited as possible causes of differences in the excess oxygen concentrations for different isotopes. For example, in the preparation of samples by the exchange of oxygen with a surrounding gas phase the samples can enter into nonequilibrium states, whereupon the difference in the diffusion coefficients for different isotopes causes their concentrations in the sample to differ. Nonetheless, we intend to base our interpretation of the isotope effect in manganites on the fact that in preparation the samples have attained a thermodynamic equilibrium state with the surrounding gas, rigorously so at equal temperature and pressure.

Under these conditions the quantity of nonstoichiometric oxygen is found to be isotope-dependent, where the quantity of the lighter isotope is greater than that of the heavier one. Hence, the situation in them is similar to the situation in Pd:H, and the very existence of the isotope effect in Pd:H is the best evidence that the same effect must exist in manganites. Of utmost importance is the publication, simultaneously with the cited theoretical paper,[4] of an experimental study[7] confirming that the giant isotope effect in manganites is indeed related to excess oxygen. Accordingly, it does not occur for all manganite compositions, but only for those in which such an excess is possible.

The analysis below applies in equal measure to Pd:H and

to manganites. It differs from Ref. 4 in that lattice vibrations are systematically taken into account; at high temperatures this feature qualitatively changes the results of Ref. 4, which are valid at moderate temperatures. The first of these systems is simpler and has been studied far more extensively. It is amenable to calculations that are valid at all temperatures, ranging from the ultraquantum to the classical limit. Without recourse to any kind of fitting parameters results have been obtained with deviations of only 2–3% from the experimental over a wide range of temperatures from 170 K to 1450 K. The crossover to filling of the lattice with protium and deuterium has been predicted at even higher temperatures.

For the second system a general expression has been successfully derived for the equilibrium isotope effect, but only at temperatures comparable with the Debye temperature or lower has it been possible to estimate the magnitude of the effect. Although at first glance an investigation at these temperatures may not appear to carry much weight, since isotope substitution takes place at far higher temperatures, the analysis below will show that in fact this is not the case: As isotope-substituted samples cool down, oxygen nonstoichiometry is established at moderate temperatures determined by the diffusion coefficient of oxygen. Strictly speaking, therefore, the nonstoichiometry here is a nonequilibrium condition, but the equilibrium approach still provides a reasonable assessment of it. Unfortunately, a total dearth of information on the diffusion coefficients and vibrational spectra of manganites permits only an order-of-magnitude estimation of the effect.

1. HYDROGENATED PALLADIUM

To determine the hydrogen concentration in Pd, it is necessary to equate the chemical potentials of hydrogen in the Pd crystal and in the hydrogen gas atmosphere. Our investigation is carried out only at low gas pressures, when occupation of the interstices by H(D) atoms is low. The chemical potentials for the gas and crystal phases are determined from the corresponding free-energy equations.

The following terms are included in determining the free energy of hydrogen in the crystal: 1) the hydrogen affinity of the crystal A; 2) a term $F_c^{\rm conf}$ associated with the configurational entropy of n hydrogen atoms distributed among the most energetically favorable N interstices (octahedral); 3) the phonon free energy $F_c^{\rm ph}$. Interaction between hydrogen atoms, direct or mediated by the lattice, is disregarded.

Whereas the structure of the first two terms is obvious, the third term requires special consideration. In general, it is given by the equation

$$F_c^{\rm ph}=\int_0^\infty d\omega\{T\ln[1-\exp(-\omega/T)]+\omega/2\}G(\omega,N,n)$$

$$(\hbar=1), \tag{1}$$

where $G(\omega,N,n)$ is the phonon density of levels in a crystal consisting of N unit cells with n hydrogen atoms in each.

Inasmuch as the mass of the hydrogen atoms is much smaller than that of the palladium atom, according to the theory of Lifshitz,[8] the absorption of hydrogen by palladium should produce discrete phonon levels above the continuous phonon spectrum. This level corresponds to vibrations of an H(D) atom relative to neighboring Pd atoms. For small numbers n the density of levels can be written in the form

$$G(\omega,N,n)=G(\omega,N)+ng(\omega),$$

$$g(\omega)=g^L(\omega)+g^c(\omega). \tag{2}$$

The explicit expression for the density of levels of the hydrogen-free crystal $G(\omega,N)$ will not be needed below; only the term proportional to n is significant. It must include the contributions $g^l(\omega)$ and $g^c(\omega)$ from localized phonons generated by hydrogen absorption and from the perturbation induced by it in the continuous spectrum of the crystal, respectively. As for localized phonons, it follows from the cubic symmetry of the crystal that each hydrogen atom generates three degenerate vibrational modes.

In regard to the perturbation of the continuous spectrum, on the other hand, here we submit physical considerations to support its negligibility. First of all, there are indications that in the pair of elastic constants $\varkappa$ and $\varkappa^{H(D)}$ characterizing interaction in pairs of atoms Pd–Pd and Pd–H(D), respectively, the first is substantially larger than the second. In fact, the Debye temperature of the crystal, which is proportional to $(\varkappa/M^{\rm Pd})^{1/2}$, and the local-phonon frequency ω_0, which is proportional to $(\varkappa^{\rm H}/M^{\rm H})^{1/2}$, are mutually commensurate (the first being equal to 0.0237 eV, and the second to 0.685 eV; Refs. 1 and 2). Moreover, the mass $M^{\rm Pd}$ of the Pd atom is two orders of magnitude greater than the mass $M^{\rm H}$ of the H atom.

It must also be borne in mind that each Pd atom has 12 nearest-neighbor Pd atoms (the crystal has a fcc lattice). In addition, each H(D) atom occupying an octahedral site has only six neighboring Pd atoms. This arrangement lessens the overall effect of H(D) atoms on the motion of Pd atoms. Finally, the free-energy contribution $g^c(\omega)$ is further reduced by virtue of the fact that this quantity is integrated over all frequencies and, hence, becomes equal to zero, since it does not alter the total number of degrees of freedom of the system [the contribution of hydrogen atoms to this number is given by the integrated function $g^l(\omega)$]. Consequently, $g^c(\omega)$ is an alternating function, further diminishing its contribution to $F_c^{\rm ph}$. This statement lends support to the above-mentioned permissibility of disregarding its contribution to the free energy.

We can therefore write

$$g(\omega)=3\delta(\omega-\omega_0). \tag{3}$$

According to Eqs. (1)–(3), the hydrogen-dependent part of the free energy of the crystal is given by the equation

$$F_c=-An+TN[u\ln u+(1-u)\ln(1-u)]+3n\omega_0/2$$
$$+3n\ln[1-\exp(-\omega_0/T)], \tag{4}$$

where $u=n/N$, $A=A^{\rm chem}-3\omega_0/2$, and $A^{\rm chem}$ is the ''chemical'' part of the hydrogen affinity of the crystal.

On the other hand, allowing for the high vibration frequency ω_M of $H_2(D_2)$ molecules in comparison with the

characteristic temperatures, the free energy of these molecules in the gas surrounding the crystal is given by the equation[9]

$$F_g = -n'D + Tn'\left(\ln\frac{n'}{n_g} - \ln\frac{\gamma}{p} - 1\right),$$

$$\gamma = T^{5/2}\left(\frac{M}{2\pi}\right)^{3/2} Z_r, \quad n' = \frac{n_c - n}{2}, \tag{5}$$

where $n_g \gg n$ is the total number of hydrogen atoms in the system, n' is the number of H_2 or D_2 molecules, $D = D^{\text{chem}} - \omega_M/2$ is the molecular dissociation energy, and $p = Tn'/V$ is the pressure of the gas. The rotational partition function Z_r is given by an expression that is written in quantum form, owing to the smallness of the masses M of the H and D atoms:

$$Z_r = g_1 Z_1 + g_2 Z_2,$$

$$Z_1 = \sum_{k=1,3\ldots} (2k+1)\exp\left(-\frac{k(k+1)}{2IT}\right),$$

$$Z_2 = \sum_{k=0,2\ldots} (2k+1)\exp\left(-\frac{k(k+1)}{2IT}\right), \tag{6}$$

where $I = Ml^2/2$ is the moment of inertia of the molecule, l is the interatomic distance, and k is the rotational quantum number. The coefficients g_1 and g_2 are equal to 3/4 and 1/4 for H_2 or to 1/3 and 2/3 for D_2. The quantity $1/2I$ is equal to 0.0074 eV for H_2 and 0.0037 eV for D_2. The classical limit for the partition function $Z_r = IT$ imparts high accuracy to the calculations beginning with 100 K.

Equating the chemical potentials of the hydrogen in the gas and in the crystal, we obtain an equation for the interstice occupation numbers:

$$u = \frac{\sqrt{p}}{[1-\exp(-\omega_0/T)]^3\sqrt{\gamma}}\exp\left(\frac{A - D/2}{T}\right). \tag{7}$$

Making use of the fact that l and the ''chemical'' contributions A^{chem} and D^{chem} to A and D do not depend on the mass of the hydrogen atom, from Eq. (7) we obtain the following equation for the ratio of the low-pressure protium and deuterium concentrations (the rotation of the molecules is regarded as classical):

$$r = \frac{n^{\text{H}}}{n^{\text{D}}} = \left(\frac{M^{\text{D}}}{M^{\text{H}}}\right)^{5/4} \exp\left(\frac{\omega_M^{\text{H}}/2 - \omega_M^{\text{D}}/2 + 3\omega_0^{\text{D}} - 3\omega_0^{\text{H}}}{2T}\right)$$

$$\times\left(\frac{1-\exp(-\omega_0^{\text{D}}/T)}{1-\exp(-\omega_0^{\text{H}}/T)}\right)^3. \tag{8}$$

The molecular vibration frequencies ω_M can be found in many tables and are equal to 0.546 eV for H_2 and 0.386 eV for D_2. The frequency of local phonons in the crystal ω_0 for low occupations is equal to 0.0685 eV for H and 0.0465 eV for D (Refs. 1 and 2).

It follows from these results that the lower the temperature, the stronger is the isotope effect. In the limits of validity of Eq. (8) at 115 K the ratio r attains a value of 4.69. The effect is far stronger in the quantum realm: Taking Eqs. (6) into account, we find that r has values of 162 and 4.5×10^8 at liquid oxygen (20 K) and liquid helium (4.2 K) temperatures, respectively. Of course, the question arises as to whether the hydrogen diffusion required to establish thermodynamic equilibrium occurs at such temperatures. Such diffusion could be driven purely by the quantum tunneling of atoms between unit cells. Moreover, the diffusion of atoms could be enhanced by illumination or by irradiation of the crystal with (e.g.) electrons.

However, even at room temperatures the isotope effect remains strong: The parameter $r = 2.26$. At just 600 K it is close to 1.46, and around 1500 K it becomes smaller than unity, i.e., the deuterium concentration becomes higher than the protium concentration. At the melting point of palladium, 1827 K, we have $r = 0.944$.

If we formally let the temperature tend to infinity in Eq. (8), then r must tend to 0.75, which is sufficiently close to the value $r_\infty = (M^{\text{H}}/M^{\text{D}})^{1/2} = 0.84$ formally obtained from Eq. (8) on the assumption that the localized phonon frequencies are proportional to $M^{1/2}$.

In a system of this kind one might expect the isotope effect to necessarily vanish altogether in the classical limit. In reality, however, the classical limit implies that the temperature greatly exceeds not only the frequency of the crystal vibrations, but also the molecular vibration frequency. If the excitation of molecular vibrations is formally taken into account, it is readily verified that the isotope effect indeed vanishes in this limit. But it is obvious at the same time that the classical limit is simply unattainable in a real system.

In seeking to compare these results with experiment, it should be mentioned that experimental data covering the broadest temperature range, from 170 K to 1450 K, are reported in Ref. 10. A comparison of these data with Eq. (8) shows that the discrepancy between them is not more than 2–3% over this entire range. Equation (8) yields good agreement with the experimental data of other authors.[1,2] It is particularly significant that such good agreement is obtained in spite of the fact that Eq. (8) does not contain a single fitting parameter and involves only frequencies determined from independent measurements. In the meantime many authors have attempted to describe the temperature dependence of the isotope effect analytically by introducing several fitting parameters in their equations (see Refs. 1 and 2). In Ref. 2, in particular, nine fitting parameters were required to describe the experimental temperature dependence of the isotope effect over a wide range of temperatures. The need for such a large number of fitting parameters is a consequence of the fact that the true temperature dependence of the isotope effect is described by the very complex temperature function (8).

2. MANGANITES

The manganites comprise far more complex systems than palladium, and experimental data pertaining to the influence of oxygen nonstoichiometry on their vibrational spectra have been nonexistent to date. In this section, therefore, we cannot possibly look for such a simple analysis as in the preceding section.

It is convenient to approach the problem with the experimental procedure used for isotope substitution in manganites. It is carried out at about 1250 K for approximately 48 h, at which time the appropriate deviation from oxygen stoichiometry is established. The isotope-substituted samples are then slowly cooled in an atmosphere of the corresponding isotope at the rate of 30 K/h, so that room temperature is attained after more than 30 h (Ref. 3). The excess oxygen concentration n should also vary during cooldown, following the temperature of the environment. However, the feasibility of precisely matching it depends on the oxygen diffusion rate at this temperature. In reality, therefore, n corresponds to equilibrium at a certain temperature intermediate between 1250 K and 300 K.

A more accurate approach should take into account the nonuniformity of the excess oxygen distribution in the sample. We note — and this is important — that the process of relaxation to the equilibrium oxygen concentration in the isotope-substituted sample by diffusion can be considerably faster than the substitution of a heavy isotope for a light one, because the latter process involves both diffusion and the substitution reaction. Moreover, diffusion can depend significantly on the content of Ca or other acceptor impurity in the manganites and can therefore proceed more rapidly in some of their compositions than in others. In principle, this consideration can account for the difference in the results of Refs. 3 and 5 as mentioned in the Introduction.

Although it is impossible to accurately determine the excess oxygen temperature without precise data on the diffusion of oxygen in manganites, we can still venture certain estimates. It is well known that the diffusion of oxygen in certain perovskites (e.g., in La_2CuO_4) is possible even at 230–250 K (Ref. 11), and the diffusion coefficient D attains 10^{-9} cm^2/s in them at room temperature. The diffusion activation energy Q usually amounts to several tenths of an electronvolt and can even exceed 1 eV. The higher its value, the more rapidly D increases as the temperature increases. If Q can be assumed to have the conservatively low value of 0.5 eV, the characteristic diffusion time (L^2/D) for a sample of length $L=0.1$ cm is equal to 1 h at 450 K. Since the diffusion coefficient is even higher at higher temperatures, we can be certain that in cooldown of the sample the final nonstoichiometry will correspond to 400–600 K.

Generally speaking, it is comparable with the typical Debye temperature of crystals, which is sufficient for the isotope effect to exist (and indeed it is even higher in certain oxides; for example, it is equal to 800 K in MgO, exceeds 1000 K in Al_2O_3, and should not be ruled out as being high in manganites as well). In any case it is far from the classical limit, at which the isotope effect is supposed to be nonexistent.

In the manganite $LMnO_3$ the role of vacancies can be assumed both by La atoms and by Mn atoms. To simplify the discussion, we include only one of these types of atoms (e.g., Mn) and, accordingly, consider a MnO crystal. Instead of the basic crystal containing N unit cells and n excess oxygen atoms in each, we consider the extended crystal containing $(N+n)$ unit cells with the same number n of Mn vacancies in each. We also assume that it exists in thermodynamic equilibrium with the gas atmosphere, even though this is an idealization of the true experimental situation.[3] In principle it is also possible to conduct experiments with thermodynamically equilibrium isotope substitution at moderate temperatures if the diffusion in them is appreciable.

If the number of Mn atoms in the interstices is disregarded, the free energy of the extended crystal is given by the equation

$$F_c^e = F_c^0(N+n) + nW^{\mathrm{chem}} + T(N+n) \times [\nu_{\mathrm{cv}} \ln_{\mathrm{cv}} + (1-\nu_{\mathrm{cv}})\ln(1-\nu_{\mathrm{cv}})] - nf(T), \tag{9}$$

where W^{chem} is the isotope-substituted component of the work function for the removal of a cation from the crystal, $\nu_{\mathrm{cv}}=n/(N+n)$ is the relative density of excess oxygen in the extended crystal, $F_c^0(N)=NH_c^{\mathrm{chem}}+Nf_0(T)$ is the free energy of the ideal crystal containing N pairs of cations and anions, and H_c^{chem} is the isotope-substituted component of the pair energy. The phonon free energies can be written in the form

$$f_0(T) = \int_0^\infty d\omega \{T \ln[1-\exp(-\omega/T)] + \omega/2\} g_0(\omega) \equiv 6T \ln\{1-\exp[-\nu_0(T)/T]\} + 3\Omega_0; \tag{10}$$

$$f(T) = \int_0^\infty d\omega \{T \ln[1-\exp(-\omega/T)] + \omega/2\} g(\omega) \equiv 3T \ln\{1-\exp[-\nu_0(T)/T]\} + 3\Omega/2. \tag{11}$$

Here $g_0(\omega)=G(\omega,N)/N$ is the density of phonon levels in the ideal crystal, and $g(\omega)$ is the variation of the density of phonon states due to the emergence of a cation vacancy. Equations (10) and (11) are written with regard for the fact that the integrated functions $g_0(\omega)$ and $g(\omega)$ give the number of degrees of freedom of the ideal crystal and its vacancy-induced variation:

$$\int_0^\infty d\omega g_0(\omega) = 6, \quad \int_0^\infty d\omega g(\omega) = 3$$

(the inclusion of two atoms in the unit cell is taken into account here). In contrast with the average frequencies of the zeroth vibrational modes Ω and Ω_0, the average frequencies ν and ν_0 depend on the temperature.

Minimizing the total free energy of the system $F_g+F_c^e$ given by Eqs. (5) and (9) with respect to the number of excess oxygen atoms, which is equal to the number of cation vacancies in the extended crystal, we obtain

$$\nu_{\mathrm{cv}} = \frac{\sqrt{p}}{\sqrt{\zeta}} \exp\left(-\frac{H_c^{\mathrm{chem}} + W^{\mathrm{chem}} + D^{\mathrm{chem}}/2 + f_0 - f - \omega_M/4}{T}\right),$$

$$\zeta = (2S+1) I T^{7/2} \left(\frac{M}{2\pi}\right)^{3/2}, \tag{12}$$

where S is the spin of the hydrogen atom. Consequently, the ratio of the concentrations of light (l) and heavy (h) atoms is given by the equation

$$r=\frac{\nu_{\rm cv}^{l}}{\nu_{\rm cv}^{h}}=\left(\frac{M^{h}}{M^{l}}\right)^{5/4}F(T)G(T),$$

$$F(T)=\exp\left(\frac{(\omega_{M}^{l}-\omega_{M}^{h})/4+3(\Omega^{l}-\Omega^{h})/2-3(\Omega_{0}^{l}-\Omega_{0}^{h})}{T}\right),$$

$$G(T)=\frac{\left[1-\exp\left(\frac{\nu^{l}}{T}\right)\right]^{3}\left[1-\exp\left(-\frac{\nu_{0}^{h}}{T}\right)\right]^{6}}{\left[1-\exp\left(-\frac{\nu^{h}}{T}\right)\right]^{3}\left[1-\exp\left(-\frac{\nu_{0}^{l}}{T}\right)\right]^{6}}\quad.\qquad(13)$$

The classical expression for the rotational partition function is used in writing Eq. (13). Equation (13) differs from (8) in that it is a functional of the density of phonon levels, not only of the crystal containing cation vacancies, but also of the ideal crystal.

It must be emphasized that Eq. (13) is just as accurate as Eq. (8). However, the currently available experimental data are too sparse to permit calculation of the functions $F(T)$ and $G(T)$ in Eq. (13). Bearing in mind that the vibration frequencies of the $^{16}O_2$ and $^{18}O_2$ molecules are equal to 0.2 eV and 0.19 eV, respectively, we can expect the first function to be very close to unity in the proximity of the Debye temperatures or higher. The same must assuredly be true of $G(T)$ at temperatures close to or below the Debye temperature. We can therefore use the quantity $(M^{h}/M^{l})^{5/4}=1.16$ to estimate r at temperatures in the vicinity of the Debye temperature. In any case we can state that the equilibrium concentration of light isotopes can be 10–15% higher than the concentration of heavy isotopes in the range of realistic working temperatures. This difference is sufficient to account for the giant isotopic shift of the Curie point (3) and other isotopic phenomena.

The author is deeply indebted to G. A. Tsirlina for suggesting the applicability of his theory of the isotope effect to Pd:H and for familiarizing him with the chemical aspects of the problem and experimental data on Pd:H.

This work has received partial support from the Russian Fund for Fundamental Research, Grant No. 98-02-16148.

*)E-mail: tsir@elch.chem.msu.ru

[1] E. Wicke and H. Brodowsky, in *Hydrogen in Metals II: Application-Oriented Properties*, edited by G. Alefeld and J. Völkl (Springer-Verlag, Berlin–New York, 1978).
[2] W. Oates, R. Laesser, T. Kuji, and T. Flanagan, J. Phys. Chem. Solids **47**, 429 (1986).
[3] G. Zhao, K. Konder, H. Keller, and K. Mueller, Nature (London) **381**, 676 (1996).
[4] E. L. Nagaev, Phys. Rev. B **58**, 12 242 (1998).
[5] I. Isaak and J. Franck, Phys. Rev. B **57**, R5602 (1998).
[6] J.-S. Zhou and J. Goodenough, Phys. Rev. Lett. **80**, 2665 (1998).
[7] J. Franck, I. Isaak, W. Chen, J. Chrzanovski, and J. Irvin, Phys. Rev. B **58**, 5189 (1998).
[8] I. M. Lifshitz, Nuovo Cimento Suppl. **3**, 716 (1956).
[9] L. D. Landau and E. M. Lifshitz, *Statistical Physics*, 3rd ed. (Pergamon Press, Oxford–New York, 1980; Nauka, Moscow, 1976).
[10] R. Laesser and G. Powell, Phys. Rev. B **34**, 578 (1986).
[11] R. Kremer, V. Hizhnyakov, and E. Sigmund, Z. Phys. B **91**, 169 (1993).

Translated by James S. Wood

Interatomic correlations in the alloy Ni–11.8 at. % Mo

V. G. Poroshin, N. P. Kulish,*) P. V. Petrenko, and N. A. Mel'nikova

T. Shevchenko Kiev State University, 252022 Kiev, Ukraine
(Submitted in final form June 17, 1999)
Fiz. Tverd. Tela (St. Petersburg) **41**, 2121–2126 (December 1999)

An updated version of the Cohen–Matsubara–Georgopoulos method of separating the components of the diffuse scattering intensity, taking into account corrections for the absorption factors, is used to find the intensity distribution in reciprocal space from short-range order in the alloy Ni–11.8 at. % Mo. It is shown that over a wide range of concentrations the short-range order intensity maximum is localized at a stationary point of the type $\{1\frac{1}{2}0\}$; this result follows from extremal sums derived in the paper for the experimental short-range order parameters. © *1999 American Institute of Physics.* [S1063-7834(99)00412-8]

Concentration fluctuations due to interatomic correlations in alloys are usually characterized by the first terms in the concentration expansion of the free energy.[1–3] For a number of ordered alloys, in which equilibrium is attained as a result of the anharmonic components of the free energy, spinodal ordering described by static concentration waves with Lifshitz wave vectors $\mathbf{k}_0$ makes a first-order phase transition.[3,4] Representative of such alloys are Au–Mn, Au–V, Au–Cr, Au–Fe, and Ni–Mo. Their distinguishing feature is the presence of diffusion peaks of the type $\{1\frac{1}{2}0\}$ in solid solutions and in hardened samples of stoichiometric composition Ni_4Mo, and superlattice reflections of the type $1/5\{420\}$, which correspond to $D1_a$ structure, appear after prolonged anneals of such samples.

Existing notions concerning the short-range order structure described by $\{1\frac{1}{2}0\}$ reflections are conflicting. They are usually formulated on a microdomain model in the presence of nonconservative antiphase boundaries[5–7] or a concentration wave packet model,[8–11] which is considered to have an atomic analog in the cluster model.[4,10–12] Attempts to reconcile these models[7] have lacked substance. It should be noted in this regard that thorough electron microscope studies of alloys with points of the type $\{1\frac{1}{2}0\}$ (Refs. 5–12) have been limited strictly to a qualitative analysis of the intensity distribution and, hence, cannot provide a quantitative description of short-range order.

In this paper we report an investigation of short-range order structure in Ni–Mo alloys using the method of diffuse x-ray scattering for single crystals.[1,2] For the investigation we have chosen an alloy containing 11.8 at. % molybdenum, i.e., an alloy close to the boundary of existence of the $D1_a$ phase, with a view toward clarifying the role of anharmonic free-energy contributions, which could introduce anomalies into the short-range order structure.

Earlier short-range order studies using x-rays in alloys of nickel with 10.7 at. % and 20.0 at. % of molybdenum[13] basis were performed within the outdated Warren–Averbach diffraction theory, which cannot support a sufficiently complete analysis of the short-range order structure or be used to describe phenomena associated with static and dynamic distortions.

The short-range order structure has been investigated more completely for hardened Ni_4Mo (Ref. 14) alloy using the Borie–Sparks separation method. However, the approximations underlying this method are incorrect for the given alloy because of an appreciable difference in the ratio of the atomic scattering functions of the components for different points of reciprocal space,[15,16] a situation that can significantly distort the interpretation of experimental data.

1. EXPERIMENTAL PROCEDURE

The alloy Ni–11.8 at. % Mo was melted in an induction furnace in an alundum crucible in an argon atmosphere. Single crystals were grown in alundum crucibles with a conical seed zone in an argon atmosphere. The crystals were cut along directions of high symmetry. For the investigated alloy the outer face of the sample coincided with the (100) plane. The short-range order state was created by a two-hour anneal at 1000 °C with subsequent gradual cooldown to room temperature.

The diffuse scattering intensity, whose distribution was used to determine the short-range order parameters,[17] was measured by means of hard $K\alpha$–Mo radiation, so that by running the apparatus in the proper working regime, higher harmonics $\lambda/2,\lambda/3,\ldots$ and the fluorescence component could be separated from the spectrum of rays monochromatized by a one-dimensionally bent LiF crystal.

On the other hand, the use of hard radiation required the introduction of corrections for the angular dependence in the absorption[18,19] for the diffuse scattering intensity from the sample and from fused quartz employed as a standard for converting the intensity into absolute electron units. With these corrections taken into account, the equation for converting the intensity of diffuse scattering from the sample into electron units $I_{sp}(\theta)$ with the aid of the measured intensity from the standard at an angle θ_0 has the form[19]

$$I_{sp}(\theta)=I_{st}(\theta_0)\frac{I_{sp}(\theta)}{I_{st}(\theta_0)}\frac{(n/2\mu L)_{sp}}{(n/2\mu L)_{st}}\times\frac{1+\gamma'\cos^2 2\theta_M\cos^2 2\theta_0}{1+\gamma'\cos^2 2\theta_M\cos^2 2\theta}. \quad (1)$$

Here $I_{st}(\theta_0)$ is the scattering intensity from the fused quartz, which is calculated with adjustment for anomalous dispersion corrections and is equal to 37.27 e.u. for molybdenum radiation at $\theta_0=45°$; L_{st} and L_{sp} are corrections to the absorption factor μ for the standard and the sample, respectively, and in general exhibit a complex dependence on the geometry of the sample arrangement, the collimation of the beams, and the x-ray absorption. For example, in the case of $K\alpha$–Mo radiation the value of the correction for the standard is $L_{st}(45°)=0.8944$ e.u., which significantly influences the scattering intensity of the standard. The parameter γ' takes into account the degree of imperfection of the monochromator crystal and is close to unity for the LiF crystal used in our work.

The modulations of diffuse scattering in alloys can be expressed in terms of components associated with short-range order and with static and dynamic displacements.[1,2,15] In the present study these components are separated by means of an updated version of the Cohen–Matsubara–Georgopoulos method,[20–23] which, like the Borie–Sparks method,[15] is based on the difference in the symmetries of the modulation of the diffuse background in reciprocal space by the indicated scattering components.

The total coherent x-ray scattering intensity in electron units for all pairs of atoms (m,n) entering the scattering volume can be expressed as follows in terms of the vectors of static ($\boldsymbol{\delta}_m$, $\boldsymbol{\delta}_n$) and dynamic $\mathbf{u}_m$, $\mathbf{u}_n$) atomic displacements:

$$I_n\left(\frac{\mathbf{s}}{\lambda}\right)=\sum_m^N\sum_n^N f_m f_n^*\exp\left\{2\pi i\frac{\mathbf{s}}{\lambda}[(\mathbf{r}_m-\mathbf{r}_n)+(\boldsymbol{\delta}_m-\boldsymbol{\delta}_n)+(\mathbf{u}_m-\mathbf{u}_n)]\right\}. \quad (2)$$

Here f_m and f_n are the atomic scattering functions, $\mathbf{r}_m$ and $\mathbf{r}_n$ are radius vectors defining the positions of the lattice sites, $\mathbf{s}/\lambda=h_1\mathbf{b}_1+h_2\mathbf{b}_2+h_3\mathbf{b}_3$ is the diffraction vector of an arbitrary point of reciprocal space with coordinates h_1,h_2,h_3, $\mathbf{b}_1$, $\mathbf{b}_2$, and $\mathbf{b}_3$ are unit vectors in reciprocal space, which satisfy the condition $|\mathbf{b}_1|=|\mathbf{b}_2|=|\mathbf{b}_3|=1/a$ for cubic crystals, a is the lattice parameters, and N is the number of atoms in the volume in question.

We then expand $\exp(2\pi i(\mathbf{s}/\lambda)\mathbf{u}_{mn})$ out to terms of first order of smallness and then average over time, and we expand $\exp(2\pi i(\mathbf{s}/\lambda)\boldsymbol{\delta}_{mn})$ out to second-order terms and average over space. Transforming from summation over m and n to a triple sum over the coordinates l,m,n of the real lattice sites, whose radius vectors are $\mathbf{r}_m-\mathbf{r}_n=\mathbf{r}_{lmn}=l(\mathbf{a}_1)/2+m(\mathbf{a}_2/2+n(\mathbf{a}_3/2)$, where $\mathbf{a}_1$, $\mathbf{a}_2$, and $\mathbf{a}_3$ are the unit vectors of the fcc structure ($|\mathbf{a}_1|=|\mathbf{a}_2|=|\mathbf{a}_3|=a$), we obtain an expression for the diffuse scattering intensity, in which the contributions from static and dynamic distortions are written separately. The expression for the diffuse scattering intensity at a given point in reciprocal space (h_1,h_2,h_3) can now be written to include 25 components. Their determination entails the formulation of a system of equations using the diffuse scattering intensities in the ith volumes of reciprocal space with those point coordinates h_1^i,h_2^i,h_3^i for which, by virtue of the symmetry of their positions relative to planes of the (001) and (011) type about the initial points of the basis volume with coordinates (h_1,h_2,h_3), the values of all 25 components remain identical. The signs of these components change according to the choice of coordinates of the ith volume. To take the signs into account, we express the coordinates of a point in the ith volume (h_1^i,h_2^i,h_3^i) in terms of the coordinates of the point in the basis volume (h_1,h_2,h_3) by the coordinate transformation rules

$$h_1^i=\pm h_{p_1}\pm L_i;\quad h_2^i=\pm h_{p_2}\pm M_i;\quad h_3^i=\pm h_{p_3}\pm N_i, \quad (3)$$

where L_i, M_i, and N_i are integers, which for fcc crystals are either all even or all odd; the subscripts p_1,p_2,p_3 take values representing any of the six combinations of the numbers $\{1,2,3\}$.

The displacement of the ith volume relative to symmetry planes of the type (100) and (110) passing through the origin do not alter the intensities at points with coordinates (h_1^i,h_2^i,h_3^i). It can be shown that, from the standpoint of contributions to the diffuse intensity, this statement implies one-to-one transformation between components of identical symmetry. This implication is formally equivalent to simple permutation of the coordinates of a point in the ith volume and reduction to the form $h_1^i(h_1),h_2^i(h_2),h_3^i(h_3)$.

The intensity of diffuse scattering by an atom at an arbitrary point (h_1^i,h_2^i,h_3^i) for the ith volume of reciprocal space, including the basis volume, can now be written as follows in terms of the components of points (h_1,h_2,h_3) of the basis volume:

$$\begin{aligned}I_D(h_1^i,h_2^i,h_3^i)=\frac{I_{ALL}(\mathbf{s}_i/\lambda)-I_{BR}(\mathbf{s}_i/\lambda)}{N}=C_AC_B(f'_{A,i}-f'_{B,i})\\ \times\{I_{SRO}+\eta_i h_1^i S[h_1(h_1^i)]Q_x^{AA}(h_1,h_2,h_3)\\ +\varepsilon_i h_1^i S[h_1(h_1^i)]Q_x^{BB}(h_1,h_2,h_3)+\eta_i h_2^i S\\ \times[h_2(h_2^i)]Q_y^{AA}(h_1,h_2,h_3)+\varepsilon_i h_2^i S[h_2(h_2^i)]\\ \times Q_y^{BB}(h_1,h_2,h_3)+\eta_i h_3^i S[h_3(h_3^i)]\\ \times Q_z^{AA}(h_1,h_2,h_3)+\varepsilon_i h_3^i S[h_3(h_3^i)]\\ \times Q_z^{BB}(h_1,h_2,h_3)+\eta_i^2(h_1^i)^2R_x^{AA}(h_1,h_2,h_3)\\ +2\eta_1\varepsilon_i(h_1^i)^2R_x^{AB}(h_1,h_2,h_3)+\varepsilon_i^2(h_1^i)^2\\ \times R_x^{BB}(h_1,h_2,h_3)+\eta_i^2(h_2^i)^2R_y^{AA}(h_1,h_2,h_3)\\ +2\eta_i\varepsilon_i(h_2^i)^2R_y^{AB}(h_1,h_2,h_3)+\varepsilon_i^2(h_2^i)^2\\ \times R_y^{BB}(h_1,h_2,h_3)+\eta_i^2(h_3^i)^2R_z^{AA}(h_1,h_2,h_3)\\ +2\eta_i\varepsilon_i(h_3^i)^2R_z^{AB}(h_1,h_2,h_3)+\varepsilon_i^2(h_3^i)^2\\ \times R_z^{BB}(h_1,h_2,h_3)\end{aligned}$$

$$
\begin{aligned}
&+\eta_i^2 h_1^i h_2^i S[h_1(h_1^i)h_2(h_2^i)]\\
&\times S_{xy}^{AA}(h_1,h_2,h_3)\\
&+2\,\eta_i\varepsilon_i h_1^i h_2^i S[h_1(h_1^i)h_2(h_2^i)]\\
&\times\times S_{xy}^{AB}(h_1,h_2,h_3)\\
&+\varepsilon_i^2 h_1^i h_2^i S[h_1(h_1^i)h_2(h_2^i)]\\
&\times S_{xy}^{BB}(h_1,h_2,h_3)\\
&+\eta_i^2 h_2^i h_3^i S[h_2(h_2^i)h_3(h_3^i)]\\
&\times S_{yz}^{AA}(h_1,h_2,h_3)\\
&+2\,\eta_i\varepsilon_i h_2^i h_3^i S[h_2(h_2^i)h_3(h_3^i)]\\
&\times S_{yz}^{AB}(h_1,h_2,h_3)\\
&+\varepsilon_i^2 h_2^i h_3^i S[h_2(h_2^i)h_3(h_3^i)]\\
&\times S_{yz}^{BB}+\eta_i^2 h_3^i h_1^i S[h_3(h_3^1)h_1(h_1^i)]\\
&\times S_{zx}^{AA}(h_1,h_2,h_3)\\
&+2\,\eta_i\varepsilon_i h_2^i h_3^i S[h_3(h_3^i)h_1(h_1^i)]\\
&\times S_{zx}^{AB}(h_1,h_2,h_3)\\
&+\varepsilon_i^2 h_3^i h_1^i S[h_3(h_3^i)h_1(h_1^i)]S_{zx}^{BB}(h_1,h_2,h_3)\}\\
&+I_{TDS}^2(\mathbf{s}_i/\lambda)+I_{TDS}^{3+4+\cdots}(\mathbf{s}_j/\lambda)-C_A C_B\\
&\times[(f_{A,i}-f_{B,i})^2-(f'_{A,i}-f'_{B,i})^2]. \qquad (4)
\end{aligned}
$$

Here I_{ALL} is the total intensity, I_{BR} is the intensity of structural reflection, $f_{A,i}$ and $f_{B,i}$ are the atomic scattering functions of components A and B of the alloy at the point with coordinates (h_1^i,h_2^i,h_3^i) for the ith volume of reciprocal space as defined by the vectors $\mathbf{s}_i/\lambda$; $f'_{A,i}=f_{A,i}e^{-M_A}$, $f'_{B,i}=f_{B,i}e^{-M_B}$; C_A and C_B are the concentration of the alloy components, M_A and M_B are the corresponding Debye–Waller constants, $\eta_i=f'_{A,i}/(f'_{A,i}-f'_{B,i})$, $\varepsilon_i=f'_{B,i}/(f'_{A,i}-f'_{B,i})$, $S[h_k(h_k^i)]$ is the sign of the coordinate h_k as determined from the transformation (3), $S[h_j(h_j^i)h_k(h_k^i)]$ is the sign of the product of the coordinates h_j and h_k from the coordinate transformation (3), and $I_{TDS}^2(\mathbf{s}_i/\lambda)$ and $I_{TDS}^{3+4+\cdots}(\mathbf{s}_i/\lambda)$ represent the contributions from two-phonon and multiphonon thermal diffuse scattering at the point with coordinates (h_1^i,h_2^i,h_3^i). The last term in Eq. (4) is attributable to modulation of the Laue background with allowance for the dynamic displacements in $f'_{A,i}$ and $f'_{B,i}$ (Ref. 23). These contributions are calculated from the total intensity apart from Bragg reflections, which are locally bounded in reciprocal space.

The intensity components Q_j^{AA} and Q_j^{BB} describe the scattering in Laue units at linear static distortions; R_j^{AA}, R_j^{AB}, and R_j^{BB} describe the same at quadratic static and dynamic distortions; S_{jk}^{AA}, S_{jk}^{AB}, and S_{jk}^{BB} describe the same at correlations of dynamic and static displacements; $I_{SRO}(h_1,h_2,h_3)$ is the intensity from short-range order.[20–23]

The proposed technique of representing the diffuse intensity in terms of the components at a point of the basis volume does not require a special search for them at points of every ith volume.

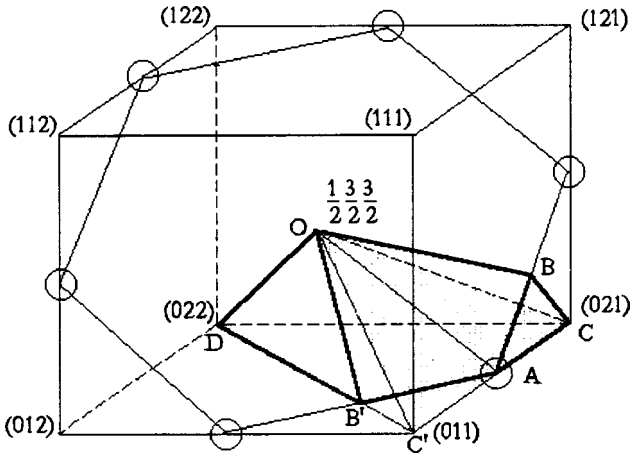

FIG. 1. Diagram of the basis volume $OBC'C$ against the background of the volume-equivalent part of the Brillouin zone $OBB'ACB$. The small circles indicate regions of diffuse scattering maxima.

2. EXPERIMENTAL RESULTS AND DISCUSSION

To investigate the short-range order structure in a single-crystal Ni–11.8 at. % Mo sample, in accordance with Eq. (4) we have separated I_{SRO} at points of reciprocal space of the initial basis volume $ODC'C$ with coordinates $(\frac{1}{2}\ \frac{3}{2}\ \frac{3}{2})$, (011), (022), (012), which is equivalent in size to the volume of the irreducible part of the first Brillouin zone $ODB'ACB$, a fragment of which is shown in Fig. 1. The measurements in the initial volume were performed with a discrete step $\Delta K_j=0.0625$, and the number of points j for the basis volume was equal to 512. The two-phonon and multiphonon thermal diffuse scattering were determined according to Refs. 24 and 25. To separate all the diffuse scattering components, we chose 44 volumes, whose point coordinates are related to the coordinates of the initial volume by the transformation rules (3) relative to symmetry planes of the type (001) and (011). It should be noted that these regions occupy a large volume of reciprocal space and, hence, corrections must be introduced, as proposed in Eq. (1), to yield correct values of the diffuse scattering intensities.

From Ref. 26 we have recruited a method of regularization of the experimental data within their error limits in order to reduce the error of determination of the scattering components due to experimental errors for the large number of unknowns involved in the system of equations (4). We have solved the system of linear equations for the scattering components after minimizing the regularization functional by the least-squares method.

Clearly, the distribution of diffuse scattering from short-range order (Fig. 2) is characterized by the presence of diffuse maxima at the sites $\{1\,\frac{1}{2}\,0\}$. The diffuse I_{SRO} peaks are more or less symmetric, but they are followed by noticeable strands stretching toward superlattice sites $\frac{1}{5}\{420\}$, which could be evidence of the existence of transition processes.

Table I shows the experimental Warren–Cowley short-range order parameters $\alpha_{lmn}^{\exp}$ for the alloy Ni–11.8 at. % Mo,

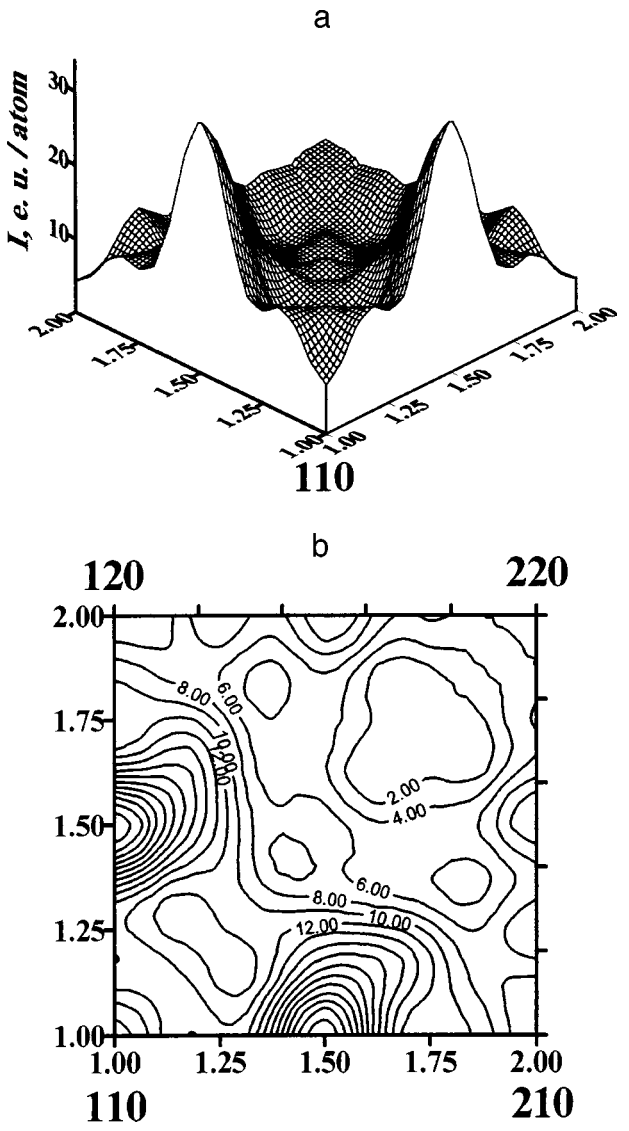

FIG. 2. Distributions of the diffuse scattering intensity (a) and equal-intensity curves (b) for points $h_1k_1l_1$ of the (001)* plane in reciprocal space of the initial basis volume.

along with the limiting short-range order parameters of the superlattices $D1_a$, DO_{22} and the hypothetical lattice N_2M_2, clusters of which can be generated by an amplified concentration wave $\{1\frac{1}{2}0\}$ (Refs. 11 and 12). These superlattices have often been used in models purported to explain the nature of the short-range order in alloys characterized by maxima of the diffuse intensity at points of the type $\{1\frac{1}{2}0\}$. The parameters $\alpha^{\exp}_{lmn}$ (Refs. 15 and 17) are calculated both by least-squares optimization and by Fourier transformation[22] according to the equation

$$I_{SRO}(h_1,h_2,h_3)=\sum_{l,m,n}\alpha^{\exp}_{lmn}\cos\pi(lh_1+mh_2+nh_3). \tag{5}$$

The results exhibit good mutual agreement. For the analysis Table I gives the short-range order parameters only for 28 coordination spheres, even though the values of $\alpha^{\exp}_{lmn}$ have been calculated to $i=150$. The short-range order intensity

TABLE I. Experimental short-range order parameters for the alloy Ni–11.8 at. % Mo and limiting short-range order parameters for a series of superlattices.

No. of coordination sphere, i	Site coordinates, lmn	Short-range order parameters			
		$\alpha^{\exp}_{lmn}$	α_{D1_a}	$\alpha_{DO_{22}}$	$\alpha_{N_2M_2}$
0	000	1.0058			
1	011	−0.1281	−1/4	−1/3	−1/3
2	002	0.1243	1/6	5/9	1/3
3	112	0.0400	1/6	1/9	1/3
4	022	−0.0530	−1/4	1/9	−1/3
5	013	−0.0203	−1/24	−1/3	−1/3
6	222	−0.0733	−1/4	−1/3	−1
7	123	0.0194	1/6	1/9	1/3
8	004	0.0841	1/6	1	1
9	033	−0.0094	−1/4	−1/3	−1/3
10	114	−0.0155	−1/4	−1/3	−1/3
11	024	0.0098	−1/24	5/9	1/3
12	233	−0.0065	−1/4	1/9	1/3
13	224	−0.0058	1/6	1/9	−1/3
14	015	0.0115	1/6	−1/3	−1/3
15	134	0.0028	1/6	−1/3	−1/3
16	125	0.0033	−1/24	1/9	1/3
17	044	0.0149	−1/4	1	1
18	035	−0.0001	1/6	−1/3	−1/3
19	334	−0.0017	1/6	−1/3	−1/3
20	006	0.0003	1/6	5/9	1/3
21	244	0.0068	1/6	5/9	1/3
22	116	−0.0075	−1/4	1/9	1/3
23	235	−0.0075	−1/4	1/9	1/3
24	026	−0.0130	−1/24	1/9	−1/3
25	145	−0.0043	−1/4	−1/3	−1/3
26	226	−0.0066	1/6	−1/3	−1
27	136	0.0055	1/6	1/9	1/3
28	444	−0.0002	−1/4	1	1

synthesized from 28 experimental parameters agree, within the error limits, with the experimental short-range order intensity. The short-range order parameters decrease substantially in order of increasing coordination sphere number. The signs of the parameters $\alpha^{\exp}_{lmn}$ agree up to $i=12$ with the signs determined for short-term annealed hardened Ni_4Mo samples.[14] On the other hand, the difference in the ratio between the values of the parameters for different coordination spheres differ appreciably. Moreover, for Ni_4Mo the parameter α_0 deviates considerably from unity, indicating the presence of additional scattering factors unaccounted for in this investigation.

A detailed analysis of the signs and ratios between the short-range order parameters shows that the correlation of the parameters $\alpha^{\exp}_{lmn}$ both for the investigated alloy containing 11.8 at. % Mo and for annealed Ni_4Mo (Ref. 14) with the limiting values $\alpha_{DO_{22}}$ is weak, and in large measure the parameters for both alloys agree to some extent with the values for the superlattices $D1_a$ and N_2M_2.

The possibility of the existence in Ni_4Mo alloys, during the initial stages of formation of the equilibrium $D1_a$ superlattice, of a hypothetical N_2M_2 structure with the alternation of NiNi MoMo atoms in the {420} plane, generating the $\{1\frac{1}{2}0\}$ reflection, has been noted in electron microscope

TABLE II. Extremal sums $\Sigma_{I,II}$ and intensity of diffuse scattering from short-range order $I_{SRO}(h_1,h_2,h_3)$ in Laue units for various stationary points of the reciprocal fcc lattice space (summation over i spheres).

Coordinates of stationary points	Extremal sums Σ_I and Σ_{II}	Intensity $I_{SRO}(h_1,h_2,h_3)$
000	$\Sigma_I=\Sigma_i\alpha_i c_i R_{i0}$	$\Sigma_i\alpha_i c_i$
001	$\Sigma_I=\frac{1}{2}\Sigma_i\alpha_i c_i(R_{i0}C_{i1}-R_{i1})$ $\Sigma_{II}=\Sigma_i\alpha_i c_i R_{i1}$	$\frac{1}{3}\Sigma_i\alpha_i c_i C_{i1}$
$\frac{1}{2}\frac{1}{2}\frac{1}{2}$	$\Sigma_I=\Sigma_i\alpha_i c_i(R_{i0}C^0_{i2}+R^0_{i2}C^0_{i1})$ $\Sigma_{II}=\Sigma_i\alpha_i c_i(R_{i0}C^0_{i2}-2R^0_{i2}C^0_{i1})$	$\Sigma_i\alpha_i c_i C^0_{i2}$
$1\ \frac{1}{2}\ 0$	$\Sigma_I=\frac{1}{2}\Sigma_i\alpha_i c_i(R_{i0}C^0_{i1}-R^0_{i1})\frac{(C_{i1}-1)}{2}$ $\Sigma_{II}=\Sigma_i\alpha_i c_i R^0_{i1}\frac{(C_{i1}-1)}{2}$	$\frac{1}{3}\Sigma_i\alpha_i c_i C^0_{i1}$ $\times\frac{(C_{il}-1)}{2}$

studies of electron-irradiated samples.[10–12] In the authors' opinion, during the earliest stages of the ordering process, when the $\{1\frac{1}{2}0\}$ reflections are still isolated, this structure can be described in terms of packets of concentration waves, each characterized by a low-amplitude wave concentration of a certain variant of $\{1\frac{1}{2}0\}$. Waves corresponding to different variants can be amplified within the limits of a region spanning several interatomic distances. Wave packets with different variants of $\{1\frac{1}{2}0\}$ can eventually become superimposed, resulting in the formation of clusters containing structural elements of other types. In addition, the interference of $\{1\frac{1}{2}0\}$ wave packets with packets of other concentration waves is possible, and this ultimately leads to an equilibrium ordered state.

A mathematical analysis of the function (5) in reciprocal space for the purpose of exposing the localization of its extrema for the fcc lattice shows that they are possible only at four types of stationary points, viz.: $\{000\}$, $\{100\}$, $\{\frac{1}{2}\ \frac{1}{2}\ \frac{1}{2}\}$, and $\{1\frac{1}{2}0\}$. The localization of the extremum positions does not depend on the values of the parameters α_{lmn}, because the first derivative of the function (5) with respect to the coordinates of reciprocal space is equal to zero, since the trigonometric term is equal to zero on each sphere. Consequently, the obtaining of an extremum at one of the stationary points, including a stationary point of the type $\{1\frac{1}{2}0\}$, does not require the introduction of concentration waves or inquiry into the condition for their amplification. From an analysis of the second derivatives of the intensity function (5) with respect to the coordinates of reciprocal space h_1,h_2,h_3 we have been able to formulate the conditions for extrema to occur at each of the four stationary points. These conditions are formulated in Table II in the form of certain extremal sums over the ith spheres, beginning with the first, for different stationary points of the fcc lattice, which are listed in the second column. For positive values of the sums I and II maxima of the short-range order intensity are observed at each stationary point; if the values of the sums I and II are negative, intensity minima are observed at points of the type $\{1\frac{1}{2}0\}$. The following abbreviated symbols are used in Table II:

$$
\begin{aligned}
R_{i0}&=l^2+m^2+n^2,\\
R_{i1}&=l^2\cos\pi l+m^2\cos\pi m+n^2\cos\pi n,\\
R^0_{i1}&=l^2\cos\frac{\pi}{2}l+m^2\cos\frac{\pi}{2}m+n^2\cos\frac{\pi}{2}n,\\
R^0_{i2}&=lm\sin\frac{\pi}{2}l\sin\frac{\pi}{2}m+nl\sin\frac{\pi}{2}l\sin\frac{\pi}{2}n\\
&\quad+mn\sin\frac{\pi}{2}m\sin\frac{\pi}{2}n,\\
C_{i1}&=\cos\pi l+\cos\pi m+\cos\pi n,\\
C^0_{i1}&=\cos\frac{\pi}{2}l+\cos\frac{\pi}{2}m+\cos\frac{\pi}{2}n,\\
C^0_{i2}&=\cos\frac{\pi}{2}l\cos\frac{\pi}{2}m\cos\frac{\pi}{2}n.
\end{aligned}
\tag{6}
$$

The short-range order parameters for each site (lmn) on the ith sphere are identical and equal to α_i. The coordination number of the ith sphere is c_i. The third column of Table II gives the short-range order intensity in Laue units $I_{SRO}(h_1,h_2,h_3)$ for each type of stationary point with allowance for the zeroth coordination sphere, which further aids in determining the type of ordering from the experimental short-range order parameters.

The results of substituting the short-range order parameters directly into the extremal sums for different short-range order states in Ni–Mo alloys are summarized in Table III. It

TABLE III. Values of extremal sums $\Sigma_{I,II}$ and short-range order intensity I_{SRO} for stationary points in Ni–Mo alloys.

				Extremal sums $\Sigma_{I,II}$ and intensities I_{SRO} for stationary points											
				000		001			$\frac{1}{2}\ \frac{1}{2}\ \frac{1}{2}$			$1\ \frac{1}{2}\ 0$			
No.	Alloy, at. % Mo	Treatment	No. of parameters i	Σ_I	I_{SRO}	Σ_I	Σ_{II}	I_{SRO}	Σ_I	Σ_{II}	I_{SRO}	Σ_I	Σ_{II}	I_{SRO}	[Ref.]
1	10.7	Harden 1000 °C	10	−3.55	−0.284	−7.92	−1.15	1.028	−0.31	−0.96	0.004	18.74	17.90	3.180	[13]
2	20.0	Same	31	44.57	1.810	−5.23	3.340	0.738	7.28	−0.60	0.021	46.28	102.2	7.706	[13]
7	11.8	Anneal 2 h 1000 °C	149	−65.95	−0.578	−50.46	9.349	0.819	11.14	8.034	0.438	89.78	127.7	5.278	This paper
		Cool	60	−46.33	−0.407	−50.70	8.507	0.817	12.18	10.15	0.447	89.07	126.5	5.270	
		2°/min	51	−37.79	−0.291	−49.35	15.95	0.870	−16.22	−20.21	0.074	63.38	96.50	4.920	

follows from an analysis of the data in this table that the ordering in the investigated Ni–Mo alloys is on the type of stationary point $\{1\frac{1}{2}0\}$ over a wide range of values of the short-range order parameters.

Consequently, ordering on the type of stationary point $\{1\frac{1}{2}0\}$ is preserved both in the region of existence of the solid solution (alloy Ni–10.7 at. % Mo) and near its boundary (alloy Ni–11.8 at. % Mo), and also for the stoichiometric composition of the hardened alloy Ni–20 at. % Mo.

*)E-mail: kulish@radphys.ups.kiev.ua

[1] M. A. Krivoglaz, *Theory of X-Ray and Thermal Neutron Scattering by Real Crystals* (Plenum Press, New York, 1969).
[2] M. Krivoglaz, *Diffraction of X-Rays and Neutrons in Nonideal Crystals* (Kiev, 1983).
[3] A. G. Khachaturyan, *Theory of Phase Transformations and the Structure of Solid Solutions* (Moscow, 1974).
[4] D. De Fontaine, Acta Metall. **23**, 553 (1975).
[5] P. R. Okamoto and I. Thomas, Acta Metall. **19**, 825 (1971).
[6] S. K. Das, P. R. Okamoto, P. M. I. Fisher, and I. Tomas, Acta Metall. **21**, 913 (1973).
[7] G. Van Tendeloo and S. Amelinck, Acta Crystallogr., Sect. B: Struct. Crystallogr. Cryst. Chem. **41**, 281 (1985).
[8] J.-P. A. A. Chevalier and W. M. Stobbs, Acta Metall. **27**, 1197 (1979).
[9] S. Banerjee, K. Urban, and M. Wilkens, Acta Metall. **32**, 299 (1984).
[10] U. D. Kulkarni and S. Banerjee, Acta Metall. **36**, 413 (1988).
[11] S. Banerjee, U. D. Kulkarni, and K. Urban, Acta Metall. **37**, 35 (1989).
[12] U. D. Kulkarni, S. Muralidhar, and S. Banerjee, Phys. Status Solidi A **110**, 331 (1988).
[13] J. E. Spruiel and E. E. Stansbury, J. Phys. Chem. Solids **26**, 811 (1965).
[14] B. Chakravarti, E. A. Starke, C. J. Sporker, and R. O. Williams, J. Phys. Chem. Solids **35**, 1317 (1974).
[15] C. J. Sparks and B. Borie, in *Local Atomic Arrangements Studied by X-Ray Diffraction*, edited by J. B. Cohen and J. E. Millard, AIP Conf. Proc. Vol. 36 (AIP, New York, 1966), p. 5.
[16] B. Borie and C. J. Sparks, Acta Crystallogr. Sect. A, **27**, 198 (1971).
[17] V. I. Iveronova and A. A. Katsnel'son, *Short-Range Order in Solid Solutions* (Moscow, 1977).
[18] N. P. Kulish, N. A. Mel'nikova, P. V. Petrenko, and V. G. Poroshin, in *Ordering of Atoms and Its Influence on the Properties of Alloys* (Sverdlovsk, 1983).
[19] N. P. Kulish, P. V. Petrenko, and V. G. Poroshin, ''Characteristics of the conversion of short-wavelength x-rays into absolute electron units,'' deposited Sept. 9, 1983 at the All-Union Institute of Scientific and Technical Information, VINITI Deposit No. 5160-83; Metallofizika (Kiev) **6**, 119 (1984).
[20] P. Georgopoulos and J. B. Cohen, J. Phys. (Paris) **38**, 7191 (1977).
[21] P. Georgopoulos and J. B. Cohen, in *Modulated Structures-1979*, AIP Conf. Proc. Vol. 53 (AIP, New York, 1979), p. 26.
[22] S. Hashimoto, Sci. Rep. Res. Inst. Tohoku Univ. A **30**, 44 (1981).
[23] J. B. Cohen, Solid State Phys. **39**, 131 (1986).
[24] N. P. Kulish, N. A. Mel'nikova, P. V. Petrenko, V. G. Poroshin, and N. L. Tsyganov, Izv. Vyssh. Uchebn. Zaved. Fiz. **32**, 82 (1989).
[25] A. L. Gritskevich, N. P. Kulish, N. A. Mel'nikova, P. V. Petrenko, V. G. Poroshin, and N. L. Tsyganov, in *Applied X-Ray Examination of Metals* (Leningrad, 1986), p. 108.
[26] B. A. Morozov, *Regular Methods for the Solution of Ill-Posed Problems* (Nauka, Fizmatgiz, Moscow, 1987).

Translated by James S. Wood

Superexchange pairing and magnetic ordering in cuprate superconductors

E. V. Orlenko and B. G. Matisov

St. Petersburg State Technical University, 195251 St. Petersburg, Russia
(Submitted December 22, 1998; resubmitted May 16, 1999)
Fiz. Tverd. Tela (St. Petersburg) **41**, 2127–2131 (December 1999)

The first analytic study of superexchange ion interaction in the cuprate layer of high-T_c superconductors is reported. It is shown that the superexchange nonadditive contributions are dominant in the onset of long-range magnetic order in a system, as well as are responsible for hole pairing to produce an energetically preferable, stable spin configuration. The Heisenberg parameter and the pair binding energy obtained *ab initio* are in a good quantitative agreement with experimental data. © *1999 American Institute of Physics.* [S1063-7834(99)00512-2]

1. The main cuprate HTSC materials exhibit a distinct layered structure.[1,2] The CuO_2 cuprate layer is common for all these compounds. It plays an important part both in the onset of superconductivity and in the manifestation of anomalous magnetic effects. For instance, in the insulating phase one observes antiferromagnetic ordering, with the Néel temperature being of the same order for materials differing in the elements sandwiched between the cuprate layers.[3] A small shift away from the stoichiometric composition, for example, by 1–2% when doped by strontium, destroys antiferromagnetism and results in the onset of short-range ferromagnetic ordering of the spin liquid with a large Heisenberg parameter. The spin statics and dynamics accompanying this phenomenon are approximated well by the Heisenberg Hamiltonian for the cuprate plane. The so-called $t-J$ model and the model of a nearly ferromagnetic Fermi liquid have been raising certain hopes until recently. However the serious criticisms launched by Anderson[4] against these two quite popular approaches raise again the issue of choosing an adequate microscopic model for the cuprate magnetism. At the same time the resonating-valence-bond model of Anderson,[5] which sheds light on the quantum-chemical origin of parallel bound-electron spin orientation and reveals the need of a more careful description of interatomic (interionic) interaction in the cuprate plane, remains valid. The fact is that statistical models, no matter to what extent they are correct,[5] are based on the Heisenberg Hamiltonian containing as a fitting parameter an exchange integral, which is either estimated from an indirect experiment or calculated in a simplified way in a two-electron approximation using Wannier functions as a basis, as is the case with the Hubbard model, or in the approximation of nearly free electrons. At the same time, as this was shown in Ref. 6, a quantum chemical analysis of interatomic interaction in itself permits one to make conclusions on the origin of spontaneous spin ordering and to calculate correctly the Heisenberg parameter used in the theory of magnetism of superconductors. This calculation is performed from first principles using the formalism of the exchange perturbation theory[6] (EPT). The algorithm of this calculation takes into account the effect of the bound-electron orbital state on the resultant total spin of the system. In this sense there is no need to invoke for the explanation of spin ordering the second-order effects associated with the lifting of spin-orbit coupling, and the magnetostriction, likewise a second-order effect. Some studies, however, pin hopes on the Jahn–Teller effect, which essentially takes into account the above-mentioned spin-orbit coupling,[7] but the Heisenberg parameter calculated here in terms of the statistical model is calculated in the two-electron approximation. And although the numerical value and the sign of the exchange parameters are admitted[7] to be extremely important for understanding the origin of the spontaneous parallel spin orientation in the HTSC material under study, on the whole a detailed microscopic analysis of exchange interactions is very complex, particularly in the conditions where they are comparable to the singlet-triplet splitting.

The superexchange nonadditive effects play an important part in magnetic ordering and electron distribution in the cuprate layer.[6] However a rigorous analytical calculation of such contributions to energy is presently lacking. Superexchange contributions are presented usually in the form of a combination of two-center exchange integrals calculated by the molecular-orbital method.[7–9] These calculations are based on the assumption of one-electron states being orthogonal,[10] which is invalid for the delocalized states of the oxygen-ion electrons.[11] Besides, one does not take into account the nonadditive three-center contributions, which, generally speaking, cannot be considered as small corrections to the pairwise ones.

This work reports on the first derivation of the ion interaction energy in the cuprate layer in an analytic form and analyzes in detail all possible three-center superexchange contributions. These contributions are shown to be of the same order of magnitude as the two-center ones. A calculation is carried out of the Heisenberg parameter for an ion chain with frustrated bonds in the vicinity of oxygen ions with a different valence, as well as of the hole pairing energy. It is demonstrated that inclusion of nonadditive superexchange terms permits one to understand the quantum mechanical nature of coexistence of the paired hole state with ferromagnetic ion-spin ordering in the cuprate plane. The calculated values of the Heisenberg parameter and of the

hole binding energy agree qualitatively with available experimental data.

2. Stoichiometric La_2CuO_4 has a bcc tetragonal structure with a space group $14/mmm$ (copper dioxide doped, for instance, by strontium, $La_{2-x}Sr_xCuO_4$, has the same lattice). NMR and muon precession experiments[12] show that the antiferromagnetic state occurs in this material due to the in-plane Cu^{2+}-ion interaction, while the interplanar magnetic coupling is weak. The magnetic form-factor of the Cu^{2+} ion measured in the antiferromagnetic state[13] corresponds to the $3d^9$ state. Having a filled electronic shell, the O^{2-} ion located between the interacting copper ions is not involved in any way in this coupling.

The electron wave function of a pair of interacting Cu^{2+} ions corresponds, in a zero approximation, to states with a total spin $S=1$ or $S=0$. Its coordinate-dependent part is asymmetric or symmetric, respectively. Then for the lattice parameter $R=7.3\,a_B$ (Ref. 6), where a_B is the Bohr radius, the Heisenberg parameter $j=\varepsilon_{singl}-\varepsilon_{tr}=-0.104\,\text{eV}$. In this case j is a negative quantity, which corresponds to an antiparallel orientation of spins at neighboring lattice sites as an energetically preferable configuration.

Similar calculations of the j parameter performed for the Cu^{2+} ions lying in neighboring layers ($R=12.38\,a_B$) yield $j=-9.7\times10^{-5}\,\text{eV}$, which also corresponds to antiparallel spin orientation, but with a very small coupling constant.

Thus the assumptions of the interplanar antiferromagnetic coupling being weak, which were made in spin models of the type of Refs. 4 and 14–16, were fully justified, and we are dealing here indeed with a two-dimensional antiferromagnetic system.

The same experiments[12] show that in the case of doping, for example, with strontium ($La_{2-x}Sr_xCuO_4$) the Néel temperature drops rapidly proportional to the doping level x. The fact is that doping with a doubly charged metal ion activates the O^{2-} ion located between copper ions, which becomes singly charged, O^-, and has now an unpaired electron. In this case when considering the interaction between two copper ions one should take into account the presence of one more electron belonging to the O^- ion, whose state is strongly delocalized and, thus, overlaps substantially the electronic states of the Cu^{2+} ions.

Consider two three-center fragments of a cuprate layer in doped La_2CuO_4, namely, $Cu^{2+}-O^--Cu^{2+}$ and $O^--Cu^{2+}-O^-$. An EPT calculation of the first fragment is presented in Ref. 6. For the sake of brevity, denote the centers in the second chain I–II–III, and the electrons belonging to these centers in the original arrangement 1, 2, and 3, respectively. Then the operator describing three-center interaction can be divided into two-center ones in the usual manner

$$\hat{W}=\hat{W}_{\text{I II}}+\hat{W}_{\text{II III}}+\hat{W}_{\text{I III}}, \tag{1}$$

where, for instance,

$$\hat{W}_{\text{I II}}=|\mathbf{R}_\text{I}-\mathbf{R}_\text{II}|^{-1}-|\mathbf{r}_1-\mathbf{R}_\text{II}|^{-1}-|\mathbf{r}_2-\mathbf{R}_\text{I}|^{-1}+|\mathbf{r}_1-\mathbf{r}_2|^{-1} \tag{2}$$

describes the interaction of the ion cores I and II, of an electron with the ''foreign'' nucleus, and of the electrons with one another, accordingly. Expressions (1) and (2) correspond to the original arrangement of electrons 1,2,3 over the centers I, II, and III. The unperturbed part of the Hamiltonian can be written

$$\hat{H}^0=\hat{H}^0_\text{I}(1)+\hat{H}^0_\text{II}(2)+\hat{H}^0_\text{III}(3), \tag{3}$$

and the coordinate-dependent part of the zero-approximation eigenfunction

$$\Phi^0(1,2,3)=\psi_\text{I}(\mathbf{r}_1)\,\psi_\text{II}(\mathbf{r}_2)\,\psi_\text{III}(\mathbf{r}_3), \tag{4}$$

where, for instance, $\mathbf{r}_1$ is the position vector of the first electron, and $\psi_\text{I}(\mathbf{r}_1)$ is a one-electron wave function centered at center I. The wave function (4) can be symmetrized using Young's diagrams in three ways corresponding to the following spin configurations: α — $(1\uparrow2\uparrow3\uparrow)$, β — $(1\uparrow2\uparrow3\downarrow)$, and γ — $(1\uparrow2\downarrow3\uparrow)$.

We invoke now the EPT algorithm,[6] by which the energy corrections due to interaction (1) can be written

$$\varepsilon_1=\langle\Phi^0(1,2,3)|\hat{V}_1|\Psi^0_i(1,2,3)\rangle, \tag{5}$$

provided

$$\det|\Delta_{ij}|\neq0,$$

where $|\Psi^0\rangle$ is an antisymmetric function of the zero approximation, $\Delta_{ij}=\langle\Psi^0_i|\Psi^0_j\rangle$, and the indices i and j run through the values α,β,γ corresponding to the Young diagrams specified. The $\hat{V}_i$ operator symmetrized in accordance with one of the Young diagrams, for example, with α, has the form[6]

$$\hat{V}_\alpha=\sum_p f_\alpha^{-1}\hat{W}_p|\Phi^p\rangle\langle\Phi^p|,$$

where the normalization factor

$$f_\alpha=\sum_p\langle\Phi^0|\Phi^p\rangle(-1)^{g_p}$$

is obtained from the condition

$$\langle\Phi^0|\Psi^0_i\rangle=1.$$

The index p corresponds to the number of electron permutation over the centers, g_p is the parity of permutation p, and $\hat{W}_p$ is the operator of interaction (1) for the case of pth electron permutation.

Secondary quantization yields the following Hamiltonian[17] for an atomic chain in the model of nearest-neighbor interaction taking into account three-center nonadditive coupling

$$\begin{aligned}\hat{H}=(3f)^{-1}\sum_\xi\Bigg\{&\sum_{i,j}\varepsilon^0_\xi(a^+_{\xi,i}a_{\xi,i}+a^+_{\xi-1,j}a_{\xi,i}\\&+a^+_{\xi+1,j}a_{\xi,1})+\sum_p\sum_{\substack{i,j,k\\i',j',k'}}(-1)^p\langle k',i'|\hat{W}_{\xi,\xi-1}|i,k\rangle\\&\times(a^+_{\xi,i'}a^+_{\xi-1,k'}a_{\xi-1,k}a_{\xi,i}+2a^+_{\xi+1,i'}a^+_{\xi,k'}a_{\xi-1,k}a_{\xi,i}\\&+2a^+_{\xi-1,i'}a^+_{\xi,k'}a_{\xi-1,k}a_{\xi+1,i})\langle j'|j\rangle(a^+_{\xi+1,j'}a_{\xi+1,j}\\&+a^+_{\xi,j'}a_{\xi+1,j}+a^+_{\xi-1,j'}a_{\xi+1,j'})\Bigg\}.\end{aligned} \tag{6}$$

Here $a^{+}_{\xi,i}$, $a_{\xi,i}$ are the operators of creation and annihilation in a one-electron state i at center ξ, $\hat{W}_{\xi,\xi-1}$ is the pairwise interaction operator of type (2) of centers ξ and $\xi-1$, and $\langle j'|j\rangle$ are exchange one-electron densities of the type $\langle \psi_{j'}(r-R_{\xi})|\psi_j(r-R_{\xi-1})\rangle$. The f factor appears as a result of normalization. The summation is carried out over all centers ξ in the chain and over one-electron states i,j,k, with due account of the permutation signs. The rule of signs in front of the corresponding matrix elements follows from the Young diagrams.

As seen from Eq. (6), there are only three kinds of exchange three-center terms, of which only the fifth and sixth are truly superexchange. The matrix elements for the first of them are

$$\langle \psi_{\xi+1,i'}(r)\psi_{\xi,k'}(r')|\hat{W}_{\xi,\xi-1}|\psi_{\xi-1,k}(r')\psi_{\xi,i}(r)\rangle \quad (a),$$

and

$$\langle \psi_{\xi+1,i'}(r)\psi_{\xi,k'}(r')|\hat{W}_{\xi,\xi-1}|\psi_{\xi,i}(r')\psi_{\xi-1,k}(r)\rangle \quad (b),$$

and for the second

$$\langle \psi_{\xi+1,i'}(r)\psi_{\xi-1,k'}(r')|\hat{W}_{\xi,\xi-1}|\psi_{\xi,k}(r')\psi_{\xi-1,i}(r)\rangle \quad (c),$$

and

$$\langle \psi_{\xi+1,i'}(r)\psi_{\xi-1,k'}(r')|\hat{W}_{\xi,\xi-1}|\psi_{\xi-1,k}(r')\psi_{\xi,i}(r)\rangle \quad (d). \tag{7}$$

Pairwise contributions to three-center interaction are provided by the fourth term in Eq. (6). All the integrals presented here are of the same order of magnitude, which is comparable to that of the direct, non-exchange contribution. Therefore the rule of signs with which these terms enter Eq. (6) acquires a particular significance. This rule is related to the way in which the wave function of the system is symmetrized in accordance with the total spin of this system.

To make the integrals (7) more revealing, they can be presented in a diagrammatic form:

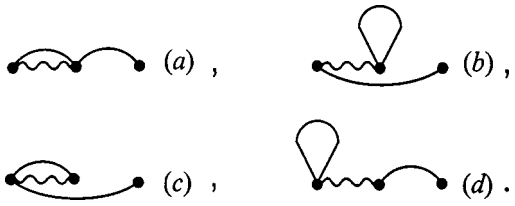

Here the points identify the centers of interacting ions, the lines depict Green's one-electron functions, and the interaction is shown with a wavy line.

We can present now the numerical values of the superexchange contributions (7) calculated for the $O^{-}-Cu^{2+}-O^{-}$ ion chain (I–II–III). The wave function of the copper-ion electron corresponds to the hydrogenic state $3d^{9}_{x^2-y^2}$ (Ref. 18)

$$\psi_2(r)=(15\cdot 2^7/16\pi\cdot 6!)^{0.5}r^2\sin^2\theta\cos 2\varphi.$$

The wave function of the oxygen-ion electrons corresponds to the $2p^5$ state[11]

$$\psi_1(r)=\sqrt{\pi/0.5^5}r\sin\theta\cos\varphi\exp(-0.5r).$$

Thus for the given center separations I–III and I–II, $R_{\mathrm{III}}=R=7.355\,a_B$ and $R_{\mathrm{II}}=R/2=3.678\,a_B$, respectively, we obtain, for instance, for the $Q_{\mathrm{I,II}}$ contribution for the I–II–III chain

$$\begin{aligned}Q_{\mathrm{I,II}}\equiv\langle\Phi(123)|\hat{V}_{\mathrm{I,II}\beta}|\Psi_\beta(123)\rangle&=R_{\mathrm{II}}^{-1}+8(1-I_1^2+I_2^2\\&-I_2I_1^2)^{-1}\times\{(-2B_{11}+K_{2112})+I_2(-B_{13}-B_{11}I_2\\&+K_{1232})-(-2B_{12}I_1+K_{2112})-I_2(-B_{12}I_1-C_{12}I_1\\&+K_{2312})\},\end{aligned} \tag{8}$$

or, displayed diagrammatically,

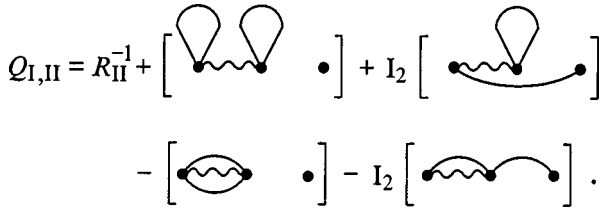

The notation adopted in Eq. (8) is as follows

$$\begin{aligned}B_{11}&=\langle\psi_1(r)||r-R/2|^{-1}|\psi_1(r)\rangle,\\C_{12}&=\langle\psi_1(r)||r-R|^{-1}|\psi_2(r-R/2)\rangle,\\B_{12}&=\langle\psi_1(r)||r-R/2|^{-1}|\psi_2(r-R/2)\rangle,\\B_{13}&=\langle\psi_1(r)||r-R/2|^{-1}|\psi_1(r-R)\rangle,\\K_{\xi\chi\tau\zeta}&=\langle\psi_a(r_1-R_\xi)\psi_b(r_2-R_\chi)||r_1-r_2|^{-1}|\\&\quad\times\psi_c(r_2-R_\tau)\psi_d(r_1-R_\zeta)\rangle,\\I_1&=\langle\psi_1(r)|\psi_2(r-R/2)\rangle,\quad I_2=\langle\psi_1(r)|\psi_1(r-R)\rangle.\end{aligned} \tag{9}$$

The numerical values of the above three-center contributions to the energy of interaction between the first and second centers calculated for the given center separation are

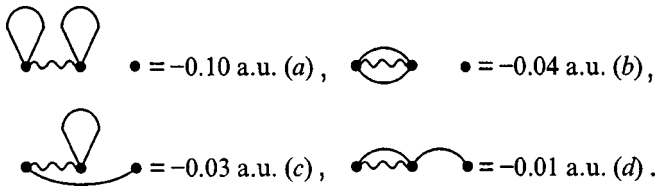

(10)

As seen from Eq. (10), one of the nonadditive three-center superexchange contributions, namely, (c), is of the same order of magnitude as the two-center direct (a) and exchange (b) ones, and therefore it can yield a correction to the exchange energy of 10 to 100%, depending on the factor which accounts for the extent of overlap of the third electron. In the given case $I_1=0.29$ and $I_2=0.17$.

The energy corrections calculated for all possible spin configurations in the chain under study are

$$\begin{aligned}E_\alpha(\uparrow\uparrow\uparrow)&=-0.64\ \text{a.u},\\E_\beta(\uparrow\downarrow\downarrow)&=-0.76\ \text{a.u},\\E_\gamma(\uparrow\downarrow\uparrow)&=-0.65\ \text{a.u}.\end{aligned} \tag{11}$$

For the similar triple of ions $Cu^{2+}-O^{-}-Cu^{2+}$, the energy corrections for the corresponding spin configurations are[6]

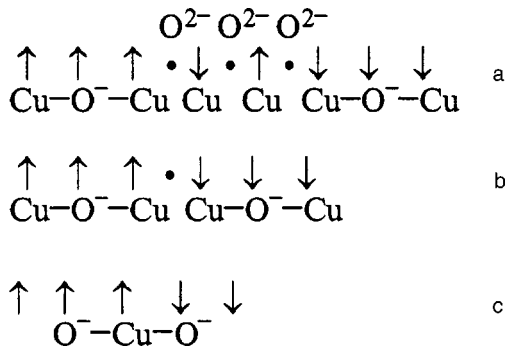

FIG. 1. Spin ordering in cuprate-layer chains.

$$E'_{\alpha}(\uparrow\uparrow\uparrow) = -0.76\ \text{a.u},$$

$$E'_{\beta}(\uparrow\updownarrow\downarrow) = -0.67\ \text{a.u},$$

$$E'_{\gamma}(\uparrow\downarrow\uparrow) = -0.64\ \text{a.u}. \qquad (12)$$

The Heisenberg parameter in the vicinity of an oxygen with a different valence is

$$J = E'_{\beta} - E'_{\alpha} = 0.09\ \text{a.u.} = 2.51\ \text{eV}.$$

Thus doping which activates oxygen ions O^- can indeed give rise to electron spin reorientation on the Cu^{2+} ions and to the onset of strong ferromagnetism.

Therefore, as shown in Ref. 13 from an analysis of experimental data, strong ferromagnetic coupling in the CuO_2 plane destroys local antiferromagnetic order. In the case of strong localization, the Φ-bond concentration would be x. As x increases, the localization length l_0 of each hole increases too, and this brings about an increase of the effective concentration of Φ-bonds. The large value of the ratio $J/|j|$ was recently shown[13] to reduce the threshold concentration x at which antiferromagnetism disappears in doped La_2CuO_4 (Refs. 19 and 20). An analysis of the energies of the corresponding spin configurations permits a conclusion on the behavior of oxygen-saturated chains.

If a cuprate-layer chain has at least two ''holes'' or, in other words, two O^- ions located far from one another, each of these ions stimulates orientation of uncompensated Cu^{2+} spins parallel to the oxygen-ion spin to produce two configurations of the type $\uparrow\uparrow\uparrow$ (Ref. 12). It can be expected that such two three-spin objects would move along the chain toward one another because of an effective attraction (11) (see Figs. 1a and 1b). On encounter, these objects combine to make up an energetically preferable configuration [see Eqs. (11) and (12)], such that the hole spins are antiparallel, and the copper ions, while retaining short-range ferromagnetic order, behave as a fluctuating spin liquid (Fig. 1c). This qualitative conclusion contradicts neither the concept of resonating valence bonds proposed by Anderson[5] nor numerical ladder-diagram calculations.[10]

Let us calculate the energy difference between the spin configurations displayed in Figs. 1a and 1c:

$$\Delta E = E_c - E_a = 0.5(E'_{\beta} - E'_{\alpha} - E_{\alpha} + E_{\beta}) = -0.41\ \text{eV}.$$

Obviously enough, the spin configuration shown in Fig. 1c is energetically preferable. Thus the energy gained in the superexchange hole-pairing mechanism is 0.41 eV.

Experiments on absorption in the medium IR range carried out on doped superconducting $La_2SrCu_2O_{6+\delta}$ samples show a resonance at a frequency corresponding to an energy gap of 0.3–0.6 eV.[14] Such peaks in the medium IR range are associated usually with the presence in the material of a superconducting phase.[20,21] An analysis was also made of possible transitions taking into account interaction with the lattice; the experimental value of the gap forming in the material was estimated as 0.34 eV.[22] Models[23] based on the polaron mechanism of pairing yield similar gap energies, from 0.3 to 0.5 eV; they involve, however, a poorly substantiated assumption[24] of a very strong attraction between two electrons residing at the same site, which overcomes the unscreened Coulomb repulsion.

3. While not claiming a theoretical description of the formation of the energy gap itself, the present authors have focused their main attention here on an explanation of the magnetic phenomena and of the hole pairing effect in the cuprate layer. Pairing is a necessary but not sufficient condition for the existence of an energy gap, which, nevertheless, coincides in order of magnitude with the calculated hole-pairing energy. Nevertheless, the presence of superexchange effects, which are introduced here *ab initio*, permits one to explain, both qualitatively and quantitatively, the coexistence of the short-range ferromagnetic order caused by co-orientation of the copper-ion electron spins with the Cooper hole pairing. In this case the size of the pair is two lattice constants, i.e., ~ 7 a.u., exactly as specified in Ref. 22.

Thus one can make the following conclusions:

(1) An analysis of superexchange interaction in the cuprate layer chains not only permits one to calculate *a priori* the Heisenberg parameter present in any spin model but offers a revealing pattern of a trend to establishment of an energetically preferable spin configuration as well. Without going into details of the dynamics of the process, one succeeds in predicting a static pattern of parallel spin orientation of the electrons belonging to copper and oxygen ions. The numerical value of this parameter is in an excellent agreement with available experimental data.[25]

(2) The superexchange three-center integrals appearing already in the first order of EPT yield energy contributions comparable in order of magnitude, which, while not exceeding, on the average, the pairwise exchange contribution, are at the same time not just small corrections to the latter. Therefore one should take into account all possible configurational superexchange terms with the corresponding signs, which provide a nonadditive contribution and, hence, contain long-range correlations. We have performed a classification and a numerical calculation of all possible three-center contributions.

(3) The calculated hole-pairing energies are in a good qualitative agreement with experimental data.

The authors are indebted to T. Yu. Latyshevskaya for assistance in a larger part of computations.

One of the authors expresses gratitude to the International Science Foundation for financial support.

[1] *Physical Properties of High-Temperature Superconductors*, edited by D. M. Ginsberg (World Scientific, Singapore, 1989; Mir, Moscow, 1990).
[2] H. Ichara and M. Hirabayashi, Bull. Electrotechn. Lab. **53**, 57 (1989).
[3] J. Mizuki and Y. Kubo, Physica C **156**, 781 (1989); R. de Renzi and C. Bucci, *ibid.* **155**, 162 (1989); G. M. Luke, B. J. Sternlieb, Y. J. Uemura, J. H. Brewer, R. Kadono, R. F. Kiefl, S. R. Kreitzman, T. M. Riseman, J. Gopalakrishnan, A. W. Sleight, M. A. Subramanian, S. Uchida, H. Takagi, and Y. Tokura, Nature (London) **338**, 49 (1989).
[4] P. W. Anderson, Adv. Phys. **46**, 1 (1997).
[5] P. W. Anderson, G. Baskaran, Z. Zou, and T. Hsu, Phys. Rev. Lett. **58**, 2790 (1987).
[6] E. V. Orlenko and T. Yu. Latyshevskaya, Zh. Éksp. Teor. Fiz. **113**, 2129 (1998) [JETP **86**, 1167 (1998)]; E. V. Orlenko and A. A. Rumyantsev, Zh. Éksp. Teor. Fiz. **97**, 439 (1990) [Sov. Phys. JETP **70**, 244 (1990)].
[7] A. S. Moskvin and A. S. Ovchinnikov, Fiz. Tverd. Tela (St. Petersburg) **40**, 1785 (1998) [Phys. Solid State **40**, 1618 (1998)]; A. S. Moskvin and Yu. D. Panov, Fiz. Tverd. Tela (St. Petersburg) **40**, 1795 (1998) [Phys. Solid State **40**, 1627 (1998)].
[8] G. M. Éliashberg, in *Physical Properties of High-Temperature Superconductors*, edited by D. M. Ginsberg (World Scientific, Singapore, 1989; Mir, Moscow, 1990), p. 505.
[9] S. Gopalan, T. M. Rice, and M. Sigrist, Phys. Rev. B **49**, 8901 (1994).
[10] M. Troyer, H. Tsunetsugy, and T. M. Rice, Phys. Rev. B **53**, 251 (1996).
[11] N. Nücker, J. Fink, J. C. Fuggle, P. J. Durham, and W. M. Temmerman, Phys. Rev. B **37**, 5158 (1988).
[12] S. A. Carter, B. Batlogg, R. J. Cava, J. J. Krajewski, W. F. Peck, Jr., and T. M. Rice, Phys. Rev. Lett. **77**, 1378 (1996).
[13] Y. Budnik *et al.*, Europhys. Lett. **5**, 647 (1988); T. Takahashi, F. Maeda, H. Arai *et al.*, Physica B **148**, 476 (1987); K. Kumagai, I. Watanabe, H. Aoke *et al. ibid.* **148**, 480 (1987).
[14] R. J. Birgenau and G. Shirane, in *Physical Properties of High-Temperature Superconductors*, edited by D. M. Ginsberg (World Scientific, Singapore, 1989; Mir, Moscow, 1990), p. 163.
[15] A. Aharony, R. J. Birgeneau, A. Coniglio, M. A. Kastner, and H. E. Stanley, Phys. Rev. Lett. **60**, 1330 (1988).
[16] P. J. Hay, J. C. Thibeault, and R. Hoffmann, J. Am. Chem. Soc. **97**, 4884 (1975).
[17] M. Moshinsky and Th. Seligman, Ann. Phys. (Leipzig) **66**, 311 (1974); E. V. Orlenko, Thesis, St. Petersburg (1990).
[18] R. J. Birgeneau, J. Skalio, and G. Shirane, Phys. Rev. B **5**, 1736 (1971).
[19] J. M. Tranquada, P. E. Cox, W. Kunnmann, H. Moudden, G. Shirane, M. Sueraga, and P. Zolliker, Phys. Rev. Lett. **60**, 156 (1988).
[20] S. G. Kaplan, T. W. Noh, P. E. Sulewski, H. Xia, and A. J. Sievers, Phys. Rev. B **38**, 5006 (1988).
[21] A. S. Barker, in *Optical Properties and Electronic Structure of Metals and Alloys*, edited by F. Abelés (North-Holland, Amsterdam, 1965); S. Tajima, S. Uchida, A. Masaki, H. Takagi, K. Kitazawa, S. Tanaka, and A. Katsui, Phys. Rev. B **32**, 6302 (1985).
[22] L. P. Gor'kov and N. B. Kopnin, Usp. Fiz. Nauk **156**, 117 (1988) [Sov. Phys. Usp. **31**, 850 (1988)].
[23] M. J. Rice and Y. R. Wang, Phys. Rev. B **36**, 8794 (1987).
[24] A. S. Davydov, *High-Temperature Superconductivity* (Naukova Dumka, Kiev, 1990), p. 174.
[25] C. J. Peters, R. J. Birgeneau, M. A. Kastner, H. Yoshizawa, Y. Endoh, J. Tranquada, G. Shirane, Y. Hidaka, M. Oda, M. Suzuki, and T. Murakami, Phys. Rev. B **37**, 9761 (1988).

Translated by G. Skrebtsov

Dependence of the superconducting transition parameters on the solid-solution composition and Te excess in $Sn_{1-z}Pb_zTe$:In

R. V. Parfen'ev and D. V. Shamshur

A. F. Ioffe Physicotechnical Institute, Russian Academy of Sciences, 194021 St. Petersburg, Russia

S. A. Nemov

St. Petersburg State Technical University, 195251 St. Petersburg, Russia

(Submitted May 17, 1999)
Fiz. Tverd. Tela (St. Petersburg) **41**, 2132–2134 (December 1999)

A low-temperature (0.4–4.2 K) measurement of the temperature dependences of the resistivity of two series of samples, $SnTe_{1+y}$ and $Sn_{0.8}Pb_{0.2}Te_{1+y}$ solid solution, doped with 5 at.% In, is reported. The parameters of the superconducting transition, namely, the critical temperatures T_c and the second critical magnetic field H_{c2}, and their dependences on tellurium excess ($0 \leqslant y \leqslant 0.06$) have been determined. The observed variation of the critical parameters with increasing tellurium excess in the samples is associated with a change in the filling by holes of the indium-impurity resonance states. © *1999 American Institute of Physics.*
[S1063-7834(99)00612-7]

Doping IV–VI compounds with indium imparts unusual physical properties to these materials, which are due to the existence of impurity resonance states within the allowed electron (hole) spectrum.[1] The indium resonance states in tin telluride and $Sn_{1-z}Pb_zTe$ solid solutions ($z \leqslant 0.4$) lie within the valence band.[2,3] The energy of the In resonance states E_{In} and their broadening Γ depend substantially on the solid-solution composition z and the indium dopant concentration N_{In}.[3] The existence of an In resonance-state band with a high density of states $N(0) \sim N_{In}$ (which exceeds the density of states in the valence band of SnTe, Refs. 3 and 4) accounts for the formation of a number of new physical phenomena, such as pinning of the Fermi hole level E_F and resonant scattering of band carriers into the In impurity states.[2,5] The onset of bulk superconductivity with critical superconducting-transition temperatures T_c in the helium region, which are relatively high for semiconductors, and with critical magnetic fields $H_{c2}(0\ \mathrm{K}) \sim 10-50$ kOe is intimately connected with the filling of the In resonance states.[2–6] It should be pointed out that SnTe and $Sn_{1-z}Pb_zTe$ without an In impurity are also superconductors, but with critical temperatures and magnetic fields lower by an order of magnitude.[7] The materials studied here, SnTe and the related solid solutions, are of interest for development of superconducting radiation receivers (bolometers) to operate in the helium-temperature region. The present work deals with the effect of tellurium excess on the superconducting transition in SnTe and $Sn_{0.8}Pb_{0.2}Te$ solid solutions doped with 5 at.%In.

1. SAMPLES

The samples were prepared by the ceramic technology, and their composition corresponded to the chemical formulas $Sn_{0.95}In_{0.05}Te_{1+y}$ and $(Sn_{0.8}Pb_{0.2})_{0.95}In_{0.05}Te_{1+y}$ ($y = 0, 0.5, 1, 1.5, 1.75, 2, 2.5, 3, 5, 6$ at.%). The ingots were produced by melting in vacuum the starting components of semiconductor-grade purity with subsequent quenching at room temperature. After crushing the ingots to a grain size $d \sim 0.1$ mm, the powder was pressed under heating ($P = 2000\ \mathrm{kg/cm^2}$). Next the samples were annealed in vacuum at 600 °C for 200 h. Electron microprobe analysis did not reveal any trace of a second phase in the samples to be studied.

2. EXPERIMENT

A study was made of the temperature dependences of the sample resistivity ρ at temperatures ranging from 0.4 to 4.2 K and magnetic fields H of up to 13 kOe. The jump in the $\rho(T)$ and $\rho(H)$ dependences indicated a transition to superconducting state. The superconducting transition was observed to occur also in studies of the dependence of the magnetic susceptibility on temperature. Note that an investigation of low-temperature heat capacity[8] established the superconductivity in $Sn_{1-x}In_xTe$ to have bulk character.

The critical parameters T_c and $H_{c2}(T)$ were determined from the condition $\rho = 0.5\rho_N$ (ρ_N is the normal-state resistivity for $T \leqslant 4.2$ K). Next the $H_{c2}(T)$ relations were used to find the derivatives $|\partial H_{c2}/\partial T|_{T \to T_c}$ for each sample. The hole concentration was derived from room-temperature Hall data using the expression $p_{300} = (eR)^{-1}$, where R is the Hall coefficient, and e is the absolute value of the electronic charge. The experimental data obtained in the work are displayed in Figs. 1 and 2.

3. DISCUSSION OF THE RESULTS

Prior to starting discussion of the results, we note that the superconducting transition observed in the $(Sn_{0.8}Pb_{0.2})_{0.95}In_{0.05}Te_{1+y}$ solid solutions studied by us, as well as in In-doped SnTe, exhibits substantially higher critical parameters [T_c reaches 3 K, and $H_{c2}(T = 0\ \mathrm{K})$, 24 kOe]

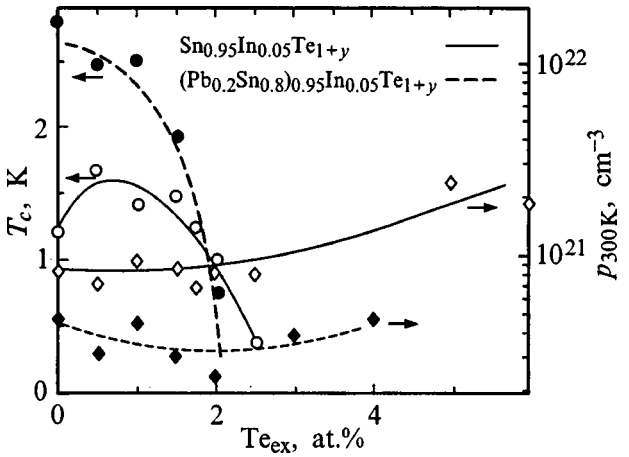

FIG. 1. Dependences of the critical superconducting-transition temperature T_c and Hall hole concentration p_{300} on tellurium excess y in the $Sn_{0.95}In_{0.05}Te_{1+y}$ and $(Sn_{0.8}Pb_{0.2})_{0.95}In_{0.05}Te_{1+y}$ solid solutions.

than in samples that do not contain an In impurity,[2,3,7] thus indicating an unusual behavior of superconductivity in materials with impurity resonance states, which interact strongly with band states.

Consider the experimental data in more detail. As seen from Figs. 1 and 2, the dependences of the superconducting parameters T_c and $|\partial H_{c2}/\partial T|_{T\to T_c}$ on Te excess y observed in SnTe and the solid solution ($z=0.2$) behave in a similar way. An increase of the Te excess in samples brings about a rapid decrease of the critical parameters and destroys superconductivity for $T>0.4$ K.

Note that the excess Te (y) in $SnTe_{1+y}$ and $Sn_{0.8}Pb_{0.2}Te_{1+y}$ is electrically active and creates metal vacancies, which in the IV–VI compounds act as acceptors (they produce two holes in the valence band per vacancy). In In-doped materials, however, one does not observe a noticeable growth of the hole concentration in the valence band (Fig. 1). This is associated with the Fermi level E_F becoming pinned by the In impurity resonance states, which, as already mentioned, generate a high density-of-states peak. Thus introduction of a Te excess into $Sn_{1-z}Pb_zTe$:In does not result in a substantial E_F shift in the valence band while at the same time increasing the filling of the In resonance states by holes (up to complete filling). This results in E_F gradually shifting out of the In band, and this shift of E_F from the center of the impurity band with the maximum density of resonance states toward its lower edge (on the electron energy scale) is accompanied by a decrease of the density of states at the Fermi level, $N(0)$, and by a decrease in the intensity of electron interaction in the band and impurity states. This is evidenced by estimates of the density of states at the Fermi level based on our experimental data and made using the relation $N(0)=2.84\times10^{14}\cdot|\partial H_{c2}/\partial T|_{T_c}\cdot\rho_N^{-1}$ and the sample resistivity measurements (Fig. 2). It is the above factors that account for the general pattern of the observed relations, which are characterized by a decrease of the critical parameters of the superconducting transition in the compositions under study as a Te excess is introduced.

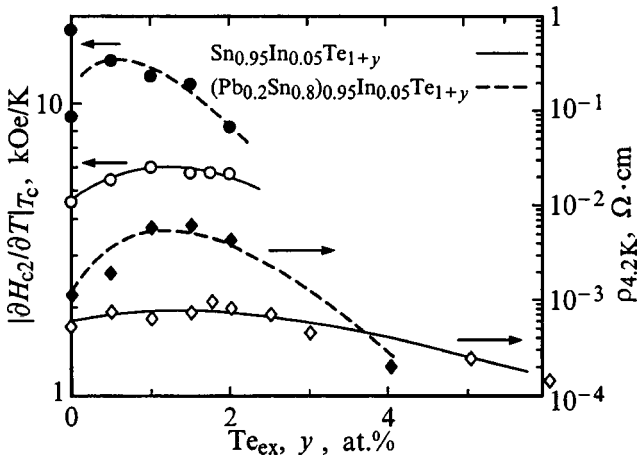

FIG. 2. Dependences of the normal-state resistivity $\rho_{4.2}$ at $T=4.2$ K and of the derivative of the second critical magnetic field with respect to temperature, $|\partial H_{c2}/\partial T|_{T\to T_c}$, on tellurium excess y introduced in the $Sn_{0.95}In_{0.05}Te_{1+y}$ and $(Sn_{0.8}Pb_{0.2})_{0.95}In_{0.05}Te_{1+y}$ solid solutions.

At the same time the behavior of the parameters of the superconducting transition in the series with $z=0$ and $z=0.2$ studied here exhibits quantitative differences. In $(Sn_{0.8}Pb_{0.2})_{0.95}In_{0.05}Te_{1+y}$ (for small y), T_c and $|\partial H_{c2}/\partial T|_{T\to T_c}$ are substantially higher; note, however, that as the Te excess (y) increases, the critical parameters decrease more rapidly than those for $Sn_{0.95}In_{0.05}Te$ (Figs. 1 and 2). These features in the experimental data can be interpreted if one takes into account the complex valence-band structure of the materials studied. One also should take into account, in accordance with Ref. 9, that as the Pb content in the $Sn_{1-z}Pb_zTe$ solid solution increases, the mutual positions of the deep extrema (supposedly at the Δ and Σ points of the Brillouin zone) vary relatively little (for $z<0.5$), whereas the In resonance states shift rapidly toward the valence-band top (the extrema at the BZ L points). As a result, the In band filling by holes in the solid solution increases with increasing z because of holes transferring from the additional extrema to the resonance states, and this is what accounts for the increase of the critical parameters. The corresponding decrease of the joint density of band states at the Fermi level should bring about a stronger Te-excess dependence of the superconducting transition parameters and of the resonance scattering intensity in the $Sn_{1-z}Pb_zTe$:In solid solution; this conclusion is in accord with the experiment.

Support of the ''Integration'' Federal program (Grant 75) and of the Russian Fund for Fundamental Research (Grant 99-02-1856) is gratefully acknowledged.

[1] V. I. Kaĭdanov and Yu. I. Ravich, Usp. Fiz. Nauk **145**, 51 (1985) [Sov. Phys. Usp. **28**, 31 (1985)].
[2] G. S. Bushmarina, I. A. Drabkin, V. V. Kompaniets, R. V. Parfen'ev, D. V. Shamshur, and M. A. Shakhov, Fiz. Tverd. Tela (Leningrad) **28**, 1094 (1986) [Sov. Phys. Solid State **28**, 612 (1986)].
[3] R. V. Parfen'ev, D. V. Shamshur, M. A. Shakhov, and Z. Chrapkiewicz, J. Alloys Compd. **219**, 313 (1995).
[4] G. S. Bushmarina, I. A. Drabkin, M. A. Kvantov, and O. E. Kvyatkovskiĭ, Fiz. Tverd. Tela (Leningrad) **32**, 2869 (1990) [Sov. Phys. Solid State **32**, 1666 (1990)].
[5] S. A. Nemov and Yu. I. Ravich, Usp. Fiz. Nauk **168**, 817 (1998).

[6] V. I. Kaĭdanov, S. A. Nemov, R. V. Parfen'ev, and D. V. Shamshur, JETP Lett. **35**, 639 (1982).
[7] R. A. Hein and P. H. E. Meijer, Phys. Rev. **179**, 497 (1969).
[8] H. Miyauchi, T. Nakajima, and E. Kanda, J. Phys. Soc. Jpn. **34**, 282 (1973).
[9] A. V. Berezin, S. A. Nemov, R. V. Parfen'ev, and D. V. Shamshur, Fiz. Tverd. Tela (St. Petersburg) **35**, 53 (1993) [Phys. Solid State **35**, 28 (1993)].

Translated by G. Skrebtsov

Landau level quantization and possible superconducting instabilities in highly oriented pyrolitic graphite

Y. Kopelevich

Instituto de Fisica ''Gleb Wataghin,'' Universidade Estadual de Campinas, Unicamp 13083-970 Campinas, São Paulo, Brazil;
A. F. Ioffe Physicotechnical Institute, Russian Academy of Sciences, 194021 St. Petersburg, Russia

V. V. Lemanov

A. F. Ioffe Physicotechnical Institute, Russian Academy of Sciences, 194021 St. Petersburg, Russia

S. Moehlecke and J. H. S. Torres

Instituto de Fisica ''Gleb Wataghin,'' Universidade Estadual de Campinas, Unicamp, 13083–970 Campinas, São Paulo, Brazil
(Received August 20, 1999)
Fiz. Tverd. Tela (St. Petersburg) **41**, 2135–2138 (December 1999)

Measurements of the basal-plane resistivity $\rho_a(T,H)$ performed on highly oriented pyrolitic graphite, with magnetic field $H \| c$-axis in the temperature interval 2–300 K and fields up to 8 T, provide evidence for the occurrence of both field-induced and zero-field superconducting instabilities. Additionally, magnetization $M(T,H)$ measurements suggest the occurrence of Fermi surface instabilities which compete with the superconducting correlations. © *1999 American Institute of Physics.* [S1063-7834(99)00712-1]

The magnetic field—temperature ($H-T$) phase diagram of conventional type-II superconductors is well known. In the Meissner state, the surface currents screen the applied magnetic field. Above the lower critical field $H_{c1}(T)$, the field penetrates the superconductor in the form of a lattice of vortices (Abrikosov lattice). Superconductivity persists up to the upper critical field $H_{c2}(T)$, described by the Abrikosov–Gor'kov theory.[1,2] On the other hand, it has been proposed[3] that the superconducting state can appear (or reappear) under application to an electron system of high enough magnetic field, such that the Landau quantization of the energy spectrum is important. In particular, when all electrons are in the lowest Landau level, the superconducting transition temperature $T_c(H)$ is expected to increase with field increasing, opposite to the $T_c(H)$ dependence in the classical low-field-limit.[3] However, superconductivity in the quantum regime has not been identified in experiments so far, remaining the subject of theoretical investigations only.

In the present work, we report the results of basal-plane resistivity $\rho_a(T,H)$ measurements performed on highly oriented pyrolitic graphite (HOPG), which provide evidence for the occurrence of superconducting correlations in both quantum and classical limits. Besides, magnetization measurements $M(T,H)$ suggest an interplay between superconducting and other Fermi surface instabilities, possibly spin-density-wave (SDW) or charge-density-wave (CDW) type.

The HOPG sample was obtained from the Research Institute ''GRAPHITE'' (Moscow). X-ray diffraction ($\Theta - 2\Theta$) measurements give the crystal lattice parameters $a=2.48$ Å and $c=6.71$ Å. The high degree of crystallites orientation along the hexagonal c-axis was confirmed from x-ray rocking curves (FWHM$=1.4°$). The geometrical sample density was 2.26 ± 0.01 g/cm^3. A cylindrical specimen with diameter of 5.2 mm, and thickness 3.14 mm, and a parallelepiped $4.9 \times 4.3 \times 2.5$ mm, both made from the same piece of HOPG, were used for magnetization and transport measurements, respectively. The c-axis was along the smallest size of the samples. The studies were performed for $H \| c$-axis. $M(T,H)$ dc magnetization was measured in fields up to 5 T and temperatures between 2 and 300 K by means of SQUID magnetometer MPMS5 (Qunatum Design). Low-frequency ($f=1$ Hz) standard four-probe resistance measurements were performed in fields up to 8 T, in the same temperature interval, with PPMS (Physical Properties Measurement System, Quantum Design).

Low-temperature portions of the basal-plane resistivity $\rho_a(T)$ measured for magnetic fields $H \leqslant 0.08$ T are shown in Fig. 1. As can be seen from Fig. 1, $\rho_a(T)$ has a well defined maximum at a temperature $T_{max}(H)$ (as defined in the inset of Fig. 1) which is decreasing function of field. Thus, $T_{max}(H)$ separates a high-temperature semiconducting-like behavior (ρ_a increases with temperature decreasing) from a low-temperature metallic-like behavior (ρ_a decreases with temperature decreasing). In the field interval $0.08 < H < 2.6$ T, the maximum in $\rho_a(T)$ does not occur (Fig. 2). With a further increase in the field, the maximum in $\rho_a(T)$ can be observed again for certain H (Fig. 3). A non-monotonous behavior of T_{max} vs H, and the competition between the metallic-like and semiconducting-like behavior can be seen in Fig. 3. At $H \geqslant 3.9$ T, $T_{max}(H)$ occurs at all measuring fields. Temperature dependences of $\rho_a(T)/\rho_a(T_{max})$ vs T for several fields in the interval $4 \leqslant H \leqslant 8$ T are shown in Fig. 4. In this high-field regime, T_{max} increases with H increasing.

Temperature dependences of normalized magnetization

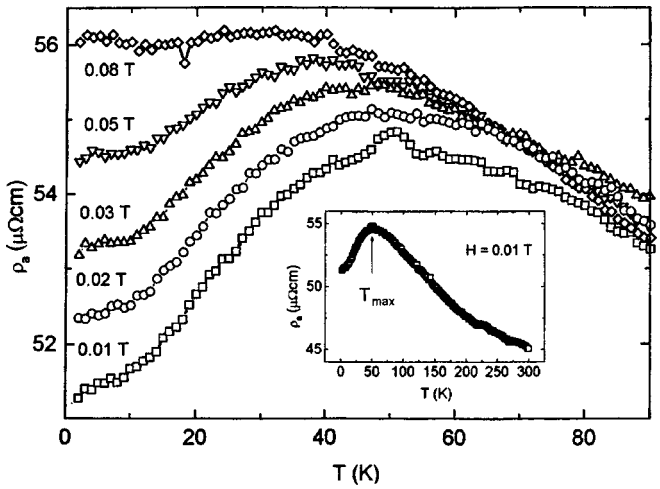

FIG. 1. Basal-plane resistivity $\rho_a(T)$ in the low-field-limit. Inset shows $\rho_a(T)$ in the whole temperature interval under study for $H=0.01$ T.

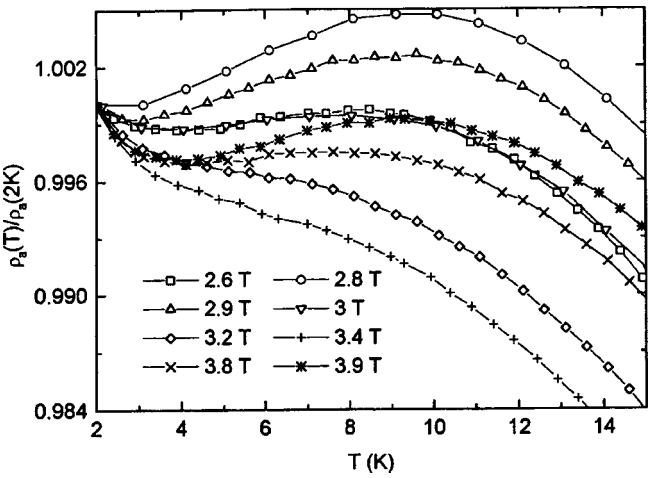

FIG. 3. Normalized resistivity $\rho_a(T)/\rho_a(2\mathrm{K})$ in the field interval where $T_{\max}(H)$ reappears.

$M(T)/|M(2\mathrm{K})|$ at various applied fields are presented in Figs. 5 and 6. The inset to Fig. 6 shows $M(T)$ measured for $H=4$, 4.5 and 5 T demonstrating that the absolute value of diamagnetic magnetization $M(T,H)$ increases with field increasing and temperature decreasing, in agreement with previous reports.[4] The novel feature is the occurrence of a minimum in $M(T)$ (Fig. 5). At low applied fields, $H<0.3$ T, the minimum in $M(T)$ takes place at nearly field-independent temperature $T_{\min}=32-35$ K. At $H>0.3$ T, $T_{\min}(H)$ is a non-monotonous function of the field. For fields $H>3$ T, $|M(T)|$ monotonously increases with temperature decreasing.

Figure 7 presents magnetization $M(H)$ and susceptibility $\chi=dM/dH$ vs H at $T=2$ K. As seen in Fig. 7, $\chi(H)$ exhibits pronounced oscillatory behavior in the field interval $1<H<3.5$ T due to de Haas–van Alphen effect coupled to the Landau level quantization. The reduction of de Haas–van Alphen oscillations at $H>3.5$ T indicates that carries occupy only lowest Landau levels at higher fields.

All the experimental results are summarized in Fig. 8, where points 1 and 2 correspond to $H(T_{\max})$ and $H(T_{\min})$, respectively. The inset in Fig. 8 depicts a high-field portion of the $H(T_{\max})$, plotted in a linear scale.

The resistivity drop below $T_{\max}(H)$ can be understood assuming the occurrence of Fermi surface instabilities at $T_{\max}(H)$ with respect to the Cooper pairs formation.

Actually, the rapid increase of $T_{\max}$ with field increasing ($H>3.9$ T, see the inset in Fig. 8) resembles very much that of the superconducting transition temperature $T_c(H)$ in the quantum limit ($H>H_{QL}$), where carriers are in the lowest Landau level.[3] The $T_c(H)$ given by[3]

$$T_c(H>H_{QL})=1.14\Omega\exp[-2\pi l^2/N_1(0)V], \qquad (1)$$

results from the increase in a $1D$ density of states $N_1(0)$ at the Fermi level, where $2\pi l^2/N_1(0)\sim 1/H^2$, $l=(\hbar c/eH)^{1/2}$, V is the BCS attractive interaction, and Ω is the energy cut-off on V. With a further increase in field, a saturation in $T_c(H)$ followed by a reduction of $T_c(H)$, is expected.[3] Thus, the saturation in $T_{\max}(H)$ occurring for $H>6$ T, see Fig. 8, is consistent with the predicted $T_c(H)$ behavior. One of the reasons for the suppression of $T_c(H)$ is the Zeeman splitting, leading to a destruction of the spin-singlet superconductivity above a spin-depopulation field $H_d>H_{QL}$. It is important to

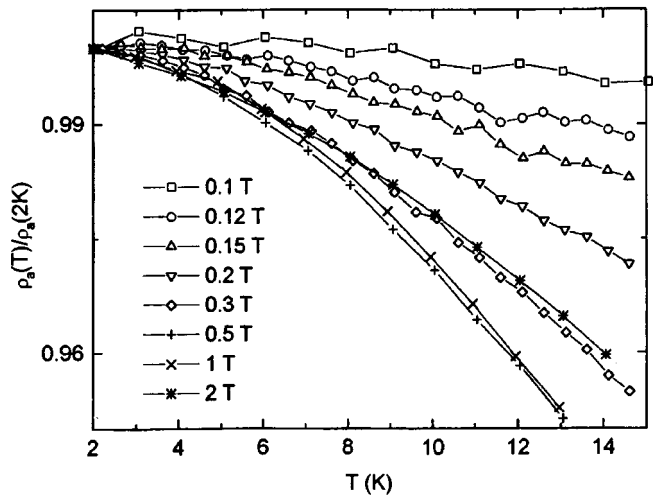

FIG. 2. Normalized resistivity $\rho_a(T)/\rho_a(2\mathrm{K})$ in the field interval where $T_{\max}(H)$ does not occur.

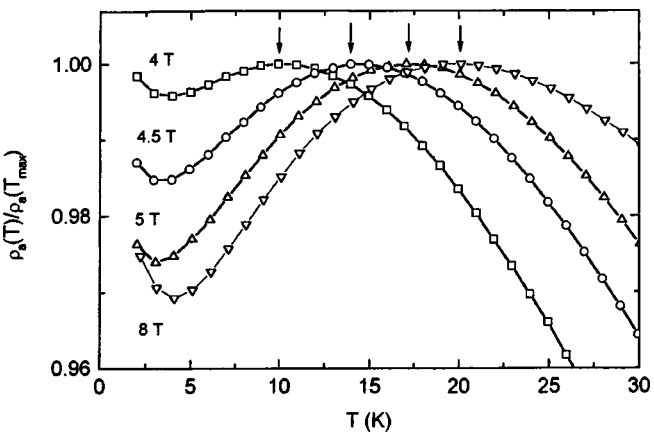

FIG. 4. Normalized resistivity $\rho_a(T)/\rho_a(T_{\max})$ in the quantum limit for several fields. Arrows indicate $T_{\max}(H)$.

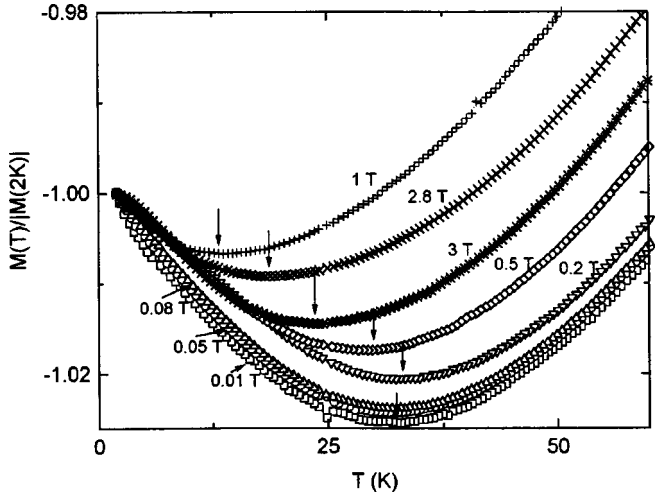

FIG. 5. Normalized magnetization $M(T)/|M(2\mathrm{K})|$ for various fields. Arrows indicate $T_{\min}(H)$.

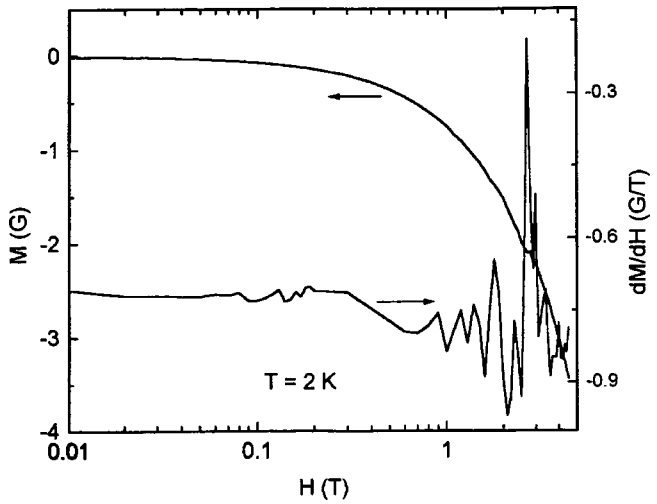

FIG. 7. Magnetization M and susceptibility $\chi = dM/dH$ vs H at $T = 2$ K. Susceptibility oscillations are due to de Haas–van Alphen effect.

note that a relatively small effective g-factor of graphite, $g^* = (m^*/m_0)g \sim 0.1$, ensures a substantial field interval above H_{QL} where both spin-up and spin-down states should be occupied[3] (here $m_e^*/m_0 = 0.058(9)$, $m_h^*/m_0 = 0.04$ are effective masses of the majority electrons and majority holes, divided by free-electron mass,[5,6] and $g \approx 2$[7]). For $H < H_{QL}$, the theory predicts an oscillatory behavior of $T_c(H)$,[3,8–10] which is also in excellent agreement with the non-monotonous $T_{\max}$ vs H behavior, found in the regime of pronounced Landau level oscillations (Figs. 3 and 8).

On the other hand, as emphasized in Ref. 3, the high-field superconductor can be a non-superconducting material in the classical low-field-limit. Assuming, however, that superconducting instabilities are responsible for the resistance drop at $T < T_{\max}(H)$ for all studied fields, one tends to verify the relation[3]

$$H_{QL} \sim (E_F/T_{c0})^2 H_{c2}(0). \tag{2}$$

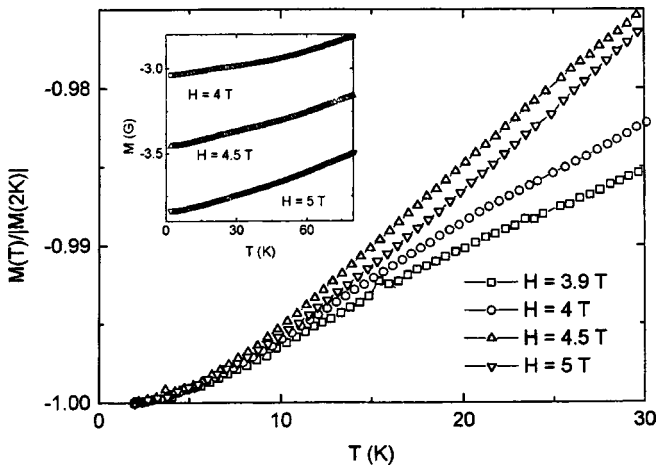

FIG. 6. Normalized magnetization $M(T)/|M(2\mathrm{K})|$ in the quantum limit for several fields. Inset exemplifies temperature dependences of magnetization at $H = 4$, 4.5 and 5 T.

Interestingly, the behavior $H(T_{\max}) \sim (T_{\max}(0) - T)^{0.5}$ (dotted line in Fig. 8) perfectly agrees with the upper critical field behavior of granular superconductors near T_c[11,12]

$$H_{c2}(T) \sim (T_{c0} - T)^{\alpha}, \tag{3}$$

where $\alpha = 0.5$ is the characteristic exponent of inhomogeneous systems of nearly isolated superconducting grains, and T_{c0} is the zero-field superconducting transition temperature. Taking the Fermi energy $E_F = 0.024$ eV,[5] and considering $T_{c0} \sim 50$ K and $H_{c2}(0) \sim 0.1$ T, one calculates using Eq. (2) that $H_{QL} \approx 2.3$ T. This value is close to the experimental value $H = 3.9$ T above which $T_{\max}$ monotonously increases with H. Supporting the occurrence of superconducting instabilities in the low-field-limit, the resistivity below ~ 50 K exhibits a strong field dependence (see Fig. 1), consistent with the field-induced suppression of superconducting correlations.

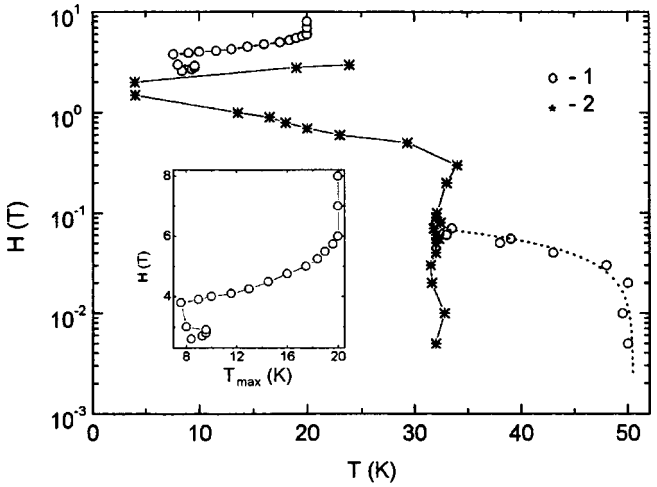

FIG. 8. Magnetic field-temperature diagram constructed from $\rho_a(T,H)$ and $M(T,H)$ data. *1* — $H(T_{\max})$ obtained from $\rho_a(T,H)$, *2* — $H(T_{\min})$ obtained from $M(T,H)$. The dotted line is the fit to the upper critical field boundary (see text) $H_{c2}(T) = A(1 - T/T_{c0})^{0.5}$ with the fitting parameters $A = 0.115$ T and $T_{c0} = 50.5$ K. Inset presents a linear plot of H vs $T_{\max}$, measured at high fields.

In the magnetization measurements, the lack of evidence for the Meissner effect should be noted, first of all. The absence of the Meissner effect at high fields is in agreement with the theory of superconductivity in the quantum limit.[3,10] On the other hand, at low fields Meissner effect can be not seen due to the small size of superconducting regions (grains). The Meissner effect can also be masked by the proximity of $T_{max}(H)$ to $T_{min}(H)$, below which $|M(T)|$ decreases. We stress that the non-monotonous behavior of T_{min} vs H (Figs. 5 and 8) excludes a trivial origin of the magnetic anomaly, such as arising, e.g., from paramagnetic impurities. In search for an explanation of the minimum in $M(T)$, one should take into account that all contributions to the temperature-dependent magnetization of graphite come from carrier states situated in a vicinity of the Fermi level.[5] At the same time, Fig. 8 demonstrates that at small fields $H(T_{max})$ line terminates exactly at the $H(T_{min})$ boundary, and that $T_{min}(H)$ rapidly increases with field above ~ 2 T, where $T_{max}(H)$ reappears. Based on these observations, it is tempting to conclude that Fermi surface instabilities, competing with superconducting instabilities, are responsible for the magnetic anomaly. These can be either CDW or SDW, both enhanced at high fields due to increase in $N_{1n}(0)$, the $1D$ density of states for the n-th Landau level,[3] which explains the $T_{min}(H)$ increase for $H>2$ T. One may further speculate that CDW or SDW states overcome the superconducting correlations at $H>0.08$ T, while superconducting correlations are stronger in the quantum limit ($H \geqslant 3.9$ T). The tendency to saturation in $\rho_a(T)$ at $T<T_{max}(H)$, in low fields (Fig. 1), as well as the ''reentrant'' ($d\rho_a/dT<0$) behavior observed for high fields (Figs. 3 and 4) are also consistent with the competition between superconductivity and CDW or SDW. At the same time, such resistance behavior is characteristic of inhomogeneous (granular) superconductors (see, e.g., Refs. 12–16). Here, a further both experimental and theoretical work is needed.

Finally, we want to comment on the semiconducting-like high-temperature behavior of $\rho_a(T)$. The HOPG is a polycrystalline layered material with a random orientation of crystallites within the layers. Thus, one may assume that the $\rho_a(T)$ is governed by the inter-crystallite boundaries. However, our zero-field value of $\rho_a(300\,\mathrm{K}) \approx 45\,\mu\Omega\cdot$cm nearly coincides with the single-crystal resistivity value.[17] Therefore, we conclude that the inter-crystallite boundary effect is negligible. On the other hand, the $\rho_a(T)$ may originate from a reduced overlap of π orbitals, leading to a reduced carrier mobility, and the dominant effect of carrier density (which decreases with temperature decreasing) on $\rho_a(T)$. Note also, that the decrease in the π-electron overlap would imply an increase in the density of states, responsible for the occurrence of superconducting correlations at high temperatures in our HOPG.

In conclusion, we demonstrated the experimental evidence for the magnetic-field-induced superconducting instabilities due to Landau level quantization and the occurrence of zero-field superconducting correlations at $T_{c0} \approx 50$ K in the highly oriented pyrographite.

This work was partially supported by FAPESP proc. N 95/4721-4, proc. N 98/14726-1, proc. N 99/00779-9, CNPq proc. N 300862/85-7, proc. N 301216/93-2, and CAPES proc. N DS-44/97-0.

[1] A. A. Abrikosov, Sov. Phys. JETP **5**, 1174 (1957).
[2] L. P. Gor'kov, Sov. Phys. JETP **9**, 1364 (1959).
[3] M. Rasolt and Z. Tešanovic, Rev. Mod. Phys. **64**, 709 (1992), and references therein.
[4] J. Heremans, C. H. Olk, and D. T. Morelli, Phys. Rev. B **49**, 122 (1994).
[5] M. P. Sharma, L. G. Johnson, and J. W. McClure, Phys. Rev. B **9**, 2467 (1974).
[6] N. B. Brandt, A. S. Kotosonov, S. V. Kuvshinnikov, and M. V. Semenov, Sov. Phys. JETP **52**, 476 (1980).
[7] G. Wagoner, Phys. Rev. **118**, 647 (1960).
[8] A. H. MacDonald, H. Akera, and M. R. Norman, Phys. Rev. B **45**, 147 (1992).
[9] M. R. Norman, H. Akera, and A. H. MacDonald, Physica C **196**, 43 (1992).
[10] H. Akera, A. H. MacDonald, and M. R. Norman, Physica C **184**, 337 (1993).
[11] G. Deutscher, O. Entin-Wohlman, and Y. Shapira, Phys. Rev. B **22**, 4264 (1980).
[12] B. I. Belevtsev, Sov. Phys. Usp. **33**, 36 (1990).
[13] R. Laibowitz, A. Broers, D. Stround, and B. R. Patton, AIP Conf. Proc. N 58, edited by H. C. Wolfe (AIP, New York, 1980), p. 278.
[14] H. M. Jaeger, D. B. Haviland, A. M. Goldman, and B. G. Orr, Phys. Rev. B **34**, 4920 (1986).
[15] A. Gerber, T. Grenet, M. Cyrot, and J. Beille, Phys. Rev. Lett. **65**, 3201 (1990).
[16] N. V. Zaitseva, Y. Kopelevich, I. I. Kochina, V. V. Lemanov, and P. P. Syrnikov, Sov. Phys. Solid State **33**, 323 (1991).
[17] M. S. Dresselhaus and G. Dresselhaus, Adv. Phys. **30**, 139 (1981), and references therein.

SEMICONDUCTORS. DIELECTRICS

Dislocation spectroscopy of crystals

S. Z. Shmurak

Institute of Solid State Physics, Russian Academy of Sciences, 142432 Chernogolovka, Moscow District, Russia

(Submitted March 5, 1999; resubmitted April 21, 1999)
Fiz. Tverd. Tela (St. Petersburg) **41**, 2139–2146 (December 1999)

A new method of studying the energy characteristics of dislocations is proposed, which is based on the investigation of the interaction of moving dislocations with purposefully introduced electronic and hole centers. A study has been made of KCl, NaCl, KBr, LiF, and KI alkali halide crystals containing electronic F and hole V_K and Me^{++} (Cu^{++}, Ag^{++}, Tl^{++}, In^{++}) centers. Investigation of the temperature dependence of the dislocation interaction with the F centers permitted determination of the position of the dislocation-induced electronic band (DEB) in the band diagram of the crystal. In KCl, the DEB is separated by ≈ 2.2 eV from the conduction-band minimum. It is shown that dislocations transport holes from the centers lying below the dislocation-induced hole band (DHB) (X^+, In^{++}, Tl^{++}, V_K) to those above the DHB (the Cu^+ and Ag^+ centers). Such a process is temperature independent. The DHB position in the crystal band diagram has been determined; in KCl it is separated by ≈ 1.6 eV from the valence-band top. The effective radii of the dislocation interaction with the electronic F and hole X^+, V_K, and Tl^{++} centers have been found. © *1999 American Institute of Physics.* [S1063-7834(99)00812-6]

Dislocations are known to affect considerably the electronic spectrum of a crystal, thus inducing a change of many physical properties (electrical, optical, and magnetic) of the latter.

A number of processes are stimulated by moving dislocations. When dislocations move in colored alkali halide (AH) crystals, one observes emission of photons and electrons accompanied by annihilation of some centers, e.g. of F and V_K, and creation of others (Cu^{++}, Ag^{++}).[1–4] In ZnS crystals, moving dislocations give rise to the onset of transient and steady-state dislocation-induced luminescence, electron emission, electroplastic effect odd in the field, and structural rearrangements in the crystal.[5–7]

In order to identify the mechanisms responsible for the effect of dislocations on the physical properties of crystals, one has first of all to understand the way in which the dislocations change the energy spectrum of a crystal. Unfortunately, despite a wealth of publications dealing with the influence of dislocations on the physical properties of crystals, the information on the energy characteristics of dislocations is extremely scant.

The present work proposes a new method for determining the energy characteristics of dislocations, which is based on studying dislocation interaction with centers introduced purposefully into AH crystals. In this way electronic and hole centers with known energy characteristics are created in a crystal. Next one investigates the variation with temperature of the concentration of these centers after the moving dislocations have interacted with them. The electronic and hole centers act in this process as energy ''tags.'' This technique permits one to obtain information on the energy parameters of the electronic and dislocation-induced hole bands in the band diagram of the crystal. Another merit of this method is that in this way one can determine the energy characteristics of moving dislocations, which are free of the impurities decorating them when they are immobile.

1. DISLOCATION INTERACTION WITH THE ELECTRONIC AND HOLE CENTERS IN IONIC CRYSTALS

Theoretical treatment of the effect of such a complex system as the dislocation on the spectrum of electronic states is a very serious problem even in the case of alkali halide crystals, whose band diagram is studied in considerable detail and the dislocation structures are known.

Quantum mechanical calculations show the existence on dislocations of bound states of both electrons and holes.[8,9] However the binding energies determined in these studies should be considered only as order-of-magnitude estimates, because they make use of the short-range (deformation) potential approximation. At the same time an analysis shows the radius of the carrier bound state to be of the order of the lattice constant, which renders the starting approximation invalid. Therefore experimental investigation of the dislocation energy characteristics obtained by studying the interaction of moving dislocations with the electronic and hole centers is of considerable interest for physics of the solid state.

A moving dislocation always interacts with electronic and hole centers. Obviously enough, if the energy level of an electronic center (EC) lies above the dislocation-induced electronic band (D_e), the dislocation will capture an electron

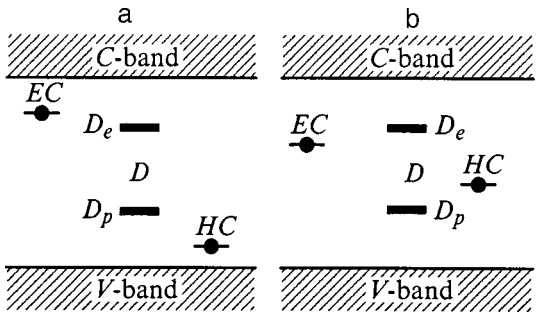

FIG. 1. Schematic energy diagram of the electronic (EC) and hole (HC) centers relative to the dislocation-induced bands. a—Electron and hole capture by a dislocation does not require activation; b—capture of electrons and holes by a dislocation is a thermally activated process.

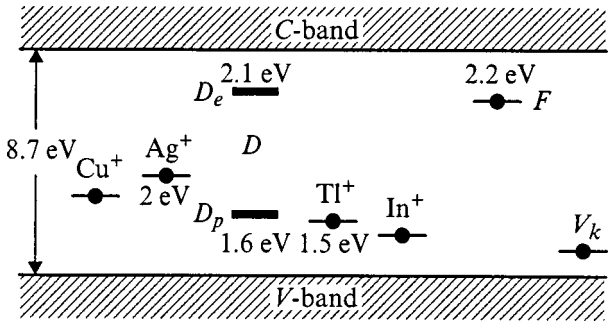

FIG. 2. Energy positions of some centers in the band diagram of the KCl crystal.

from the EC. This process does not require any activation energy, because dropping to a lower lying state is energetically favorable for an electron. Conversely, it is as favorable for a hole to rise up in the crystal band diagram. Therefore if the dislocation-induced hole band (D_F) is located energywise higher than the hole center (HC), the capture of a hole by a dislocation can likewise occur without any activation energy. The above no-activation processes are depicted in Fig. 1(a). These processes will be seen experimentally as a temperature-independent decrease of the concentration of the electronic and hole centers following a plastic deformation of a sample.

Figure 1b shows the energy positions of the hole and electronic centers for the case where the capture by dislocations of electrons and holes in interaction with these centers requires an activation energy. In these conditions, the number of the centers destroyed by dislocations will depend on the temperature at which the crystal is strained.

Thus electronic and hole centers act as specific energy tags, so that by studying their interaction with dislocations one can determine the energy characteristics of the latter in AH crystals.

About 30 types of various centers are presently known to exist in AH crystals, and their energy characteristics were determined. The studies of dislocation interaction with the electronic and hole centers were performed on centers of the simplest type, which do not interfere with the motion of dislocations. By varying properly the temperature at which the centers were introduced, the concentration of the impurities (Cu, Tl, Ag, In), as well as the irradiation dose, we were able to introduce in a controlled manner the electronic F centers and the V_K, Cu^{++}, Tl^{++}, Ag^{++}, and In^{++} hole centers.[1] The electronic and hole centers were created by irradiating a crystal with Co^{60} gamma-rays.

Irradiation at 300 K produces electronic F centers. The holes (p) in crystals doped with one impurity (Me^+) become distributed among the Me^+ activator centers and the shallow, optically inactive X centers. The number of the X^+ (Xp) and Me^{++} (Me^+p) centers can be easily found by solving the rate equations describing this process.

For $n_p \ll n_a^0$, $n_p \ll n_X^0$ we have

$$n_a = \frac{W_a n_a^0 n_p}{W_a n_a^0 + W_X n_X^0}, \quad n_X = \frac{W_X n_X^0 n_p}{W_a n_a^0 + W_X n_X^0},$$

where n_a^0 and n_X^0 are the numbers of the Me^+ and X centers, W_a and W_X are the hole capture probabilities by the Me^+ and X centers, n_p is the number of holes, and n_a and n_X are the numbers of the Me^+ and X^+ centers, respectively.

If $W_a n_a^0 \gg W_X n_X^0$, then $n_a \approx n_p$, i.e. practically all holes are captured by the Me^+ centers. For $n_p > n_a^0 + n_X^0$ all the X and Me^+ centers are filled.

If $n_p > n_a^0$, $n_p - n_a^0 < n_X^0$, but $(n_p - n_a^0) W_a / W_X > n_X^0$, then the holes are first captured by the Me^+ centers, to become later distributed among the X and Me^+ centers. Their final concentrations are $n_X \approx n_p - n_a^0$; $n_a \approx n_a^0$.

Thus by varying properly the irradiation dose (n_p) and the activator concentration n_a, one can change the number of the Me^+ and X^+ centers within a broad range.

The interaction of dislocations with the electronic centers was studied, as a rule, in the conditions where $W_a n_a^0 \gg W_X n_X^0$, and with the hole centers, for $W_a n_a^0 < W_X n_X^0$.

If a sample was codoped with two impurities (Me_1^+ and Me_2^+), their concentrations n_{a1}^0 and n_{a2}^0 were chosen so as to meet the condition $W_{ai} n_{ai}^0 \gg W_X n_X^0$ ($i = 1,2$). In this case the holes will be distributed among the Me_1^+ and Me_2^+ activator centers. The positions of some centers in the band diagram of the crystal are shown schematically in Fig. 2.

In this work, the energy characteristics of dislocations will be determined from our experimental data.[1,2,4,5,10,11]

2. INTERACTION OF DISLOCATIONS WITH ELECTRONIC CENTERS

Investigation of the F absorption band profile before and after a deformation showed plastic strain to result in a decrease of the number of the F centers, i.e., in an increase of the crystal transmission.[2,3] The variation of the number of the F centers with strain is shown graphically in Fig. 3. One readily sees that the crystals studied by us exhibit a linear relation between the number of destroyed F centers and the strain, at least up to $\varepsilon \approx 8\%$. Because plastic deformation is intimately connected with the motion of dislocations, the destruction of the F centers is a result of their interaction with dislocations (D). This process can be described schematically as $D + F \rightarrow e_d$, where e_d is the dislocation-captured electron.

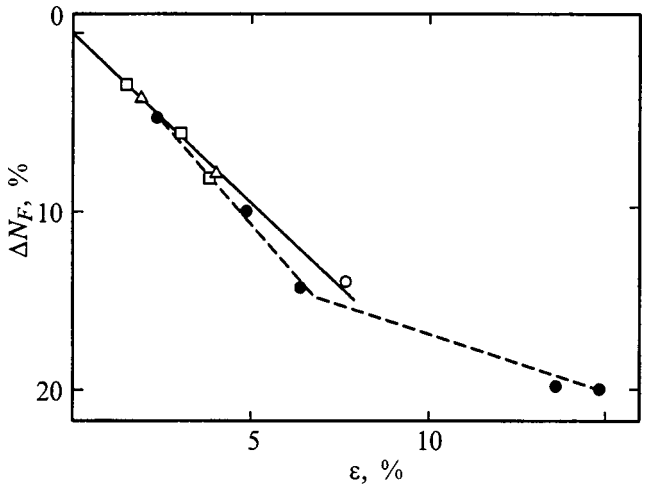

FIG. 3. Variation of the number of F centers with strain for the KCl crystals irradiated by Co^{60} gamma rays (to a dose of 2×10^5 rad) at 300 K. Open symbols—data obtained in Refs. 1, 2, filled symbols—data of Ref. 3.

In accordance with the above concepts, in order to determine the position of the dislocation-induced electronic band in the band diagram of a crystal one has to study the temperature dependence of the number of the F centers destroyed by dislocations, $\Delta N_F=\Delta N(T)$.

However ΔN_F decreases rapidly with decreasing T, and because it is small already at $T=300$ K, the temperature dependence of ΔN_F can be measured only with a large error. The pattern of the $\Delta N_F=\Delta N(T)$ variation can be found more accurately by measuring the temperature dependence of the luminescence generated in deformation of colored AH crystals doped with Me^+ ions. The strain-induced luminescence (SIL) occurs in two stages

$$(1)\quad D+F\rightarrow e_d,$$

$$(2)\quad e_d+Me^{++}\rightarrow(Me^+)^*\rightarrow Me^+ + h\nu_{Me^+}. \qquad (1)$$

In the first stage, which has just been discussed, dislocations capture electrons, which later recombine with holes localized at the Me^+ centers to generate the intracenter luminescence of the activator ($h\nu_{Me^+}$).

In all the crystals studied, the SIL intensity (J) decreases exponentially with decreasing temperature (see Table I)

$$J=J_0\exp(-\Delta U/kT).$$

As follows from Table I, the activation energy ΔU for the given type of the crystal does not change when the activator is replaced, although the positions of the Ag, Cu, and Tl activator energy levels are different. This permits a conclusion that only the first SIL stage, the interaction of dislocations with the F centers, is thermally activated and governs the temperature dependence of the SIL. Therefore the experimentally determined activation energy ΔU is actually the energy difference between the states of the electron at the F center (U_F) and at the dislocation (U_E), $\Delta U=U_F-U_E$. This means that the dislocation-induced electronic band lies above the F center level by ΔU (Table I).

TABLE I. SIL activation energy (ΔU) and the binding energy of a dislocation-bound electron (U_e). The accuracy of ΔU determination 0.01 eV.

Crystal	Activator	ΔU, eV	U_e, eV
KCl	Cu	0.08	
	Ag	0.09	
	Tl	0.78	2.1
	Undoped intentionally	0.06–0.1*	
KBr	Cu	0.13	1.85
NaCl	Cu	0.11	2.55
KI	Tl	0.05	1.73
LiF	Undoped intentionally	0.1	4.83

Note: *Data taken from Ref. 3, the others—from Ref. 10.

3. EFFECTIVE RANGE OF THE DISLOCATION INTERACTION WITH THE *F* CENTERS

The number of the F centers destroyed by moving dislocations (ΔN_F) can be written

$$\Delta N_F=Sr_FN_F, \qquad (2)$$

where S is the area swept by the moving dislocations, r_F is the effective dislocation interaction range with the F centers, and N_F is the F-center concentration. Because the plastic strain

$$\varepsilon=Sb/2\Omega, \qquad (3)$$

where b is the dislocation Burgers vector, and Ω is the crystal volume, we find from Eqs. (2) and (3)

$$r_F=b\Delta N_F/2\varepsilon N_F\Omega. \qquad (4)$$

The values of r_F for various ε are listed in Table II.[10]

As seen from Table II, within experimental accuracy r_F does not depend on ε and is approximately equal to the lattice constant at 300 K. Thus at room temperature dislocations capture electrons from F centers into the dislocation-induced electronic band from a region with a cross section equal approximately to one lattice constant.

4. INTERACTION OF DISLOCATIONS WITH HOLE CENTERS

The holes created in an AH crystal by an ionizing radiation (at 300 K) are captured, as already mentioned, into shallow, optically inactive traps, namely, the X centers[1] and the activator Me^+ centers. By properly varying the activator concentration and the irradiation dose, one can control in a purposeful manner the concentration of the X^+ and Me^+ centers. When a colored crystal is illuminated with F light, the F electrons recombine with the holes bound to optically active Me^+ centers to generate the activator luminescence

TABLE II. Effective range of F center destruction by dislocations vs strain obtained for a KCl crystal at 300 K.

ε, %	0.3	0.4	0.6	0.8	0.9	1.5	2.1	3	3.8	4.1	7.8	15
r_F/b	0.9	0.8	1.0	1.1	0.8	0.9	0.8	1	1.0	0.9	0.9	0.7

Note: For $r_F/b=20\%$, $N_F=3\times10^{16}$ cm^{-3}.

TABLE III. Temperature dependence of the relative number of the Me^{++} centers (N_a) created in KCl–Ag and KCl–Cu crystals.

T, K	300	250	200	180	150	110
N_{Ag}, rel. units.	1	0.9	1.1	1.05	1	0.95
N_{Cu}, rel. units.	1	1.2	1.07	1.2	1	1

Note: The accuracy of N_a determination is 20%.

$$Me^{++}+e\rightarrow(Me^{+})^{*}\rightarrow Me+h\nu_{Me^{+}}. \quad (5)$$

Application of a strain to KCl, KBr, NaCl, and KI crystals doped by Me^{+} ions ($Ag^{+}, Cu^{+}, Tl^{+}, In^{+}$) at 300 K brings about an increase in the intensity of the activator luminescence (J_a) stimulated by the F light. In the beginning, J_a grows rapidly with strain, to reach subsequently saturation at $\varepsilon\approx 2.5\%$. This process, which was called by us strain-induced sensitization (SIS) has a dislocation nature and occurs in two stages.[11] In the first stage, dislocations capture holes (p) from the optically inactive, shallow hole traps, the X^{+} centers (denote them by P^{+}), and transfer them subsequently to the Me^{+} centers (the second SIS stage):

$$(1)\ D+P^{+}\rightarrow P+Dp,$$

$$(2)\ Dp+Me^{+}\rightarrow Me^{++}+D. \quad (6)$$

The number of the strain-created Me^{+} centers was determined by the technique described in Ref. 11. One measured the number of photons (N_ν) emitted in the activator luminescence band in a strained sample illuminated until the intensity of the activator luminescence stimulated by the F light reached the pre-strain level. Obviously enough, the number of the strain-created Me^{++} centers measured by the above technique is $N_a=N_\nu\eta^{-1}$, where η is the quantum yield of the intracenter luminescence.

A study of the temperature dependence of SIS, i.e. of the number of the strain-generated Me^{++} centers, showed that for the KBr–Cu, KI–Tl, as well as the KCl–Cu, KCl–Ag crystals the SIS process is temperature independent within the temperature range of 77–300 K (Table III).

At the same time the number of the strain-generated Me^{++} centers in the Tl- and In-doped KCl crystals falls off exponentially with decreasing T (Fig. 4). The SIS activation energy for the KCl–Tl and KCl–In crystals is 0.06 and 0.045 ± 0.020 eV, respectively.

Based on the above considerations, the SIS temperature dependences permit one to determine the position of the dislocation-induced hole band (DHB) in the band diagram of the crystal. It was found that the DHB lies below the levels of the Cu^{+} and Ag^{+} centers but above those of the Tl^{+} and In^{+} centers by 0.06 and 0.045 eV, respectively.

The available experimental data[12,13] permit a conclusion that the Ag^{+} and Cu^{+} levels in KCl crystals are ≈ 2 and ≈ 1.7 eV away from the valence-band maximum, respectively. Although the exact position of the thallium level in the band diagram of the crystal is unknown, an analysis of the data presented in Ref. 14 suggests that it lies $\approx 1.5-1.7$ eV away from the top of the valence band. This means that the DHB is located ≈ 1.6 eV above the valence-band top in the KCl crystal.

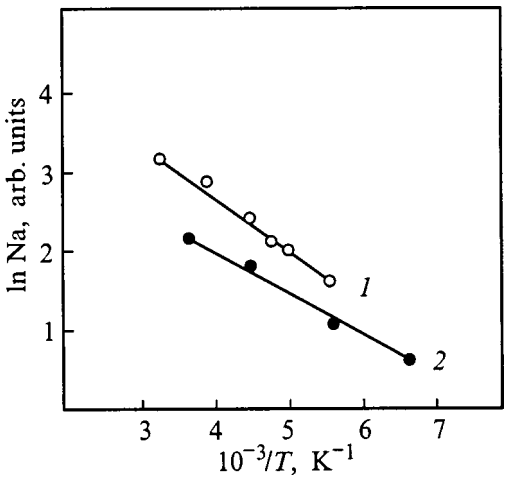

FIG. 4. Temperature dependences of the number of the strain-created Me^{++} centers in doped KCl crystals irradiated by gamma rays (to a dose of 2×10^5 rad). (*1*) KCl–In, (*2*) KCl–Tl.

If these deductions are correct, then, if two activators (a_1 and a_2) with the levels above and below the DHB, accordingly, are introduced into a crystal one may expect plastic deformation to transfer holes from the lower (a_1) to the upper (a_2) level. This process should become manifest in a decrease of the a_1 band in intensity and an increase of the a_2 band intensity in the luminescence spectrum stimulated by the F light (FL).

For such an experiment to be successful, the FL bands of the a_1 and a_2 activators should not overlap. The Tl^{+} and Cu^{+} activators in KCl crystals meet this condition.[15] An investigation of these samples supported the above assumptions. One observed a decrease in the number of Tl^{++} centers and an increase in the Cu^{+} concentration in strained KCl–Cu–Tl crystals.

The FL spectrum of the original sample (Fig. 5) exhibits two bands peaking at 300 and 400 nm. They coincide with the spectra of intracenter luminescence of the Tl^{+} and Cu^{+} centers, respectively. This means that the observed luminescence is generated in accordance with the scheme (5).

Plastic strain results in a considerable change of the spectral pattern, namely, the intensity of the $\lambda_{max}=300$ nm and corresponding to the intracenter luminescence of the Tl^{+} centers decreases, and the band at $\lambda_{max}=400$ nm, for which the Cu^{+} centers are responsible, increases in intensity. The evolution of the spectrum is monotonic and comes to an end at a strain $\varepsilon\approx 10\%$. This process of intensity redistribution between the FL bands in the KCl–Cu–Tl crystals is observed to occur within the temperature range from 100 to 300 K studied by us.

For certain relations between the concentrations of the Tl^{+} and Cu^{+} activator centers the number of the Tl^{++} centers destroyed in the course of deformation (Δn_{Tl}) is equal, within the $\sim 10\%$ error range, to the number of the created Cu^{++} centers (Δn_{Cu}). This implies that hole transport by dislocations takes place from the Tl^{++} to Cu^{+} centers. The equality ($\Delta n_{Cu}=\Delta n_{Tl}$) persists within the 100–300-K range studied.

The temperature independence of the SIS process in KCl–Cu–Tl crystals indicates that both the first and the sec-

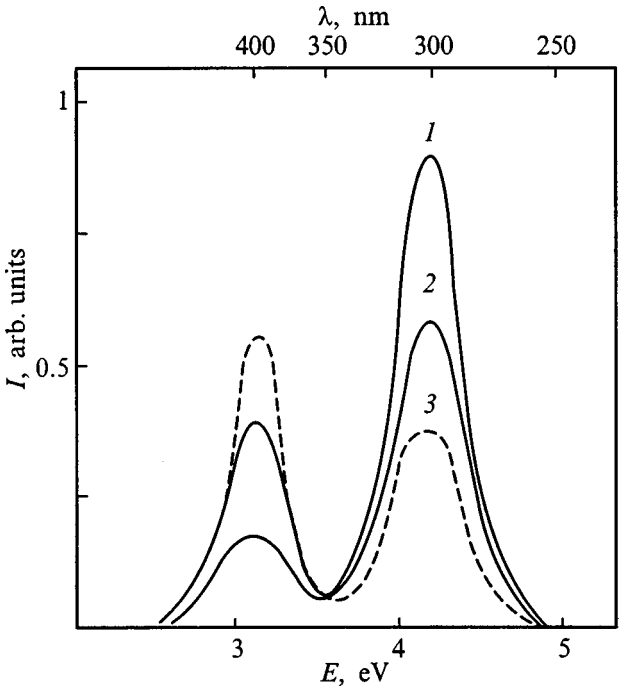

FIG. 5. Variation of the spectrum of F-stimulated luminescence of KCl–Cu–Tl crystals under plastic deformation. The crystals were irradiated by Co^{60} gamma rays (to a dose of 2×10^5 rad), $T=300$ K. (*1*) unstrained crystal, (*2*,*3*) following deformation of up to 3 and 8% strain, respectively.

ond stage of SIS (6) do not involve thermal activation. In other words, in each stage holes are raised in the gap, both when they transfer from the Tl^{++} centers to the dislocation-induced hole band and when they are promoted from the DHB to the Cu^{+} centers.

Thus the experiments carried out on KCl–Cu–Tl crystals confirm the above conclusions of the position of the dislocation-induced hole band in the band diagram of the crystal (Fig. 2).

5. EFFECTIVE RANGE OF DISLOCATION INTERACTION WITH HOLE CENTERS

Assuming the dislocations to be distributed uniformly throughout the crystal, the volume from which the dislocations can capture holes is $\Omega_p=Sr_p$ (where r_p is the effective range of dislocation interaction with hole centers). Recalling Eq. (3) we obtain

$$r_p=\Omega_p b/2\Omega\varepsilon. \tag{7}$$

5.1. Interaction of dislocations with the X^+, Tl^{++}, and Cu^{++} centers

As already mentioned, in AH crystals doped with one activator (Cu, Ag, Tl, or In) one observes an increase in the number of the Me^{++} centers through transfer of holes by dislocations from the shallow X^+ to the Me^+ centers. The SIS process is completed in the crystals studied by the time when $\varepsilon=\varepsilon_0\approx2.5-3.0\%$. Further increase of the strain does not increase the Me^{++} concentration. This implies that at ε_0 the dislocations capture the holes bound to the X^+ centers present throughout the crystal volume, so that $\Omega_p=\Omega$.

TABLE IV. The temperature at which the V_K centers become mobile (T_V), and the activation energy of the hopping diffusion of V_K centers (E_V).

Crystal	KCl	KBr	KI	NaCl
T_V, K	170	140	90	130
E_V, eV	0.53	-	0.28	-

Equation (7) permits one to determine the effective dislocation interaction range with the X^+ centers as $r_X\approx(20-16)\,b$.

The constancy of ε_0 (within the experimental accuracy) for crystals containing activators whose levels lie both above (Cu, Ag) and below (Tl or In) the dislocation-induced hole band implies that only the interaction of dislocations with the X^+ centers determines the kinetics of the dislocation-induced sensitization in crystals doped by one of the above-mentioned activators. This point is an additional argument for the validity of the method used to determine the effective range of dislocation interaction with the X^+ centers.

It should be noted that the strain ε_0 at which the F-stimulated activator luminescence reaches saturation in the crystals with one activating dopant studied by us does not depend on temperature within the T interval of 77 to 300 K covered in this investigation. Hence r_X is likewise temperature independent.

Equation (7) permits one also to determine the effective range of dislocation interaction with the Tl^{++} centers (r_{Tl}). The hole transport by dislocations from the Tl^{++} to Cu^{+} centers is complete by $\varepsilon_0\approx8\%$, and therefore $r_{Tl}\approx6\,b$. Because the value of ε_0 for the process under discussion does not depend on T, r_{Tl}, as r_X, should be constant within the 77–300 K range.

The effective dislocation interaction range with the X^+ and Tl^{++} centers determined in the above manner is a lower estimate of the true values of r_X and r_{Tl}, because both r_X and r_{Tl} were obtained, as already mentioned, under the assumption of dislocations being distributed uniformly throughout the crystal. Generally speaking, this assumption does not adequately describe the situation realizing in a strained crystal.

Note that the effective dislocation interaction range with the hole X^+ and Tl^{++} centers is larger by 16 and 6 times, respectively, than that with the electronic F centers ($r_F\approx b$). This appears only natural, because the capture of electrons by dislocations from the F centers is a thermally activated process, whereas the hole capture from the X^+ and Tl^{++} centers does not require activation.

5.2. Interaction of dislocations with the V_K centers

At temperatures below the ones specified in Table IV holes become self-trapped in the regular lattice of AH crystals to form V_K centers.[16]

At 77 K, the V_K centers are immobile. Above T_V, the V_K centers are destroyed, and the holes are captured by other traps (e.g., by the Me^+ centers) or recombine with the electrons localized at electronic traps. Despite the considerable

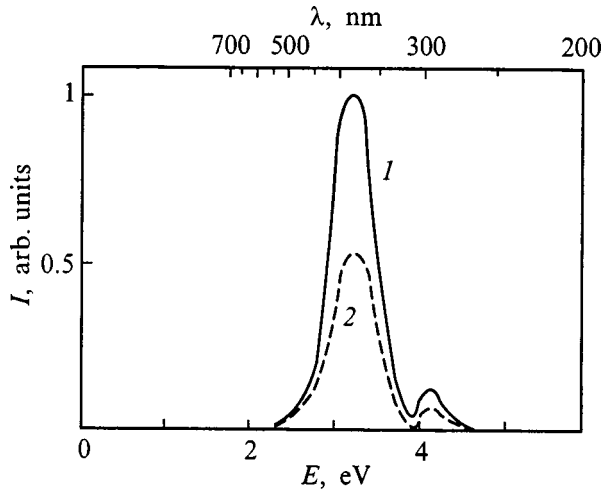

FIG. 6. Effect of plastic strain on the F-stimulated luminescence of self-trapped excitons in KI crystals irradiated by gamma rays at 77 K to a dose of 2×10^5 rad. (*1*) original sample, (*2*) sample strained to 4% at 77 K.

interest in the V_K centers on the side of many researchers, the position of this center in the crystal band diagram is still not known accurately.

The number of V_K centers in a crystal can be judged from the intensity of the F-stimulated band generated by the luminescence of the self-trapped excitons. This process is described by the well-known scheme

$$e+V_K\rightarrow h\nu.$$

Unfortunately, the luminescence of self-trapped excitons in the KCl crystals, which have been studied by us most comprehensively, is observed to occur only for $T<20$ K.[17] We investigated the interaction of dislocations with V_K centers in KBr, KI, and NaCl. The spectrum of the F-stimulated luminescence of self-trapped excitons at 77 K in KI crystals colored at the same temperature contains[18,19] two bands, at $\lambda_1=300$ nm and $\lambda_2=370$ nm (Fig. 6). In KBr, a similar spectrum contains only one band at $\lambda_{max}=281$ nm (Fig. 7).[18] Plastic strain affects considerably the spectral characteristics of the F-stimulated luminescence. In KI crystals one observes a decrease in intensity of both FL bands, which correlates with the increase of the strain (Fig. 6). Doped samples exhibit, besides the decrease of the exciton luminescence, a considerable growth of the activated luminescence, for instance, of that due to Cu ions ($\lambda_{max}=395$ nm) in KBr–Cu (Fig. 7).

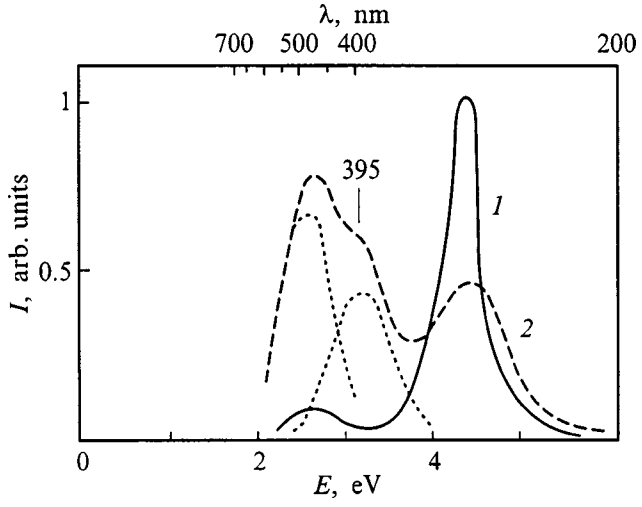

FIG. 7. Same as in Fig. 6, but for the KBr–Cu crystal. Dashed line—decomposition of curve *2* into components.

The enhancement of the activator luminescence implies that plastic deformation at 77 K of crystals colored at the same temperature, both irradiated and strained at 300 K, results in an increase of the Me^{++}-ion concentration. The holes participating in the process of strain-induced sensitization are captured by dislocations from the V_K centers, which is evidenced by the drop in the exciton luminescence intensity when the crystal is being strained. This decrease is not a consequence of a possible change in the quantum yield of the exciton luminescence, because plastic deformation of a control sample performed before the irradiation does not affect the FL intensity.

The V_K centers can be destroyed also by recombination of the electrons released in a strained sample. However an estimate of the number of the V_K centers destroyed in this process, made from an analysis of the intensity of the luminescence observed, is one to two orders of magnitude smaller than the total number of these centers destroyed in the course of the deformation. The strain-induced sensitization processes occur above and below the hole self-trapping temperature (Table IV), and therefore the transport of holes from the V_K to Me^+ centers in the samples both irradiated at 77 K and colored at 300 K is effected by moving dislocations.

Indeed, if the holes became mobile in dislocation interaction with the V_K centers at $T<T_V$, then on moving away from the dislocation they would become self-trapped immediately with the formation of V_K centers. Therefore such a process would not provide the experimentally observed substantial decrease of the V_K concentration. This can only mean that the holes from the V_K centers are captured by moving dislocations.

The effective range of dislocation interaction with the V_K centers (r_V) can be readily determined from (7). As follows from Figs. 6 and 7, at $\varepsilon=4\%$ the volume from which the dislocations capture the holes bound to V_K centers in KI and KBr–Cu crystals is $\Omega_p=0.5\Omega$; substituting this in Eq. (7) yields $r_V=6b$.

Having found the position of the dislocation-induced hole band in the crystal band diagram, one can solve the inverse problem, namely, determine the position of the hole centers in the energy spectrum of the crystal by studying the interaction of dislocations with these centers.

As already mentioned, the number of the In^{++} centers (N_{In}) created in KCl–In crystals decreases exponentially with decreasing T, i.e. the SIS process in these samples is thermally activated, $N_{In}=N_0\exp(-\Delta U_p/kT)$, where N_0 is a constant, and ΔU_p is the activation energy. Because ΔU_p in KCl–In is 0.045 ± 0.02 eV, the In level lies 0.045 eV below the dislocation-induced hole band.

In the KI and KBr–Cu crystals studied by us one observes destruction of the V_K centers as a result of the holes

transferring from the latter into the dislocation-induced hole band. According to the above concepts, this implies that the V_K level is located below the DHB in the band diagram of the crystal. The DHB, in its turn, lies below the Cu^+ level in KBr.

It should be noted that the levels of the Me^+ and Me^{++} centers lie at different energies. The Me^{++} level is most probably located below the Me^+ level in the band diagram. If the position of a level of a center remains unchanged relative to the dislocation-induced hole band (i.e. always above or always below the DHB) while varying as a result of the charge exchange with moving dislocations, then the change in the position of the center induced by the charge exchange should not affect in any way the SIS process. For the Tl, In, Cu, and Ag impurities studied here, charge exchange most probably does not change the position of the levels with respect to the DHB. Indeed, the Tl^{++} and Tl^+, In^{++} and In^+ levels lie below the DHB (the levels of Tl^+ and In^+, as pointed out earlier, by 0.06 and 0.045 eV, respectively). If the Ag^{++} or Cu^{++} levels were below the DHB, then the strain at which the SIS is observed to saturate (ε_0) in the 77–300 K range would depend on T, and the values of ε_0 for crystals doped with Ag or Cu would be different at different T. The independence of ε_0 of temperature and the equal values of ε_0 for the KCl–Cu and KCl–Ag crystals indicate most probably the validity of this conjecture.

Thus an investigation of the interaction of dislocations with purposefully introduced centers has permitted us to determine the position of the dislocation-induced electronic and hole bands in the band diagram of a number of ionic crystals.

Support of the Russian Fund for Fundamental Research (Grant 98-02-16644) and of the Ministry of Science and Technology (''Surface Atomic Structures'' program, Grant 3.10.99) is gratefully acknowledged.

[1] S. Z. Shmurak, Izv. Akad. Nauk SSSR, Ser. Fiz. **40**, 1886 (1976).
[2] F. D. Senchukov and S. Z. Shmurak, Fiz. Tverd. Tela (Leningrad) **12**, 9 (1970) [Sov. Phys. Solid State **12**, 6 (1970)].
[3] C. D. Clark and J. H. Crawford, Adv. Phys. **22**, 117 (1973).
[4] A. V. Poletaev and S. Z. Shmurak, Zh. Éksp. Teor. Fiz. **87**, 657 (1984) [Sov. Phys. JETP **60**, 520 (1984)].
[5] S. I. Bredikhin and S. Z. Shmurak, Zh. Éksp. Teor. Fiz. **76**, 1028 (1979) [Sov. Phys. JETP **49**, 520 (1979)].
[6] M. P. Kulakov and S. Z. Shmurak, Phys. Status Solidi A **59**, 147 (1980).
[7] A. V. Poletaev and S. Z. Shmurak, Pisma Zh. Tekh. Fiz. **7**, 1352 (1981) [Sov. Tech. Phys. Lett. **7**, 577 (1981)].
[8] P. R. Emtage, Phys. Rev. **163**, 865 (1967).
[9] É. A. Kaner and É. P. Fel'dman, Zh. Éksp. Teor. Fiz. **61**, 419 (1971) [Sov. Phys. JETP **34**, 222 (1971)].
[10] M. I. Molotskii and S. Z. Shmurak, Phys. Lett. A **166**, 286 (1992).
[11] F. D. Senchukov and S. Z. Shmurak, Zh. Éksp. Teor. Fiz. **65**, 2356 (1973) [Sov. Phys. JETP **38**, 1177 (1973)].
[12] Ch. B. Lushchik, H. F. Käämbre, Yu. L. Lukanzever, N. E. Lushchik, E. S. Tiisler, and I. V. Jaek, Izv. Akad. Nauk SSSR, Ser. Fiz. **33**, 863 (1969).
[13] Ch. B. Lushchik, H. F. Käämbre, N. E. Lushchik, E. S. Tiisler, and I. V. Jaek, Trudy IFA ÉSSR **35**, 5 (1969).
[14] T. A. Kuketaev, N. E. Lushchik, and Ch. B. Lushchik, Trudy IFA ÉSSR **39**, 123 (1972).
[15] I. A. Markova-Osorgina and S. Z. Shmurak, JETP Lett. **24**, 472 (1976).
[16] M. N. Kabler, *Point Defects in Solids VI* (Plenum Press, New York, 1972).
[17] D. Pooly and W. A. Runciman, J. Phys. C **3**, 1815 (1970).
[18] M. N. Kabler, Phys. Rev. **136**, A1296 (1964).
[19] R. A. Kink and G. G. Liidja, Fiz. Tverd. Tela (Leningrad) **7**, 1641 (1965) [Sov. Phys. Solid State **7**, 1331 (1965)].

Translated by G. Skrebtsov

Negative Poisson coefficient of fractal structures

V. V. Novikov*)

Odessa State Polytechnic University, 270044 Odessa, Ukraine

K. W. Wojciechowski

Institute of Molecular Physics, Polish Academy of Sciences, 60-179 Poznań, Poland

(Submitted in final form April 22, 1999)
Fiz. Tverd. Tela (St. Petersburg) **41**, 2147–2153 (December 1999)

On the basis of a fractal model the macroscopic elastic properties of an inhomogeneous medium with random structure have been determined. It is shown that if the ratio of the bulk moduli of the phases $K_2/K_1 \to 0$, then the percolation threshold p_c the Poisson coefficient is equal to 0.2. A study of the behavior of a two-phase medium with negative Poisson coefficient is carried out. © *1999 American Institute of Physics.* [S1063-7834(99)00912-0]

Typical materials surrounding us have positive Poisson coefficients $\nu > 0$ (Ref. 1). However, in recent years it has been shown that under certain conditions the Poisson coefficient can be less than zero ($\nu < 0$).[2–15]

Such media have still not received adequate theoretical study. In the present paper the Poisson coefficient of an inhomogeneous medium with random structure is investigated on the basis of an iteration method of averages which has proven to be highly effective in the study of conductivity and the dielectric and elastic properties of composites.[16–20]

Studies of the elastic properties of inhomogeneous media with random structure and large differences in the properties of their components have been performed in the majority of cases using numerical methods on percolation lattices.[21–28] In particular, studies have been carried out of transitions of an unconnected set of bonds or sites into a connected set, and *vice versa*.[29–33] It has been established that at the critical point (the percolation threshold) p_c a connected set forms a percolation cluster which is a self-similar set, i.e., a fractal,[32–35] and the bulk modulus has the scaling dependence

$$K \approx (p - p_c)^{\tau} \text{ in the elastic region } (p \geqslant p_c), \tag{1}$$

$$K \approx (p - p_c)^{s} \text{ in the highly elastic region } (p \leqslant p_c), \tag{2}$$

where p is the concentration of whole bonds, and the critical indices τ and s depend only on the dimensionality of the space d.

Typical representatives of such materials are polymers, and colloidal and composite materials.[35–37]

It should be noted that the problem of determining elastic properties on a percolation lattice will be formulated completely if we determine the Hamiltonian on the considered set of sites and bonds whose geometrical characteristics (number of sites or bonds, distance to the most distant elements, degree of meander, etc.) are prescribed statistically. In this case the Hamiltonian describing the elastic properties of the percolation system should satisfy certain requirements. Specifically, elastic connectivity should be realized: the lattice for $p \geqslant p_c$ should have finite macromoduli of elasticity, vanishing as $p \to p_c + 0$; the tensor properties of the elasticity of extended chains forming the percolation cluster should be correctly reproduced; and free states of the Hamiltonian should be invariant with respect to rotations.

The first condition is satisfied, for example, by the Born model;[29] however, it does not satisfy the second condition and as a result leads to a system of equations analogous to the Kirchhoff equations for electric currents in a network of resistances, and as a consequence to the result that the critical index τ is equal to the critical index of the conductivity *t*.

Kantor and Webman[23] suggested a Hamiltonian that takes account of changes in the energy of the system due to changes in the angles between the bonds of the lattice. This Hamiltonian satisfies all three conditions and as a result leads to a correct description of the elastic properties of percolation systems.[24–28]

It is also necessary to mention that some configurations of bonds (local regions) can possess unusual properties, in particular a negative Poisson coefficient $\nu < 0$. Thus, for example, the chain of bonds depicted in Fig. 1 when stretched out not only lengthens but also ''thickens.'' If such configurations make the defining contribution to the macroscopic properties of the system, then this can lead to the result that the Poisson coefficient will be negative.

Numerical studies[24] of planar ($d = 2$) elastic random percolation networks have shown that if their linear dimension $L < 0.2\zeta$, then the Poisson coefficient of the system will be negative, and if $L > 0.2\zeta$, the Poisson coefficient will be positive (ζ is the correlation length). In this case, if $L/\zeta \to \infty$, the limiting value of the Poisson coefficient will be equal to $\nu = 0.08 \pm 0.04$ and is a universal constant, i.e., it does not depend on the relative values of the local elastic characteristics; if $L/\zeta \to 0$, then $\nu = -\frac{1}{3}$; if $L/\zeta = 5$, then $\nu = 0$.

Averaging of the local elastic properties of percolation (fractal) systems can be done in different ways. In what follows we propose an averaging method based not on a discrete (percolation) lattice, but on a continuum ''droplet'' model which takes account of the tensor nature of the elastic

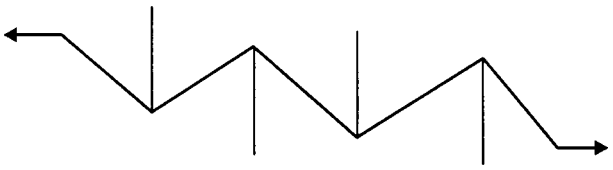

FIG. 1. Configuration of a chain of bonds of a percolation system.

properties. The approach is based on the transfer-matrix method.[22]

In the description of percolation systems, along with fractal geometry use is also made of various analogs of the renormalization-group (RG) method, which is based on the idea of scale invariance,[32,33] which has led to fruitful results in the theory of temperature phase transitions.[38]

In the present paper we present the results of numerical calculations of the elastic properties of a random medium based on an iteration method of averaging, which is based on results of fractal geometry and renormalization-group transformations.[16–20]

1. STRUCTURAL MODEL

The basic set of bonds Ω was obtained with the help of an iteration process the first step of which ($k=0$) starts off with a finite lattice in a space of dimensionality $d=2$ or $d=3$ with probability p_0 that a bond between neighboring lattice sites is whole—''painted'' with a certain color. Bonds painted with the same color are assumed to possess the same properties. In the following steps ($k=1, 2, \ldots, n$) each bond in the lattice is replaced by the lattice obtained in the preceding step (Fig. 2). The iteration process terminates when the properties of the lattice cease to depend on the number of the iteration. Thus, we obtained lattices with linear dimensions L_n (L_n is much greater than the correlation length), on which the effective physical properties were determined. The set of bonds obtained with the help of this iteration procedure, $\Omega_n(l_0,p_0)$, depends on the size of the initial lattice l_0 and the probability p_0.[16–18]

The probability that a set of bonds will form a connected set at the kth step, $R(l_k,p_k)$, was defined as the ratio of the number of connected sets to the total number of casts (to the number of ways of coloring the lattice) of bonds for fixed values of l_0 and p_0. The function $R(l_k,p_k)$, being a polynomial of degree N, where N is the number of bonds in the lattice, whole or otherwise (if the dimensionality of the lattice is $d=2$, then $N=2l_0^k$), can be determined with whatever accuracy is desired for any p_0 and l_0.

On the basis of fractal models of the structure of a random inhomogeneous medium constructed on various initial rectangular lattices: 3×3, 4×4, 5×4, 5×5, 6×6, 9×8, 9×9 for $d=2$ and $3\times3\times3$ for $d=3$ (Ref. 16) we have determined the percolation threshold p_c, the critical indices for the correlation length ν_p, the densities of the percolation cluster β and the fractal dimensionality d_f. We have shown that the geometrical properties of the obtained fractal sets at the percolation threshold coincide with the properties of the percolation cluster if the linear dimensions of the initial lattice $l_0\geqslant8$ for $d=2$ and $l_0\geqslant3$ for $d=3$.

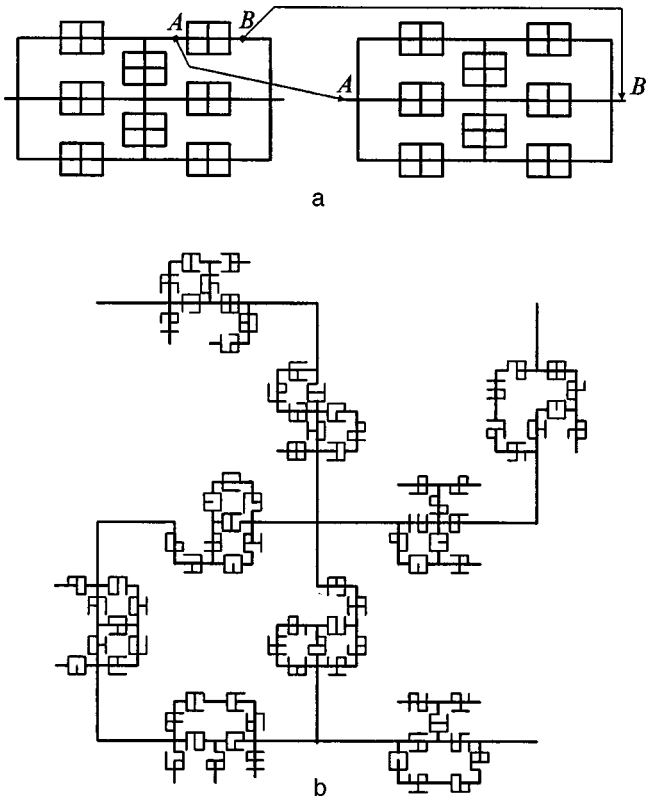

FIG. 2. Illustration of the renormalization-group transformation on a rectangular lattice for the case $l_0=2$: a — $p_0=1$; b — $p_0=0.75$.

Next we considered the effective elastic properties of an inhomogeneous medium imbedded in a space of dimensionality $d=3$. To calculate these properties we used the function $R(p)$ based on the $3\times3\times3$ model ($l_0=3$, $d=3$) (Fig. 3).

2. ELASTIC PROPERTIES

Let us consider a two-phase system with distribution function

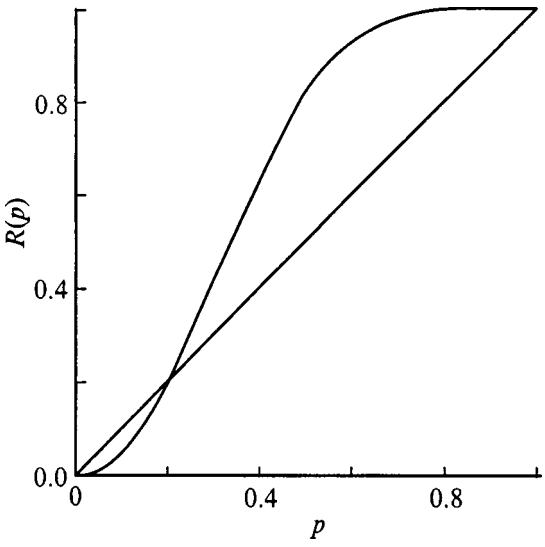

FIG. 3. Probability of formation of connected sets versus concentration of whole bonds ($l_0=3$, $d=3$).

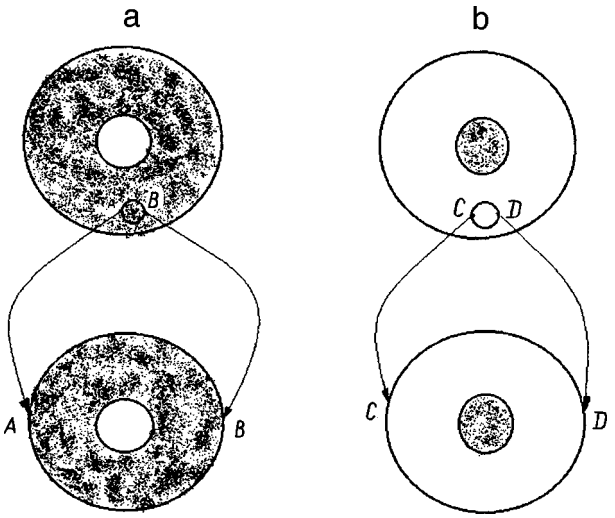

FIG. 4. Toward a model of the structure of a connected set (a) and an unconnected set (b) of whole bonds (the ''droplet'' model) at different steps (scales) of the iteration.

$$P_0(C)=(1-p_0)\,\delta(C-C_2^{(0)})+p_0\,\delta(C-C_1^{(0)}), \tag{3}$$

where $\delta(x)$ is the Dirac δ function, p_0 is the probability that the given local region possesses the property $C_1^{(0)}$ (it possesses the property $C_2^{(0)}$ with probability $1-p_0$).

After k steps of renormalization-group transformations the density function takes the form

$$P_k(C)=(1-p_k)\,\delta(C-C_2^{(k)})+p_k\,\delta(C-C_1^{(k)}). \tag{4}$$

As $k\to\infty$

$$P_k(C)=\delta(C-C_{ef}), \tag{5}$$

where C_{ef} are the effective properties of the medium, and $p_k=R(l_{k-1},p_{k-1})$ is the concentration of whole bonds at the kth step.

The effective properties of the structural model can be determined in general according to the following scheme: first the properties of the various configurations are found in the first step; these properties are then averaged and assigned as inputs to the following step, etc.[16] Averaging of the properties of all possible configurations of the set of bonds leads to quite cumbersome calculations. Therefore we use an approximate method which consists in not calculating the properties of configurations obtained for casts of whole bonds in the lattice, but rather in distinguishing two types of configurations of sets of bonds: connected sets (CS) and unconnected sets (UCS), and then transforming from discrete models (on lattices) to continuum models in which the connected and unconnected sets together form a continuous medium. To model the structure of connected and unconnected sets we used the droplet model (ball in a homogeneous medium, see Fig. 4).

Thus, at each step (scale) of the iterative calculation of the elastic properties the structures of the connected and unconnected sets are modeled by composite ''droplets'': a connected set — in a continuous mass of ''elastic'' phase is found an inclusion in the form of a ball (droplet) of ''soft'' phase (Fig. 4a); an unconnected set — in a continuous mass of ''soft'' phase is found an inclusion in the form of a ball (droplet) of ''elastic'' phase (Fig. 4b). The fractions of connected sets and unconnected sets at each step of the calculations were defined to be equal to $p_k=R(l_{k-1},p_{k-1})$ and $1-p_k=R(l_{k-1},p_{k-1})$, respectively.

The effective elastic properties (bulk modulus K and shear modulus μ) of the connected and unconnected sets based on the droplet model were determined with the help of formulas obtained in the physics of inhomogeneous media[39,40] with allowance for the tensor nature of the elastic properties.

The scheme of the calculation of effective properties has the following form: 1) the function $R(p,l)$ is determined on the basis of the fractal model (on lattices); 2) at the kth iteration step of the calculations the concentration of connected sets is calculated according to the formula

$$p_k=R(p_{k-1},l_{k-1}), \tag{6}$$

and the elastic properties, on the basis of the ''droplet'' model according to formulas of the form

$$C_c^{(k)}=f_1(C_c^{(k-1)},C_n^{(k-1)},p_{(k-1)}) \quad \text{(for a connected set)}, \tag{7}$$

$$C_n^{(k)}=f_2(C_c^{(k-1)},C_n^{(k-1)},p_{(k-1)}) \quad \text{(for an unconnected set)}, \tag{8}$$

where f_1 and f_2 are known functions which depend on the structural model and the elastic properties of the connected and unconnected sets at the $(k-1)$-th step, these being $C_c^{(k-1)}$ and $C_n^{(k-1)}$, respectively.

The effective properties of the inhomogeneous medium C_{ef} satisfy the inequalities

$$C_c^{(k)}\geqslant C_{ef}\geqslant C_n^{(k)}.$$

In the limit $k\to\infty$ the sequence $C^{(k)}$ converges to C_{ef}

$$\lim_{k\to\infty} C_c^{(k)}=\lim_{k\to\infty} C_n^{(k)}=C_{ef}. \tag{9}$$

To calculate the elastic properties of fractal structures according to the given scheme it is desirable to have an analytical dependence for the function $R(p)$.

If starting lattices of small linear dimensions $l_0<5$ for $d=2$ are used to construct the fractal set, then the function $R(p)$ can be found analytically. For lattices with $l_0>5$ ($d=2$) and $l_0\geqslant 3$ for dimensionality $d=3$ finding an analytical expression for $R(p)$ leads to cumbersome expressions which can be investigated only numerically.[33]

Fitting the results of numerical calculations of the function $R(p)$ for a $3\times3\times3$ lattice[16] showed that the function

$$R(p)=p^2(4+8p-14p^2-40p^3+16p^4+288p^5+655p^6+672p^7-376p^8+112p^9-14p^{10}), \tag{10}$$

which was obtained earlier in Ref. 39 gives a good fit to the numerical results.

The percolation threshold p_c according to formula (10) [p_c is the solution of the equation $p=R(p)$] is equal to ~ 0.2085, i.e., the unconnected set transforms into a connected set at $p_c=0.2085$ (Fig. 3).

To calculate the elastic properties of a percolation system with the aid of the step-by-step (iterative) averaging

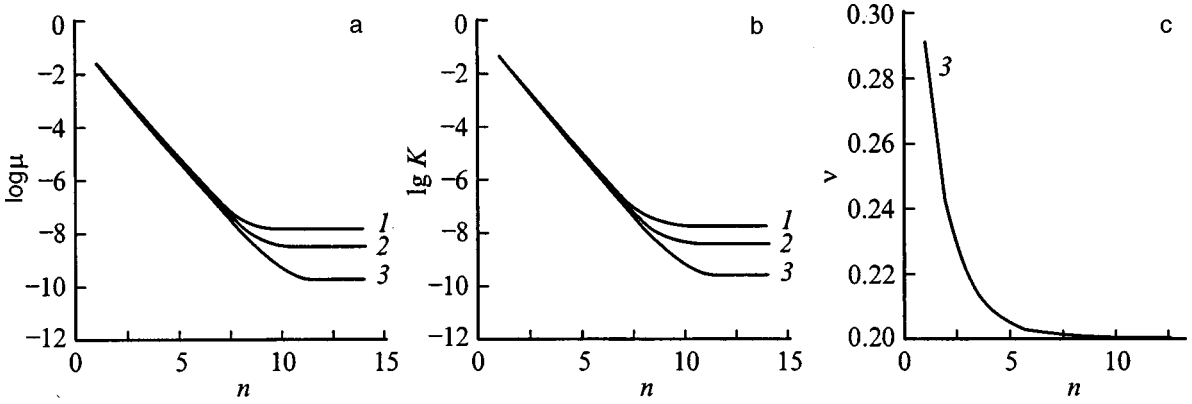

FIG. 5. Dependence of the elastic properties on the number of the iteration n for *1*) $p=0.2088$, *2*) $p=0.2092$, and *3*) $p=0.2098$: (a) logarithm of the shear modulus $\log\mu$; (b) logarithm of the bulk modulus $\log K$; (c) Poisson coefficient ν.

method we used the Hashin–Shtrikman formulas,[40,41] which are based on the structural model ''ball in a homogeneous medium'' (Fig. 4).

For a connected set the bulk modulus K_c and the shear modulus μ_c at the $(i+1)$-th step have the form[40,41]

$$K_c^{(i+1)}=K_c^{(i)}+\frac{(1-p_i)(K_n^{(i)}-K_c^{(i)})}{1+p_i a_c^{(i)}(K_n^{(i)}-K_c^{(i)})}, \tag{11}$$

$$\mu_c^{(i+1)}=\mu_c^{(i)}+\frac{(1-p_i)(\mu_n^{(i)}-\mu_c^{(i)})}{1+p_i b_c^{(i)}(\mu_n^{(i)}-\mu_c^{(i)})}, \tag{12}$$

where

$$a_c^{(i)}=\frac{3}{3K_c^i+4\mu_c^i}; \quad b_c^{(i)}=\frac{6(K_c^{(i)}+2\mu_c^{(i)})}{5\mu_c^{(i)}(3K_c^{(i)}+4\mu_c^{(i)})}, \tag{13}$$

$K_c^0=K_1$ and $\mu_c^0=\mu_1$ are the bulk modulus and the shear modulus of the ''elastic'' phase, respectively, and $K_n^0=K_2$ and $\mu_n^0=\mu_2$ are the bulk modulus and shear modulus of the ''soft'' phase, respectively (K_1, K_2, μ_1, and μ_2 are the elastic properties of the phases of the inhomogeneous medium).

For an unconnected set the elastic properties $K_n^{(i+1)}$ and $\mu_n^{(i+1)}$ are given by formulas obtained from formulas (11)–(13) by interchanging the indices $c\leftrightarrow n$ and $p_i\leftrightarrow(1-p_i)$.

3. RESULTS OF CALCULATIONS

Figure 5 plots the dependence of the logarithm of the shear modulus μ (Fig. 5a), the logarithm of the bulk modulus K (Fig. 5b), and the Poisson coefficient (Fig. 5c) of the fractal set on the iteration number n. Up to the point at which they level off to a horizontal dependence the curves of the elastic properties have a fractal character. The departure to a horizontal dependence points to an upper bound on the fractal asymptotic behavior, i.e., to the fact that the elastic properties of the system do not depend on scale (on iteration number).

Figure 6a plots the logarithm of the bulk modulus K as a

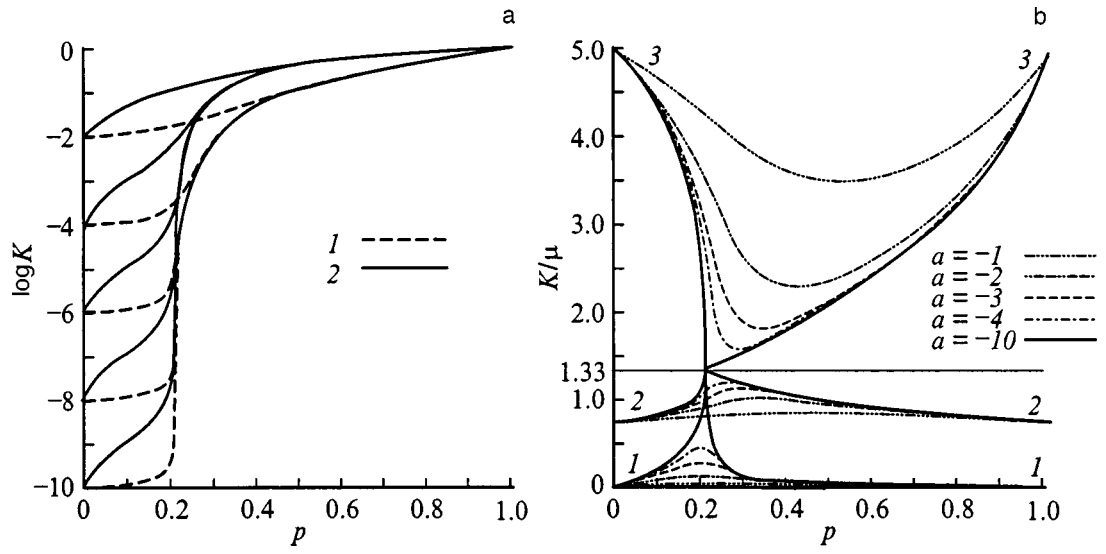

FIG. 6. Elastic properties. (a) — logarithm of the bulk modulus versus p [$a=\log(K_2/K_1)$]; *1* — $K_1/\mu_1=K_2/\mu_2=5$; *2* — $K_1/\mu_1=K_2/\mu_2=0.025$. (b) — ratio of the bulk modulus to the shear modulus K/μ: *1* — $K_1/\mu_1=K_2/\mu_2=0.025$; *2* — $K_1/\mu_1=K_2/\mu_2=0.75$; *4* — $K_1/\mu_1=K_2/\mu_2=5$.

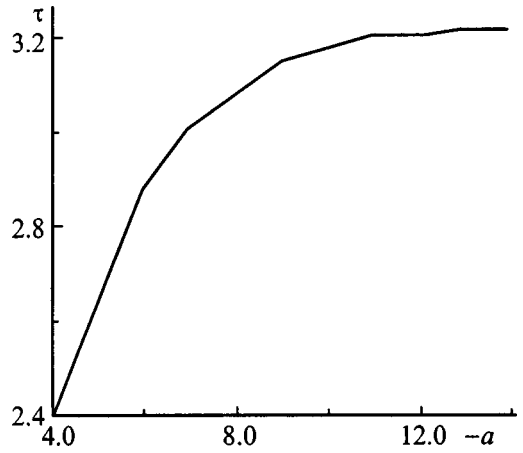

FIG. 7. Critical index of the bulk modulus for $p>p_c$ $[a=\log(K_2/K_1)]$.

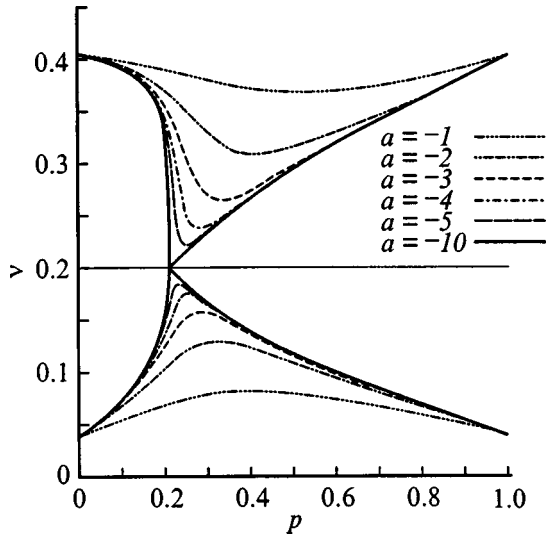

FIG. 8. Dependence of the effective Poisson coefficient on the volume concentration of the ''rigid'' component p for various ratios of the elastic moduli of the phases $a=\log(K_2/K_1)$.

function of the volume concentration of the ''rigid'' component p. On the basis of these calculations we determined the index τ for the elastic region

$$K\sim(p-p_c)^{\tau}, \quad p>p_c \tag{14}$$

and the index s for the highly elastic region

$$k\sim(p_c-p)^{s}, \quad p<p_c. \tag{15}$$

The dependence of the logarithmic derivative

$$\tau=\lim_{p\to p_c+0}\frac{\Delta(\log K)}{\Delta(\log(p-p_c))} \tag{16}$$

on the ratio of the bulk moduli of the phases $a=\log(K_2/K_1)$ is plotted in Fig. 7.

The critical index τ, which is determined by the singular behavior of the bulk modulus K near the critical point p_c+0, is equal according to the results of our numerical calculations, to 3.25 ± 0.05 (Fig. 7), which is somewhat less than the values given in Ref. 23 ($\tau=3.55$) and Ref. 28 ($3.64<\tau<3.85$), and coincides with the results of Ref. 22 ($\tau=3.26$).

Our calculations for the highly elastic region ($p<p_c$) showed that the critical index s depends on the elastic properties of the phases and varies from $s=0.52\pm0.02$ at $K_1/\mu_1=K_2/\mu_2=5$ to $s=0.75\pm0.05$ at $K_1/\mu_1=K_2/\mu_2=0.025$.

In the vicinity of the percolation threshold the ratio of the bulk modulus to the shear modulus K/μ tends to a constant value (Fig. 6b). We found that $(K/\mu)\cong1.33$. This result is in agreement with Refs. 23 and 27, which obtained a theoretical proof of the equality $(K/\mu)=(4/d)$ in the limit $p\to p_c$.

Figure 8 plots the results of calculations of the dependence of the effective Poisson coefficient on the volume concentration of the ''rigid'' phase for assorted values of $a=\log(K_2/K_1)$. The calculations were made for values of the Poisson coefficients of the phases that encompass their wide spectrum of possible values, extending from -0.9 to 0.4 (Figs. 8 and 9). It follows from the figures that at the percolation threshold the Poisson coefficient is equal to $\nu=0.2$ (in the limit $K_2/K_1\to0$). Here the functional dependence of the Poisson coefficient on the volume content of the phases of the inhomogeneous medium (Figs. 8 and 9) is nonmonotonic and for arbitrary elastic properties of the phases passes through the point $(p_c, 0.2)$, i.e., in the vicinity of the percolation threshold the effective Poisson coefficient is positive even for negative values of the Poisson coefficient of the local regions (phases) of the inhomogeneous medium. The Poisson coefficient changes sign far from the threshold p_c: if $\nu_1<0$ and $K_1\gg K_2$, then ν changes sign at a concentration of the ''rigid'' phase $p>p_c$; if $\nu_1<0$ and $K_1\ll K_2$, then ν changes sign for $p<p_c$, i.e., in this case the medium at first offers resistance to a change in its shape and only for $p>p_c$ does it offer resistance to a change in the volume of the medium.

In addition to the material presented above, we will attempt to estimate the dependence of the Poisson coefficient

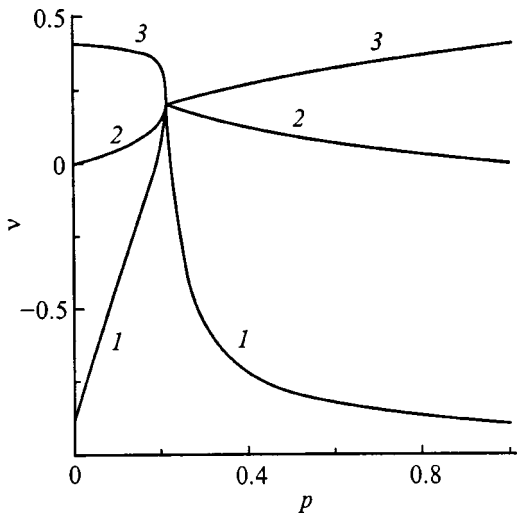

FIG. 9. Dependence of the Poisson coefficient on the volume concentration of the ''rigid'' component p. *1* — $\nu_1=\nu_2=-0.9$; *2* — $\nu_1=\nu_2=0$; *3* — $\nu_1=\nu_2=0.4$.

on the structure of the material, basing our derivation on Refs. 10 and 23.

To explain the dependence of the Poisson coefficient on the structure, Kantor and Webman[23] proposed the dependence

$$\mu/K=\frac{Z}{8}, \tag{17}$$

where Z is the coordination number of the percolation lattice.

If we assume that the Poisson coefficient for a d-dimensional isotropic inhomogeneous medium is given by[10]

$$\nu=\frac{Kd-2\mu}{d(d-1)K+2\mu}=\frac{d-b}{d(d-1)+b}, \quad b=2\mu/K, \tag{18}$$

then we obtain that if $b>d$ then $\nu<0$ ($\nu=-1$ in the limit $b/d\to\infty$); if $b=d$ then $\nu=0$; if $b<d$ then the maximum value of ν is equal to $(1/d-1)$ (in the limit $b/d\to 0$).

Now, if we substitute relation (17) into Eq. (18), we can write

$$\nu=\frac{d-Z/4}{d(d-1)+Z/4}. \tag{19}$$

Hence it follows that the Poisson coefficient at the percolation threshold is positive ($\nu>0$) if $Z<4d$, equal to zero ($\nu=0$) if $Z=4d$, and negative ($\nu<0$) if $Z>4d$.

Thus we can conclude that by making the appropriate choice of the structure of the inhomogeneous medium (the coordination number Z), we can obtain a material with negative Poisson coefficient far from the percolation threshold.

The proposed method for constructing a fractal model of the structure of a random medium and the step-by-step (iterative) method of determining the elastic properties are in good agreement with a numerical model of the elastic properties of percolation systems and can be used to predict the elastic properties both of percolation systems and of materials with a finite difference in the properties of their component phases.

To summarize, we have determined the critical index of the bulk modulus K in the elastic region: $\tau=3.25\pm0.05$. We have elucidated the dependence of the index s on the elastic properties of the phases of the medium in the highly elastic region.

We have shown that in the limit $p\to p_c$, $K/\mu\to 1.33$, and the Poisson coefficient of a percolation system near the threshold p_c is independent of the properties of the phases of the inhomogeneous medium and at the percolation threshold is equal to 0.2. The dependence of the effective Poisson coefficient ν on the volume concentration of the ''rigid'' component p of an inhomogeneous medium with random structure is nonmonotonic.

We have shown that a percolation system can have a negative Poisson coefficient if the lattice has coordination number $Z>4d$.

This work was carried out with the support of the Polish Committee for Scientific Research (Grant No. KBN 8T11F 010 08p04) and the Ukrainian Ministry of Science (Grant No. F4/1644-97 in Topic Area 4/4.526 and Grant No. 2/1502-97 in Topic Area 05.06/03218).

*)E-mail: novikov@te.net.ua

[1] L. D. Landau and E. M. Lifshitz, *Theory of Elasticity*, 3rd English ed. (Pergamon Press, Oxford, 1986).
[2] R. F. Almgren, J. Elast. **15**, 427 (1985).
[3] A. G. Kolpakov, Prikl. Mekh. Tekh. Fiz. **49**, 969 (1985).
[4] D. J. Bergman, Phys. Rev. B **33**, 2013 (1986); D. J. Bergman and E. Duering, Phys. Rev. B **34**, 8199 (1986); E. Duering and D. J. Bergman, Phys. Rev. **37**, 9460 (1988).
[5] R. Lakes, Science **235**, 1038 (1987).
[6] K. W. Wojciechowski, Mol. Phys. **61**, 1247 (1987); K. W. Wojciechowski, Phys. Lett. A **137**, 61 (1989); K. W. Wojciechowski and A. C. Brańka, Phys. Rev. A **40**, 7222 (1989).
[7] B. D. Caddock and K. E. Evans, J. Phys. D **22**, 1877 (1989); K. E. Evans and B. D. Caddock, J. Phys. D **22**, 1883 (1989).
[8] R. Lakes, Adv. Mater. **5**, 293 (1993); see also references therein.
[9] D. H. Boal, U. Seifert, and J. C. Schillcock, Phys. Rev. E **48**, 4274 (1993).
[10] K. W. Wojciehowski, Mol. Phys. Rep. **10**, 129 (1995).
[11] E. O. Martz, R. S. Lakes, and J. B. Park, Cellular Polymers **15**, 349 (1996).
[12] D. Prall and R. Lakes, Int. J. Mech. Sci. **39**, 305 (1997).
[13] U. D. Larsen, O. Sigmund, and S. Bouwstra, J. Macromech. Systems **6**, 99 (1997).
[14] P. S. Theocaris, G. E. Stavroulakis, and P. D. Panagiotopoulos, Arch. Appl. Mech. **67**, 274 (1997).
[15] G. Y. Wei and S. F. Edwards, Physica A **258**, 5 (1998).
[16] V. V. Novikov and V. P. Belov, Zh. Éksp. Teor. Fiz. **106**, *3(9)*, 780 (1994) [JETP **79**, 428 (1994)].
[17] V. V. Novikov, O. P. Poznansky, and V. P. Privalko, Sci. Eng. Compos. Mater. **4**, 49 (1995).
[18] V. V. Novikov and O. P. Poznan'skiĭ, Fiz. Tverd. Tela (St. Petersburg) **37**, 830 (1995) [Phys. Solid State **37**, 451 (1995)].
[19] V. V. Novikov, Teplofiz. Vys. Temp. **34**, 698 (1996).
[20] V. V. Novikov, Fiz. Met. Metalloved. **4**, 27 (1997).
[21] S. Feng and P. N. Sen, Phys. Rev. Lett. **52**, 216 (1984).
[22] S. Feng and M. Sahimi, Phys. Rev. B **31**, 1671 (1985).
[23] Y. Kantor and I. Webman, Phys. Rev. Lett. **52**, 1981 (1984).
[24] D. J. Bergman and Y. Kantor, Phys. Rev. Lett. **53**, 511 (1984).
[25] S. Arbabi and M. Sahimi, Phys. Rev. B **38**, 7173 (1988).
[26] H. J. Herrmann and H. E. Stanley, J. Phys. A **21**, 1829 (1988).
[27] S. Arbabi and M. Sahimi, Phys. Rev. B **47**, 695 (1993).
[28] M. Sahimi and S. Arbabi, Phys. Rev. B **47**, 703 (1993).
[29] P. de Gennes, *Scaling Concepts in the Physics of Polymers* (Benjamin, New York, 1966).
[30] H. E. Stanley, *Introduction to Phase Transitions and Critical Phenomena* (University Press, Oxford, 1971).
[31] A. Coniglio and H. E. Stanley, Phys. Rev. Lett. **52**, 1068 (1984).
[32] D. Stauffer and A. Aharony, *Introduction to Percolation Theory* (Taylor & Francis, London, 1992).
[33] P. J. Reynolds, H. E. Stanley, and W. Klein, Phys. Rev. B **21**, 1223 (1980).
[34] B. B. Mandelbrot, *The Fractal Geometry of Nature* (Freeman, San Francisco, 1982).
[35] D. A. S. Weitz and M. Oliveira, Phys. Rev. Lett. **52**, 1433 (1984).
[36] V. P. Privalko and V. V. Novikov, *The Science of Heterogeneous Polymers: Structure and Thermophysical Properties* (Wiley, Chichester, 1995).
[37] L. Pietronero and E. Tosatti, *Fractals in Physics* (North-Holland, Amsterdam, 1986).
[38] K. G. Wilson and J. B. Kogut, Phys. Rep. **9**, 75 (1974).
[39] J. Bernasconi, Phys. Rev. B **18**, 2185 (1978).
[40] Z. Hashin and S. A. Shtrikman, J. Mech. Phys. Solids **11**, 127 (1963).
[41] Z. Hashin, J. Appl. Meteorol. **50**, 481 (1983).

Translated by Paul F. Schippnick

Weak exchange interactions in the heteronuclear crystal $CuPr_2(CCl_3COO)_8 \cdot 6H_2O$

V. K. Voronkova and Yu. V. Yablokov

Kazan' Physicotechnical Institute, Russian Academy of Sciences, 420029 Kazan', Russia

J. Legendziewicz and M. Bożechowska

Wrocław University, 50-383 Wrocław, Poland
(Submitted in final form May 27, 1999)
Fiz. Tverd. Tela (St. Petersburg) **41**, 2154–2157 (December 1999)

The new heteronuclear crystal $CuPr_2(CCl_3COO)_8 \cdot 6H_2O$, constructed of chains containing copper and praseodymium atoms, has been synthesized and investigated by EPR at 9.3 GHz at temperatures ranging from room temperature down to 10 K. At temperatures $T \sim 300 - 130$ K, EPR spectra are observed which are characteristic of isolated polyhedra of copper ions with $g_z = 2.330 \pm 0.005$, $g_{x,y} = 2.053 \pm 0.005$, $A_z = 139 \times 10^{-4}\ \mathrm{cm}^{-1}$, and $A_{x,y} < 26 \times 10^{-4}\ \mathrm{cm}^{-1}$. At temperatures $T < 130$ K a complex spectrum is observed, associated with the appearance of weak exchange interactions between the copper ions in the chain ($J_{\mathrm{Cu-Cu}} \Sigma S_i \cdot S_{i+1}$), comparable in magnitude with the hyperfine interactions $J_{\mathrm{Cu-Cu}} = 0.015\ \mathrm{cm}^{-1}$ at $T = 10$ K. The magnitude of the exchange interaction decreases smoothly as the temperature is raised. It is conjectured that orbitals of the praseodymium ions participate in the process of indirect exchange between the copper ions. © *1999 American Institute of Physics.* [S1063-7834(99)01012-6]

With the aim of studying the character and peculiarities of the interaction of ions of the iron group and rare-earth ions, we have carried out a study of the interactions of ions of divalent copper and trivalent rare-earth ions in the quasi-one-dimensional heteronuclear compounds $CuRe_2(CCl_3COO)_8 \cdot 6H_2O$ (Re^{3+} is a rare-earth ion).[1,2] The present paper reports results of an EPR study of the compound with the praseodymium ion ($Re^{3+} = Pr^{3+}$), which is a non-Kramers ion.[3,4]

1. EXPERIMENTAL RESULTS

Thorough structural studies have been performed on the crystalline compound $CuNd_2(CCl_3COO)_8 \cdot 6H_2O$ (Ref. 1); for the crystalline compound $CuPr_2(CCl_3COO)_8 \cdot 6H_2O$ it has been established that it is isostructural with the former compound (triclinic space group $P1$, $Z = 2$). The parameters of its unit cell have been determined: $a = 1180.5(2)$, $b = 1219.0(2)$, $c = 2001.7(2)$ pm, $\alpha = 98.94(1)$, $\beta = 106.68(1)$, $\gamma = 102.05(1)°$. The crystal consists of heteronuclear chains. A fragment of a chain of the crystal $CuNd_2(CCl_3COO)_8 \cdot 6H_2O$ (Ref. 1) is shown in Fig. 1. The chain consists of two structurally nonequivalent polyhedra of the rare-earth ions Re_1 and Re_2, which are joined by a CuO_4 fragment. Two water molecules of the polyhedra of the Re_1 and Re_2 ions finish off the polyhedron of the copper ion to a distorted octahedron.

The EPR studies were performed on a single crystal of $CuPr_2(CCl_3COO)_8 \cdot 6H_2O$ at the frequency 9.3 GHz in the temperature range from room temperature down to 10 K.

At room temperature a spectrum is observed that is characteristic of isolated copper centers ($3d^9$, $I = 3/2$) with allowed hyperfine structure. The angular dependence of the EPR spectra at room temperature is described by the parameters $g_z = 2.330 \pm 0.005$ (0.230, 0.287, and 0.930 are the direction cosines for g_z in the XYZ coordinate system chosen with the Z axis aligned with the b axis of the crystal and the X axis in the bc plane), $A_z = 139 \times 10^{-4}\ \mathrm{cm}^{-1}$, $g_{x,y} = 2.053 \pm 0.005$, and $A_{x,y} < 26 \times 10^{-4}\ \mathrm{cm}^{-1}$.

Figure 2 displays the temperature dependence of the EPR spectra of a $CuPr_2(CCl_3COO)_8 \cdot 6H_2O$ crystal for the magnetic field aligned with the z axis of the g tensor. As the temperature is lowered from room temperature down to 130 K, the shape of the spectrum does not alter substantially (Figs. 2a and 2b). At temperatures $T < 130$ K the picture of the hyperfine splitting begins to change: the four components of the hyperfine structure decay into a series of components and symmetrically located lateral signals beyond the limits of the spectrum appear which are characteristic at high ($290 - 130$ K) temperatures. The spectra in Figs. 2c–2g illustrate the smoothness of the observed transformation of the spectra. The distance to the lateral signals from the center of the spectrum increases as the temperature is lowered (Figs. 2d–2g). For the magnetic field oriented parallel with the other axes for which hyperfine splitting is manifested, a similar picture is observed although the shape of the resulting spectrum varies depending on the orientation (Fig. 3). The lateral signals are preserved for all orientations including the orientation of the magnetic field along the X and Y axes of the g tensor, where hyperfine splittings are not observed. As can be seen from Fig. 3, the ratio of intensities of the lateral signals to the main spectrum decreases when the magnetic field is tilted away from the Z axis of the g tensor. Note that the spectra in Fig. 2 were taken under different conditions; therefore they do not reflect the increase in the intensity of

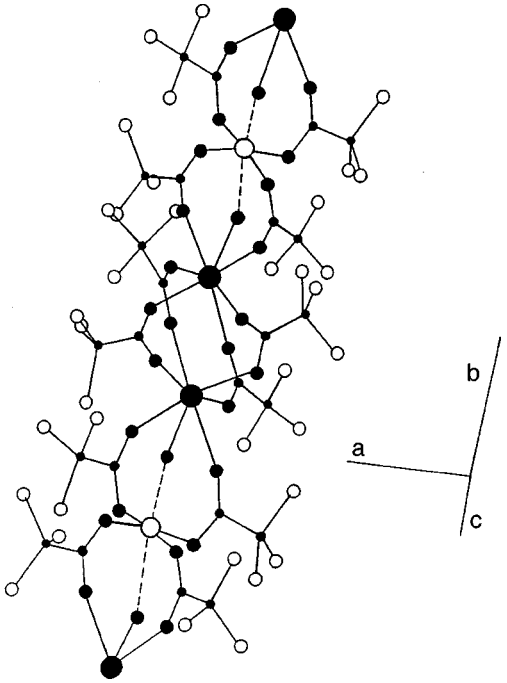

FIG. 1. Fragment of a chain of the compound $CuNd_2(CCl_3COO)_8 \cdot 6H_2O$, isostructural with the compound $CuPr_2(CCl_3COO)_8 \cdot 6H_2O$ (Ref. 1). Ligand atoms of carbon C and oxygen O, and neodymium atoms (Nd_1, Nd_2) are denoted by small, medium, and large filled circles, respectively, while the large and medium-size empty circles represent copper Cu and chlorine Cl atoms, respectively. Two water molecules are not shown in the figure, one each per neodymium polyhedron, the directions of the Nd–O bonds for which are nearly perpendicular to the plane of the figure.

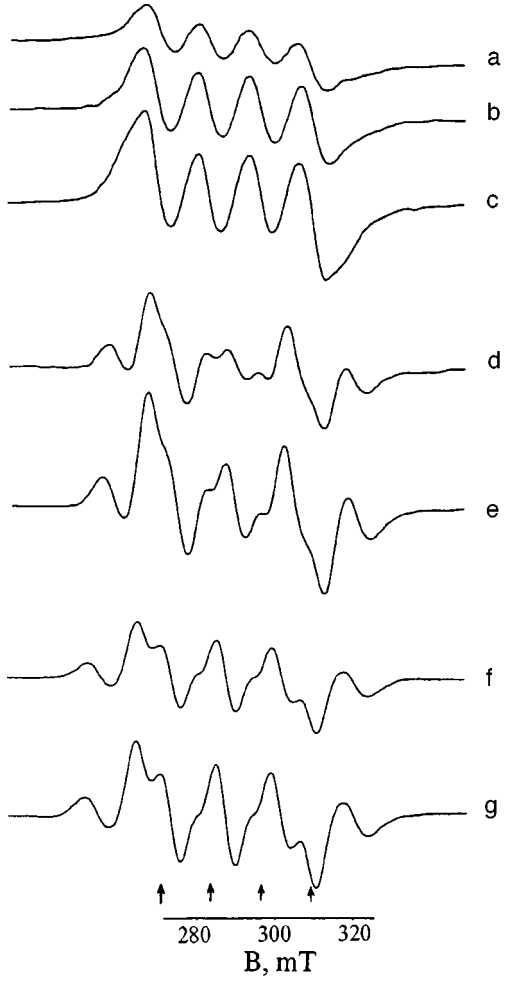

FIG. 2. Temperature dependence of the EPR spectra ($\nu = 9.3$ GHz) of a $CuPr_2(CCl_3COO)_8 \cdot 6H_2O$ crystal for the magnetic field oriented along the z axis of the g tensor ($g_z = 2.330$, $A_z = 13$ mT): a — $T = 290$ K (16), b — 190 K (8), c — 127 K (8), d — 73 K (4), e — 40 K (4), f — 18 K (1), g — 10 K (1). The numbers in parentheses are the relative amplification of the spectra, with the amplitude of modulation being equal to 2.4 G and 1.4 G for spectra a–e and f–g, respectively.

the EPR spectra observed when the temperature is lowered. In order to graphically demonstrate the change in the position of the signals in the low-temperature spectrum in comparison with the high-temperature spectrum, the positions of the four components of the hyperfine structure are marked in Fig. 2g to correspond to the splittings in Figs. 2a and b. The distances between the lateral signals in the low-temperature spectrum and the outer arrows corresponding to the signals with $m = \pm 3/2$ (m is the projection of the nuclear spin of the copper ion), are equal to 14 mT for the orientation presented in Fig. 2, and increase in units of the field as the field is tilted away from this orientation but remain fixed in units of energy and are equal to $0.015\ cm^{-1}$.

As will be shown below, the observed transformation of the spectra with temperature is evidence of the appearance of a weak exchange interaction between the copper ions for $T < 130$ K and a smooth weakening of this interaction down to zero in the temperature region 130–290 K.

2. DISCUSSION OF RESULTS

The investigated compound is constructed of chains in which the copper-ion fragments alternate with praseodymium-ion dimer fragments (Fig. 1). Rare-earth ions are characterized by short paramagnetic relaxation times,[3–5] and the interaction with rapidly relaxation ions can lead to a broadening of the EPR spectrum of the copper ions. References 6 and 7 established experimentally and investigated theoretically peculiarities of the temperature dependence of the spectra of $[CuNd_2\ (C_4O_4)_4)(H_2O)_{16}]\ 2H_2O$ constructed of copper and neodymium ions due to variation of the paramagnetic relaxation rate of neodymium. We showed there that the shape and position of the spectrum depend substantially on the ratio of the magnitude of the exchange interaction between these ions and the paramagnetic relaxation rate of neodymium. Because of this, the spectrum can vary from the spectrum characteristic of copper-ion centers at high temperatures to the spectrum corresponding to the Cu–Nd fragment at low temperatures. As the temperature is lowered from room temperature, the transformation of the spectrum shows up primarily in a broadening of the ''copper'' spectrum with its subsequent shift. Broadening of the ''copper'' signal as the temperature is decreased was also observed in $CuNd_2(CCl_3COO)_8 \cdot 6H_2O$, which is isostructural with $CuPr_2(CCl_3COO)_8 \cdot 6H_2O$ (Ref. 8). For the copper–praseodymium crystal broadening of the signal with decreasing temperature is absent.

Trivalent praseodymium is a non-Kramers ion and the ground state of this ion can be a non-Kramers doublet or an

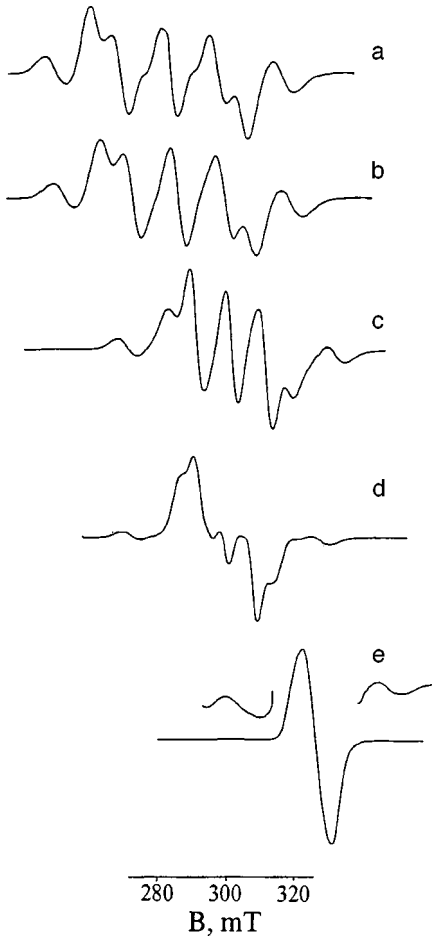

FIG. 3. Angular dependence of the EPR spectra ($\nu = 9.3$ GHz) of a $CuPr_2(CCl_3COO)_8 \cdot 6H_2O$ crystal at $T = 10$ K, $\Theta = 0$ (a), 20 (b), 55 (c), 70 (d), and 90 (e). $\Theta = 0$ corresponds to the magnetic field being oriented along the z axis of the g tensor.

isolated singlet.[4,9] If we assume that the latter situation is realized in the given crystal, where the ground state of the praseodymium ion is an isolated nonmagnetic singlet, then the absence of an interaction between the praseodymium and copper ions at low temperatures becomes understandable.

At the same time, the change in the picture of the hyperfine splitting at low temperatures in comparison with the high-temperature spectrum points to the presence of a weak exchange interaction between the copper ions in the chain. The authors of Ref. 10 investigated features of the EPR spectrum for a chain of copper ions bound by a weak exchange interaction, less in magnitude (or comparable) than the hyperfine splitting, in the instance of the compound $[N(n\text{-}Bu)_4]_2\,[Cu(mnt)_2]$. In this crystal with triclinic symmetry the planar anions $Cu(mnt)_2]^{2-}$ $[mnt = (C_4N_2S_2)^{2-}]$ form chains which are effectively isolated from one another by cations. The intrachain distance between the copper ions is 9.403 Å. It has been shown experimentally and theoretically for this compound that the weak exchange interaction between the copper ions can lead not to an averaging of the hyperfine structure, but to the appearance of additional splittings and the presence of lateral signals in the spectrum, the distance to which from the outer components of the hyperfine structure is of the same order of magnitude as the isotropic exchange J.

For a one-dimensional system the isotropic exchange interaction is described by the Hamiltonian $H_{ex} = J\Sigma S_i S_{i+1}$, where $S_i = 1/2$ for a copper ion at the ith site of the chain.

The exchange interaction between ions in the chain is significantly greater in magnitude than the hyperfine interaction and leads to averaging of the hyperfine splitting and the appearance in the spectrum of an isolated exchange-narrowed signal. If the exchange interaction is less than the hyperfine splitting, then the interaction between neighboring centers along the chain will differ depending on what relation obtains between the projections of the nuclear spin for neighboring sites: $m_i = m_{i+1}$ or $m_i \# m_{i+1}$, where $m = 3/2$, $1/2$, $-1/2$, or $-3/2$. Such a situation was analyzed in detail in Ref. 10. Taking the indicated nonequivalence into account, the chain can be considered as constructed of statistically distributed equivalent and nonequivalent ions. Therefore, the chain can be represented as consisting of fragments, inside which all centers have the same projection of the nuclear spin m. In Ref. 10 it was shown that since the probability of the formation of a fragment of length N decreases with increase of N, to model the spectrum of a chain with a weak interaction it is sufficient to consider fragments with $N \leqslant 3$. Taking the isotropic exchange interaction between the spins inside a fragment into account does not alter the position of a signal with prescribed m. The signals split after considering the interaction of the total spin S_N of an N-dimensional fragment with the spins of neighboring fragments. The interaction with the two neighboring fragments is described by the Hamiltonian $H = J(S_{N-1}S_N + S_N S_{N+1})$.

The model spectra of each fragment depend on which fragments are located to the right and the left of the given fragment. All situations were analyzed in Ref. 10 with allowance for the probability of their occurrence and the authors restricted the discussion to an account of the three situations responsible for 60% of the spectrum: (m,m,m), (m,d,m), and (d,m,m) or (m,m,d), where m is a monomer and d is a dimer.

An analysis of the model spectrum showed that the lateral lines in the spectrum in this case are associated with splitting of the components $m = \pm 3/2$ of the hyperfine structure into three components $h\nu - J$, $h\nu$, and $h\nu + J$. This maximum splitting is connected with the exchange interaction in the sequence (m,m,m). Each component of the hyperfine structure splits, but in the central part of the spectrum the splittings of different sequences of the fragment are superimposed, giving a complicated shape to the spectrum as a whole. The EPR spectra observed at low temperatures in $CuPr_2(CCl_3COO)_8 \cdot 6H_2O$ agree qualitatively with the model spectra presented in Ref. 10, leaving no doubt that the nature of the complicated splitting picture is associated with the weak exchange interaction between the copper ions in the given chain in analogy with the compound $[N(n\text{-}Bu)_4]_2$ $[Cu(mnt)_2]$ although the magnitude of the exchange interaction in the compound investigated here is essentially comparable with the magnitude of the hyperfine splitting in the parallel orientation and only the relation $A < J < 2A$ is fulfilled. In Ref. 10 it was shown that in this case it is necessary

to consider not fragments with the same m but fragments for which $|m_i - m_{i+1}| \leqslant 2$ and, as in the case for $J < A$, splitting from the position corresponding to $m = \pm 3/2$ in the absence of an interaction, out to the lateral signals is determined by the magnitude of the exchange interaction J. For the compound investigated here, the magnitude of the interaction does not depend on the orientation and for $T = 10$ K is equal to $0.015\ \mathrm{cm}^{-1}$.

The detected interaction is very small in magnitude, but comparable in magnitude with other examples of weak exchange interactions[11] detected between copper ions at distances not less than in the investigated compound (the distance between the interacting copper ions in the given chain is $R = 12.7$ Å). In principle, the distance between the copper ions in neighboring chains is less than within a chain, but the absence of bridge elements linking the copper ions of two neighboring chains allows us to maintain that the detected interaction is realized within the chains.

As can be seen from the temperature dependence of the spectra in Fig. 2, the magnitude of the exchange interaction increases smoothly with decreasing temperature. At room temperature the interaction is not detected. A dependence of the exchange interaction on the temperature was detected for many compounds with a weak ($J < 0.1\ \mathrm{cm}^{-1}$) exchange interaction between the copper ions. There is even an example of a change of sign of J with temperature.[11] Although in the majority of cases there is a tendency to link the temperature dependence of the exchange with thermal expansion of the crystal with increase of the temperature, there are grounds to assume that other mechanisms can in principle be responsible for this effect, and their roles in different crystals can differ.[11]

In $CuPr_2(CCl_3COO)_8 \cdot 6H_2O$ the nearest copper ions in the chains are linked by a dimer fragment of praseodymium ions (Fig. 1). The structure of the chain allows us to conclude that the praseodymium subsystem may have an influence on the temperature dependence of the interaction between the copper ions. Note that the EPR spectra of the isostructural crystal $CuNd_2(CCl_3COO)_8 \cdot 6H_2O$ indicate the absence of a temperature dependence of the parameters of the spin–spin interaction in this crystal in the temperature range $20-5$ K while the exchange interaction in the praseodymium compound in the indicated temperature interval continues to grow. It can be expected that the orbitals of the praseodymium ions take part in the indirect exchange between the copper ions and the efficiency of the interaction increases as the temperature is lowered, noting that lowering the temperature results in a decrease of the population of the excited magnetic states of the praseodymium ion. At high temperatures, when the excited magnetic states of the praseodymium ion are populated, rapid fluctuations in the praseodymium subsystem, as, for example, is discussed in Ref. 12, modulate the exchange interaction between the copper ions, making it practically equal to zero at room temperature. The expected change in the properties of the praseodymium ions in the temperature interval from room temperature down to 10 K due to the change in the population of the nonmagnetic ground state and the excited magnetic states is responsible for the smooth change in the efficiency of the interaction between the copper ions. Note that the suggestion has already been made in the literature that the orbitals of the rare-earth ion with diamagnetic ground state participate in the indirect exchange between copper ions.[13]

Thus, although EPR spectra of the praseodymium ion are not detected, it can be conjectured that a study of the heteronuclear compound $CuPr_2(CCl_3COO)_8 \cdot 6H_2O$ demonstrates the influence of the praseodymium subsystem on the efficiency of indirect exchange between the copper ions and the possibility that they may play the role of a regulator of this interaction. In the investigated compound the magnitude of the interaction is small, and we are talking here about a change in very small quantities. But precisely because the magnitude of the interaction does not exceed the hyperfine splittings, we have obtained an accurate value of this interaction and its variation from the EPR spectra.

This work was carried out with the support of the Russian Fund for Fundamental Research (Grant No. 98-02-16588).

[1] I. Kutlu, G. Meyer, G. Oczko, and J. Legendziewicz, Eur. J. Solid State Inorg. Chem. **34**, 231 (1997).
[2] G. Oczko, J. Legendziewicz, J. Mrozinski, and G. Meyer, Eur. J. Solid State Inorg. Chem. **38** (1998).
[3] A. Abragam and B. Bleaney, *Electron Paramagnetic Resonance of Transition Ions* (Clarendon Press, Oxford, 1970).
[4] S. A. Al'tshuler and B. M. Kozyrev, *Electron Paramagnetic Resonance* (Academic Press, New York, 1964).
[5] I. N. Kurkin, *Paramagnetic Resonance*, Vol. 5 (Izdat. Kazan. Univ., Kazan', 1969), p. 31.
[6] V. K. Voronkova, E. Guskovska, Ya. Legenzhevich, and Yu. V. Yablokov, Fiz. Tverd. Tela (St. Petersburg) **39**, 2057 (1997) [Phys. Solid State **39**, 1838 (1997)].
[7] K. M. Salikhov, R. T. Galeev, V. K. Voronkova, Yu. V. Yablokov, and J. Legendziewicz, Ann. Phys. (N.Y.) **14**, 457 (1998).
[8] V. K. Voronkova, J. Legendziewicz, G. Oczko, and Yu. V. Yablokov, Third European ESR Meeting, Abstract P128 (Leipzig, 1997).
[9] K. R. Lea, M. J. M. Leask, and W. P. Wolf, J. Phys. Chem. Solids **23**, 1381 (1962).
[10] K. W. Plumlee, B. M. Hoffman, and J. A. Ibers, J. Chem. Phys. **63**, 1926 (1975).
[11] S. K. Hoffmann, W. Hilszer, and J. Goslar, Appl. Magn. Reson. **7**, 289 (1994).
[12] D. Davidov, V. Zevin, R. Levin, D. Shaltiel, and K. Baberschke, Phys. Rev. B **15**, 2771 (1977).
[13] O. Guillou, O. Kahn, R. L. Oushoorn, K. Boubekeur, and P. Batail, Inorg. Chim. Acta **198–200**, 110 (1992).

Translated by Paul F. Schippnick

DEFECTS. DISLOCATIONS. PHYSICS OF STRENGTH

Dislocations and disclinations in the gradient theory of elasticity

M. Yu. Gutkin

Institute for Problems in Mechanical Engineering, Russian Academy of Sciences, 199178 St. Petersburg, Russia

E. C. Aĭfantis

Aristotle University of Thessaloniki, 54006 Thessaloniki, Greece; Michigan Technological University, Houghton, MI 49931, USA

(Submitted April 16, 1999)
Fiz. Tverd. Tela (St. Petersburg) **41**, 2158–2166 (December 1999)

The results of application of gradient theory of elasticity to a description of elastic fields and dislocation and disclination energies are considered. The main achievement made in this approach is the removal of the classical singularities at defect lines and the possibility of describing short-range interactions between them on a nanoscopic level. Non-singular solutions for stress and strain fields of straight disclination dipoles in an infinite isotropic medium have been obtained within a version of the gradient theory of elasticity. A description is given of elastic fields near disclination lines and of specific features in the short-range interactions between disclinations, whose study is impossible to make in terms of the classical linear theory of elasticity. The strains and stresses at disclination lines are shown to depend strongly on the dipole arm d. For short-range interaction between disclinations, where d varies from zero to a few atomic spacings, these quantities vary monotonically for wedge disclinations and nonmonotonically in the case of twist disclinations, and tend uniformly to zero as disclinations annihilate. At distances from disclination lines above a few atomic spacings, the gradient and classical solutions coincide. As in the classical theory of elasticity, the gradient solution for the wedge-disclination dipole transforms to the well-known gradient solution for a wedge dislocation at distances d substantially smaller than the interatomic spacing.
 [S1063-7834(99)01112-0]

1. Traditional description of the elastic fields and energy of disclinations is based on solutions obtained within the linear theory of elasticity.[1–3] In the isotropic case, the corresponding expressions for the strain and stress tensors are fairly simple, which permits one to use them widely when modeling the structure and mechanical behavior of a variety of materials ranging from conventional metals, alloys, and composites[3,4] to nanoparticles,[3,5,6] nanostructural materials,[6–9] metallic glasses,[3,6,7,10–13] and thin-film heteroepitaxial systems.[14,15] Some components of these fields, however, undergo a discontinuity at disclination lines, which entails considerable inconveniences in theoretical description of the situations where one has to know the stresses and strains near disclination lines. This relates, for instance, to disclination models of grain boundaries, metallic-glass structure, and mechanical behavior of nanocrystalline materials, where one has to deal with high-density disclination ensembles. Thus one meets here the same problems as in using the well-known solutions for elastic fields in the vicinity of dislocations[1,16] or cracks,[17,18] which are treated in the classical linear theory of elasticity.

The first attempts to modify the elastic fields of these defects while staying within continuum models were directed at taking into account the effect of couple stresses.[18–26] Dislocations,[19–25] disclinations,[25,26] and cracks[18] were considered both in the Cosserat continuum and in a micropolar medium. The solutions found for the elastic stresses and strains differed from those obtained in the classical theory of elasticity, while containing, nevertheless, the same singularities at the dislocation and disclination lines and crack tips.

Following the classification of Kunin,[27] the Cosserat and micropolar continua may be considered as having a weak nonlocality in the elastic properties, which manifests itself in the appearance in the expression for the elastic energy of differential operators of second and higher orders on the displacement field, and of the corresponding additional material constants. Treatment of defects in media with a strong nonlocality, where the elastic stress and strain tensors are connected through integral relations, provides substantially better results; indeed, the singularities in the stress fields at the dislocation[27–31] and disclination[31] lines, as well as at crack tips,[29,32,33] disappear. The quasicontinuum models[27,28] taking into account the discrete structure of the solid were found to be the most efficient. One obtained in a closed analytic form stress fields for straight screw and edge dislocations, which are zero at the dislocation line and reach maximum values at

a distance from the latter, to finally decay with weak oscillations relative to the classical solution. At the same time solution of the same problems within the elastic continuum model with the stresses related to strains through integrals required introduction of an *a priori* form of an integral kernel in the definition. The solutions for screw dislocations were obtained in a different analytic form and reduced to the classical representation in the limiting case of local elasticity.[29] The solution for screw dislocations was derived only in an integral form, and no such passage to the limit could be made.[29] No weak oscillations characteristic of a quasicontinuum were observed. Interestingly, the solutions for displacement fields and elastic strains retained the form obtained in classical local elasticity, i.e., the existing classical singularities remained. Note that although Ref. 31 used completely analogous models of a nonlocal continuum, these features of the nonlocal solutions were not pointed out there.

Thus within the continuum theories of elasticity considered one has not succeeded until present in constructing models of line defects (dislocations and disclinations) which would combine such properties as the absence of singularities in the stress and strain fields at defect lines with a simple analytic formulation convenient for use in physical applications. The above-mentioned quasicontinuum models[27,28] satisfy these requirements, but a transition to quasicontinuum entails inevitably formidable technical difficulties when considering real nonuniform nanostructural systems. It appears therefore reasonable to continue the search for continuum models which would produce results consistent with experimental observations; results which would, for instance, permit one to estimate the displacements and strains near defect cores and compare them with real values that can be obtained from electron microscope images and computer models.

One of the possible ways to solve this problem lies in replacing the conventional Hooke's law governing the relations in linear theory of elasticity with its simple gradient modification[34]

$$\sigma=\lambda(\mathrm{tr}\,\varepsilon)I+2\mu\varepsilon-c\nabla^2[\lambda(\mathrm{tr}\,\varepsilon)I+2\mu\varepsilon], \tag{1}$$

where λ and μ are the conventional Lamé constants, σ and ε are the tensors of conventional elastic stresses and strains, I is the identity tensor, ∇^2 is the Laplacian, and $c>0$ is a gradient coefficient, which is zero for the conventional Hooke's law. Note that Eq. (1) is a particular case of an extremely cumbersome constitutive relation derived by Mindlin[35] who took into account in the elastic energy second gradients of the elastic-strain tensor. Application of the constitutive relation (1) (Refs. 34 and 36–38) and of similar relations[39,40] to crack problems eliminated the classical singularities from the elastic displacement and strain fields at crack tips. True, the elastic stress fields retained their form with the conventional singularities, but nevertheless this was not considered significant, because the elastic stress tensor cannot be rigorously defined at the atomic level.

The successful elimination of singularities from solutions for cracks stimulated the interest in applying Eq. (1) to an analysis of the elastic fields of dislocations[41] and disclinations.[42] It was found that in the case of dislocations elastic strains vanish at the dislocation line and reach maximum values in absolute magnitude of about 12% (screw dislocations) and 3–14% (edge dislocations) at a distance $\approx\sqrt{c}$ from it. Significantly, estimation of the gradient coefficient c for a lattice with a parameter a yielded $\sqrt{c}\approx a/4$.[34] An analysis of total displacement fields around single dislocations and dislocation dipoles showed that this gradient theory of elasticity leads in a natural way to two characteristic lengths, namely, $r_0\approx 5\sqrt{c}$, which may be considered as the dislocation core radius, and $d_0\approx 10\sqrt{c}$, which corresponds to the radius of strong elastic short-range interaction between dislocations. Then one can introduce two valid estimates for the case of the conventional lattice dislocation in a crystal, $r_0\approx 1.25\,a_0$ and $d_0\approx 2.5\,a_0$. Outside the dislocation core, gradient solutions transform rapidly to the classical ones. Note that the total displacement field of an edge dislocation looses in such a treatment the characteristic logarithmic singularity at the dislocation line. Moreover, the displacements calculated in this way agree well in order of magnitude with experimental observations and computer simulations of unsplit dislocations.[41]

Although the elastic stress fields remained the same as in classical elasticity, the elimination of singularities from the elastic strain fields resulted also in their disappearance from the expressions for the elastic dislocation energies.[41] Whereas when calculating the dislocation energy in terms of classical elasticity one had to introduce an elastic-field cutoff at the dislocation core and take the core energy separately into account, the solutions obtained within the gradient theory of elasticity offer a possibility of side-stepping this disadvantage to perform straightforward calculations, which yield for the elastic energy W per unit dislocation length

$$W=\mu b^2 A\left\{\ln\frac{R}{2\sqrt{c}}+\gamma-B\right\}, \tag{2}$$

where b is the Burgers dislocation vector, R is the outer dimension of a body, $\gamma=0.577\ldots$ is Euler's constant, and $A=1/(4\pi)$, $B=0$ for a screw dislocation, and $A=1/[4\pi\times(1-\nu)]$, $B=\pi A$ for an edge one.

We obtained earlier[42] gradient solutions for elastic strain fields generated by dipoles of straight disclinations of all three types, i.e., wedge and twist ones. It was shown that in the cases of both cracks and dislocations the solutions no longer contain the singularities characteristic of the classical theory of elasticity. Elastic strains take on zero or finite values at the disclination lines. These finite values depend strongly on the dipole arm d and vary monotonically (wedge disclinations) or nonmonotonically (twist disclinations) in short-range disclination-dipole interactions, where $d<10\sqrt{c}$. When disclinations annihilate ($d\to 0$), the elastic strains tend smoothly to zero. As in the case of dislocations, the gradient solution transforms to classical far away from the disclination lines, where $r\gg 10\sqrt{c}$. Interestingly, when the dipole arm d becomes much smaller than the characteristic dimension $\sqrt{c}$, the elastic fields of a wedge-disclination dipole transform to those of an edge dislocation,[41] similar to the corresponding case in classical theory of elasticity.[1–3]

Despite such obvious merits of using the constitutive relation (1) in a description of the elastic fields of

cracks,[34,36–40] dislocations,[41] and disclinations,[42] as elimination of singularities in the displacement and elastic strain fields and in obtaining reasonable values for these quantities at defect cores, this approach has a substantial shortcoming of a general nature, namely, the elastic stress fields retain their classical form and classical singularities at defect lines and crack tips. To eliminate this disadvantage, we employed[43] for the description of dislocations in place of Eq. (1) a more general constitutive gradient-theory relation

$$(1-c_1\nabla^2)\sigma=(1-c_2\nabla^2)[\lambda(\mathrm{tr}\,\varepsilon)I+2\mu\varepsilon], \tag{3}$$

now already with two different gradient coefficients c_1 and c_2, considered earlier by Ru and Aifantis.[44] The latter proposed[44] a fairly simple mathematical procedure, similar to the one employed in Ref. 36, for solution of Eq. (3) for a boundary problem using a well-known classical solution of the same boundary problem. Indeed, it can be readily verified[36,41,42] that for $c_1\equiv 0$ the right-hand side of Eq. (3) yields a classical solution for the stress field, which we shall denote by σ^0, and the solution for the displacement field is found from the inhomogeneous Helmholtz equation

$$(1-c_2\nabla^2)u=u^0, \tag{4}$$

where u^0 is the classical solution of the same boundary problem with stresses prescribed at the boundary. Equation (4) yields a similar equation

$$(1-c_2\nabla^2)\varepsilon=\varepsilon^0 \tag{5}$$

for determination of the ε elastic strain field in the gradient theory of elasticity through the classical solution ε^0. As follows from Eqs. (3) and (5), the gradient solution for the σ stress field in the $c\neq 0$ case can be derived directly from the equation

$$(1-c_1\nabla^2)\sigma=\sigma^0, \tag{6}$$

where σ^0 is the classical solution for the same boundary problem.

Thus in order to solve Eq. (3), one can solve separately Eqs. (5) and (6), whose right-hand sides are actually the classical solutions ε^0 and σ^0, subject to additional boundary conditions caused by the presence of gradient terms. In the case of dislocations such an additional boundary condition was the matching of the classical and gradient solutions at an infinite distance from the dislocation.[43] It should be pointed out that a similar approach was employed in a consideration of the screw dislocation and a mode-III crack aimed at finding asymptotic solutions at a dislocation line and a crack tip.[44] It was shown that the gradient solutions contain no longer singularities either in the strain or stress fields. Exact solutions of Eq. (3) were obtained for straight edge and screw dislocations.[43] Neither elastic strains, nor stresses or dislocation energies contained singularities at defect lines. The expression for the screw-dislocation elastic energy derived in this approach retains the form (2) but with c_1 substituted for c, and in the case of the edge dislocation one has to make the same replacement and set $B=-1/2$. It was shown also that elastic stresses reach the largest value of the order of $\mu/4-\mu/2$ at a distance $\approx a/4$ from the dislocation line.

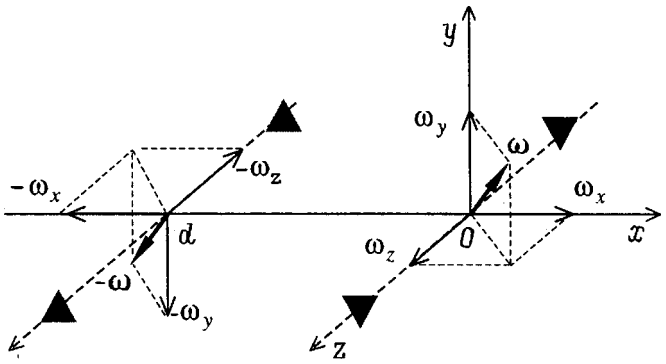

FIG. 1. Dipole of straight disclinations with Frank vectors $\pm\omega$.

In the present work we are presenting solutions of Eq. (3) derived for straight disclination dipoles.

2. Consider a disclination dipole made up of two parallel disclinations with Frank vectors $\pm\omega$ ($\omega=\omega_x e_x+\omega_y e_y+\omega_z e_z$). The projections ω_x and ω_y relate to the strengths of the twist components of these disclinations, and ω_z is the strength of their wedge component (Fig. 1). Let the disclinations lie in the $y=0$ plane along the z axis of the Cartesian frame and cross the x axis at the points $x=-d$ (negative disclination) and $x=0$ (positive disclination).

2.1. *Classical solution.* The classical solution for elastic strains, ε^0_{ij}, in units of $1/[4\pi(1-\nu)]$ can be written in the form[1]

$$\varepsilon^0_{xx}=-\omega_x z\left\{(1-2\nu)\left(\frac{x}{r_1^2}-\frac{x+d}{r_2^2}\right)-\frac{2xy^2}{r_1^4}+\frac{2(x+d)y^2}{r_2^4}\right\}$$
$$-\omega_y z\left\{(1-2\nu)\left(\frac{y}{r_1^2}-\frac{y}{r_2^2}\right)+\frac{2x^2y}{r_1^4}-\frac{2(x+d)^2y}{r_2^4}\right\}$$
$$+\omega_z\left\{(1-2\nu)\ln\frac{r_1}{r_2}+\frac{y^2}{r_1^2}-\frac{y^2}{r_2^2}\right\},$$

$$\varepsilon^0_{yy}=-\omega_x z\left\{(1-2\nu)\left(\frac{x}{r_1^2}-\frac{x+d}{r_2^2}\right)+\frac{2xy^2}{r_1^4}-\frac{2(x+d)y^2}{r_2^4}\right\}$$
$$-\omega_y z\left\{(1-2\nu)\left(\frac{y}{r_1^2}-\frac{y}{r_2^2}\right)-\frac{2x^2y}{r_1^4}+\frac{2(x+d)^2y}{r_2^4}\right\}$$
$$+\omega_z\left\{(1-2\nu)\ln\frac{r_1}{r_2}+\frac{x^2}{r_1^2}-\frac{(x+d)^2}{r_2^2}\right\},$$

$$\varepsilon^0_{zz}=0,$$

$$\varepsilon^0_{xy}=\omega_x z\left\{\frac{y}{r_1^2}-\frac{y}{r_2^2}-\frac{2x^2y}{r_1^4}+\frac{2(x+d)^2y}{r_2^4}\right\}$$
$$+\omega_y z\left\{\frac{x}{r_1^2}-\frac{x+d}{r_2^2}-\frac{2xy^2}{r_1^4}+\frac{2(x+d)y^2}{r_2^4}\right\}$$
$$-\omega_z\left\{\frac{xy}{r_1^2}-\frac{(x+d)y}{r_2^2}\right\},$$

$$\varepsilon^0_{xz}=-\omega_x\left\{(1-2\nu)\ln\frac{r_1}{r_2}+\frac{y^2}{r_1^2}-\frac{y^2}{r_2^2}\right\}+\omega_y\left\{\frac{xy}{r_1^2}-\frac{(x+d)y}{r_2^2}\right\},$$

$$\varepsilon^0_{yz}=\omega_x\left\{\frac{xy}{r_1^2}-\frac{(x+d)y}{r_2^2}\right\}-\omega_y\left\{(1-2\nu)\ln\frac{r_1}{r_2}+\frac{x^2}{r_1^2}-\frac{(x+d)^2}{r_2^2}\right\}, \tag{7}$$

where $r_1^2=x^2+y^2$ and $r_2^2=(x+d)^2+y^2$.

Then the classical solution for the elastic stresses σ^0_{ij} in units of $\mu/[2\pi(1-\nu)]$ can be cast as[1]

$$\sigma^0_{xx}=\varepsilon^0_{xx}(\nu=0),\quad \sigma^0_{yy}=\varepsilon^0_{yy}(\nu=0),$$

$$\sigma^0_{zz}=-\omega_x z\,2\nu\left\{\frac{x}{r_1^2}-\frac{x+d}{r_2^2}\right\}-\omega_y z\,2\nu\left\{\frac{y}{r_1^2}-\frac{y}{r_2^2}\right\}+\omega_z 2\nu\ln\frac{r_1}{r_2},$$

$$\sigma^0_{xy}=\varepsilon^0_{xy},\quad \sigma^0_{xz}=\varepsilon^0_{xz},\quad \sigma^0_{yz}=\varepsilon^0_{yz}. \tag{8}$$

2.2. *Gradient solution.* As already pointed out, solving Eq. (3) reduces to a separate solution of Eqs. (5) and (6), with the classical solutions ε^0 and σ^0 given, respectively, by Eqs. (7) and (8) to be substituted in their right-hand sides. The procedure of solving Eq. (5) with the right-hand side of Eq. (7) is described by us in considerable detail in Ref. 42, and Eq. (6) with the right-hand side of Eq. (8) is solved in much the same way. We are giving here only the final results.

The solutions of interest here can be presented as a superposition of the classical solutions and additional ''gradient'' terms

$$\varepsilon_{ij}=\varepsilon^0_{ij}+\varepsilon^{gr}_{ij},\quad \sigma_{ij}=\sigma^0_{ij}+\sigma^{gr}_{ij}, \tag{9}$$

where ε^{gr}_{ij} is given, in units of $1/[4\pi(1-\nu)]$, by the expressions

$$\varepsilon^{gr}_{xx}=\omega_x z\left\{4c_2x\frac{x^2-3y^2}{r_1^6}-4c_2(x+d)\frac{(x+d)^2-3y^2}{r_2^6}-\frac{2x}{r_1\sqrt{c_2}}\left(\nu-\frac{y^2}{r_1^2}\right)K_1\left(\frac{r_1}{\sqrt{c_2}}\right)+\frac{2(x+d)}{r_2\sqrt{c_2}}\left(\nu-\frac{y^2}{r_2^2}\right)K_1\left(\frac{r_2}{\sqrt{c_2}}\right)\right.$$
$$\left.-2x\frac{x^2-3y^2}{r_1^4}K_2\left(\frac{r_1}{\sqrt{c_2}}\right)+2(x+d)\frac{(x+d)^2-3y^2}{r_2^4}K_2\left(\frac{r_2}{\sqrt{c_2}}\right)\right\}+\omega_y z\left\{4c_2y\frac{3x^2-y^2}{r_1^6}-4c_2y\frac{3(x+d)^2-y^2}{r_2^6}\right.$$
$$+\frac{2y}{r_1\sqrt{c_2}}\left(1-\nu-\frac{x^2}{r_1^2}\right)K_1\left(\frac{r_1}{\sqrt{c_2}}\right)-\frac{2y}{r_2\sqrt{c_2}}\left(1-\nu-\frac{(x+d)^2}{r_2^2}\right)K_1\left(\frac{r_2}{\sqrt{c_2}}\right)-2y\frac{3x^2-y^2}{r_1^4}K_2\left(\frac{r_1}{\sqrt{c_2}}\right)$$
$$\left.+2y\frac{3(x+d)^2-y^2}{r_2^4}K_2\left(\frac{r_2}{\sqrt{c_2}}\right)\right\}+\omega_z\left\{2c_2\frac{x^2-y^2}{r_1^4}-2c_2\frac{(x+d)^2-y^2}{r_2^4}+(1-2\nu)K_0\left(\frac{r_1}{\sqrt{c_2}}\right)\right.$$
$$\left.-(1-2\nu)K_0\left(\frac{r_2}{\sqrt{c_2}}\right)-\frac{x^2-y^2}{r_1^2}K_2\left(\frac{r_1}{\sqrt{c_2}}\right)+\frac{(x+d)^2-y^2}{r_2^2}K_2\left(\frac{r_2}{\sqrt{c_2}}\right)\right\},$$

$$\varepsilon^{gr}_{yy}=\omega_x z\left\{-4c_2x\frac{x^2-3y^2}{r_1^6}+4c_2(x+d)\frac{(x+d)^2-3y^2}{r_2^6}+\frac{2x}{r_1\sqrt{c_2}}\left(1-\nu-\frac{y^2}{r_1^2}\right)K_1\left(\frac{r_1}{\sqrt{c_2}}\right)-\frac{2(x+d)}{r_2\sqrt{c_2}}\left(1-\nu-\frac{y^2}{r_2^2}\right)K_1\left(\frac{r_2}{\sqrt{c_2}}\right)\right.$$
$$\left.+2x\frac{x^2-3y^2}{r_1^4}K_2\left(\frac{r_1}{\sqrt{c_2}}\right)-2(x+d)\frac{(x+d)^2-3y^2}{r_2^4}K_2\left(\frac{r_2}{\sqrt{c_2}}\right)\right\}+\omega_y z\left\{-4c_2y\frac{3x^2-y^2}{r_1^6}+4c_2y\frac{3(x+d)^2-y^2}{r_2^6}\right.$$
$$-\frac{2y}{r_1\sqrt{c_2}}\left(\nu-\frac{x^2}{r_1^2}\right)K_1\left(\frac{r_1}{\sqrt{c_2}}\right)+\frac{2y}{r_2\sqrt{c_2}}\left(\nu-\frac{(x+d)^2}{r_2^2}\right)K_1\left(\frac{r_2}{\sqrt{c_2}}\right)+2y\frac{3x^2-y^2}{r_1^4}K_2\left(\frac{r_1}{\sqrt{c_2}}\right)-2y\frac{3(x+d)^2-y^2}{r_2^4}K_2\left(\frac{r_2}{\sqrt{c_2}}\right)\Bigg\}$$
$$+\omega_z\left\{-2c_2\frac{x^2-y^2}{r_1^4}+2c_2\frac{(x+d)^2-y^2}{r_2^4}+(1-2\nu)K_0\left(\frac{r_1}{\sqrt{c_2}}\right)-(1-2\nu)K_0\left(\frac{r_2}{\sqrt{c_2}}\right)+\frac{x^2-y^2}{r_1^2}K_2\left(\frac{r_1}{\sqrt{c_2}}\right)\right.$$
$$\left.-\frac{(x+d)^2-y^2}{r_2^2}K_2\left(\frac{r_2}{\sqrt{c_2}}\right)\right\},$$

$$\varepsilon_{zz}^{gr}=0,$$

$$\varepsilon_{xy}^{gr}=\omega_x z\left\{4c_2y\frac{3x^2-y^2}{r_1^6}-4c_2y\frac{3(x+d)^2-y^2}{r_2^6}-\frac{2x^2y}{r_1^3\sqrt{c_2}}K_1\left(\frac{r_1}{\sqrt{c_2}}\right)+\frac{2(x+d)^2y}{r_2^3\sqrt{c_2}}K_1\left(\frac{r_2}{\sqrt{c_2}}\right)-2y\frac{3x^2-y^2}{r_1^4}K_2\left(\frac{r_1}{\sqrt{c_2}}\right)\right.$$
$$\left.+2y\frac{3(x+d)^2-y^2}{r_2^4}K_2\left(\frac{r_2}{\sqrt{c_2}}\right)\right\}+\omega_y z\left\{-4c_2x\frac{x^2-3y^2}{r_1^6}+4c_2(x+d)\frac{(x+d)^2-3y^2}{r_2^6}-\frac{2xy^2}{r_1^3\sqrt{c_2}}K_1\left(\frac{r_1}{\sqrt{c_2}}\right)\right.$$
$$\left.+\frac{2(x+d)y^2}{r_2^3\sqrt{c_2}}K_1\left(\frac{r_2}{\sqrt{c_2}}\right)+2x\frac{x^2-3y^2}{r_1^4}K_2\left(\frac{r_1}{\sqrt{c_2}}\right)-2(x+d)\frac{(x+d)^2-3y^2}{r_2^4}K_2\left(\frac{r_2}{\sqrt{c_2}}\right)\right\}$$
$$+\omega_z\left\{4c_2y\frac{x}{r_1^4}-4c_2y\frac{x+d}{r_2^4}-\frac{2xy}{r_1^2}K_2\left(\frac{r_1}{\sqrt{c_2}}\right)+\frac{2(x+d)y}{r_2^2}K_2\left(\frac{r_2}{\sqrt{c_2}}\right)\right\},$$

$$\varepsilon_{xz}^{gr}=\omega_x\left\{-2c_2\frac{x^2-y^2}{r_1^4}+2c_2\frac{(x+d)^2-y^2}{r_2^4}\right.$$
$$-(1-2\nu)K_0\left(\frac{r_1}{\sqrt{c_2}}\right)+(1-2\nu)K_0\left(\frac{r_2}{\sqrt{c_2}}\right)$$
$$\left.+\frac{x^2-y^2}{r_1^2}K_2\left(\frac{r_1}{\sqrt{c_2}}\right)-\frac{(x+d)^2-y^2}{r_2^2}K_2\left(\frac{r_2}{\sqrt{c_2}}\right)\right\}$$
$$+\omega_y\left\{-4c_2y\frac{x}{r_1^4}+4c_2y\frac{x+d}{r_2^4}+\frac{2xy}{r_1^2}K_2\left(\frac{r_1}{\sqrt{c_2}}\right)\right.$$
$$\left.-\frac{2(x+d)y}{r_2^2}K_2\left(\frac{r_2}{\sqrt{c_2}}\right)\right\},$$

$$\varepsilon_{yz}^{gr}=\omega_x\left\{-4c_2y\frac{x}{r_1^4}+4c_2y\frac{x+d}{r_2^4}+\frac{2xy}{r_1^2}K_2\left(\frac{r_1}{\sqrt{c_2}}\right)\right.$$
$$\left.-\frac{2(x+d)y}{r_2^2}K_2\left(\frac{r_2}{\sqrt{c_2}}\right)\right\}+\omega_y\left\{2c_2\frac{x^2-y^2}{r_1^4}\right.$$
$$-2c_2\frac{(x+d)^2-y^2}{r_2^4}-(1-2\nu)K_0\left(\frac{r_1}{\sqrt{c_2}}\right)$$
$$+(1-2\nu)K_0\left(\frac{r_2}{\sqrt{c_2}}\right)-\frac{x^2-y^2}{r_1^2}K_2\left(\frac{r_1}{\sqrt{c_2}}\right)$$
$$\left.+\frac{(x+d)^2-y^2}{r_2^2}K_2\left(\frac{r_2}{\sqrt{c_2}}\right)\right\},\qquad(10)$$

and σ_{ij}^{gr}, in units of $\mu/[2\pi(1-\nu)]$, by the expressions

$$\sigma_{xx}^{gr}=\varepsilon_{xx}^{gr}(\nu=0,\ c_2\leftrightarrow c_1),\quad \sigma_{yy}^{gr}=\varepsilon_{yy}^{gr}(\nu=0,\ c_2\leftrightarrow c_1),$$

$$\sigma_{zz}^{gr}=\omega_x z\,2\nu\left\{\frac{x}{r_1\sqrt{c_1}}K_1\left(\frac{r_1}{\sqrt{c_2}}\right)-\frac{x+d}{r_2\sqrt{c_1}}K_1\left(\frac{r_2}{\sqrt{c_1}}\right)\right\}$$
$$+\omega_y z\,2\nu\left\{\frac{y}{r_1\sqrt{c_1}}K_1\left(\frac{r_1}{\sqrt{c_1}}\right)-\frac{y}{r_2\sqrt{c_1}}K_1\left(\frac{r_2}{\sqrt{c_1}}\right)\right\}$$
$$+\omega_z\,2\nu\left\{K_0\left(\frac{r_1}{\sqrt{c_1}}\right)-K_0\left(\frac{r_2}{\sqrt{c_1}}\right)\right\},$$

$$\sigma_{xy}^{gr}=\varepsilon_{xy}^{gr}(c_2\leftrightarrow c_1),\quad \sigma_{xz}^{gr}=\varepsilon_{xz}^{gr}(c_2\leftrightarrow c_1),$$

$$\sigma_{yz}^{gr}=\varepsilon_{yz}^{gr}(c_2\leftrightarrow c_1),\qquad(11)$$

where $K_n(r_k/\sqrt{c_l})$ is the nth-order modified Bessel function of the second kind (Macdonald's function), with $n=0,1,2$; $k,l=1,2$.

In the limiting case, where the gradient coefficients c_1 and c_2 vanish and the constitutive relation (3) reduces to the standard Hooke's law for an isotropic medium, the gradient terms ε_{ij}^{gr} and σ_{ij}^{gr} vanish too. Note that after the substitution of c for c_2 the strain tensor components (10) coincide fully with the solution[42] found using the constitutive relation (1).

The elastic strain and stress fields (9) thus derived do not contain any longer the classical singularities at disclination lines. Indeed, consider, for instance, the strains and stresses at the line of a positive disclination ($x=0, y=0$) (Fig. 1). Taking into account the asymptotic behavior

$$K_0\left(\frac{r_1}{\sqrt{c_l}}\right)\Big|_{r_1\to 0}\to-\gamma+\ln\frac{2\sqrt{c_l}}{r_1},\quad K_1\left(\frac{r_1}{\sqrt{c_l}}\right)\Big|_{r_1\to 0}\to\frac{\sqrt{c_l}}{r_1},$$

$$K_2\left(\frac{r_1}{\sqrt{c_l}}\right)\Big|_{r_1\to 0}\to\frac{2c_l}{r_1^2}-\frac{1}{2},$$

we obtain from (10) for $r_1\to 0$ the following expressions for the strains (in units of $1/[4\pi(1-\nu)]$)

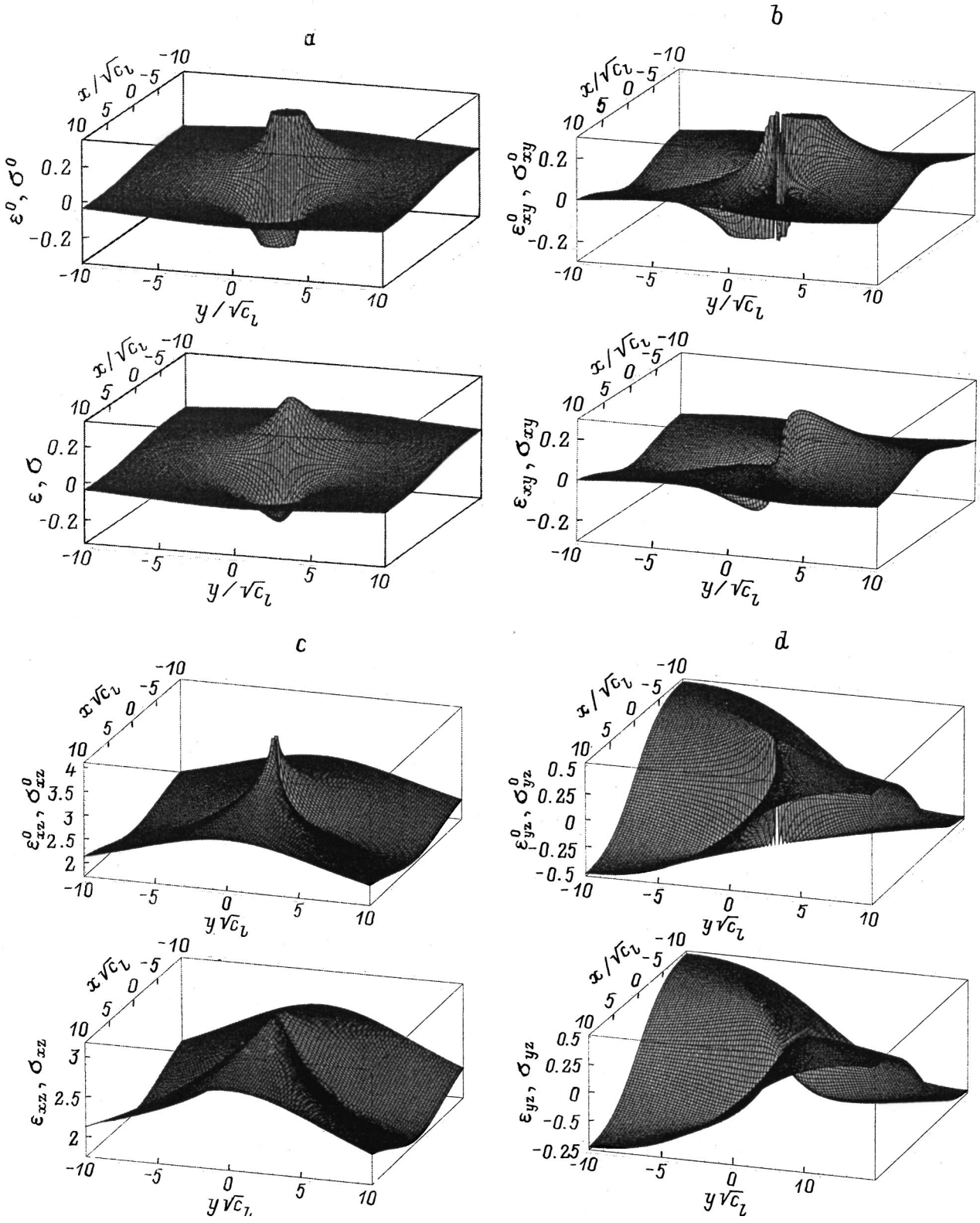

FIG. 2. Distribution of the tensor components of elastic strains (a) ε^0, ε; (b) ε^0_{xy}, ε_{xy}; (c) ε^0_{xz}, ε_{xz}; (d) ε^0_{yz}, ε_{yz}; and elastic stresses (a) σ^0, σ, (b) σ^0_{xy}, σ_{xy}; (c) σ^0_{xz}, σ_{xz}; (d) σ^0_{yz}, σ_{yz} near the line of a positive twist disclination with a Frank vector $\omega=(\omega_x,0,0)$ calculated for $d=10^4\sqrt{c_l}$, $l=1,2$. The strains are plotted in units of (a,b) $\omega_x z/[4\pi(1-\nu)\sqrt{c_2}]$ and (c,d) $\omega_x/[4\pi(1-\nu)]$, and the stresses, in units of (a) $\mu\omega_x z(1+\nu)/[6\pi(1-\nu)(1-2\nu)\sqrt{c_1}]$, (b) $\mu\omega_x z/[2\pi(1-\nu)\sqrt{c_1}]$, and (c,d) $\mu\omega_x/[2\pi(1-\nu)]$. The upper plots reproduce (a) the classical solutions ε^0_{ij}, σ^0_{ij}, and the lower ones, the gradient solutions ε_{ij}, σ_{ij}.

$$\varepsilon_{xx}|_{r_1\to 0}=\omega_x z\left\{\frac{1-2\nu}{d}-\frac{4c_2}{d^3}+\frac{2\nu}{\sqrt{c_2}}K_1\left(\frac{d}{\sqrt{c_2}}\right)+\frac{2}{d}K_2\left(\frac{d}{\sqrt{c_2}}\right)\right\}+\omega_z\left\{\frac{1}{2}-(1-2\nu)\times\left(\gamma+\ln\frac{d}{2\sqrt{c_2}}\right)-\frac{2c_2}{d^2}-(1-2\nu)K_0\left(\frac{d}{\sqrt{c_2}}\right)+K_2\left(\frac{d}{\sqrt{c_2}}\right)\right\},$$

$$\varepsilon_{yy}|_{r_1\to 0}=\omega_x z\left\{\frac{1-2\nu}{d}+\frac{4c_2}{d^3}-\frac{2(1-\nu)}{\sqrt{c_2}}K_1\left(\frac{d}{\sqrt{c_2}}\right)-\frac{2}{d}K_2\left(\frac{d}{\sqrt{c_2}}\right)\right\}+\omega_z\left\{-\frac{1}{2}-(1-2\nu)\times\left(\gamma+\ln\frac{d}{2\sqrt{c_2}}\right)+\frac{2c_2}{d^2}-(1-2\nu)K_0\left(\frac{d}{\sqrt{c_2}}\right)-K_2\left(\frac{d}{\sqrt{c_2}}\right)\right\},$$

$$\varepsilon_{zz}|_{r_1\to 0}=0,$$

$$\varepsilon_{xy}|_{r_1\to 0}=\omega_y z\left\{-\frac{1}{d}+\frac{4c_2}{d^3}-\frac{2}{d}K_2\left(\frac{d}{\sqrt{c_2}}\right)\right\},$$

$$\varepsilon_{xz}|_{r_1\to 0}=\omega_x\left\{-\frac{1}{2}+(1-2\nu)\left(\gamma+\ln\frac{d}{2\sqrt{c_2}}\right)+\frac{2c_2}{d^2}+(1-2\nu)K_0\left(\frac{d}{\sqrt{c_2}}\right)-K_2\left(\frac{d}{\sqrt{c_2}}\right)\right\},$$

$$\varepsilon_{yz}|_{r_1\to 0}=\omega_y\left\{\frac{1}{2}+(1-2\nu)\left(\gamma+\ln\frac{d}{2\sqrt{c_2}}\right)-\frac{2c_2}{d^2}+(1-2\nu)K_0\left(\frac{d}{\sqrt{c_2}}\right)+K_2\left(\frac{d}{\sqrt{c_2}}\right)\right\}, \qquad (12)$$

and from (11), for the stresses (in units of $\mu/[2\pi(1-\nu)]$)

$$\sigma_{xx}|_{r_1\to 0}=\varepsilon_{xx}(\nu=0,\ c_2\leftrightarrow c_1)|_{r_1\to 0},$$

$$\sigma_{yy}|_{r_1\to 0}=\varepsilon_{yy}(\nu=0,\ c_2\leftrightarrow c_1)|_{r_1\to 0},$$

$$\sigma_{zz}|_{r_1\to 0}=\omega_x z 2\nu\left\{\frac{1}{d}-\frac{1}{\sqrt{c_1}}K_1\left(\frac{d}{\sqrt{c_1}}\right)\right\}-\omega_z 2\nu\left\{\gamma+\ln\frac{d}{2\sqrt{c_1}}+K_0\left(\frac{d}{\sqrt{c_1}}\right)\right\},$$

$$\sigma_{xy}|_{r_1\to 0}=\varepsilon_{xy}(c_2\leftrightarrow c_1)|_{r_1\to 0},$$

$$\sigma_{xz}|_{r_1\to 0}=\varepsilon_{xz}(c_2\leftrightarrow c_1)|_{r_1\to 0},$$

$$\sigma_{yz}|_{r_1\to 0}=\varepsilon_{yz}(c_2\leftrightarrow c_1)|_{r_1\to 0}. \qquad (13)$$

Equations (12) and (13) are convenient to use in studies of the short-range elastic interaction between disclinations, which was impossible to do within the classical linear theory of elasticity. A comprehensive analysis of the variation of strain fields near a disclination as a function of the dipole arm d was made in Ref. 42. Because the solution for strains derived above using Eq. (3) coincides in form with that obtained in Ref. 42 for the relation (1), we shall restrict ourselves here only to the main conclusions drawn in the quoted paper. First, elastic strains take on at disclination lines zero or finite values, depending on which component and of what disclination (twist or edge) is being considered. Second, the finite values of strains depend strongly on the dipole arm d and vary monotonically (wedge) or nonmonotonically (twist disclinations) under short-range disclination dipole interaction, where $d<10\sqrt{c_l}$. When disclinations annihilate $(d\to 0)$, the elastic strains tend smoothly to zero. Finally, as in the classical theory of elasticity,[1–3] the elastic fields of the wedge disclination dipole transform to those of an edge dislocation[41] when the dipole arm d becomes much smaller than the characteristic dimension $\sqrt{c_2}$.

Because the coordinate-dependent parts of the strain and stress fields (9) are very similar (in the shear components they coincide for $c_1=c_2$, and in the normal ones, for $c_1=c_2$ and $\nu=0$), the same conclusions apply to the stress field as well.

When considering the long-range disclination interaction, where $d\gg\sqrt{c_l}$, the elastic fields at the disclination line are described by approximate expressions for the strains (in units of $1/[4\pi(1-\nu)]$)

$$\varepsilon_{xx}|_{r_1\to 0}\approx\omega_x(1-2\nu)\frac{z}{d}+\omega_z\left\{\frac{1}{2}-(1-2\nu)\left(\gamma+\ln\frac{d}{2\sqrt{c_2}}\right)\right\},$$

$$\varepsilon_{yy}|_{r_1\to 0}\approx\omega_x(1-2\nu)\frac{z}{d}-\omega_z\left\{\frac{1}{2}+(1-2\nu)\times\left(\gamma+\ln\frac{d}{2\sqrt{c_2}}\right)\right\},$$

$$\varepsilon_{zz}|_{r_1\to 0}=0,$$

$$\varepsilon_{xy}|_{r_1\to 0}\approx-\omega_y\frac{z}{d},$$

$$\varepsilon_{xz}|_{r_1\to 0}\approx-\omega_x\left\{\frac{1}{2}-(1-2\nu)\left(\gamma+\ln\frac{d}{2\sqrt{c_2}}\right)\right\},$$

$$\varepsilon_{yz}|_{r_1\to 0}\approx\omega_y\left\{\frac{1}{2}+(1-2\nu)\left(\gamma+\ln\frac{d}{2\sqrt{c_2}}\right)\right\}, \qquad (14)$$

and for the stresses (in units of $\mu/[2\pi(1-\nu)]$):

$$\sigma_{xx}|_{r_1\to 0}=\varepsilon_{xx}(\nu=0,\ c_2\leftrightarrow c_1)|_{r_1\to 0},$$

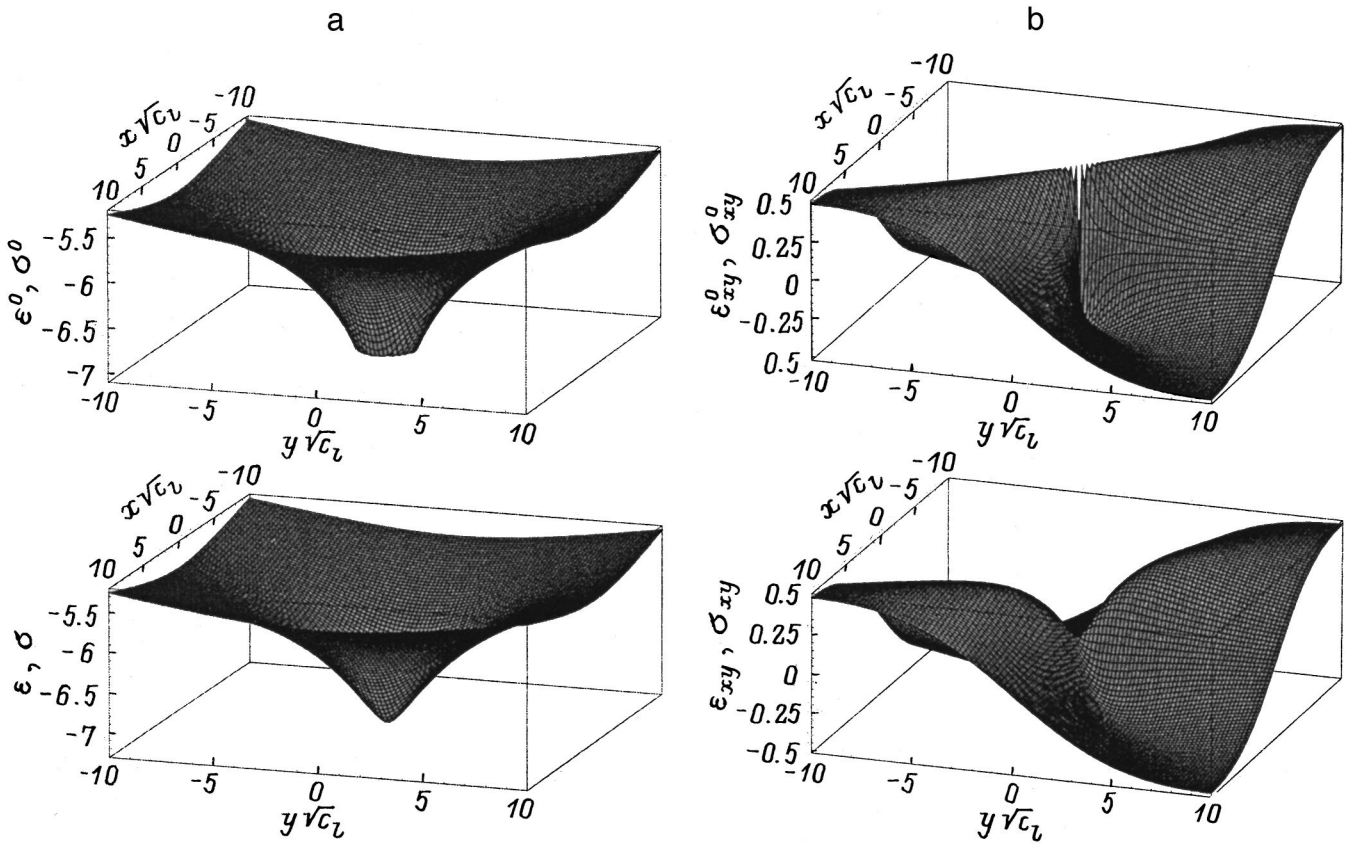

FIG. 3. Distribution of the tensor components of elastic strains (a) ε^0, ε; (b) ε^0_{xy}, ε_{xy}; and elastic stresses (a) σ^0, σ, (b) σ^0_{xy}, σ_{xy} near the line of a positive wedge disclination with a Frank vector $\omega=(0,0,\omega_z)$ calculated for $d=10^4\sqrt{c_l}$, $l=1,2$. The strains are plotted in units of $\omega_z/[4\pi(1-\nu)]$, and the stresses, in units of (a) $\mu\omega_z(1+\nu)/[6\pi(1-\nu)(1-2\nu)\sqrt{c_1}]$ and (b) $\mu\omega_z/[2\pi(1-\nu)]$. The upper plots reproduce (a) the classical solutions ε^0_{ij}, σ^0_{ij}, and the lower ones, the gradient solutions ε_{ij}, σ_{ij}.

$$\sigma_{yy}|_{r_1\to 0}=\varepsilon_{yy}(\nu=0,\ c_2\leftrightarrow c_1)|_{r_1\to 0},$$

$$\sigma_{zz}|_{r_1\to 0}\approx\omega_x 2\nu\frac{z}{d}-\omega_z 2\nu\left\{\gamma+\ln\frac{d}{2\sqrt{c_1}}\right\},$$

$$\sigma_{xy}|_{r_1\to 0}=\varepsilon_{xy}(c_2\leftrightarrow c_1)|_{r_1\to 0},$$

$$\sigma_{xz}|_{r_1\to 0}=\varepsilon_{xz}(c_2\leftrightarrow c_1)|_{r_1\to 0},$$

$$\sigma_{yz}|_{r_1\to 0}=\varepsilon_{yz}(c_2\leftrightarrow c_1)|_{r_1\to 0}. \qquad (15)$$

3. Figures 2 and 3 exemplify the distribution of different components of elastic strain and stress fields (9) near positive disclinations constructed for $d=10^4\sqrt{c_l}$. Figure 2 presents for a twist disclination with a Frank vector $\omega=(\omega_x,0,0)$ the elastic dilatation ε ($\varepsilon=\varepsilon_{nn}$) and the shear components of the strain field, as well as the hydrostatic component σ ($\sigma=\sigma_{nn}/3$) and the shear components of the stress field. One can obtain similar distributions of elastic fields for a twist disclination with a Frank vector $\omega=(0,\omega_y,0)$ by interchanging the x and y axes in Fig. 2 and the indices on the shear components of the strains and stresses, as well as in the units of their measurement. Figure 3 shows the components ε, ε_{xy} and σ, σ_{xy} for a wedge disclination with a Frank vector $\omega=(0,0,\omega_z)$. The upper plots in Figs. 2 and 3 are the classical solutions ε^0_{ij} and σ^0_{xy} exhibiting characteristic singularities at the disclination lines, and the lower ones, the gradient solutions ε_{ij} and σ_{ij}, which do not have such singularities. One readily sees that the gradient and classical solutions coincide at distances from the disclination lines in excess of $(5-10)\sqrt{c_l}$, i.e., at a few interatomic separations.

Thus treatment of disclinations in terms of a linear gradient theory of elasticity based on the constitutive relation (3) results in a complete elimination of singularities from the elastic strain and stress fields in the vicinity of disclination lines. The gradient solution (9) permits one to calculate strains and stresses directly near a dislocation line and to analyze short-range interactions in dense disclination ensembles. The results obtained can be of advantage when constructing physical models of the structure and mechanical behavior of metallic glasses and nanostructural materials, as well as of conventional metals and alloys at large plastic strains.

Support of the INTAS program and, partially, of the ''Physics of Solid-State Nanostructures'' program of the RF (Grant 97-3006) is gratefully acknowledged.

[1] R. de Wit, *Continuum Theory of Disclinations* (Mir, Moscow, 1977).
[2] V. A. Likhachev and R. Yu. Khaĭrov, *Introduction to the Theory of Disclinations* (LGU, Leningrad, 1975).
[3] V. I. Vladimirov and A. E. Romanov, *Disclinations in Crystals* (Nauka, Leningrad, 1986).

[4] V. V. Rybin, *Large Plastic Deformations and Fracture of Metals* (Metallurgiya, Moscow, 1986).
[5] V. G. Gryaznov and L. I. Trusov, Prog. Mater. Sci. **37**, 290 (1993).
[6] A. E. Romanov, Mater. Sci. Eng., A **164**, 58 (1993); Nanostruct. Mater. **6**, 125 (1995).
[7] M. Yu. Gutkin and I. A. Ovid'ko, Nanostruct. Mater. **2**, 631 (1993); Philos. Mag. A **70**, 561 (1994).
[8] M. Yu. Gutkin, K. N. Mikaelyan, and I. A. Ovid'ko, Nanostruct. Mater. **6**, 779 (1995); Phys. Status Solidi A **153**, 337 (1996).
[9] A. A. Nazarov, A. E. Romanov, and R. Z. Valiev, Scr. Mater. **34**, 729 (1996).
[10] I. V. Zolotukhin, *Physical Properties of Amorphous Metallic Materials* (Metallurgiya, Moscow, 1986).
[11] I. A. Ovid'ko, *Defects in Condensed Media: Glasses, Crystals, Quasicrystals, Liquid Crystals, Magnets, and Superfluid Liquids* (Znanie, Leningrad, 1991).
[12] M. Yu. Gutkin, I. A. Ovid'ko, and A. E. Romanov, Radiat. Eff. Defects Solids **129**, 239 (1994).
[13] V. A. Likhachev and V. E. Shudegov, *Principles of Organization of Amorphous Structures* (SPGU, St. Petersburg, 1999).
[14] J. S. Speck, A. C. Daykin, A. Seifert, A. E. Romanov, and W. Pompe, J. Appl. Phys. **78**, 1696 (1995).
[15] A. E. Romanov, W. Pompe, and J. S. Speck, J. Appl. Phys. **79**, 4037 (1996).
[16] J. P. Hirth and J. Lothe, *Theory of Dislocations* (McGraw-Hill, New York, 1968; Atomizdat, Moscow, 1972).
[17] G. P. Cherepanov, *Mechanics of Brittle Fracture* (Nauka, Moscow, 1974).
[18] N. F. Morozov, *Mathematical Aspects of the Theory of Cracks* (Nauka, Moscow, 1984).
[19] F. A. McClintock, Acta Metall. **8**, 127 (1960).
[20] M. Mişicu, Acad. Sci., Paris **10**, 35 (1965).
[21] C. Teodosiu, Acad. Sci., Paris **10**, 1461 (1965).
[22] Z. Knésl and F. Semela, Int. J. Eng. Sci. **10**, 83 (1972).
[23] J. P. Nowacki, Bull. Acad. Pol. Sci., Ser. Sci. Tech. **21**, 585 (1973); *ibid.* **22**, 379 (1974); Arch. Mech. **29**, 531 (1977).
[24] W. Nowacki, Arch. Mech. **26**, 3 (1974).
[25] S. Minagawa, Lett. Appl. Eng. Sci. **5**, 85 (1977); Int. J. Eng. Sci. **12**, 447 (1977).
[26] L. Lejček, Czech. J. Phys., Sect. B **33**, 447 (1983); *ibid.* **35**, 655 (1985); *ibid.* **35**, 726 (1985).
[27] I. A. Kunin, *Theory of Continua with a Microstructure. Nonlocal Theory of Elasticity* (Nauka, Moscow, 1975).
[28] A. D. Brailsford, Phys. Rev. **142**, 383 (1966).
[29] A. C. Eringen, J. Phys. D **10**, 671 (1977); J. Appl. Phys. **54**, 4703 (1983); in *The Mechanics of Dislocations*, edited by E. C. Aifantis and J. P. Hirth (ASM, Metals Park, 1985), p. 101.
[30] K. L. Pan, Radiat. Eff. Defects Solids **133**, 167 (1995).
[31] Y. Z. Povstenko, J. Phys. D **28**, 105 (1995); Int. J. Eng. Sci. **33**, 575 (1995); *Proceedings of Euromech-Mecamat, EMMC2: Mechanics of Materials with Intrinsic Length Scale*, edited by A. Bertram, S. Forest, and F. Sidoroff (Magdeburg, 1998), p. 299.
[32] A. C. Eringen, C. G. Speziale, and B. S. Kim, J. Mech. Phys. Solids **25**, 339 (1977).
[33] N. Ari and A. C. Eringen, Cryst. Lattice Defects Amorphous Mater. **10**, 33 (1983).
[34] B. S. Altan and E. C. Aifantis, Scr. Metall. Mater. **26**, 319 (1992); J. Mech. Behav. Mater. **8**, 231 (1997).
[35] R. D. Mindlin, Int. J. Solids Struct. **1**, 417 (1965).
[36] C. Q. Ru and E. C. Aifantis, Acta Mech. **101**, 59 (1993).
[37] E. C. Aifantis, J. Mech. Behav. Mater. **5**, 355 (1994).
[38] D. J. Unger and E. C. Aifantis, Int. J. Fract. **71**, R27 (1995).
[39] G. E. Exadaktylos and E. C. Aifantis, J. Mech. Behav. Mater. **7**, 93 (1996).
[40] I. Vardoulakis, G. Exadaktylos, and E. C. Aifantis, Int. J. Solids Struct. **33**, 4531 (1996).
[41] M. Yu. Gutkin and E. C. Aifantis, Scr. Mater. **35**, 1353 (1996); *ibid.* **36**, 129 (1997); Phys. Status Solidi A (in press).
[42] M. Yu. Gutkin and E. C. Aifantis, Phys. Status Solidi A (in press).
[43] M. Yu. Gutkin and E. C. Aifantis, Scripta Mater. (in press).
[44] C. Q. Ru and E. C. Aifantis, Preprint (1993), unpublished.

Translated by G. Skrebtsov

Kinetics of structural relaxation and regularities of plastic flow of metallic glasses

A. Yu. Vinogradov

Togliatti Polytechnic Institute, 445667 Togliatti, Russia;
University of Osaka, 855-8585 Osaka, Japan

K. Kitagawa

University of Kanazawa, 920-8667 Kanazawa, Japan

V. A. Khonik*)

Voronezh State Pedagogical University, 394043 Voronezh, Russia;
University of Kanazawa, 920-8667 Kanazawa, Japan

(Submitted March 19, 1999; accepted for publication May 25, 1999)
Fiz. Tverd. Tela (St. Petersburg) **41**, 2167–2173 (December 1999)

On the basis of a calculation of the structural relaxation rate and an experimental acoustical-emission determination of the temperature of the transition from localized to uniform flow it is argued that the type of plastic deformation of metallic glasses is uniquely determined by the kinetic structure of the relaxation. In the case of a kinetically hindered structural relaxation, which is characteristic for tests of initial samples at temperatures $T<380-420$ K, a localized dislocational deformation is realized. At higher temperatures, ''memory'' of the thermal prehistory of the samples is lost (aging at room temperature), the structural relaxation rate grows abruptly and plastic flow becomes uniform viscoplastic flow. © *1999 American Institute of Physics.* [S1063-7834(99)01212-5]

It is well known that depending on the conditions of the experiment, metallic glasses (MG's) exhibit either ''heterogeneous'' plastic flow, localized in slip bands, or ''homogeneous'' (uniform) flow, occurring without any traces of localization of deformation.[1,2] It was originally assumed[3,4] that the change-over of the type of flow takes place near T_g, in the range $100-150$ K, where T_g is the glass transition temperature. Another point of view has it that the type of flow is controlled by the homologous temperature T_h: for $T_h \leqslant (0.65-0.70)T_g$ the flow is localized whereas at higher temperatures homogeneous flow arises.[5,6] This point of view has gained wide acceptance despite the absence of direct experimental evidence.

Metallic glasses are strongly nonequilibrium structures, which results in the spontaneous occurrence of processes of structural relaxation. During the last decade experimental facts have accumulated indicating that the micromechanisms of homogeneous and localized flows are not controlled by the absolute or homologous temperature, but by kinetic structural relaxation during the test. Thus, a study of the return of the shape of weakly deformed metallic glasses has shown that different types of plastic deformation (heterogeneous or homogeneous) induce substantially different internal stress fields.[7] In connection with this, it was established that the type of deformation depends on the thermal prehistory of the sample, and not on the homologous temperature.[7,8] In turn, the thermal prehistory determines the rate of structural relaxation during the test. It has been suggested that under conditions of kinetically hindered structural relaxation plastic deformation is localized and is realized via a dislocationlike mechanism whereas under conditions of intense structural relaxation plastic flow is homogeneous and viscous.[9–11]

Metallic glasses are prepared by quenching at room temperature. As a result of storage until the start of testing, the structural relaxation rate is greatly reduced, so that subsequent deformation at this temperature occurs under conditions of kinetically hindered structural relaxation. The goal of the present paper is to calculate the viscosity and kinetics of structural relaxation for specific glasses and to show that as a result of heating above room temperature memory of the thermal prehistory (storage at room temperature) is lost near $T=400$ K, leading to an abrupt increase in the structural relaxation rate. In line with the above, plastic flow under such conditions (i.e., under conditions of intense structural relaxation) should become homogeneous. *In situ* acoustic emission measurements confirmed that the type of flow does indeed change over near $T=400$ K.

1. KINETICS OF STRUCTURAL RELAXATION UNDER CONDITIONS OF A COMPLICATED THERMAL PREHISTORY

Analysis of numerous measurements of the properties of metallic glasses resulting from structural relaxation indicate that the kinetics of relaxation can be described by a first-order differential equation (see, e.g., Refs. 11–13). Let $N(E,T,t)dE$ be the volume density of ''relaxation centers,'' activating at the temperature T at the time t with activation energy in the interval $[E,E+dE]$. Then the kinetics of the variation of N after storage at the temperature T_R for a time t_R is described by the simple equation

$$N_R=N_0(E)\exp(-\nu t_R\exp(-E/kT_R)), \tag{1}$$

where ν is the frequency of attempts to overcome the activation barrier, k is the Boltzmann constant, and $N_0(E)$ is the initial energy spectrum of the irreversible structural relaxation forming during preparation of the glass. We emphasize that Eq. (1) assumes that N decreases irreversibly with time.

Next let the metallic glass after annealing at the temperature T_R during the time t_R be heated at a constant rate $\dot{T}$ to a temperature $T=T_R+\dot{T}t$, where t is the heating time. Writing down the corresponding differential equation of relaxation and integrating it, we can calculate the spectral density of the relaxation centers at the termination of heating

$$N_T=N_R\exp\left(-\nu\int_0^t\exp\left(-\frac{E}{k(T_R+\dot{T}t')}\right)dt'\right)$$
$$=N_R\exp(-\nu I). \tag{2}$$

Here N_R is given by Eq. (1), and the integral I is equal to

$$I=\frac{k}{E\dot{T}}\left[T^2\exp\left(-\frac{E}{kT}\right)-T_R^2\exp\left(-\frac{E}{kT_R}\right)\right]. \tag{3}$$

Finally, let the metallic glass be annealed at the temperature T during the time τ after termination of the linear heating. Then the volume spectral density of relaxation centers is

$$N_\tau=N_T\exp\left(-\nu\tau\exp\left(-\frac{E}{kT}\right)\right), \tag{4}$$

where N_T is given by Eq. (2). The structural relaxation rate after such heat treatment can be found by integrating over the entire energy spectrum

$$S(T)=\int_0^{E_m}\left(-\frac{\partial N_\tau}{\partial\tau}\right)dE$$
$$=\nu\int_0^{E_m}N_0(E)\exp\left(-\nu t_R e^{-\frac{E}{kT_R}}\right.$$
$$\left.-\nu I(E,T)-\nu\tau e^{-\frac{E}{kT}}-\frac{E}{kT}\right)dE. \tag{5}$$

Here E_m is the upper bound of the energy spectrum of structural relaxation and $I(E,T)$ is given by Eq. (3).

In the presence of an external load, irreversible structural relaxation causes homogeneous macroscopic plastic deformation.[11,13,14] The kinetics of the accumulation of deformation under the given experimental conditions is governed by the energy spectrum $N_0(E)$, the volume Ω in which the elementary act of structural relaxation is realized, and the degree of orienting influence of the external load on this act, which is characterized by some parameter C (for details, see Refs. 11, 13, and 14). It turns out that by analysis of the experimental kinetics of homogeneous plastic deformation it is possible to reconstruct not the energy spectrum of structural relaxation of a the specific metallic glass under study but only the product $N_0\Omega C$ (Refs. 15 and 16). Correspondingly, it is not possible to calculate numerically the rate of structural relaxation by Eq. (5). It is possible, however, to calculate the relative structural relaxation rate of a hypothetical ''freshly quenched'' glass whose room-temperature storage time is equal to zero. In this case, the structural relaxation rate is equal to

$$R(T)=S(T)/S_0(T), \tag{6}$$

where $S_0(T)$ is given by Eq. (5) at $t_R=0$. In this case, in Eqs. (5) and (6) in place of $N_0(E)$ we can substitute the dependence $N_0(E)\Omega C=f(E)$, determined experimentally.

We will also calculate the temperature dependence of the Newtonian shear viscosity η of the glass after the above-indicated heat treatment. By definition, $\eta=\sigma/\dot{\varepsilon}$, where σ is the applied shear stress and $\dot{\varepsilon}$ is the induced rate of shear deformation. Within the framework of the ideas of Refs. 11, 13, and 14, the rate of shear deformation can be represented in the form

$$\dot{\varepsilon}(T)=\sigma\Omega C\int_0^{E_m}\left(-\frac{\partial N}{\partial\tau}\right)dE=\sigma\Omega CS(T). \tag{7}$$

Thus, the shear viscosity is equal to

$$\eta(T)=\left(\nu\int_0^{E_m}f(E)\exp\left(-\nu t_R e^{-\frac{E}{kT_R}}\right.\right.$$
$$\left.\left.-\nu I(E,T)-\nu\tau e^{-\frac{E}{kT}}-\frac{E}{kT}\right)dE\right)^{-1}. \tag{8}$$

Equations (6) and (8) were calculated numerically. In the calculations the heating rate was taken to be equal to 10 K/min, the frequency of attempts was taken to be equal to $10^{13}\,\mathrm{s}^{-1}$, and the function $f(E)$ for the metallic glass $Co_{57}Fe_5Ni_{10}Si_{11}B_{17}$ (used as the subject material in the subsequent acoustic-emission measurements, see below) was determined earlier by analysis of the kinetics of non-isothermal creep (see Refs. 8 and 16):

$$f(E)=3.07\times10^{-13}\exp(3.27\times E[\mathrm{eV}])[\mathrm{m^2eV^{-1}N^{-1}}].$$

Values of the temperature dependence of the relative rate of structural relaxation calculated according to Eq. (6) are plotted in Fig. 1 for typical room-temperature storage times t_R ($0.25\,\mathrm{year}\leqslant t_R\leqslant 2\,\mathrm{years}$) and various times τ ($5\,\mathrm{min}\leqslant\tau\leqslant 500\,\mathrm{min}$) of subsequent annealing at the temperature T. The upper bound of the spectrum E_m was chosen to be 2.5 eV, which corresponds roughly to the activation energy of crystallization. It can be seen that as a result of heating to 380–420 K the relative rate becomes equal to unity (i.e., it becomes equal to the structural relaxation rate of the ''freshly quenched'' glass). This implies that the glass loses its ''memory'' of its thermal prehistory. We emphasize that this result is essentially independent of both the times t_R and τ (see Fig. 1) and the choice of values of the frequency of attempts and the heating rate for heating the samples to the temperature T (we tested the values $10^{12}\leqslant\nu\leqslant10^{14}\,\mathrm{s}^{-1}$ and $0.1\leqslant\dot{T}\leqslant100\,\mathrm{K/min}$).

A similar conclusion follows by calculating the temperature dependence of the Newtonian viscosity according to (8). The corresponding results are plotted in Fig. 2 for the case $\tau=20\,\mathrm{min}$ and various times of aging at room temperature. It can be seen that as a result of heating to 70–80 K above room temperature, the viscosity decreases roughly fourfold.

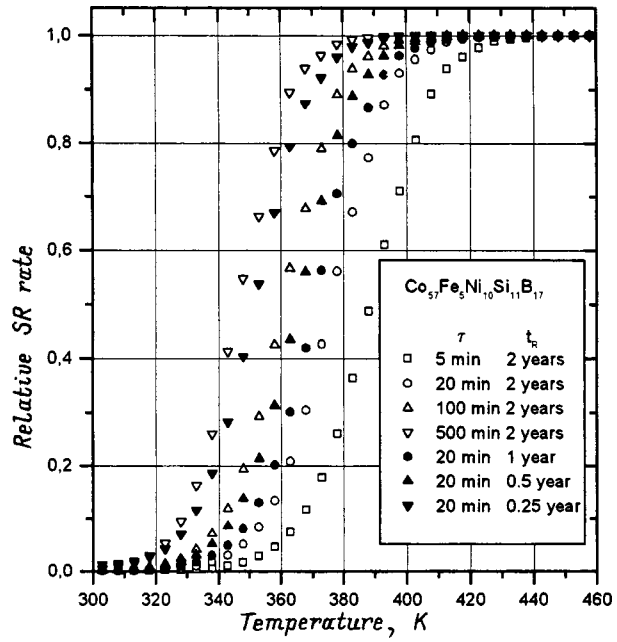

FIG. 1. Temperature dependence of the relative rate of structural relaxation of the metallic glass $Co_{57}Fe_5Ni_{10}Si_{11}B_{17}$ as a function of storage time at room temperature t_R and annealing time τ at the temperature T. The frequency of attempts was $\nu=10^{13}\,s^{-1}$.

Near $T\approx 380$ K the rate of falloff of the viscosity with temperature decreases by several-fold. Obviously, the abrupt falloff of the viscosity in the temperature interval $300<T<380$ K is connected with the presence of ''memory'' of extended storage at room temperature whereas for $T>380-400$ K this ''memory'' is absent. The increase in the annealing time τ raises the absolute values of the viscosity (in proportion to τ), but the nature of the dependence $\eta(T)$ does not change: ''memory'' of its thermal prehistory is lost near $T\approx 380-400$ K.

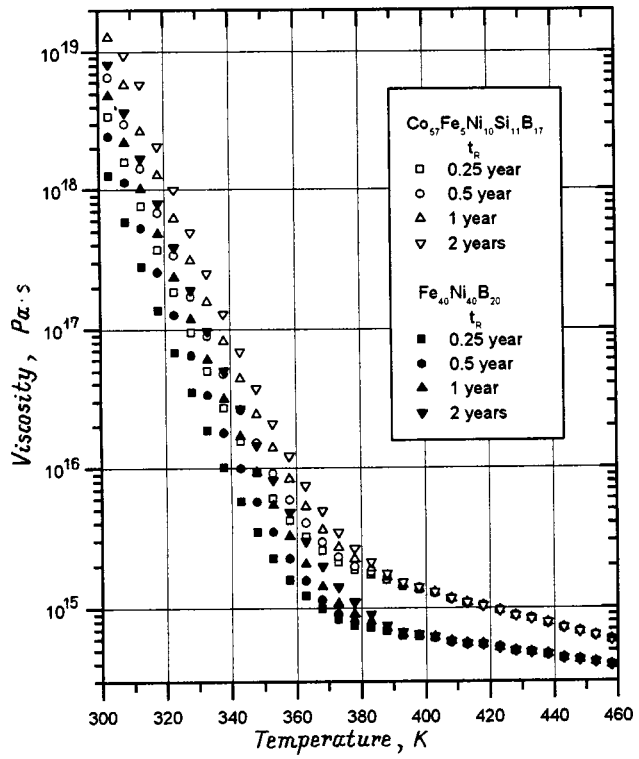

FIG. 2. Temperature dependence of the Newtonian viscosity of the metallic glasses $Co_{57}Fe_5Ni_{10}Si_{11}B_{17}$ and $Fe_{40}Ni_{40}B_{20}$ as functions of storage time at room temperature. The isothermal holding time $\tau=20$ min and frequency of attempts $\nu=10^{13}\,s^{-1}$.

We also stress that the temperature of loss of thermal ''memory'' is determined primarily by the prior heat treatment and the specifics of the relaxation law (4), and not by the activation-energy spectrum of the specific metallic glass in question. To test this assertion, we performed the above-described calculations for the metallic glass $Fe_{40}Ni_{40}B_{20}$, whose activation-energy spectrum was determined from the kinetics of its non-isothermal creep using the technique mentioned above.[16] In this case, for the relative relaxation rate we obtained results that coincided almost completely with those plotted in Fig. 1. The results of our calculation of the temperature dependence of the viscosity are shown in Fig. 2. As can be seen, the absolute values of the viscosity of the metallic glasses $Co_{57}Fe_5Ni_{10}Si_{11}B_{17}$ and $Fe_{40}Ni_{40}B_{20}$ differ by a small factor, but the nature of the dependence $\eta(T)$ remains unchanged, and ''memory'' of prior heat treatment disappears after heating to $T\approx 380-400$ K.

In the absence of ''memory'' of the thermal prehistory of the sample, the structural relaxation takes place with the maximum rate possible for the given 'freshly quenched'' glass at the given temperature. We think that in this case plastic flow of the metallic glass at the usual deformation rates ($\dot{\varepsilon}\propto 10^{-5}-10^{-6}\,s^{-1}$) is homogeneous viscoplastic flow and takes place via the mechanism of directed structural relaxation.[11,13,14] If this hypothesis is correct, then the transition from localized dislocationlike flow to homogeneous viscoplastic deformation with increase of the temperature should occur near $T=400$ K. Our *in situ* measurements of the acoustic emission (AE) in the metallic glass $Co_{57}Fe_5Ni_{10}Si_{11}B_{17}$ confirmed this hypothesis.

The idea of these experiments is quite simple. It is well known that a localized plastic deformation induces an intense, temporally discrete acoustic emission.[17–20] Acoustic-emission pulses in this case are distributed randomly in time and nonuniformly over the length of the sample[17–20] and are very similar to such pulses in crystalline materials deformed by a dislocation mechanism. According to the ideas of Refs. 11, 13, and 14, homogeneous flow is nothing but a structural relaxation oriented by an external stress. The structural relaxation itself in this case is represented as a set of irreversible uncorrelated atomic rearrangements in volumes on the order of the volume of the first coordination sphere. Thus it is reasonable to assume that such rearrangements do not lead to a mensurable acoustic emission since acoustic radiation presumes correlated motion of a large number of atoms.[21] In Ref. 8 it was shown that during deformation of the metallic glass $Co_{57}Fe_5Ni_{10}Si_{11}B_{17}$ acoustic emission indeed disappears already at the deformation temperature $T=473$ K. This temperature corresponds completely to homogeneous flow.[7] Thus, using acoustic emission as an indicator, it is possible to determine the change in the type of flow brought about by varying the temperature of the experiment.

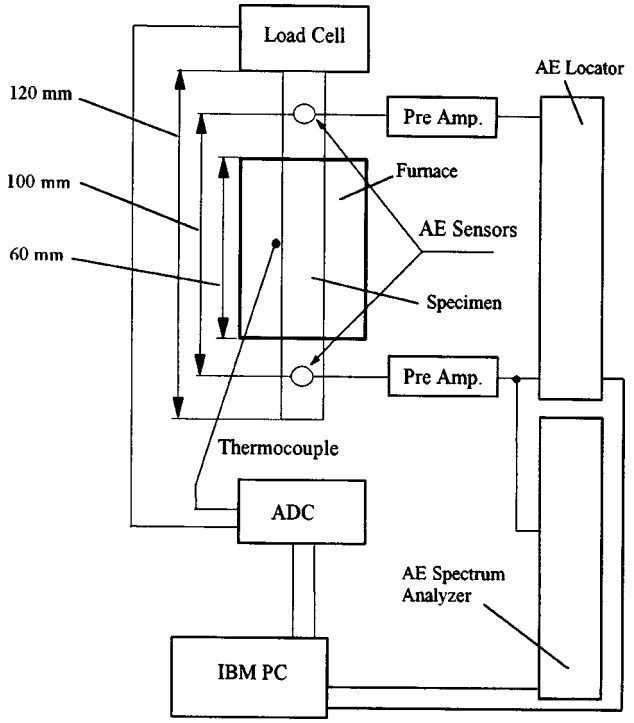

FIG. 3. Block diagram of the experimental setup for investigating acoustic emission of metallic glasses during plastic deformation.

2. EXPERIMENTAL

2.1. Samples and mechanical tests

In these experiments, we used the glass $Co_{57}Fe_5Ni_{10}Si_{11}B_{17}$, obtained by the standard method of single-mill spinning in the form of a tape of thickness 15 μm and width 14 mm. The tape was stored at room temperature for roughly two years up to the beginning of the experiments. A transmission electron microscope (JEOL 2000EX) and x-ray measurements were used to monitor the noncrystallinity of the structure before and after the mechanical tests at different temperatures. The tests were performed using two substantially different deformation rates $(7.0\pm0.4)\times10^{-5}\,s^{-1}$ and $(7.0\pm0.4)\times10^{-7}\,s^{-1}$. The working length of the samples was chosen to be equal to 120 mm.

The samples were heated to the required temperature at the rate 10 K/min. The preliminary annealing time before the startup of loading, τ, at the test temperatures $T=293$, 313, 333, 353, 373, 393, 413, 433, 453, and 473 K was 20 min. The temperature was stabilized with an accuracy of ±2 K in the center of the furnace near the central part of the sample of length 60 mm, as shown in Fig. 3. The upper and lower ends of the sample extended outside the furnace to safeguard the working conditions of the acoustic-emission sensors mounted to them. The test temperatures were substantially lower than the temperature of the onset of crystallization, which according to the data of the differential scanning calorimeter (Rigaku-Denki DSC-8230 calorimeter) was 830 K for a heating rate $\dot{T}=10$ K/min. X-ray diffraction measurements and transmission electron microscopy did not reveal any traces of crystallization after the tests.

2.2. Acoustic-emission measurements

The acoustic-emission signals were recorded with the aid of a controllable computer setup, schematically depicted in Fig. 3. Two AE900M miniature wideband acoustic-emission sensors (NF Electronic Instruments) with diameter 3 mm were mounted on the surface of the sample at a distance of 15 mm from the clamps of the testing machine. The acoustic-emission signal was amplified by 40 dB by a low-noise preamplifier, passed through a band-pass filter (20–1000 kHz) and finally amplified by an amplifier with regulated (up to 60 dB) gain. We used two measuring systems simultaneously. The first was a simple two-channel acoustic-emission locator to determine the coordinates of the acoustic-emission sources along the axis of the sample and to determine the activity of the acoustic emission (the number of acoustic-emission pulses per unit time) as a function of time, deformation, and loading. The second system was an acoustic-emission spectrum analyzer, which allowed us to determine the shape of the signal and its frequency spectrum with a discretization frequency of 4 MHz and 12-bit amplitude resolution. Details of the measurement and processing of the acoustic-emission signals are described in Ref. 22. The threshold stress was determined to be 2 dB higher than the peak noise level.

The acoustic-emission sources in the metallic glasses give specific signals with a characteristic spectrum.[17,23] Therefore, the use of a spectrum analyzer allowed us to distinguish the ''true'' acoustic-emission signals from the ''false'' signals coming from the testing machine and the electrical circuits. The acoustic-emission locator allowed us to separate out the pulses coming from the cold (outside the furnace) and heated parts of the sample.

3. EXPERIMENTAL RESULTS

Figure 4 shows characteristic distributions of the activity of the sources of the acoustic-emission signals along the longitudinal coordinate X of the samples deformed at four different temperatures with deformation rate $7\times10^{-5}\,s^{-1}$. The acoustic emission in the case of deformation at room temperature arises at a total deformation $\varepsilon\approx0.005$. With further growth of ε the acoustic-emission sources activate and disappear in various cross sections of the sample, which indicates a nonuniform spatiotemporal distribution of plastic deformation. The last spike of acoustic activity immediately precedes rupture of the sample at $\varepsilon=0.014$.

Increasing the deformation temperature to $T=373$ K has no qualitative effect on the spatiotemporal distribution of the acoustic-emission sources although the magnitude and number of acoustic-emission pulses grows substantially. For $T=393$ K the acoustic-emission pulses begin to appear at larger deformations, and their total number and amplitude decrease. Further increase of the deformation temperature causes a progressive falloff in the number and amplitude of pulses of the acoustic activity, so that for $T=453$ K acoustic emission does not arise (an isolated series of acoustic-emission pulses in Fig. 4 precedes rupture of the sample). A similar picture of the variation of the spatiotemporal distribution of acoustic emission with increase of the deformation

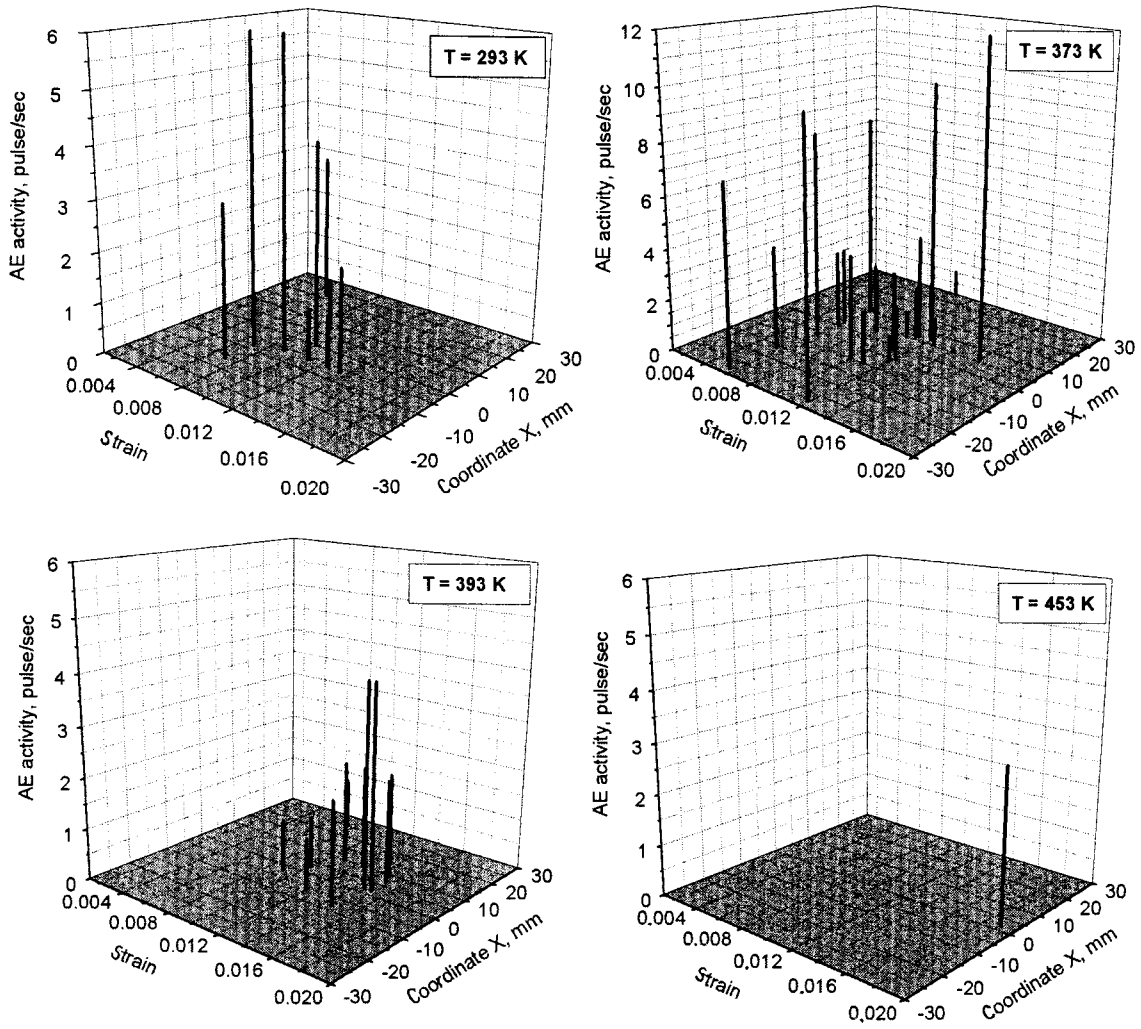

FIG. 4. Distribution of activity of acoustic emission sources along the length of samples deformed at the indicated temperatures with deformation rate $\dot{\varepsilon}=7\times10^{-5}\,\mathrm{s}^{-1}$.

temperature is observed for the deformation rate $\dot{\varepsilon}=7\times10^{-7}\,\mathrm{s}^{-1}$. The difference is that acoustic emission disappears at a lower temperature, $T=413\,\mathrm{K}$.

4. DISCUSSION

On the whole, acoustic emission of the investigated glass at room temperature is no different from the case of other metallic glasses.[17–20] The pulsed nature of acoustic emission is a clear indication of the intense plastic shear formation despite the macroscopic quasi-brittle behavior. Plastic flow at room temperature is realized under conditions of kinetically hindered structural relaxation.[10] We believe for precisely this reason that the glass is exhibiting ''crystalline'' (dislocationlike) plasticity. Room temperature plays a special role in the deformation behavior of metallic glasses. This role is defined by the extended annealing of the samples at this temperature before start of the experiment. Even moderate heating brings about a dramatic growth of the structural relaxation rate and an extraordinarily large drop in the viscosity, as can be seen from the results plotted in Figs. 1 and 2. The growth of the number of acoustic-emission pulses observed when the temperature is raised 60–70 K above room temperature (Fig. 4) reflects a decrease in the degree of localization of deformation as a consequence of growth of the structural relaxation rate and decrease of the viscosity of the structure. This decrease leads to a qualitative change in the type of plastic flow from dislocationlike under conditions of kinetically hindered structural relaxation to homogeneous deformation under conditions of intense structural relaxation. According to the acoustic-emission data, this transition begins at 353–373 K and ends near 413–453 K, depending on the deformation rate. At higher temperatures plastic flow is homogeneous, as follows from the following facts. First, disappearance of acoustic emission indicates the absence of dislocationlike plasticity. Note that currently available acoustic-emission apparatus make it possible to detect conservative motion of a small number (10–100) of dislocations in a crystal.[21] Second, measurements of the return of the shape are a definite indication that plastic flow of metallic glasses based on Ni, Fe, and Co for $T=473\,\mathrm{K}$ and $\dot{\varepsilon}=8\times10^{-5}\,\mathrm{s}^{-1}$ is homogeneous.[7] In addition, one should recall the results[24] of a direct determination of the surface density of slip bands of the metallic glass $Fe_{40}Ni_{40}P_{14}B_6$, which showed that it

grew up to $T \approx 350$ K and subsequently fell to zero near $T \approx 500$ K. These results are in direct agreement with the results of the present study.

Thus, a change in the type of flow can be interpreted in terms of a change in the kinetic relationship between the deformation rate and the rate of structural relaxation in the heated state. If the structural relaxation rate is such that the mechanism of ''directed structural relaxation''[11,13,14] cannot bring about plastic deformation with the rate prescribed by the testing machine, the flow is localized dislocationlike in nature. In the contrary case, plastic deformation is simply structural relaxation, oriented by an external stress.

Note that the temperatures at which the type of flow changes for the metallic glass under study are roughly half the glass transition temperature ($T_g \approx 813$ K for $\dot{T} = 10$ K/min). This being the case, the $\sigma - \varepsilon$ diagrams undergo practically no change as a result of the change in the type of flow. This is direct evidence that contrary to the conclusions of Refs. 4–6 and 25, neither the homologous temperature nor the character of the load–extension curves can be used to determine the type of plastic flow of metallic glasses.

Also note that the final stages of homogeneous flow immediately before rupture should be accompanied by localization of deformation and correspondingly by abrupt growth of the rate of local deformation. This can lead to a change in the ratio between the structural relaxation rate and the local deformation rate, thereby causing a local change in the type of flow and the occurrence of an acoustic emission. This is probably why rupture is preceded by an acoustic-emission spike.

The above allows us to predict the plastic behavior of metallic glasses under isothermal conditions if we take their thermal prehistory into account. We assume that under the given experimental conditions a metallic glass deforms uniformly, and we estimate the rate of isothermal structural relaxation in the simple approximation of a ''flat spectrum'' $[N_0 \neq f(E)]$. With good accuracy we may assume that at every moment of time elementary acts of structural relaxation are realized with activation energies belonging to the interval $[E_0, E_0 + dE_0]$, where E_0 is the so-called characteristic activation energy.[11,13,26] In this case the structural relaxation rate is proportional to $\partial E_0 / \partial t$, where t is the current time. Taking into account that under isothermal conditions for the case of a ''flat spectrum'' $E_0 = kT \ln \nu t$ (Ref. 26), we obtain that the structural relaxation rate decreases with time as t^{-1}. Therefore, sufficiently extended isothermal storage unavoidably leads to the impossibility of homogeneous deformation via directed structural relaxation and to a change in the type of deformation to dislocationlike deformation. Localized plastic flow, by virtue of the above, should take place at any temperature (below the glass transition temperature) if the preliminary annealing time is long enough.

To summarize, there are sufficient grounds to assume that the type of plastic flow of metallic glasses is unambiguously controlled by the kinetics of structural relaxation. Extended annealing of the samples at room temperature leads to a dramatic drop in the structural relaxation rate. This is why metallic glasses deform at this temperature via a dislocationlike mechanism. Even moderate heating above room temperature brings about an abrupt increase in the structural relaxation rate and a drop in the viscosity of the structure by several orders of magnitude, which in turn changes the type of deformation to homogeneous viscoplastic.

The authors express their gratitude to N. P. Kobelev (Institute of Solid-State Physics, Russian Academy of Sciences, Chernogolovka, Russia) for his assistance.

This work was carried out with the partial financial support of the Ministry of General and Professional Education of the Russian Federation within the scope of Grant No. 97-0-7.0-161 on Fundamental Natural Science.

*)E-mail: khonik@kanazawa-u.az.jp

[1] C. A. Pampillo, J. Mater. Sci. **10**, 1194 (1975).
[2] T. Masumoto and R. Maddin, Mater. Sci. Eng. **19**, 1 (1975).
[3] T. Masumoto, Sci. Rep. Res. Inst. Tohoku Univ. A **26**(4–5), 246 (1977).
[4] T. Masumoto and T. Murata, Mater. Sci. Eng. **25**, 71 (1976).
[5] F. Spaepen, Acta Metall. **25**, 407 (1977).
[6] A. S. Argon, Acta Metall. **27**, 47 (1979).
[7] A. T. Kosilov, V. A. Kuz'mishchev, and V. A. Khonik, Fiz. Tverd. Tela (Leningrad) **34**, 3682 (1992) [Sov. Phys. Solid State **34**, 1971 (1992)].
[8] A. Yu. Vinogradov, V. A. Mikhaĭlov, and V. A. Khonik, Fiz. Tverd. Tela (St. Petersburg) **39**, 885 (1997) [Phys. Solid State **39**, 787 (1997)].
[9] O. P. Bobrov, I. A. Safonov, and V. A. Khonik, Fiz. Tverd. Tela (St. Petersburg) **36**, 1703 (1994) [Phys. Solid State **36**, 931 (1994)].
[10] V. A. Khonik, J. Phys. IV **6**, C8-591 (1996).
[11] V. I. Belyavskiĭ, O. P. Bobrov, A. T. Kosilov, and V. A. Khonik, Fiz. Tverd. Tela (St. Petersburg) **38**, 30 (1996) [Phys. Solid State **38**, 16 (1996)].
[12] M. R. J. Gibbs, J. E. Evetts, and J. A. Leake, J. Mater. Sci. **18**(1), 278 (1983).
[13] O. P. Bobrov, A. T. Kosilov, V. A. Mikhaĭlov, and V. A. Khonik, Izv. Ross. Akad. Nauk, Ser. Fiz. **60**, 124 (1996).
[14] A. T. Kosilov, V. A. Mikhaĭlov, V. V. Sviridov, and V. A. Khonik, Fiz. Tverd. Tela (St. Petersburg) **39**, 2008 (1997) [Phys. Solid State **39**, 1796 (1997)].
[15] O. P. Bobrov and V. A. Khonik, Fiz. Met. Metalloved. **85**(6), 103 (1998).
[16] V. A. Mikhaĭlov and V. A. Khonik, Fiz. Tverd. Tela (St. Petersburg) **39**, 2186 (1997) [Phys. Solid State **39**, 1953 (1997)].
[17] A. Vinogradov and A. Leksovskii, Mater. Sci. Forum **210–213**, 2 (1996), p. 549.
[18] A. Yu. Vinogradov, A. M. Leksovskiĭ, and V. V. Smirnov, Pis'ma Zh. Tekh. Fiz. **12**, 641 (1986) [Sov. Tech. Phys. Lett. **12**, 265 (1986)].
[19] A. P. Braginskiĭ, A. Yu. Vinogradov, and A. M. Leksovskiĭ, Pis'ma Zh. Tekh. Fiz. **12**, 1085 (1986) [Sov. Tech. Phys. Lett. **12**, 459 (1986)].
[20] A. Yu. Vinogradov, A. M. Leksovskiĭ, and V. V. Yakovenko, Metallofizika (Kiev) **11**, 29 (1988).
[21] C. Scruby, H. Wadley, and J. E. Sinclair, Philos. Mag. **44**(2), 249 (1981).
[22] A. Vinogradov, M. Nadtochiy, S. Hashimoto, and S. Miura, Mater. Trans., JIM **36**(3), 426 (1995).
[23] A. Yu. Vinogradov and A. M. Leksovskii, *Progress in Acoustic Emission VIII*, edited by T. Kishi, Y. Mori, Y. Higo, and M. Enoki (The Japanese Society for Non-Destructive Inspection, 1996), p. 153.
[24] V. P. Alekhin, V. Pompe, K. Vettsig, V. Grabner, and I. Édel'man, Metalloved. Term. Obrab. Met. No. 5, 33 (1982).
[25] Y. Kawamura, T. Shibata, and A. Inoue, Sci. Rep. Res. Inst. Tohoku Univ. A **43**(2), 107 (1997).
[26] W. Primak, Phys. Rev. **100**, 1677 (1955).

Translated by Paul F. Schippnick

MAGNETISM AND FERROELECTRICITY

Thermal expansion of $Sc_xTi_{1-x}Fe_2$ itinerant magnets

N. I. Kourov and V. A. Kazantsev

Institute of Metal Physics, Ural Division, Russian Academy of Sciences, 620219 Ekaterinburg, Russia

A. G. Volkov

Ural State Technical University, 620002 Ekaterinburg, Russia

(Submitted March 18, 1999)
Fiz. Tverd. Tela (St. Petersburg) **41**, 2174–2178 (December 1999)

A study of the thermal expansion coefficient (TEC) of the $Sc_xTi_{1-x}Fe_2$ itinerant magnets has been made within the 5–1200 K range at the transition from the $TiFe_2$ antiferromagnet ($T_N=270$ K) to the $ScFe_2$ ferromagnet ($T_C=540$ K). A negative TEC magnetic contribution $\alpha_m(T)$ has been found, which is associated with the formation of spin-fluctuation-induced local magnetic moments in both the magnetically ordered and the paramagnetic state. The specific features in the $\alpha_m(T)$ dependence are shown to be due to the shape of the density-of-states function near the Fermi level. © *1999 American Institute of Physics.* [S1063-7834(99)01312-X]

The $Sc_xTi_{1-x}Fe_2$ intermetallic compounds form a continuous series of quasibinary solid solutions ordering in a $C14$-type ($P6_3/mmc$) hexagonal structure. The unit cell of this structure has three specific sites: $2a$ with $\bar{3}m$ symmetry, $6h$ with $mm2$ symmetry, and $4f$ with $3mm$ symmetry. The first two sites are occupied by iron atoms. In the $ScFe_2$ compound, these two iron species possess the same moments, which for $T<T_C=540$ K are ferromagnetically (F) ordered.[1,2] By contrast, in $TiFe_2$ iron atoms have local moments (μ_{Fe2}) only in the $6h$ site, whereas when in the $2a$ site, their moments $\mu_{Fe1}=0$. Note that the local μ_{Fe2} moments in $TiFe_2$ are ordered antiferromagnetically (A) for $T<T_N\approx 270$ K.

As follows from paramagnetic susceptibility measurements,[3] in $Sc_xTi_{1-x}Fe_2$ alloys the moment averaged per iron atom varies within the interval $\mu_{Fe}=(1.5-2.5)\mu_B$ throughout the whole concentration range x. At the same time the spontaneous moment per iron atom measured at $T=4.2$ K $\mu_{Fe}^S=(0.2-0.6)\mu_B$.[1–3] Such a difference between the local moments at the iron atom in the magnetically ordered and paramagnetic states permits one to consider the $Sc_xTi_{1-x}Fe_2$ alloys as itinerant magnets.

As the concentration x increases, the scandium nonmagnetic ions substitute in a random way for titanium atoms at the $4f$ sites. This process is accompanied by the concentration-driven $F-A$ phase transition. The transition from A- to F-ordered $Sc_xTi_{1-x}Fe_{1.97}$ alloy samples studied[1)] occurs primarily within the $0.05<x<0.15$ concentration region. Alloys with concentrations in the transitional region contain at temperatures below a certain T_f both the F- and A-types of long-range order, which quite frequently is considered as evidence for the existence of a canted magnetic structure. Mössbauer studies show[2] that it is in this concentration region that the moments of the iron atoms occupying the $2a$ sites change, and one observes[3] an anomalous behavior of the lattice parameters as functions of x. Within the transitional concentration region the alloys also exhibit a noticeable hysteresis in the temperature dependences of the lattice parameters near $T_f<[T_C,T_N]$, where the canted magnetic structure transfers to the F- or A-types of collinear moment ordering.

To reveal the specific features of the magnetic and structural states of the $Sc_xTi_{1-x}Fe_2$ itinerant magnets, it was of interest to study the thermal expansion coefficient α. Three aspects of the problem appeared to be of most significance, namely, investigation of the nature of variation of the TEC magnetic component, $\alpha_m(T)$, in the vicinity of the concentration-driven $F-A$ phase transition; determination of the behavior of the $\alpha_m(T)$ coefficient near the Curie and Néel temperatures, as well as for $T\leqslant T_f$ for alloys in the transitional concentration region; and establishing the role of spin fluctuations in the $\alpha(T)$ dependence in both the magnetically ordered and the paramagnetic state.

We studied $Sc_xTi_{1-x}Fe_2$ alloys ($x=0, 0.1, 0.4, 0.6$, and 1), which were prepared in an arc furnace filled with pure argon by the technique described in Refs. 1 and 2. The ingots ~ 30 g in weight were homogenized by remelting while turning them over several times. After that, these ingots were annealed in purified helium at $T\sim 1000\,^\circ$C for more than 72 h, followed by cooling down to room temperature during 24 h. X-ray diffraction measurements confirmed the alloys under study to have the $C14$ structure. The samples used to measure the $\alpha(T)$ coefficient were $6\times 6\times 15$ mm in size. The TEC was measured within the 5–300-K range on a capacitance dilatometer in the equilibrium mode to within not worse than 1.5×10^{-7} K^{-1}, and from 300 to 1200 K, on an ULVAC-RIKO dilatometer (Japan) in a dynamic mode at a rate of 5 K/min with an error of not over 5×10^{-7} K^{-1}. The results of the measurements of

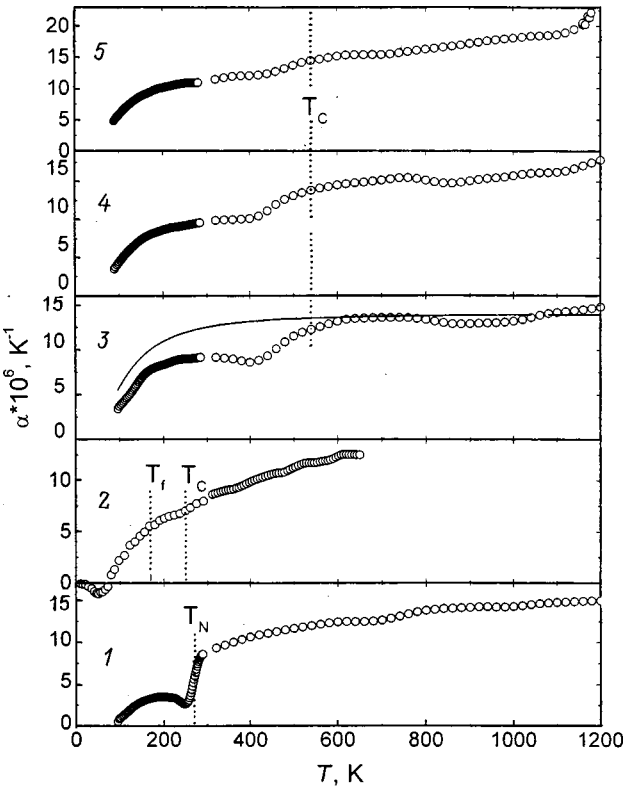

FIG. 1. Temperature dependences of the thermal expansion coefficient $\alpha(T)$ in the $Sc_xTi_{1-x}Fe_2$ itinerant magnets. x: (*1*) 0, (*2*) 0.1, (*3*) 0.4, (*4*) 0.6, (*5*) 1. The solid line reproduces the Debye-Grüneisen contribution to $\alpha(T)$ for one of the alloys studied. The dotted lines identify the magnetic-ordering points T_C, T_N, and T_f.

magnetic properties relevant to the discussion below can be found in Refs. 1–3.

Figure 1 shows the experimentally determined temperature dependences of TEC for the $Sc_xTi_{1-x}Fe_2$ alloys studied. Taking into account the phase diagram of the magnetic state of the itinerant magnets we are considering,[3] one sees anomalies in the $\alpha(T)$ curves for all F alloys with $x=0.4, 0.6$, and 1 near T_C, and for the A alloy with $x=0$ near T_N, which appear only natural to associate with the action of a negative magnetic contribution to TEC. Incidentally, the presence of a negative component in the $\alpha(T)$ coefficient for the $x=0.1$ alloy in the transitional concentration region results even in a sign reversal of the TEC measured in an experiment for $T<T_f<T_C$. Besides, as follows from Fig. 1, for $T>[T_C,T_N]$ the pattern of the $\alpha(T)$ dependences differs from that expected to occur in the paramagnetic temperature region practically for all the samples studied.

It is known[4] that in a general case the $\alpha(T)$ dependence for magnets can be represented as a sum of a magnetic $\alpha_m(T)$, a lattice $\alpha_L(T)$, and an electronic $\alpha_e(T)$ contribution

$$\alpha(T)=\alpha_m(T)+\alpha_L(T)+\alpha_e(T)\,. \tag{1}$$

Note that because of the electronic contribution $\alpha_e(T)$ being small compared with the other components, there appears no sense in taking it into account except in the low-temperature domain ($T\ll\Theta_D$, where Θ_D is the Debye temperature).

The magnetic component of the TEC is usually considered proportional to the squared spontaneous magnetization $M_S(T)$ (see, e.g., Refs. 4 and 5 and references therein). It has a negative sign and reaches its maximum value $\alpha_m(T_C,T_N)\approx -M_S^2(0)$, where $M_S(0)$ is the spontaneous magnetization at $T=0$ K, at the Curie or the Néel temperature. In the paramagnetic region, the $\alpha_m(T)$ contribution should be zero.

The temperature dependence of the nonmagnetic $\alpha_L(T)$ contribution is determined, as a rule, by the Debye–Grüneisen function for known values of the Debye temperature and of the $\alpha_L(T)$ term substantially above Θ_D.[4] As follows from measurements of the low-temperature heat capacity $C_p(T)$,[6] in the alloys under study $\Theta_D\sim 280$ K. Hence in the paramagnetic temperature region (in the case of the $Sc_xTi_{1-x}Fe_2$ alloys, for $T>[T_C,T_N$, and $\Theta_D]$) the $\alpha(T)$ dependence should saturate, as this indeed is seen from Fig. 1, where the solid line shows the contribution of the Debye–Grüneisen type for the $x=0.4$ sample.

The experimental data displayed in Fig. 1 show also that the temperature dependence of TEC does indeed initially weaken strongly above T_C and T_N and, accordingly, Θ_D in all the alloys studied. We did not, however, see $\alpha(T)$ to saturate up to the highest temperatures in the interval covered. This suggests that relation (1) takes into account not all of the mechanisms responsible for the temperature dependence of TEC of the $Sc_xTi_{1-x}Fe_2$ alloys. In particular, the variation of the thermal-expansion coefficient with temperature in itinerant magnets should be affected substantially by spin fluctuations.[5,7,8]

The $\alpha(T)$ dependence should contain,[8] besides the one-electron, lattice, and magnetic contributions, a spin-fluctuation term

$$\alpha_{sf}=\alpha_{sf}^{(1)}+\alpha_{sf}^{(2)}+\alpha_{sf}^{(3)}\,, \tag{2}$$

where

$$\alpha_{sf}^{(1)}=\frac{5}{3V\varkappa}U^2\tilde{g}(\mu)\frac{d\langle m^2\rangle}{dT}, \tag{2a}$$

$$\alpha_{sf}^{(2)}=-\frac{5}{V\varkappa}U\langle m^2\rangle\frac{dD^{-1}}{dT}, \tag{2b}$$

$$\alpha_{sf}^{(3)}=-\frac{20}{9V\varkappa}UD^{-1}\langle m^2\rangle/T, \tag{2c}$$

where U is the intratomic Coulomb repulsion parameter, V is the volume, $\varkappa$ is the isothermal compression constant, T is the temperature in energy units,

$$D^{-1}=\begin{cases}\gamma M_{q0}^2, & \text{for } T<[T_C,T_N]\\ -\dfrac{2}{3}n_{ef}/m-\dfrac{1}{3}U\tilde{g}(\mu)+X(q_0,0), & \text{for } T>[T_C,T_N]\end{cases} \tag{3}$$

is the denominator of the dynamic susceptibility at the wave vector equal to that of the magnetic superlattice q_0 $[D^{-1}=D^{-1}(q_0,0)]$, M_{q0} is the magnetization at the corresponding wave vector, $\langle m^2\rangle$ is the square of the spin-density fluctuation amplitude determined by the fluctuation-dissipation theorem [for $D^{-1}>a$, we have $\langle m^2\rangle=(bT)^2D(D^{-1}+a)^{-1}$,[8] otherwise, i.e., for $T\approx[T_C,T_N]$, $\langle m^2\rangle\sim(T/T_0)^{4/3}$, Ref. 5], a and b are parameters of the q and ω dependence of the Pauli susceptibility $\chi_0(q,\omega)$ (see, e.g., Ref. 5), μ is the chemical potential,

$$m^2=M_{q0}^2+\langle m^2\rangle,$$

$$X(q,\omega)=D^{-1}(q,\omega)-D^{-1}(0,0)\approx aq^2-ib\omega/q,$$

$$n_{ef}=\sum_{\alpha=\pm1}\alpha\int d\varepsilon g_0(\varepsilon)f(\varepsilon-\mu-\alpha Um)/2,$$

$$\tilde{g}(\mu)=2\prod_{\alpha=\pm1}g_0(\mu+\alpha Um)/\sum_{\alpha=\pm1}g_0(\mu+\alpha Um),$$

$$\gamma=[n_{ef}/m-U\tilde{g}(\mu)]/m^2$$

is the spin-wave stiffness constant.

As follows from Eqs. 2a–2b, for $D^{-1}\ll1$ (i.e., first of all, near the magnetic transition temperature) the $\alpha_{sf}^{(3)}$ term in (2) is negligible compared to the other two. Therefore we are going to deal in what follows with the $\alpha_{sf}^{(1)}$ and $\alpha_{sf}^{(2)}$ components of the spin-fluctuation contribution to the TEC.

The first term in Eq. (2) is positive and, for $T>[T_C,T_N]$, is linear in temperature $[d\langle m^2\rangle/dT\approx b^2TD(D^{-1}+a)^{-1}]$, as the conventional one-electron contribution. However this term is considerably in excess of α_e, because it is directly proportional to the susceptibility $(D=1+U\chi\approx U\chi)$. Thus the unusually strong temperature dependence of the TEC of $Sc_xTi_{1-x}Fe_2$ revealed for $T>[T_C,T_N$, and $\Theta_D]$ can be accounted for by the existence in the $\alpha(T)$ dependence studied by us of a spin-fluctuation contribution (in particular, of $\alpha_{sf}^{(1)}$).

According to the experimental data displayed in Fig. 1, in the vicinity of $T^*\geqslant700$ K the $\alpha(T)$ curves exhibit practically for all the alloys studied a dip, which cannot be interpreted if only the conventional electronic and anharmonic components are taken into account.[4] It is in this temperature region that one found[3,9] features in the temperature dependences of the magnetic susceptibility $\chi(T)$ and electrical resistivity $\rho(T)$, which can be connected with the temperature-induced creation of localized magnetic moments (LMM) in itinerant magnets. This correlation finds explanation within the approach developed in Refs. 7 and 8. Because the $\alpha_{sf}^{(2)}$ term is proportional to the derivative of the inverse susceptibility with respect to temperature, the break in the $\chi^{-1}(T)$ dependence (observed to occur with decreasing slope) should give rise to the appearance of a dip in the $\alpha(T)$ polytherm (at the same temperature).

Thus it appears only natural to assign the deviation from the TEC temperature dependence of the Debye–Grüneisen type found in the $Sc_xTi_{1-x}Fe_2$ alloys practically throughout the temperature range studied not so much to the conventional magnetic as to the above-mentioned spin-fluctuation contributions.

Figure 2 plots the total magnetic-fluctuation contribution to the TEC of the $Sc_xTi_{1-x}Fe_2$ itinerant magnets derived from $\alpha(T)$ measurements and calculations of $\alpha_L(T)$ from the Debye–Grüneisen function for the values of Θ_D found in Ref. 6, as well as from our TEC data obtained at $T\sim1000$ K ($T\gg[T_C,T_N$, and $\Theta_D]$).[2)] It is assumed here that within the temperature range studied the one-electron contribution $\alpha_e(T)$ is negligible compared to the lattice one, $\alpha_L(T)$, and to the magnetic-fluctuation term $\alpha_{m,sf}(T)=\alpha_m(T)+\alpha_{sf}(T)$. One readily sees that the $\alpha_{m,sf}(T)$ component derived from experimental data by the above method has a negative sign and a strong temperature dependence practically throughout the temperature range studied by us (below 1000 K).

Besides the feature in the paramagnetic temperature region considered above, the $\alpha_{m,sf}(T)$ curves exhibit a second anomaly as well, namely, near the magnetic disordering temperature. In the case of $TiFe_2$, the latter has a clearly pronounced λ pattern. However as the Sc content increases and one crosses over to F alloys, it washes out and decreases in depth. It should also be pointed out that, as follows from heat capacity measurements for $TiFe_2$, the $C_p(T)$ curve exhibits at the Néel temperature only an insignificant jump.[6]

This behavior of TEC near the Curie and Néel temperatures can be associated with the concentration and temperature dependences of the $\alpha_{sf}^{(2)}$ term in the spin-fluctuation contribution, because, by Eqs. (2b) and (3) (see also Refs. 7 and 8), in the magnetically ordered region

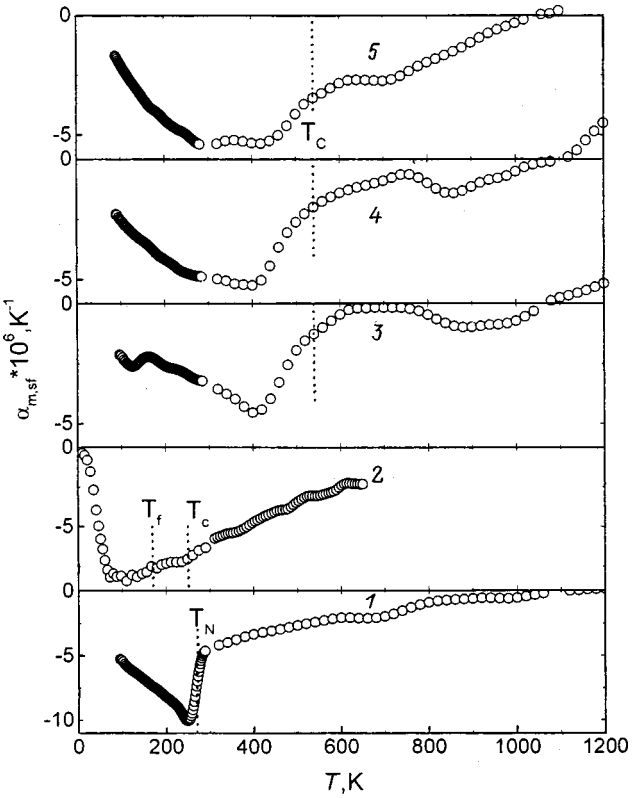

FIG. 2. Temperature dependences of the TEC magnetic-fluctuation component $\alpha_{m,sf}(T)$ in the $Sc_xTi_{1-x}Fe_2$ itinerant magnets. The curves are numbered as in Fig. 1. The dotted lines identify the magnetic-ordering points T_C, T_N, and T_f.

$$\alpha_{sf}^{(2)} = -\frac{5}{3V\varkappa}\gamma U\langle m^2\rangle dM_{q0}^2/dT$$

and reveals a λ-type anomaly. However the sign of this TEC component is determined by the fine structure of the density-of-states function. In the case of $TiFe_2$, the Fermi energy is located near a local minimum in $g_0(\varepsilon)$,[11] and $Um\tilde{g}(\mu) > n_{ef}$, and therefore the spin stiffness constant γ is negative.[3)] As a result, the λ anomalies in $\alpha_m(T)$ and $\alpha_{sf}^{(2)}$ have the same negative sign (because $dM_{q0}^2/dT<0$) and, when added, amplify one another. At the same time for $ScFe_2$, whose Fermi energy lies near the top of a local maximum of $g_0(\varepsilon)$,[12] $\gamma>0$. As a consequence of the λ feature, $\alpha_{sf}^{(2)}(T)>0$ while $\alpha_m(T)<0$, i.e. they have opposite signs and, when added in $\alpha_{m,sf}(T)$, weaken one another. This brings about a washout and decrease in depth of the minimum of $\alpha_{m,sf}(T)$ near the magnetic ordering temperature with increasing Sc concentration. At the same time the positive sign of the spin stiffness constant indicates the relative smallness of $\tilde{g}(\mu)$ and, hence, the comparatively small magnitude of the $\alpha_{sf}^{(1)}(T)$ contribution. Therefore the sum $\alpha_m(T)+\alpha_{sf}^{(2)}(T)$ remains noticeable in magnitude compared to the $\alpha_{sf}^{(1)}(T)$ term, despite the trend the two above terms exhibit to canceling one another.

We have also to point out other features of the thermal properties associated with the spin-fluctuation component. First of all, note the absence in the heat capacity of the contributions corresponding to the $\alpha_m(T)$, $\alpha_{sf}^{(1)}(T)$, and $\alpha_{sf}^{(3)}(T)$ terms in the TEC.[13] In their place, the $C_p(T)$ relation contains, besides a term similar to $\alpha_{sf}^{(2)}(T)$, a paramagnon component, which is positive throughout the temperature range studied and increases with T.[13] It should be borne in mind that the paramagnon component of $C_p(T)$ depends only weakly on the position of the chemical potential and the density of states at $\varepsilon=\mu$. As a result, the paramagnon contribution to the heat capacity should be practically the same for all Sc concentrations. Taking this into account, and that the paramagnon component is proportional to the log susceptibility, it should be expected that the contribution to the heat capacity similar to $\alpha_{sf}^{(2)}$ is small and lies within experimental accuracy. Therefore the magnetic-fluctuation components of $C_p(T)$ and $\alpha_{m,sf}(T)$ behave differently. In particular, the jump in the $C_p(T)$ and $\alpha_{m,sf}(T)$ relations observed at magnetic ordering in weakly itinerant magnets may differ by a few times, exactly what we have observed in the $Sc_xTi_{1-x}Fe_2$ alloys.

We also stress that the $\alpha_{sf}^{(3)}(T)$ component is negative throughout the temperature range studied. Although this term vanishes at the magnetic transition, it becomes noticeable both to the right and to the left of it. This gives rise to an additional distortion of the λ anomaly. In view of the small depth of the λ anomaly, taking into account the $\alpha_{sf}^{(3)}(T)$ term results in a shift of the minimum of $\alpha_{m,sf}(T)$ to the left of T_C or T_N along the temperature axis, as well as makes possible for $\alpha_{m,sf}(T)$ to become negative in the paramagnetic temperature region.

Another reason for $\alpha_{m,sf}(T)$ to become negative for $T>T_C$ or T_N may be the saturation of the local magnetic moments, which is observed to occur with increasing temperature. Because in the vicinity of and above the LMM saturation temperature ($\tilde{g}=0$) the spin stiffness coefficient should be positive[5] (at the same time in the paramagnetic region $dD^{-1}/dT \approx \gamma d\langle m^2\rangle/dT$, and the derivative $d\langle m^2\rangle/dT$ is always positive), we have for all alloys for $T>[T_C, T_N]$, near or above the LMM saturation temperature, $\alpha_{sf}^{(2)}<0$. The latter inequality, together with $\alpha_{sf}^{(3)}(T)$ being negative for all T, and with the vanishing of $\alpha_{sf}^{(1)}(T)$ at LMM saturation, accounts for the magnetic-fluctuation contribution remaining negative up to the highest temperatures covered. Hence one may conclude that the $\alpha_{m,sf}(T)$ relations established experimentally for the $Sc_xTi_{1-x}Fe_2$ alloys with $x\neq 0.1$ (i.e. the alloys beyond the transitional concentration region) are in accord with the predictions of the spin-density fluctuation theory.[5,7,8,13]

Of particular interest are TEC studies made in a magnetically ordered state of the $x=0.1$ alloy in the transitional concentration region, in which (according to the phase diagram of magnetic state[3]) a transition to a canted magnetic structure takes place at $T<T_f\sim 170$ K. As follows from the thermal expansion studies of the $x=0.1$ alloy displayed in Figs. 1 and 2, as well as from its magnetic properties,[3] the magnetic moment and the $\alpha_{m,sf}(T)$ coefficient of this sample undergo a considerable variation throughout the temperature region studied.

A comparison of these data with measurements[2] of the magnetization $M(T)$ and the phase diagram[3] of the magnetic state of the alloy system under study, made with due account of the itinerant nature of magnetism permits a conclusion that the LMMs of the $x=0.1$ alloy undergo an anomalously strong variation in the $T\leqslant T_f$ region. It is in this temperature region that one observes a minimum in the $\alpha_{m,sf}(T)$ curve. Recalling Eq. (2), we suggest that the low-temperature anomaly in $\alpha_{m,sf}(T)$ found in the $x=0.1$ alloy in the transitional concentration region can also be associated with LMM generation, which is due, however, not only to thermal but to concentration-driven spin-density fluctuations as well. A theoretical approach which would permit description of large concentration-driven spin density fluctuations is presently lacking. Therefore a comprehensive analysis of the $\alpha_{m,sf}(T)$ features at $x=0.1$ cannot be done within the spin-fluctuation approach.

At the same time a low-temperature anomaly (for $T<\Theta_D$) in $\alpha(T)$ of a similar kind, which results in a sign reversal of the TEC, is known to occur in other nonmagnetic materials as well (see, e.g., Ref. 4), where it is associated with specific features of the phonon spectrum. In the $Sc_{0.1}Ti_{0.9}Fe_{1.97}$ alloy studied by us one may expect a substantial deviation of the phonon spectrum from the Debye shape. This is evidenced, in particular, by the anomalous lattice-parameter variation observed[1,2] to occur for $T\leqslant T_f$ in alloys in the transitional concentration region. By Refs. 1 and 2, these alloys are structurally and magnetically unstable. This assumes, in its turn, a softening of the phonon spectrum, i.e., the appearance of dips in the Debye-type density-of-states curve. In these conditions, the $\alpha(T)$ curve obtained experimentally for the $x=0.1$ alloy can apparently be described if

one knows exactly the phonon spectrum, or using model approximations, for instance, a two-well atomic potential for atomic interaction in a solid. In the latter case the TEC can be approximated by a sum of two terms, namely, of the conventional Debye and the Schottky-model contribution.

Thus our studies of thermal expansion of the $Sc_xTi_{1-x}Fe_2$ itinerant magnets show that irrespective of their magnetic state in a $C14$-type lattice, the TEC is dominated by the contribution associated with spin-fluctuation-induced LMM effects. The negative $\alpha_{m,sf}(T)$ component, as well as the LMMs, are observed to undergo the strongest variation near the T_C, T_N, T_f, and T^* characteristic temperatures. A more accurate theoretical description of the magnetic contribution to the temperature dependences of TEC, χ, and M originating from spin-density fluctuation effects in both the magnetically ordered and paramagnetic states of the $Sc_xTi_{1-x}Fe_2$ itinerant magnets would obviously require precise data on their electronic and phonon spectra. The results of electronic band-structure calculations made for the limiting F ($ScFe_2$) and A ($TiFe_2$) alloys can be found in Refs. 11 and 12. The phonon spectrum of the $Sc_xTi_{1-x}Fe_2$ alloys has not yet been studied appropriately.

The authors express their gratitude to S. M. Podgornykh for TEC measurements on the $Sc_{0.1}Ti_{0.9}Fe_{1.97}$ alloy in the low-temperature region ($T<100$ K).

Partial support of the ''Integration'' project (Grant No. 88) is gratefully acknowledged.

[1)] A deviation from the stoichiometric $Sc_xTi_{1-x}Fe_2$ composition is necessary for the alloys to order in the $C14$ hexagonal structure, otherwise the alloys of the system under study order preferentially in a $C15$-type cubic structure (see, e.g., Refs. 1–3 and references therein).

[2)] 1000 K was chosen as the limiting temperature, because, according to the phase diagram of the Sc–Fe system[10] and studies[3,9] of the magnetic and electrical properties, at higher temperatures the $Sc_xTi_{1-x}Fe_2$ alloys undergo a structural transformation. As seen from Fig. 1, the transition to a new structural state at $T>1000$ K results in a strong increase of the TEC.

[3)] Note that for $Um \ll \mu$ we have $\gamma \approx [g'(\mu)]^2/g(\mu) - g''(\mu)/3$.

[1] Y. Nishihara and Y. Yamaguchi, J. Phys. Soc. Jpn. **54**, 1122 (1985).
[2] Y. Nishihara and Y. Yamaguchi, J. Phys. Soc. Jpn. **55**, 920 (1986).
[3] N. I. Kourov, I. I. Piratinskaya, and Yu. N. Tsiovkin, Fiz. Met. Metalloved. **78**, 69 (1994).
[4] S. I. Novikova, *Thermal Expansion of Solids* (Nauka, Moscow, 1974).
[5] T. Moriya, *Spin Fluctuations in Itinerant Electron Magnetism* (Springer, Berlin, 1988; Mir, Moscow, 1988).
[6] N. I. Kourov, Fiz. Met. Metalloved. **79**, 30 (1995).
[7] A. G. Volkov, S. V. Kortov, and A. A. Povzner, Fiz. Nizk. Temp. **22**, 1144 (1996) [Low Temp. Phys. **22**, 875 (1996)].
[8] P. V. Gel'd, A. A. Povzner, and A. G. Volkov, Dok. Akad. Nauk SSSR **333**, 321 (1993) [Phys. Dokl. **38**, 470 (1993)].
[9] N. I. Kourov and Yu. N. Tsiovkin, Fiz. Met. Metalloved. **80**, 53 (1995).
[10] *Phase Diagrams of Iron-Based Binary and Multi-Component Systems*, edited by O. A. Bannykh and M. E. Drits (Metallurgiya, Moscow, 1986).
[11] S. Ishida, S. Asano, and J. Ishida, J. Phys. Soc. Jpn. **54**, 3925 (1985).
[12] S. Ishida and S. Asano, J. Phys. Soc. Jpn. **54**, 4688 (1985).
[13] A. A. Povzner and A. G. Volkov, Fiz. Tverd. Tela (St. Petersburg) **38**, 643 (1996) [Phys. Solid State **38**, 356 (1996)].

Translated by G. Skrebtsov

The relation between the electronic and magnetic structures of manganites in the tight-binding approximation

S. M. Dunaevskiĭ

St. Petersburg Nuclear Physics Institute, Russian Academy of Sciences, 188350 Gatchina, Russia
(Submitted April 2, 1999)
Fiz. Tverd. Tela (St. Petersburg) **41**, 2179–2182 (December 1999)

Analytic expressions for the dispersion curves $E(\mathbf{k})$ of $RMnO_3$ (R=La, Pr, Nd, Sm, and other RE elements) have been obtained in the tight-binding approximation for the main types of magnetic ordering on the Mn sublattice. The first calculation of $E(\mathbf{k})$ taking into account the oxygen subsystem and mutual ordering of the manganese and RE sublattices is reported. The results obtained permit a qualitative interpretation of some features observed in the behavior of the rare-earth manganites. © *1999 American Institute of Physics.* [S1063-7834(99)01412-4]

1. The doped manganites $R_{1-x}L_xMnO_3$ (R=La, Pr, Nd, Sm; L=Ca, Ba, Sr) have been subjects of considerable current experimental and theoretical investigations, which were initiated by the observation of extremely diverse phase diagrams in these compounds. It has presently become obvious that a correct quantitative description of phase diagrams and transport properties of manganites within the $x=0.16-0.4$ range, where a crossover from the paramagnetic dielectric to the ''ferromagnetic'' phase with metallic conduction occurs with decreasing temperature, requires simultaneous inclusion of lattice (polaron), magnetic, and correlation effects. Nevertheless, qualitative interpretation of the anomalies observed in electrical conductivity near the Curie point is based on the ''double-exchange'' model of Zener, which was considered theoretically by Anderson–Hasegawa (AH) for two manganese ions.[1] The AH results are widely employed in present studies making use of a model Hamiltonian of the system H, which is usually written as a sum of the double-exchange Hamiltonian H_{DE},[2,3] the Heisenberg Hamiltonian for localized (classical) spins, and the energy of interaction of these spins with the external magnetic field H_m. This approach does not take into account the existence in the system of oxygen and rare-earth (RE) elements, and does not explain the experimentally observed features in the behavior of the RE manganites.

The present work deals with an analytic calculation of the spectrum of e_g electrons in manganites for different types of magnetic ordering in the system. One has obtained for the first time the dispersion curves $E(\mathbf{k})$ taking into account the oxygen subsystem and the mutual ordering of the manganese and RE sublattices. As in most of the present studies, the carrier spin is supposed to be always aligned with the local manganese-ion spin formed by three t_{2g} electrons.

2. Consider first only the manganese sublattice in the ideal cubic structure of an ABO_3 perovskite. The double-exchange Hamiltonian can be represented as a conventional tight-binding Hamiltonian in which the hopping integral between various manganese-ion orbitals depends on the mutual arrangement of the nearest localized magnetic moments (in the simplest case this relation has the AH form[1])

$$H=H_{DE}+H_m,$$

$$H_{DE}=\sum_{i\alpha\sigma}\varepsilon_{i\alpha\sigma}d^+_{i\alpha\sigma}d_{i\alpha\sigma}+\sum_{ij\alpha\beta\sigma'\sigma}t^{\sigma\sigma'}_{ij\alpha\beta}\left(\frac{\theta_{ij\alpha\beta}}{2}\right)d^+_{i\alpha\sigma}d_{j\beta\sigma'}+\frac{U}{2}\sum_{i\sigma}n_{i\sigma}n_{i-\sigma},$$

$$t^{\sigma\sigma'}_{ij\alpha\beta}\left(\frac{\theta_{ij\alpha\beta}}{2}\right)=t_{ij\alpha\beta}\cos\left(\frac{\theta_{ij\alpha\beta}}{2}\right)(\sigma=\sigma');\quad \pm t_{ij\alpha\beta}\sin\left(\frac{\theta_{ij\alpha\beta}}{2}\right)(\sigma\neq\sigma'),$$

$$H_m=-g\mu_B B\sum_i S^z_i+\sum_{ij}J_{ij}\mathbf{S}_i\mathbf{S}_j. \qquad (1)$$

Here (1) the indices i and j label the unit cells, α and β — the type of the atom, $\varepsilon_{i\alpha\beta}$ is the energy of the unperturbed d level of the α-type Mn^{4+} ion, and σ is the spin index, which can take only two values; $\theta_{ij\alpha\beta}$ is the angle between the local magnetic moment of the nearest ions of Mn.

There are several main types of magnetic ordering on the manganese sublattice in perovskites, namely, *A*, antiferromagnetic ordering of nearest-neighbor (100) ferromagnetic planes observed in $LaMnO_3$, *G*, antiferromagnetic ordering of nearest neighbors ($CaMnO_3$), *C* — antiferromagnetic ordering in the (100) plane, and *F* — ferromagnetic ordering. In case *A*, the perovskite unit cell contains two inequivalent manganese atoms. Disregarding the degeneracy of the e_g orbital, one can construct four Bloch combinations

$$|\chi_{\alpha\sigma}\rangle=\frac{1}{\sqrt{N}}\sum e^{ikR_i}|\varphi_{\alpha\sigma}(r-R_i)\rangle, \qquad (2)$$

where $\varphi_{\alpha\sigma}(r-R_i)$ is the d-orbital, and $\alpha=1,2$ is an index labeling various types of atoms in the unit cell. If the degeneracy of the e_g orbital is taken into account, one should introduce into Eqs. (1) and (2) an index labeling the orbital type. In this case the dispersion relations in an analytic form can be obtained only for the case of ferromagnetic ordering.[4]

One can conveniently consider the case of canted antiferromagnetism characteristic of low doping levels, where $S_z = S\cos(\theta/2)$ and $S_x = \pm S\sin(\theta/2)$ in the neighboring (001) planes, and $S_y = 0$. The A type of magnetic ordering occurs for a polar angle $\theta = \pi$. The matrix of the Hamiltonian written in the Hartree–Fock approximation and taking into account Coulomb interaction, which generalizes the AH results, has the form

$$H_{mn}(\mathbf{k}) = \begin{pmatrix} \varepsilon_d' - JS & 0 & t(k_z)\cos\frac{\theta}{2} & t(k_z)\sin\frac{\theta}{2} \\ 0 & \varepsilon_d' + J(S+1) & -t(k_z)\sin\frac{\theta}{2} & t(k_z)\cos\frac{\theta}{2} \\ t(k_z)\cos\frac{\theta}{2} & -t(k_z)\sin\frac{\theta}{2} & \varepsilon_d' - JS & 0 \\ t(k_z)\sin\frac{\theta}{2} & t(k_z)\cos\frac{\theta}{2} & 0 & \varepsilon_d' + J(S+1) \end{pmatrix}. \tag{3}$$

Here $\varepsilon_d' = \varepsilon_d + t(\mathbf{k}_\perp) + U\langle n_{-\sigma}\rangle$, $t(\mathbf{k}_\perp) = 2t(\cos k_x a_x + \cos k_y a_y)$, $t(k_z) = 2t\cos k_z a_z$, and t is the hopping integral between the d-orbitals of manganese atoms (which in the perovskite lattice are separated by oxygen atoms and, strictly speaking, are not nearest neighbors).

The four bands of the corresponding secular equation $\det[H_{mn}(\mathbf{k}) - E(\mathbf{k})I] = 0$ can be presented as

$$E_{\alpha\sigma}(\mathbf{k}) = \varepsilon_d + U\langle n_{-\sigma}\rangle + t(\mathbf{k}_\perp) + J/2 \pm [J^2(S+1/2)^2 + t^2(k_z) \pm 2J(S+1/2)t(k_z)\cos\theta/2]^{1/2}. \tag{4}$$

In the approximation of strong intratomic exchange, $JS \gg t$, the lowest band can be described as

$$E_\uparrow(\mathbf{k}) = \varepsilon_d + U\langle n_\downarrow\rangle - JS + t(\mathbf{k}_\perp) + t(k_z)\cos\theta/2, \quad (t<0).$$

The spectrum for the G-type canted antiferromagnetic structure is found in a similar way

$$E_{\alpha\sigma}(\mathbf{k}) = \varepsilon_d + U\langle n_{-\sigma}\rangle + J/2 \pm [J^2(S+1/2)^2 + t^2(\mathbf{k}) \pm 2J(S+1/2)t(\mathbf{k})\cos\theta/2]^{1/2}, \tag{5}$$

where $t(\mathbf{k}) = 2t(\cos k_x a_x + \cos k_y a_y + \cos k_z a_z)$. Now

$$E_\uparrow(\mathbf{k}) = \varepsilon_d + U\langle n_\downarrow\rangle - JS + t(\mathbf{k})\cos\theta/2.$$

In the C-type canted antiferromagnetic structure, the unit cell doubles in content in the XY plane (a_x and a_y have to be multiplied by $2^{1/2}$), and the dispersion relations take on the form

$$E_{\alpha\sigma}(\mathbf{k}) = \varepsilon_d + U\langle n_{-\sigma}\rangle + t(\mathbf{k}_z) + J/2 \pm [J^2(S+1/2)^2 + t^2(\mathbf{k}_\perp) \pm 2J(S+1/2)t(\mathbf{k}_\perp)\cos\theta/2]^{1/2}, \tag{6}$$

with

$$E_\uparrow(\mathbf{k}) = \varepsilon_d + U\langle n_\downarrow\rangle - JS + t(\mathbf{k}_z) + t(\mathbf{k}_\perp)\cos\theta/2.$$

The ferromagnetic structure has only two spectral branches

$$E_\uparrow(\mathbf{k}) = \varepsilon_d - JS + U\langle n_\downarrow\rangle + t(\mathbf{k}),$$
$$E_\downarrow(\mathbf{k}) = \varepsilon_d + J(S+1) + U\langle n_\uparrow\rangle + t(\mathbf{k}). \tag{7}$$

It should be pointed out that when one uses for the hopping integral relations which depend on the difference between the azimuthal angles φ_{ij} as well, Eqs. (4)–(7) retain their form.

Similar results can be obtained also from the one-band Kondo Hamiltonian (see Refs. 5 and 6) by taking into account the nearest-neighbor interaction

$$H_{DE} = \sum_{ij\sigma} (t_{ij} d_{i\sigma}^+ d_{j\sigma} + \text{H.c.}) + \frac{U}{2}\sum_{i\sigma} n_{i\sigma} n_{i-\sigma} - J_H \sum_{i\sigma\sigma'} \mathbf{S}_i d_{i\sigma}^+ \boldsymbol{\sigma}_{\sigma\sigma'} d_{i\sigma'}, \tag{8}$$

but this model yields only two branches of the spectrum. In Eq. (8), t_{ij} is the hopping integral of the e_g electron between manganese atoms i and j, U is the intratomic Coulomb integral, $d_{i\sigma}^+$ ($d_{i\sigma}$) are the creation (annihilation) operators for the e_g electron at site i, σ is the spin index ($\sigma = \uparrow$ or $\downarrow$ in the local reference frame associated with the atomic spin S_i), $\boldsymbol{\sigma}$ is the e_g-electron vector spin operator, J_H is the intratomic exchange (Hund) integral, and J_{ij} are the exchange parameters of the Heisenberg Hamiltonian for the local magnetic moments due to the manganese t_{2g} electrons. The dispersion relations obtained here correct and complement the dispersion relations $E(\mathbf{k})$ derived earlier (Refs. 5 and 7, respectively) for a number of magnetic structures (A,G,C, and F). A tight-binding analysis of more complex types of magnetic ordering can be carried out only numerically.

3. Substitution of Nd, Pr, and other RE elements for La atoms results in an increase of the number of magnetically inequivalent atoms in the ABO_3 perovskite unit cell, because magnetic ions start to occupy the B site. Under certain conditions ordering of local magnetic moments of RE elements may set in, which should be taken into account when calculating the dispersion relation for carriers in perovskites. Let us assume only one (ferromagnetic) sublattice to exist in the manganese subsystem. Then the Hamiltonian matrix for canted mutual ordering on the d- and f-sublattices can be written in a form similar to Eq. (4)

$$H_{mn}(\mathbf{k})=\begin{pmatrix} \varepsilon_1-J_1S_1+t_{11}(\mathbf{k}) & 0 & t_{12}(\mathbf{k})\cos\frac{\theta}{2} & t_{12}(\mathbf{k})\sin\frac{\theta}{2} \\ 0 & \varepsilon_1+J_1(S_1+1)+t_{11}(\mathbf{k}) & -t_{12}(\mathbf{k})\sin\frac{\theta}{2} & t_{12}(\mathbf{k})\cos\frac{\theta}{2} \\ t_{12}(\mathbf{k})\cos\frac{\theta}{2} & -t_{12}(\mathbf{k})\sin\frac{\theta}{2} & \varepsilon_2-J_2S_2+t_{22}(\mathbf{k}) & 0 \\ t_{12}(\mathbf{k})\sin\frac{\theta}{2} & t_{12}(\mathbf{k})\cos\frac{\theta}{2} & 0 & \varepsilon_2+J_2(S_2+1)+t_{22}(\mathbf{k}) \end{pmatrix}. \quad (9)$$

For ferromagnetically ordered sublattices ($\theta=0$) the dispersion relations are

$$E^{\sigma}_{1,2}(\mathbf{k})=\frac{1}{2}[\varepsilon^{\sigma}_1(\mathbf{k})+\varepsilon^{\sigma}_2(\mathbf{k})\pm\sqrt{[\varepsilon^{\sigma}_1(\mathbf{k})-\varepsilon^{\sigma}_2(\mathbf{k})]^2+4t^2_{12}(\mathbf{k})}],$$

$$\varepsilon^{\sigma}_i(\mathbf{k})=\varepsilon^{\sigma}_i+U\langle n_{i-\sigma}\rangle+t_{ii}(\mathbf{k}),\quad \varepsilon^{\uparrow}_i=\varepsilon_i-J_iS_i,$$

$$\varepsilon^{\downarrow}_i=\varepsilon_i+J_i(S_i+1),$$

$$t_{ii}(\mathbf{k})=2t_{ii}[\cos(k_xa_x)+\cos(k_ya_y)+\cos(k_za_z)],\quad i=1,2,$$

$$t_{12}(\mathbf{k})=2t_{12}\sum_i\cos(\mathbf{k}\mathbf{r}_i),$$

$$\mathbf{r}_{\mathrm{I}}=\frac{1}{2}(a_x,a_y,a_z),\quad \mathbf{r}_{\mathrm{II}}=\frac{1}{2}(a_x,a_y,-a_z),$$

$$\mathbf{r}_{\mathrm{III}}=\frac{1}{2}(a_x,-a_y,a_z),\quad \mathbf{r}_{\mathrm{IV}}=\frac{1}{2}(-a_x,a_y,a_z). \quad (10)$$

In Eqs. (9) and (10), $\varepsilon_1\equiv\varepsilon_d$, ε_2 is the $5d$-orbital energy, J_2S_2 is the intratomic exchange energy for the $5d$-electron of an RE element (for lanthanum this energy is zero), t_{12} is the hopping integral between the manganese d-orbital and the $5d$-orbital of the nearest RE atom, and summation is run over four inequivalent neighbors. If one neglects the smallest Koster–Slater parameter, $V_{dd\delta}$, this integral equals $2V_{dd\pi}/3$. A numerical estimation of $V_{dd\pi}$ made using Harrison's table[8] yielded $V_{dd\pi}=0.3-0.4$ eV. The calculated value of the hopping integral is of the same order of magnitude as that of the hopping integral between manganese ions ($\approx 0.1-0.2$ eV). Transition of the manganese d-electron to the $6s$-orbital of an RE atom is impossible for symmetry considerations, and therefore it can be disregarded in the calculations.

For mutual antiferromagnetic ordering one readily obtains

$$E_{1,2}(\mathbf{k})=\frac{1}{2}[\varepsilon^{\uparrow}_1(\mathbf{k})+\varepsilon^{\downarrow}_2(\mathbf{k})\pm\sqrt{[\varepsilon^{\uparrow}_1(\mathbf{k})-\varepsilon^{\downarrow}_2(\mathbf{k})]^2+4t^2_{12}(\mathbf{k})}],$$

$$E_{3,4}(\mathbf{k})=\frac{1}{2}[\varepsilon^{\downarrow}_1(\mathbf{k})+\varepsilon^{\uparrow}_2(\mathbf{k})\pm\sqrt{[\varepsilon^{\downarrow}_1(\mathbf{k})-\varepsilon^{\uparrow}_2(\mathbf{k})]^2+4t^2_{12}(\mathbf{k})}]. \quad (11)$$

As follows from a comparison of the two above expressions with Eq. (7), where $t\equiv t_{11}$, taking into account the RE subsystem results in a shift and substantial broadening of the band. In a general case and for an arbitrary angle θ the analytic expressions for $E(\mathbf{k})$ become very cumbersome. However assuming the self-consistent energies of the d- and f-levels to be approximately equal, $\varepsilon_d\cong\varepsilon_f\cong\varepsilon_0$, and $t_{11}=t_{22}$, $\Delta_i=J_iS_i\cong J_i(S_i+1)$, $i=1,2$, one can derive the following dispersion relations

$$E_{\alpha}(\mathbf{k})=\varepsilon_0+t_{11}(\mathbf{k})\pm\{(\Delta^2_1+\Delta^2_2)/4+t^2_{12}(\mathbf{k})\pm[(\Delta^2_1-\Delta^2_2)^2/4+t_{12}(\mathbf{k})(\Delta_1+\Delta_2)^2-4t^2_{12}(\mathbf{k})\Delta_1\Delta_2\sin^2\theta/2]^{1/2}\}^{1/2},$$

$$\alpha=1,\ldots,4, \quad (12)$$

which for $\theta=0$ and π transfer to Eqs. (10) and (11). Inclusion of Coulomb interaction in the Hartree–Fock approximation results in ε_0 in Eq. (12) becoming replaced by $\varepsilon_0+U\langle n_{-\sigma}\rangle$. As follows from this relation, replacement of lanthanum (for which $\Delta_2=0$) by any RE element with a nonzero Δ_2 shifts all bands down and broadens them simultaneously. For $\Delta_2=\Delta_1$, Eq. (12) yields dispersion relations for the manganese bcc lattice. The band energy will be minimum for ferromagnetic mutual ordering of the manganese and RE sublattices. For close to antiferromagnetically ordered sublattices, the band width can become smaller than that for lanthanum manganite ($\Delta_2=0$), which will give rise to a decrease in the conductivity of the compounds. This result correlates qualitatively with the experimentally observed differences of the phase diagrams of Pr-, Nd-, and Sm-based manganites[9,10] from that of $La_{1-x}L_xMnO_3$.

4. One can take explicitly into account within the tight-binding approach the strongest t_{pd} coupling between the d-orbitals of manganese and the p-orbitals of oxygen, which was thus far neglected in model approximations. Inclusion of p–d coupling in band-structure calculations requires at the very least a consideration of a 6×6 Hamiltonian matrix, whose explicit form for three atoms is given in Ref. 10. Using the solutions found in the above work, one readily obtains approximate $\mathbf{k}$-space dispersion relations for a type G magnetic structure with inclusion of the nearest-neighbor interaction:

$$E_1(\mathbf{k})=\varepsilon_d-JS-t^2_{pd}(\mathbf{k})\frac{1+\cos(\theta_{12}/2)}{\varepsilon_p-\varepsilon_d+JS},$$

$$E_2(\mathbf{k})=\varepsilon_d-JS-t^2_{pd}(\mathbf{k})\frac{1-\cos(\theta_{12}/2)}{\varepsilon_p-\varepsilon_d+JS},$$

$$E_3(\mathbf{k}) = \varepsilon_p - 2t_{pd}^2(\mathbf{k}) \frac{\varepsilon_d' - \varepsilon_p - \Delta \cos(\theta_{12}/2)}{(\varepsilon_d' - \varepsilon_p)^2 - \Delta^2},$$

$$E_4(\mathbf{k}) = \varepsilon_p - 2t_{pd}^2(\mathbf{k}) \frac{\varepsilon_d' - \varepsilon_p + \Delta \cos(\theta_{12}/2)}{(\varepsilon_d' - \varepsilon_p)^2 - \Delta^2},$$

$$E_5(\mathbf{k}) = \varepsilon_d + J(S+1) - t_{pd}^2(\mathbf{k}) \frac{1 - \cos(\theta_{12}/2)}{\varepsilon_p - \varepsilon_d - J(S+1)},$$

$$E_6(\mathbf{k}) = \varepsilon_d + J(S+1) - t_{pd}^2(\mathbf{k}) \frac{1 + \cos(\theta_{12}/2)}{\varepsilon_p - \varepsilon_d - J(S+1)}. \quad (13)$$

Here, $t_{pd}(\mathbf{k}) = (t_{pd}/3)(\cos k_x a_x + \cos k_y a_y + \cos k_z a_z)$, $\varepsilon_d' = \varepsilon_d + J/2$, $\Delta = J(S+1/2)$, and the bands are arranged in the order of increasing energy provided there is strong intratomic exchange, $\Delta > t_{pd}$. The order of the bands can vary depending on the actual values of the parameters Δ, t_{pd}, and $\varepsilon_p - \varepsilon_d$. For $\Delta \gg t_{pd}$, the upper unfilled band will be the ''oxygen'' band $E_3(\mathbf{k})$, whose width depends on the type of magnetic ordering in the manganese subsystem. An estimate[11] of the parameters shows that for manganites $\Delta < t_{pd}$, and for certain relations connecting the parameters the upper unfilled band can be a *d*-type band. In all cases, the shape of all six bands depends on the angle between the magnetic moments of the neighboring manganese ions, and the width of these bands does not vanish even under antiferromagnetic ordering. This theoretical conclusion has recently found experimental support in the observation[12] of antiferromagnetic ordering on the manganese subsystem coexisting with metallic conduction.

5. The main result of this work is the inclusion of *p*–*d* and *d*–*d* interactions on the oxygen–manganese and RE (lanthanum)–manganese subsystems in band-structure calculations of the $R_{1-x}L_xMnO_3$ perovskites, which has not been made thus far in theory. Unfortunately, simultaneous inclusion of these interactions and of the e_g-level degeneracy precludes obtaining within the tight-binding approximation an analytic description of the electronic structure $E(\mathbf{k})$ for various types of magnetic ordering of perovskites throughout the Brillouin zone. Nevertheless, analytic dispersion relations $E(\mathbf{k})$ are of considerable importance when estimating the conditions for the onset of electronic phase separation in perovskites. The results of these studies will be presented in a separate paper.

Support of the ''Neutron Studies of Matter'' program is gratefully acknowledged.

[1] P. W. Anderson and H. Hasegawa, Phys. Rev. **100**, 675 (1955).
[2] E. Müller-Hartmann and E. Dagotto, Phys. Rev. B **54**, R6819 (1996).
[3] K. Kubo and N. Ohata, J. Phys. Soc. Jpn. **33**, 21 (1972).
[4] H. Shiba, R. Shina, and A. Takahashi, J. Phys. Soc. Jpn. **66**, 941 (1997).
[5] L. J. Zou, Q. Q. Zheng, and H. Q. Lin, Phys. Rev. B **56**, 13669 (1997).
[6] Y. A. Dimashko and A. L. Alistratov, Phys. Rev. B **50**, 1162 (1994).
[7] L. P. Gor'kov and V. Z. Kresin, JETP Lett. **67**, 934 (1998).
[8] W. A. Harrison, *Electronic Structure and the Properties of Solids* (Freeman, San Francisco, 1980; Mir, Moscow, 1983).
[9] R. Maezono, S. Ishihara, and N. Nagaosa, Phys. Rev. B **57**, R13993 (1998).
[10] S. M. Dunaevskiĭ, A. L. Malyshev, V. V. Popov, and V. A. Trunov, Fiz. Tverd. Tela (St. Petersburg) **39**, 1831 (1997) [Phys. Solid State **39**, 1636 (1997)].
[11] S. M. Dunaevskiĭ, Fiz. Tverd. Tela (St. Petersburg) **40**, 1861 (1998) [Phys. Solid State **40**, 1687 (1998)].
[12] T. Akimoto, Y. Maruyama, Y. Moritomo, A. Nakamura, K. Hirota, K. Ohoyama, and M. Ohashi, Phys. Rev. B **57**, R5594 (1998).

Translated by G. Skrebtsov

Spectra of spin-wave excitations of a 71° domain boundary in a cubic ferromagnet

A. M. Alekseev, A. F. Popkov, and A. I. Popov

Moscow State Institute of Electronic Engineering, 103498 Moscow, Russia
(Submitted January 15, 1999; accepted for publication April 15, 1999)
Fiz. Tverd. Tela (St. Petersburg) **41**, 2183–2186 (December 1999)

Features of the long-wavelength part of the spectrum of spin waves localized on a 71° domain boundary of a cubic ferromagnet are examined on the basis of a qualitative analysis and simultaneous numerical solution of the Landau–Lifshitz equations and the equation of magnetostatics. © *1999 American Institute of Physics.* [S1063-7834(99)01512-9]

The spectra of spin-wave excitations of domain boundaries (DB's) of a uniaxial ferromagnet have been examined in a number of works.[1–3] References 4 and 5 described three branches of the vibrations of a domain boundary in the band forbidden for bulk spin waves: two low-frequency bands corresponding to translational vibrations of the domain boundaries, and the unidirectional Gilinskiĭ branch, corresponding to high-frequency vibrations of the spins, localized near a domain boundary, whose amplitude decays without limit on its periphery. In Ref. 5, high-frequency branches detached from the boundary of the continuous spectrum were also discovered by numerical calculations. Reference 6 investigated the vibrational spectrum of the 180° Bloch domain boundary (BDB) in a cubic ferromagnet with induced uniaxial anisotropy, which corresponds to the anisotropy of iron–yttrium garnet films. In the present work we have found branches corresponding to translations of a domain boundary, oscillations of the thickness of a domain boundary, and also the Gilinskiĭ branch and one high-frequency branch split off from the boundary of the continuous spectrum. We also investigate spectra of spin-wave excitations of a domain boundary in an orthorhombic and a tetragonal ferromagnet, the anisotropy of which corresponds to the anisotropy of bismuth-substituted iron–garnet films grown in the [110] direction and the [100] direction, respectively.[7,8] However, all theoretical works on DB-localized spin waves have been limited to a study of 180° walls. Recently, experimental observations of spin waves have been made on 90° as well as 180° domain boundaries in a cubic ferromagnet.[9] A theory of spin-wave excitations of Bloch domain boundaries with tilt angle of the magnetization different from 180° is still lacking. In this paper, using numerical methods we investigate the vibrational spectrum of a 71° Bloch domain boundary in a cubic ferromagnet. Such walls arise in materials with cubic anisotropy, which is characteristic, in particular, of iron–yttrium garnet, the most frequently applied material in experiments on observation of spin waves.[10]

1. BASIC EQUATIONS

Spin-wave excitations of a domain boundary of a ferromagnet are described by the Landau–Lifshitz equations and the equation of magnetostatics

$$\frac{M}{\gamma}\frac{\partial\varphi}{\partial t}\sin\vartheta=\frac{\delta E}{\delta\vartheta},\quad -\frac{M}{\gamma}\frac{\partial\vartheta}{\partial t}\sin\vartheta=\frac{\delta E}{\delta\varphi}, \tag{1}$$

$$\operatorname{div}(\mathbf{h}_d+4\pi\mathbf{M})=0, \tag{2}$$

where $\mathbf{M}=M\mathbf{m}$ is the magnetization vector, $\mathbf{m}$ is the corresponding unit vector, $\mathbf{m}=(\sin\vartheta\cos\varphi,\sin\vartheta\sin\varphi,\cos\vartheta)$, γ is the gyromagnetic ratio, $\mathbf{h}_d$ is the demagnetization field, which in the magnetostatic approximation is expressed in terms of the magnetic potential Ψ: $\mathbf{h}_d=\nabla\Psi$, E is the energy of the ferromagnet, which includes the inhomogeneous exchange energy, the magnetic anisotropy energy, and the energy of the demagnetization fields

$$E=A((\nabla\vartheta)^2+\sin^2\vartheta(\nabla\varphi)^2)+E_a(\varphi,\vartheta)-\frac{1}{8\pi}\left(\left(\frac{\partial\Psi}{\partial x}\right)^2+\left(\frac{\partial\Psi}{\partial y}\right)^2\left(\frac{\partial\Psi}{\partial z}\right)^2\right)-M\left(\frac{\partial\Psi}{\partial x}\sin\vartheta\cos\varphi+\frac{\partial\Psi}{\partial y}\sin\vartheta\cos\varphi+\frac{\partial\Psi}{\partial z}\cos\vartheta\right).$$

Here A is the exchange interaction constant and E_a is the magnetic anisotropy energy. In the crystallographic system the anisotropy energy of a cubic ferromagnet is written as

$$E_a=K_1(m_x^4+m_y^4+m_z^4),$$

where K_1 is the cubic anisotropy constant. If $K_1>0$, the easy axes are directions of the type [111]; therefore it is convenient to transform to the new system of coordinates $\mathbf{e}_x=[111]$, $\mathbf{e}_y=[11\bar{2}]$, $\mathbf{e}_z=[\bar{1}10]$. Thus

$$E_a=K_1\left(\frac{\sin^4\vartheta\sin^4\varphi}{2}+\frac{\cos^4\vartheta}{2}+\frac{2}{3}\sin^4\vartheta\cos^4\varphi+\sin^2\vartheta\cos^2\vartheta\sin^2\varphi+\frac{2\sqrt{2}}{3}\sin^4\vartheta\cos\varphi\sin^3\varphi-2\sqrt{2}\sin^2\vartheta\cos^2\vartheta\cos\varphi\sin\varphi\right).$$

We will consider a Bloch wall in which the tilt of the magnetization is in the XY plane [the crystallographic plane $(\bar{1}10)$] from the direction [111] to the direction $[11\bar{1}]$, the normal to which coincides with the z axis (Fig. 1). In spheri-

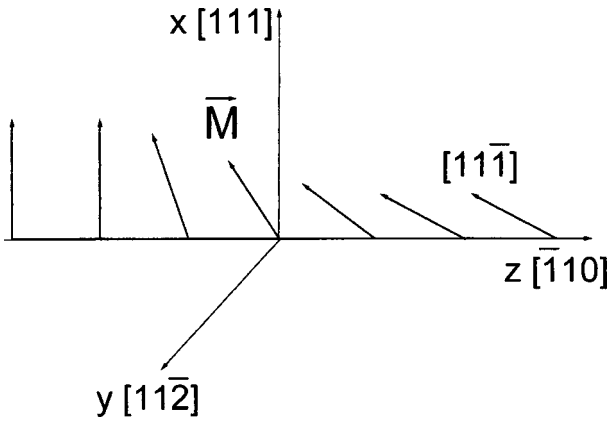

FIG. 1. Static structure of a 71° domain boundary of a cubic ferromagnet.

cal coordinates the structure of a 71° Bloch domain boundary, obtained by solving the static Landau–Lifshitz equation, is described as follows:

$$\vartheta=\frac{\pi}{2},\quad \varphi_0=\alpha+\arctan\left(\frac{1}{\sqrt{2}}\tanh\left(\frac{z}{\sqrt{3}}\right)\right),$$

$$\alpha=\arctan\frac{1}{\sqrt{2}}, \tag{3}$$

where the z coordinate is normalized by $\sqrt{A/K_1}$. Domain-boundary vibrations are described by a small deviation of the magnetization from its equilibrium distribution (3)

$$\vartheta=\frac{\pi}{2}+\theta(z)\sin(\omega t-k_x x-k_y y),$$

$$\varphi=\varphi_0(z)+\phi(z)\cos(\omega t-k_x x-k_y y),$$

$$\Psi=\psi(z)\sin(\omega t-k_x x-k_y y). \tag{4}$$

Substituting expressions (4) in the Landau–Lifshitz equations (1) and the magnetostatic equation (2), we obtain a linearized system describing vibrations of the magnetization at the domain boundary

$$\begin{cases}\dfrac{\partial^2\theta}{\partial z^2}=(k^2+a(\varphi_0))\,\theta+\omega\phi+\dfrac{1}{Q}\dfrac{\partial\psi}{\partial z},\\[2ex] \dfrac{\partial^2\phi}{\partial z^2}=\omega\theta+(k^2+b(\varphi_0))\,\phi-\dfrac{1}{Q}(k_x\sin\varphi_0-k_y\cos\varphi_0)\,\psi,\\[2ex] \dfrac{\partial^2\psi}{\partial z^2}=\dfrac{\partial\theta}{\partial z}+(k_x\sin\varphi_0-k_y\cos\varphi_0)\,\phi+k^2\psi,\end{cases}$$

$$a(\varphi_0)=\frac{3}{2}\sin^4\varphi_0+2\cos^4\varphi_0+2\sqrt{2}\cos\varphi_0\sin^3\varphi_0$$
$$+2\sqrt{2}\cos\varphi_0\sin\varphi_0-\sin^2\varphi_0-\frac{2}{3},$$

$$b(\varphi_0)=\sin^4\varphi_0+\frac{4}{3}\cos^4\varphi_0+\frac{10\sqrt{2}}{3}\cos\varphi_0\sin^3\varphi_0$$
$$-2\sqrt{2}\cos^3\varphi_0\sin\varphi_0-7\cos^2\varphi_0\sin^2\varphi_0. \tag{5}$$

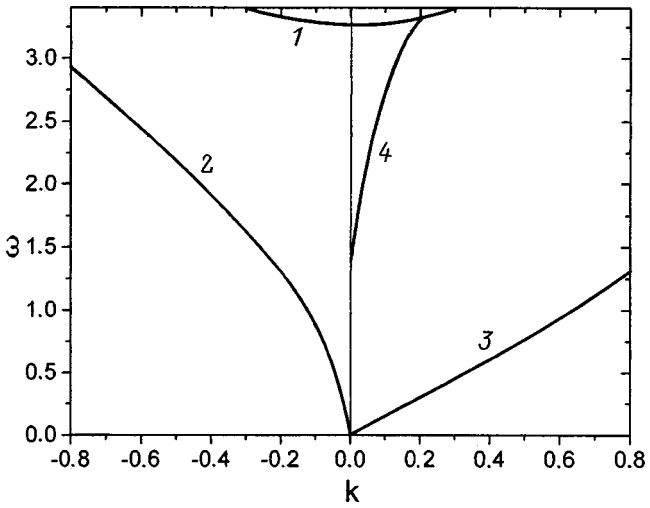

FIG. 2. Spectrum of localized spin waves on a 71° domain boundary of a cubic ferromagnet with Q factor $Q=0.05$ for wave propagation in the [110] direction. *1* — boundary of the continuous spectrum, *2, 3* — Goldstone mode, *4* — Gilinskiĭ mode.

Here the coordinates x,y,z and the wave number k are normalized by $\sqrt{K_1/A}$, the frequency ω by $2\gamma K_1/M$, and the magnetic potential ψ by $4\pi M\sqrt{A/K_1}$. The Q factor $Q=K_1/2\pi M^2$. The magnetic potential ψ and the angles ϕ,θ should satisfy the boundary condition $\theta,\phi,\psi=0$ as $z\to\pm\infty$.

The angle φ_0 in Eqs. (5) varies from zero to $\arctan 2\sqrt{2}\approx 71°$. It follows from system (5) that the symmetry axis is the direction perpendicular to the bisector of the angle formed by the magnetization on neighboring domains, i.e., the spectrum of spin waves propagating in this direction is symmetric with respect to a change of sign of the wave number.

To find the spectrum of spin-wave excitations of a 71° Bloch domain boundary, we used a numerical method proposed in Ref. 5. As $z\to\pm\infty$, system (5) transforms to a system of differential equations with constant coefficients. The solution of such a system is used as an initial approximation at large enough values of z. Integrating Eqs. (5) by the Runge–Kutta method from the initial values at large $\pm z$ to the joining point, we obtain the Wronskian, consisting of the left triple and the right triple of solutions at this point. If the Wronskian is equal to zero, then the frequency for which such calculations were performed is the eigenfrequency. In the numerical calculation we set the Q factor equal to $Q=0.05$, which corresponds in order of magnitude with values of the Q factor in iron–yttrium garnet ($Q\approx 0.02$) and some ferrites with spinel structure (for $NiFe_2O_4$ $Q\approx 0.08$).

2. SPECTRA OF SPIN WAVES LOCALIZED ON A 71° DOMAIN BOUNDARY

The results of our numerical calculation are plotted in Figs. 2–4. It can be seen that for the vibrations propagating perpendicular to the symmetry axis (Fig. 2) the spectrum has the same form as in a uniaxial ferromagnet. The unidirectional Gilinskiĭ branch is characterized by a negative dispersion ($\partial^2\omega/\partial k^2<0$, which is analogous to results obtained earlier for other forms of anisotropy energy. This branch

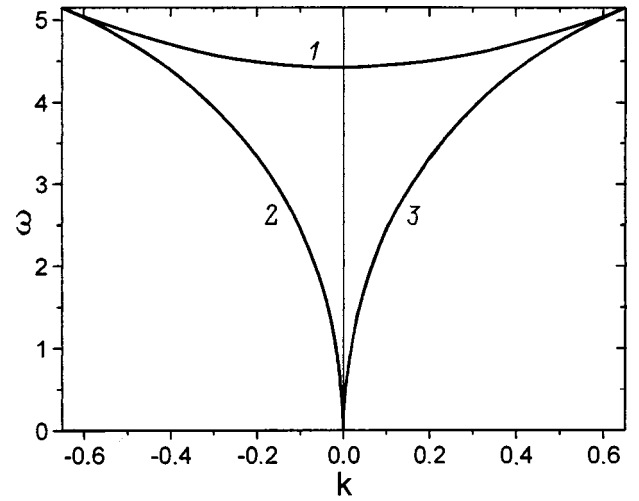

FIG. 3. Spectrum of localized spin waves on a 71° domain boundary of a cubic ferromagnet with Q factor $Q=0.05$ for wave propagation in the [001] direction. *1* — boundary of the continuous spectrum, *2, 3* — Goldstone mode.

exists only for vibrations propagating between directions of the magnetization in neighboring domains, i.e., in the interval of values of γ_0 from 0 to 71°, which is a peculiarity of this type of wall. It is not ruled out that the Gilinskiĭ branch also exists for other types of domain boundaries only in directions lying between easy axes. In all possible directions the Gilinskiĭ branch has a linear asymptotic behavior. To determine the gap in the high-frequency branch, we used the method employed in Ref. 11 in a treatment of a uniaxial ferromagnet. This method is based on peculiarities of the behavior of Eqs. (5) at infinity. Let us consider the case of the propagation of vibrations perpendicular to the symmetry axis, when $\gamma_0=\arctan(k_y/k_x)=\alpha$. As $z\to\pm\infty$, system (5) goes over to a system with constant coefficients, whose solutions are a superposition of three exponentials with characteristic arguments p, which for small values of the wave

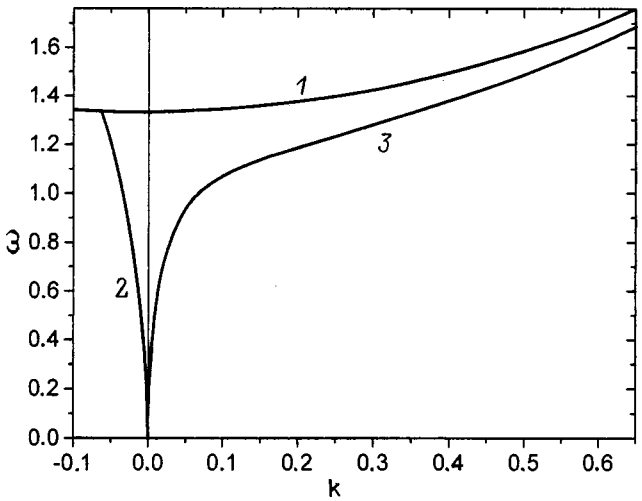

FIG. 4. Spectrum of localized spin waves on a 71° domain boundary of a cubic ferromagnet with Q factor $Q=0.05$ for wave propagation in the [111] direction. *1* — boundary of the continuous spectrum, *2, 3* — Goldstone mode.

number can be calculated using perturbation theory. In the first nonvanishing approximation in $k\ll 1$ we find

$$p_3=k\mu,\quad \mu=\sqrt{\frac{a_0(b_0+\sin^2\gamma_0/Q)-\omega_0^2}{b_0(1/Q+a_0)-\omega_0^2}},$$

$$p_{1,2}=\sqrt{\frac{1}{2}\left(b_0+a_0+\frac{1}{Q}\pm\sqrt{\left(b_0-a_0-\frac{1}{Q}\right)^2+4\omega_0^2}\right)}, \tag{6}$$

where $a_0=b_0=4/3$. Inside the domains the behavior of the solutions is determined by the most slowly decaying terms, i.e., by the exponentials with characteristic argument p_3. Now let us solve the third equation of system (5) with the help of the Green's function $G(z-\xi)=-\exp(-k|z-\xi|)/2k$

$$\psi=\frac{1}{2}\int_{-\infty}^{+\infty}\exp(-k|z-\xi|)(\cos\varphi_0\sin\gamma_0 - \sin\varphi_0\cos\gamma_0)\phi(\xi)d\xi-\frac{1}{2k}\times\int_{-\infty}^{+\infty}\exp(-k|z-\xi|)\frac{\partial\theta(\xi)}{\partial\xi}d\xi.$$

For large values of z the localized solutions are characterized by an exponential falloff with dominating argument p_3, i.e., $\theta=C_1\exp(-k\mu|z|)+O(k)$, $\phi=C_2\exp(-k\mu|z|)+O(k)$. Hence we find

$$\frac{\partial\psi}{\partial z}=\frac{\mu}{1+\mu}C_1-\frac{\sin\gamma_0}{1+\mu}C_2,$$

$$k\psi\to 0,\quad \text{for}\quad z\to\pm\infty. \tag{7}$$

Substituting Eq. (7) into Eqs. (5), we obtain the system

$$\begin{cases}\left(a_0+\dfrac{\mu}{(1+\mu)Q}\right)C_1+\left(\omega_0-\dfrac{\sin\gamma_0}{(1+\mu)Q}\right)C_2=0,\\ \omega_0C_1+b_0C_2=0.\end{cases} \tag{8}$$

Equations (8) coincide if the determinant of the system is equal to zero. From the condition that the determinant be equal to zero we find a second expression for μ

$$\mu=\frac{(b_0-\omega_0\sin\gamma_0)/Q}{b_0(a_0+1/Q)-\omega_0^2}-1. \tag{9}$$

Equating expressions (6) and (9), we obtain three values for ω_0:

$$\omega_0=\pm\sqrt{a_0b_0}, \tag{10}$$

$$\omega_0=\frac{1}{2}\left(\sin\gamma_0\left(a_0+\frac{1}{Q}\right)+\frac{b_0}{\sin\gamma_0}\right). \tag{11}$$

The frequency given by formula (11) for any value of Q falls into the band of the continuous spectrum. The other two symmetric solutions determine the magnitude of the gap of the Gilinskiĭ branch for a 71° Bloch domain boundary in a cubic ferromagnet, which in physical variables is given by the formula

$$\omega_0 = \pm \frac{8\gamma K_1}{3M}.$$

Expression (10) is valid for walls with any tilt angle of the magnetization vector. The coefficients a_0 and b_0, which take the values $a(\varphi_0)$ and $b(\varphi_0)$ at infinity, are determined by the type of the anisotropy energy.

The low-frequency branch of the vibrations, which corresponds to translational shifts of the domain boundary in the long-wavelength limit (the Goldstone mode) has a linear asymptotic limit in the direction perpendicular to the symmetry axis. In all other directions the dependence of the frequency on the wave number for the branch of the translational vibrations in the long-wavelength region goes as the square-root. Such behavior of the low-frequency branches is analogous to the peculiarities of spin waves at a 180° Bloch domain boundary.

At a wall of the type under consideration, the spectrum has a number of distinguishing peculiarities: first, for the vibrations propagating along the symmetry axis the boundary of the continuous spectrum lies higher than for the vibrations propagating perpendicular to the symmetry axis, which is a distinguishing feature of the problem under consideration from the case of a 180° Bloch domain boundary; second, the spectral branches of a Goldstone mode coalesce with the continuous spectrum at a finite value of the wave number (Fig. 3). In the case in which the spin waves propagate along an easy axis the left branch of the Goldstone mode ends at the boundary of the continuous spectrum, as does the Gilinskiĭ branch, while the right branch approaches this boundary asymptotically (Fig. 4). As the Q factor is increased, the asymmetry of the spectrum of vibrations of the domain boundary decreases, but the bottom of the band of the continuous spectrum approaches the Gilinskiĭ branch. If $Q \gg 1$, then the Gilinskiĭ branch coalesces completely with the boundary of the band of bulk spin waves.

Thus, the general form of the spectrum of spin-wave excitations of a 71° Bloch domain boundary is analogous to the spectrum of a 180° Bloch domain boundary, but also has distinguishing features connected with the noncollinear arrangement of the magnetization vector on neighboring domains.

This work was supported by grants from the Russian Fund for Fundamental Research No. 98-02-16469 and No. 97-02-16183.

[1] J. M. Winter, Phys. Rev. **124**, 452 (1961).
[2] J. F. Janak, Phys. Rev. **134**, 411 (1964).
[3] M. I. Kurkin and A. P. Tankeev, Fiz. Met. Metalloved. **36**, 1149 (1973).
[4] I. A. Gilinskiĭ, Zh. Éksp. Teor. Fiz. **68**, 1032 (1975) [Sov. Phys. JETP **41**, 511 (1975)].
[5] A. V. Mikhaĭlov and I. A. Shimokhin, Zh. Éksp. Teor. Fiz. **97**, 1966 (1990) [Sov. Phys. JETP **70**, 1109 (1990)].
[6] A. V. Mikhailov and I. A. Shimokhin, Phys. Rev. B **48**, 9569 (1993).
[7] N. E. Kulagin, A. F. Popkov, V. T. Synogach, and H. J. Dötsch, Appl. Phys. **81**, 2336 (1997).
[8] A. M. Alekseev, A. F. Popkov, and A. I. Popov, Izv. Vyssh. Uchebn. Zaved. Elektron. **1**, 13 (1998).
[9] V. T. Synogach and H. Dötsch, Phys. Rev. B **54**, 15 266 (1996).
[10] A. G. Gurevich and G. A. Melkov, *Magnetic Oscillations and Waves* (Fizmatlit., Moscow, 1994).
[11] I. A. Shimokhin, Phys. Status Solidi B **167**, 243 (1991).

Translated by Paul F. Schippnick

Resonant microwave conductivity response to ac current in $La_{0.7}Pb_{0.3}MnO_3$ crystals

N. V. Volkov, G. A. Petrakovskiĭ, and K. A. Sablina

L. V. Kirenskiĭ Institute of Physics, Siberian Branch of the Russian Academy of Sciences, 660036 Krasnoyarsk, Russia

(Submitted April 20, 1999)
Fiz. Tverd. Tela (St. Petersburg) **41**, 2187–2192 (December 1999)

An experimental study of the effect of low-frequency transport current on the microwave conductivity of single-crystal $La_{0.7}Pb_{0.3}MnO_3$ is reported. In the absence of an external magnetic field, the microwave conductivity response to a current follows a relaxation behavior. In a nonzero external magnetic field, the response spectrum exhibits a peak of resonant amplitude enhancement. The resonant response has a nonlinear nature. The temperature and field dependences of the main parameters of the microwave response correlate directly with the behavior of the magnetoresistance. The results obtained are analyzed within the oscillator approximation. Electronic phase separation is proposed as a possible mechanism for the current action. © *1999 American Institute of Physics.* [S1063-7834(99)01612-3]

Perovskite-structure manganites with a common formula $R_{1-x}A_xMnO_3$ (where R stands for rare-earth ions, and A stands for Sr, Ba, Ca, and Pb) have been recently attracting attention due to their unusual magnetic and electronic properties.[1] Most of this interest centers on the giant magnetoresistance (GMR) observed in some compositions.[2] At the same time there is still no full understanding of the mechanisms responsible for the GMR and other magnetoelectric effects. A substantial contribution to the solution of this problem could come from invoking nontraditional experimental methods, for instance, those aimed at studying the response of a system to combined action of various factors. Besides, one could expect in this case new manifestations of the GMR, as well as new effects having application potential.

In this connection, the microwave conductivity response to an ac current in single-crystal $La_{0.7}Pb_{0.3}MnO_3$ exhibiting GMR, which was detected by us,[3] turned out to be very interesting. The nature of the response depended on the amplitude of the ac voltage across the sample and its frequency, as well as on the external magnetic field. This observation is a one more demonstration of an intimate relation between the magnetic and electrical properties of perovskite-type manganese oxides. This communication reports the results of a detailed investigation of this phenomenon.

1. EXPERIMENTAL

The studies were carried out on $La_{0.7}Pb_{0.3}MnO_3$ single crystals grown by spontaneous crystallization from a melt solution.[3] The sample representing a polished plate measuring $4\times2\times0.1$ mm^3 was placed at the antinode of a microwave electric field in a rectangular cavity ($\nu=10$ GHz). The cavity was connected in a reflection-type magnetic-resonance spectrometer arrangement. The electric current was fed into the sample through spring-loaded needle contacts. One measured the microwave power P_c reflected from the cavity with the sample as a function of temperature, external magnetic field, and the frequency and amplitude of the ac voltage across the sample.

It is well known[4] that if the sample dimensions are much smaller than the wavelength of the electromagnetic radiation, and the skin-layer thickness is larger than or comparable to the smallest sample dimension (in our case this condition was met), the variation of P_c can be related in a single-valued way to that of the complex dielectric permittivity

$$\varepsilon=\varepsilon'-i\varepsilon''=\varepsilon'-i\frac{\sigma_{MW}}{\omega}, \tag{1}$$

where σ_{MW} is the conductivity in the microwave range and ω is the wavelength of the electromagnetic radiation. For conducting media one usually has $\varepsilon'\ll\varepsilon''$. Indeed, in our experiments we did not find any variation of the cavity resonance frequency which could be related to that of ε'. The microwave response signal was generated by variations of the cavity Q-factor. The relative change in the Q-factor caused by a change in the conductivity $\Delta\sigma_{MW}$ can be written[5]

$$\frac{\Delta Q}{Q_0}=\frac{Q_0}{\omega_0 W_0}\Delta\sigma_{MW}\int_{V_S}E^2dV. \tag{2}$$

Equation (2) was derived by the perturbative technique, $Q_0=\omega_0 W_0/(P_s+P_r)$ is the intrinsic Q-factor of the cavity complete with the sample, P_r and P_s are, respectively, the microwave power losses in the cavity walls and the sample, W_0 is the power stored in the cavity, and ω_0 is the cavity resonance frequency. The output signal of the spectrometer linear microwave detector is related to the variation of the microwave conductivity $\Delta\sigma_{MW}$ through

$$\frac{\Delta U}{U_0}=\frac{1}{2}\frac{\Delta Q}{Q_0}, \tag{3}$$

where U_0 is the microwave-detector output voltage, which is proportional to the power incident on the cavity P_{in}, and

ΔU is the change of the microwave-detector output voltage caused by a change in σ_{MW}. Finally we have

$$\Delta U = c\Delta\sigma_{MW}, \tag{4}$$

where c is a quantity remaining constant during the measurement.

Determination of the absolute value of σ_{MW} meets with certain difficulties, but we were interested in the variation of the conductivity $\Delta\sigma_{MW}$ caused by an external action. $\Delta\sigma_{MW}$ was measured in arbitrary units. For definiteness, we shall call in what follows the variation of the microwave conductivity generated by the action of a current the microwave response of a sample.

The dc resistivity ρ and the magnetoresistance $[\rho(0)-\rho(H)]/\rho_0=\Delta\rho/\rho_0$ were measured by the standard four-probe technique.

2. EXPERIMENTAL RESULTS

Our study of the effect of transport current on the conductivity of $La_{0.7}Pb_{0.3}MnO_3$ single crystals in the microwave range revealed the following. If one applied across a sample an ac voltage $U_\sim$ of frequency f, the microwave response signal corresponding to $\Delta\sigma_{MW}$ could be represented as a sum of harmonic components of the modulating voltage frequency

$$\Delta\sigma_{MW}(t)=\sum_{i=1}^{n} A_i\cos(ift), \tag{5}$$

where i is the harmonic number, and A_i is the amplitude of the ith harmonic component in the response signal.

In the absence of an external magnetic field ($H=0$), the microwave response signal contains only even harmonics, with the main contribution being due to the component of the $2f$ frequency. This is a direct consequence of the response being independent of the polarity of the voltage applied to the sample. The temperature dependence of $\Delta\sigma_{MW}$ was presented in Ref. 3. We may recall that it coincided completely with the behavior of the sample magnetoresistance. As for the dependence of the microwave response signal on the frequency f of the applied voltage U, it is shown in Fig. 1. The data are given for $T=300$ K. We see that σ_{MW} is most sensitive to low-frequency currents. The amplitude of $\Delta\sigma_{MW}$ falls off rapidly with increasing frequency.

When an external magnetic field is applied, the response signal amplitude decreases slightly throughout the frequency range covered while remaining a smooth function of f. At the same time at a certain frequency f_0 there appears a peak of the resonantly enhanced microwave-response amplitude. Note that it is the first harmonic [see Eq. (5)] of the signal, which was absent in the $H=0$ case, that contributes to the response enhancement. As H increases, the amplitude of the resonance peak grows to exceed considerably the $H=0$ response. Indeed, at $T=300$ K and a field $H=7$ kOe the signal increases by nearly 10 times. Besides the direct resonant change $\Delta\sigma_{MW}$ at frequency f_0, the spectrum contains also harmonics of higher frequencies multiples of the current frequency. Namely, one detected sample response peaks at frequencies $f_0/3$ and $f_0/5$, with higher-order multiples also observed sometimes.

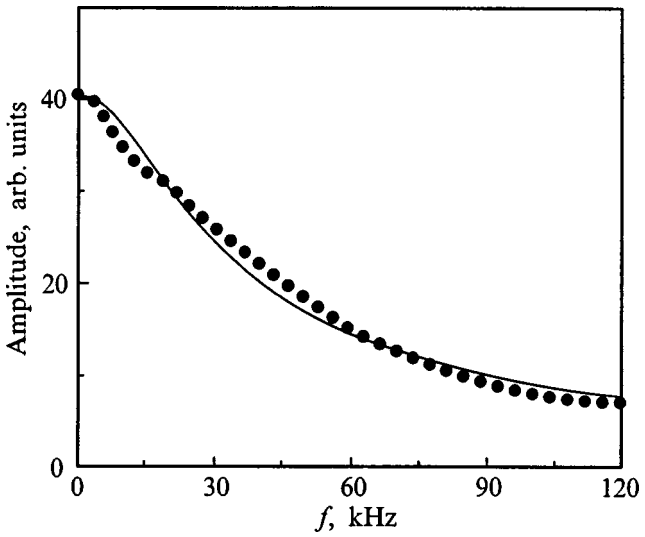

FIG. 1. Amplitude of the microwave-conductivity response signal $\Delta\sigma_{MW}$ vs frequency f of the ac voltage U acting on a sample. External magnetic field $H=0$, $U_\sim=500$ mV, $T=300$ K. Solid line: approximation (see text for explanation).

We studied the behavior of the resonant microwave-response enhancement in a field $H=7$ kOe at different temperatures (Fig. 2). In these measurements, the voltage across

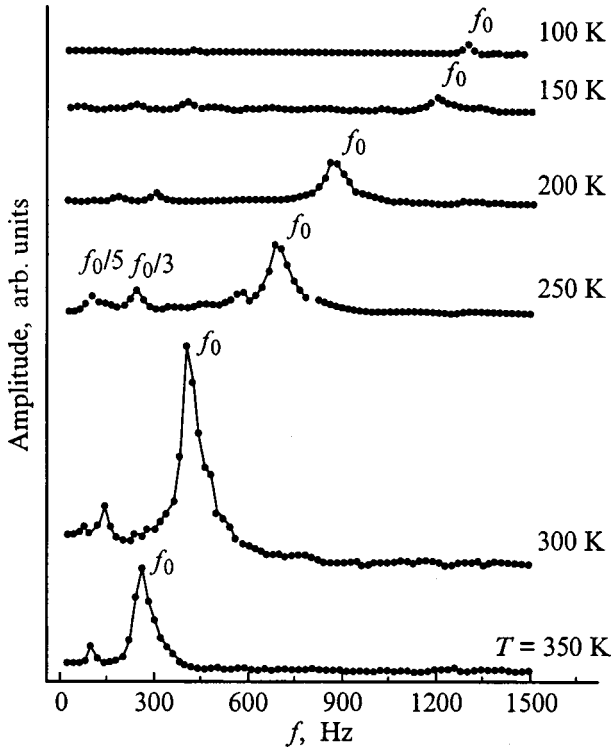

FIG. 2. Amplitude of the microwave-conductivity response signal $\Delta\sigma_{MW}$ vs the frequency f of the voltage $U_\sim$ applied across the sample placed in a magnetic field $H=7$ kOe. Different curves are plots obtained at different temperatures for $U_\sim=500$ mV. f_0 is the main-peak frequency; also shown are peaks of the sample response to frequency multiples of f_0.

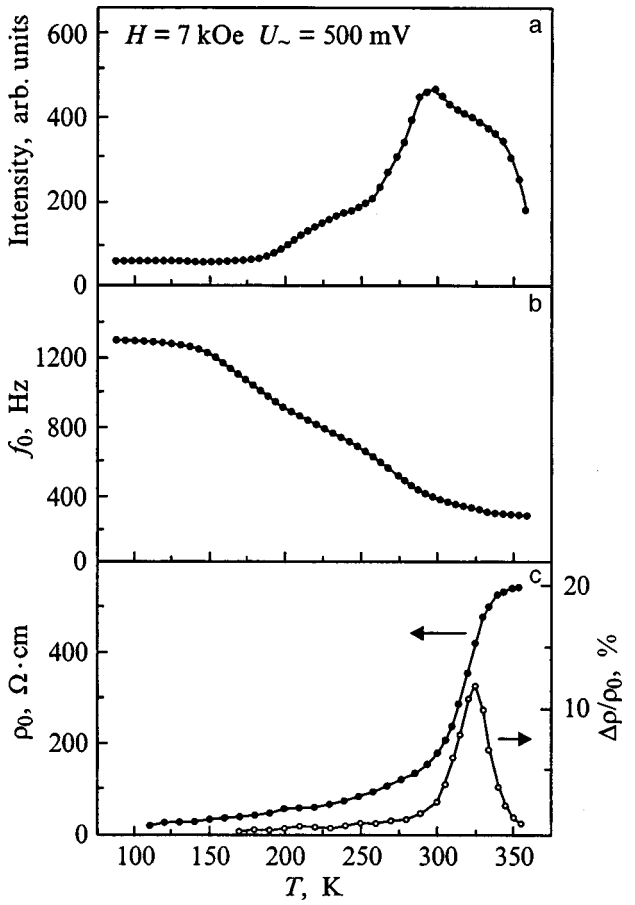

FIG. 3. Temperature dependences of the intensity (a) and frequency (b) of the peak in the microwave-conductivity resonance response $\Delta\sigma_{MW}$ of a sample to an ac voltage; $U_{\sim}=500$ mV, $H=7$ kOe; (c): temperature dependence of the resistivity ρ_0 and magnetoresistance $\Delta\rho/\rho_0$ in a field $H=7$ kOe.

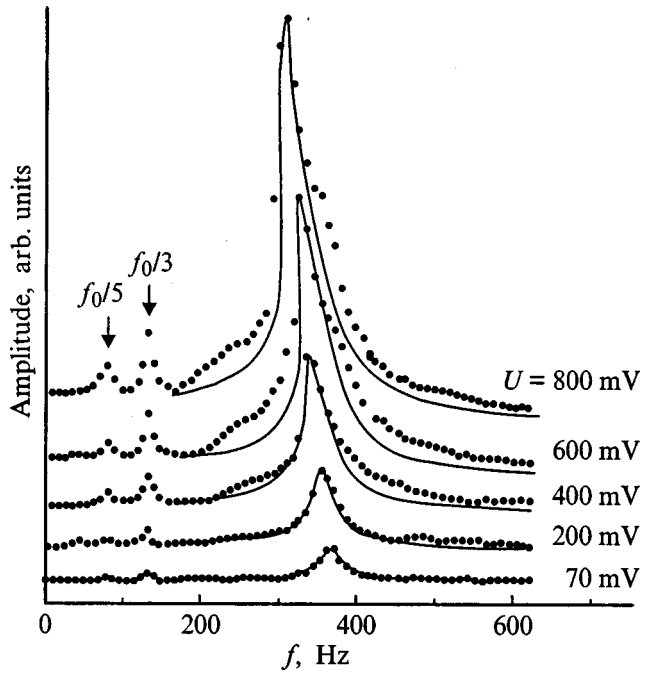

FIG. 4. Microwave-conductivity resonance response $\Delta\sigma_{MW}$ obtained for different values of $U_{\sim}$ in an external magnetic field $H=7$ kOe at $T=300$ K. Solid lines: calculations made in the nonlinear-oscillator approximation (see text for explanations).

the sample was maintained constant ($U_{\sim}=500$ mV). The peak in the dependence of $\Delta\sigma_{MW}$ on the frequency f of the voltage acting on the sample becomes noticeable at $T\sim100$ K. As the temperature increases, the peak grows in intensity and shifts toward lower frequencies. The peak of the resonant $\Delta\sigma_{MW}$ amplitude enhancement reaches the maximum intensity at about $T\sim300-320$ K. The peak amplitude decreases rapidly with a further increase of temperature. The variation of the resonant response frequency f_0 is the strongest within the temperature region from 150 to 300 K. Figure 3a and 3b illustrates graphically the phenomenon. Note the coincidence of the main features in the above-mentioned relations with the behavior of the magnetoresistance $\Delta\rho/\rho_0$ in the crystals studied (Fig. 3c). The peak of the resonance response reaches a maximum at $T\sim300$ K, where $\Delta\rho/\rho_0$ starts to grow rapidly. The drop in the response intensity is accompanied by a decrease of $\Delta\rho/\rho_0$. None of these two effects is observed for $T>T_c\sim360$ K.

Figure 4 presents a part of the family of resonant microwave response curves obtained by varying the ac voltage $U_{\sim}$ across the sample. The temperature $T=300$ K and the magnetic field $H=7$ kOe were fixed. One readily sees that as $U_{\sim}$ increases, the resonance line increases in intensity too, and becomes distorted. The maximum of the curve shifts toward lower frequencies. The peaks at the $f_0/3$ and $f_0/5$ frequencies do not change position in the spectrum. This behavior is typical of forced oscillations in nonlinear systems under harmonic excitation. It can be added that at large $U_{\sim}$ amplitudes the resonance curve exhibits a slight hysteresis with increasing and decreasing frequency f. This deviation of the resonance curve from single-valuedness is also a consequence of the nonlinearity of the system under study.

Interestingly, if one fixes $U_{\sim}$ at a given temperature but varies the external magnetic field, a similar family of resonance curves is obtained (Fig. 5). This permits a conclusion that the amplitude of the exciting force depends on a combination of the quantities H and $U_{\sim}$.

Note that different samples could differ slightly in the magnitude of f_0, the width and shape of the resonant response peaks at a fixed temperature. At the same time the pattern of the above effects did not change in any way. We associate the observed differences with the quality of the single crystals used, including nonuniform impurity distribution over the sample. This conclusion is corroborated indirectly by studies of the magnetic resonance in the crystals.

3. DISCUSSION

The influence itself of both dc and ac transport current on the electrical properties of $La_{0.7}Pb_{0.3}MnO_3$ single crystals turned out to be unexpected. The observed effect is apparently one more manifestation of the unusual electrical and magnetic properties of perovskite-like manganese oxides, so that the mechanisms of the current action and of the GMR in the crystals under study have the same nature. This is supported, first, by all the main features found in the study of the

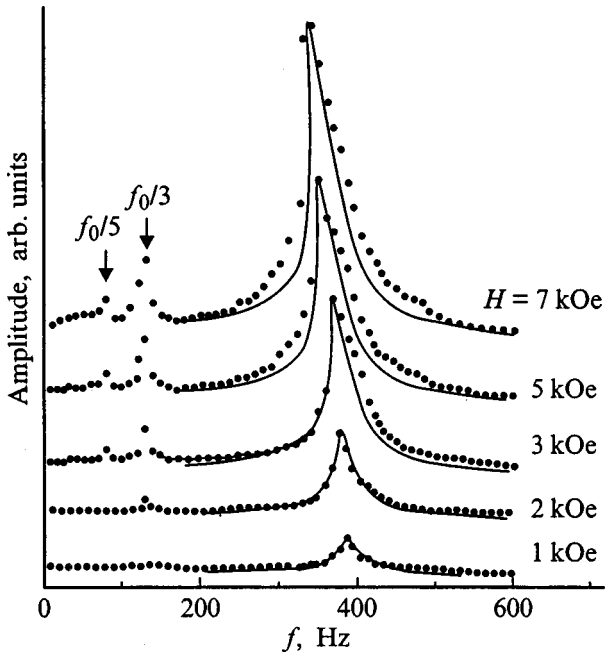

FIG. 5. Microwave-conductivity resonance response $\Delta\sigma_{MW}$ obtained for different strengths of external magnetic field, $U_{\sim}=500$ mV, and $T=300$ K. Solid lines: calculations made in the nonlinear-oscillator approximation (see text for explanations).

temperature dependences being correlated, and, second, by the behavior of the above effects in an external magnetic field.

In order to describe in detail the response of a system to a change in an external parameter, one has to know its internal structure, i.e., its inherent interactions and the mechanisms by which the current and magnetic field act on the state of the substance. Unfortunately, the main question of the mechanisms of the current action on microwave conductivity, as of the nature of the other magnetoelectric phenomena in manganites, remains unanswered.

On the other hand, the internal structure of a system can be judged from its response to a perturbation. Thus an analysis of the dynamic behavior of σ_{MW} as a function of the amplitude and frequency of the modulating voltage, temperature, and magnetic field may provide additional information concerning the nature of interactions in the system under study.

Consider first the $H=0$ case. The dependence of the response amplitude on the frequency of the ac voltage applied to the sample (Fig. 1) is characteristic of the case where the processes accounting for the variation of the propeties of the system occur at a finite rate. As a result, the response of the system lags behind the external perturbation (the magnetic aftereffect is a particularly revealing example of such a behavior). In the simplest case, the $\sigma_{MW}(t)$ function is determined only by one relaxation time τ_r. This can be written mathematically as follows[6]

$$\frac{\partial\sigma_{MW}}{\partial t}=-\frac{\sigma_{MW}-\sigma^e_{MW}}{\tau_r}, \tag{6}$$

where σ^e_{MW} is the equilibrium value of the microwave conductivity to which the system relaxes. We shall assume the perturbation to be small, in which case the response can, in a first approximation, be presented as[3]

$$\sigma^e_{MW}=\xi U^2+\sigma_0, \tag{7}$$

where ξ is a constant, the quadratic dependence on U is a consequence of the independence of $\Delta\sigma_{MW}$ of the polarity of the applied voltage, and σ_0 is the dc component of the microwave conductivity, which is not seen in an experiment. We present the ac voltage in the form

$$U=U_0e^{ift}. \tag{8}$$

Because of the lag, the microwave conductivity can be written

$$\sigma_{MW}=A_2e^{i(2ft-\delta)}+\sigma_0, \tag{9}$$

where $2f$ corresponds to the response at the doubled perturbation frequency, and A_2 is the response amplitude. Substituting (7), (8), and (9) into Eq. (6) yields

$$A_2=\frac{\xi U_0^2}{1+(2f\tau_r)^2}(\cos\delta+2f\tau_r\sin\delta), \tag{10}$$

$$\tan(\delta)=2f\tau_r, \tag{11}$$

The relations thus obtained fit with a good accuracy to experimental data for $\xi=162$ ($U_{\sim}=500$ mV) and $\tau_r=4.4\times10^{-5}$ s.

Thus invoking only one time constant τ_r is a good enough approximation to determine the response time of a sample to an applied voltage. We have essentially employed a classical relaxation model of an overdamped oscillator, in which the friction coefficient is much larger than the characteristic oscillator natural frequency. Actually, the processes affecting the variation of the electrical properties of a material under study should most likely be characterized by a spectrum of time constants (which corresponds to an ensemble of oscillators with a certain distribution function). The approximation we have used is equivalent to introducing some average effective time constant. A more substantial conclusion could be drawn after a special investigation of the behavior of the system response to a perturbation in time.

We shall instead dwell on the microwave response of a sample to an ac current in an external magnetic field. Of particular significance here is the resonant enhancement of the response amplitude at the f_0, $f_0/3$, and $f_0/5$ frequencies, while at all other frequencies the response signal exhibits usual relaxation. Thus the dynamic behavior of the microwave conductivity of a sample in an external magnetic field is characterized by two time constants ($\tau_r\sim10^{-3}$ s and $\tau_0\sim1/f_0\sim10^{-3}$ s) differing by two orders of magnitude. This difference permits one, in a first approximation, to consider the processes responsible for each of the times separately.

As follows from the above experimental data, we have here obviously forced oscillations in a nonlinear dynamic system. It appears only natural to choose as a first step the simplest model, i.e., a nonlinear oscillator. Within this approximation, the equation of motion for the dynamic behavior of the microwave conductivity σ_{MW} of the system under study can be written

$$\frac{d^2x}{dt^2}+2\delta\frac{dx}{dt}+f_0^2x+g(x)=P\cos(\Omega t). \tag{12}$$

Here $x=\sigma_{MW}/\sigma_n$ is a dimensionless variable, σ_n is an arbitrary normalization factor, δ is the damping parameter, f_0 is the natural frequency of a linear oscillator, P is the amplitude of the external force, Ω is its frequency, $g(x)=-\partial U(x)/\partial x$ is a function characterizing the nonlinearity, and $U(x)$ is the oscillator potential energy.

The properties of the system determining the natural oscillation frequency f_0 vary with temperature, and at a fixed temperature f_0 remains constant. This can be seen from the constancy of the peak positions at the $f_0/3$ and $f_0/5$ frequencies in the response spectrum. The variation of the oscillator frequency with oscillation amplitude is a consequence of the nonlinearity (nonisochronism). The presence in the response spectrum of odd harmonics only permits a conclusion that the $g(x)$ function must be odd. The nonlinear relations characterizing the properties of a system are usually approximated with a polynomial. Thus we can write to the seventh power of x

$$g(x)=\alpha x^3+\beta x^5+\gamma x^7. \tag{13}$$

Further analysis shows that within the model considered here δ also remains constant at a fixed temperature. The quantities $U_\sim$ and H determine the amplitude of the external force

$$P=P(U_\sim,H). \tag{14}$$

We restrict ourselves to obtaining the solution of Eq. (12) for the frequency of the external force. In the case of weak nonlinearity it can be solved, for instance, by harmonic approximation[7]

$$f^2=(f_m^2-2\delta^2)\pm\sqrt{\frac{P^2}{A^2}-4\delta^2(f_m^2-\delta^2)}, \tag{15}$$

where

$$f_m^2=f_0^2\left(1+\frac{3}{4}\alpha A^2+\frac{5}{8}\beta A^4+\frac{35}{64}\gamma A^6\right) \tag{16}$$

is the squared frequency of the same nonlinear system for $\delta=0$ and A is the amplitude. Using the skeleton curve equation (16), one can readily find the experimental values of the α, β, and γ parameters. The best fit was obtained for $\alpha=-1.25\times10^{-5}$, $\beta=2.45\times10^{-10}$, and $\gamma=-1.5\times10^{-15}$, irrespective of which external perturbation parameter, $U_\sim$ or H, was varied. Next, by fitting the solution of (15) to experimental data (Figs. 4 and 5), one obtains the form of the relation (14). Calculations show that the external force P is a linear function of both $U_\sim$ and H. Note that within the approximation employed here the theoretical resonant-response curves reproduce well enough the experimental relations.

Knowing $g(x)$, one could reconstruct the potential function of the system under study and reproduce qualitatively the complete pattern of the motion of the nonlinear oscillator. We are more interested, however, in the physical meaning of the relations obtained, because they are connected with actual interactions in the material. Unfortunately, as this was pointed out more than once, the understanding of the mechanisms involved is far from being unambiguous.

As before,[3] we espouse the viewpoint that the mechanism underlying the phenomena considered here is phase separation[2,8]. Our opinion is supported by additional magnetic-resonance studies of single-crystal $La_{0.7}Pb_{0.3}MnO_3$. Within a broad temperature range below T_c one observes two magnetic-resonance absorption lines, which correspond to two magnetic phases in the sample. Field-frequency relations permit their identification as the ferromagnetic (FM) and paramagnetic phases. Moreover, the relation between the phase volumes at a fixed temperature is governed by the external magnetic field. It is this phenomenon that underlies the mechanism accounting for the GMR.

In our case, the transport current, as well as the magnetic field, influences the volume ratio of the phases differing in the magnetic state and, accordingly, in the conductivity. This affects the microwave conductivity of a sample.[3] Incidentally, the response of a sample to the action of a current is of the opposite sign to that of the magnetic field. This can be qualitatively understood based on the following considerations. The total free energy of a two-phase system is given by the expression[9]

$$E=E_V+E_S+E_Q+E_M. \tag{17}$$

Here E_V and E_S are, respectively, the volume and surface energies of the conduction electrons, E_Q is the Coulomb interaction energy between regions with different electron concentrations, and E_M is the magnetic energy, which includes the energies of the s–d exchange, direct exchange coupling, and interaction with the external field. A variational analysis of Eq. (17) yields the equilibrium dimensions of the phase nonuniformities. External magnetic field acts on the magnetic part of the free energy, E_M, which results in an increase of the FM-phase volume of the crystal.[10] Transport current increases the kinetic energy of the conduction-band electrons (through the change of E_V and E_S), which brings about destruction of the ferromagnetism and, accordingly, a decrease of the FM-phase volume in the crystal.

The response of a system to ac current is governed by the dynamics of phase volume variation. In this case the frequency f_0 should apparently reflect the characteristic size of the phase nonuniformity. As the temperature increases, the volume of the minor phase increases and, as a result, the frequency f_0 decreases, while the resonance response grows in intensity (Fig. 3). Above T_c, the sample becomes spatially uniform.

Within the oscillator approach, a two-phase system can be described in terms of the bistable oscillator model. In this case the presence of two characteristic time scales, τ_r and τ_0, can be explained as follows. The relaxation behavior corresponds to motion in the vicinity of one of the equilibrium states (intrawell dynamics), whereas the other scale characterizes the average time required to cross the potential barrier (global dynamics).

Thus our experimental studies have revealed two characteristic scenarios of the behavior of microwave conductivity in single-crystal $La_{0.7}Pb_{0.3}MnO_3$ samples acted upon by an ac current. In the absence of an external magnetic field,

the response has a relaxation pattern with a characteristic relaxation time $\tau_r \sim 10^{-5}$ s. When placed in an external magnetic field, the low-frequency response spectrum exhibits, superposed on the relaxation behavior, peaks of resonantly enhanced response amplitude. An analysis of the results made in terms of the oscillator approach yielded the parameters of the system determining the nature of possible interactions, which are responsible for the observed magnetoelectric effects.

It may be pointed out in conclusion that the temporal behavior of the conductivity of manganites subjected to a magnetic field presents a certain interest. As far as we know, no relevant studies have thus far been carried out, although this aspect of the problem is crucial from the standpoint of applications of the GMR effect.

[1] A. J. Millis, Nature (London) **392**, 147 (1998).
[2] É. L. Nagaev, Usp. Fiz. Nauk **166**, 833 (1996).
[3] N. V. Volkov, G. A. Petrakovskiĭ, K. A. Sablina, and S. V. Koval', Fiz. Tverd. Tela (St. Petersburg) **41**, 2007 (1999) [Phys. Solid State **41**, 1842 (1999)].
[4] L. D. Landau and E. M. Lifshits, *Electrodynamics of Continuous Media* (Pergamon Press, Oxford, 1960; Nauka, Moscow, 1982)].
[5] Yu. E. Gordienko and B. G. Borodin, Prib. Tekh. Éksp. No. 1, 189 (1984).
[6] S. Tikazumi, *Physics of Ferromagnetism* (Mir, Moscow, 1987).
[7] V. V. Migulin, V. I. Medvedev, E. R. Mustel', and V. N. Parygin, *Fundamentals of the Theory of Oscillations* (Nauka, Moscow, 1978).
[8] L. G. Gor'kov, Usp. Fiz. Nauk **168**, 664 (1998).
[9] É. L. Nagaev, *Magnets with Complex Exchange Interactions*, (Nauka, Moscow, 1988).
[10] E. L. Nagaev, Zh. Éksp. Teor. Fiz. **114**, 2225 (1998) [JETP **87**, 1214 (1998)].

Translated by G. Skrebtsov

LOW-DIMENSIONAL SYSTEMS AND SURFACE PHYSICS

Interaction between the exciton and nuclear spin systems in a self-organized ensemble of InP/InGaP size-quantized islands

R. I. Dzhioev, B. P. Zakharchenya, V. L. Korenev, and M. V. Lazarev

A. F. Ioffe Physicotechnical Institute, Russian Academy of Sciences, 194021 St. Petersburg, Russia
(Submitted September 20, 1999)
Fiz. Tverd. Tela (St. Petersburg) **41**, 2193–2199 (December 1999)

Magnetic interaction between spin-polarized nuclei and optically oriented excitons in a self-organized ensemble of size-quantized InP islands in an InGaP matrix has been studied in a magnetic field in Faraday geometry. The effective magnetic fields generated by polarized nuclei at excitons have been measured. The strengths of these fields were found to be different for active and inactive excitons because of the difference between the excitonic g factors. The heavy-hole g factor has been determined. The active and inactive excitonic states were found to be coupled through cross-relaxation. © *1999 American Institute of Physics.* [S1063-7834(99)01712-8]

The ground state of the $e1-hh1$ $(1s)$ heavy-hole exciton in a zincblende quantum well is fourfold degenerate with the angular-momentum projection $M=s+j=\pm 1,\pm 2$ on the growth axis $z\|[001]$ of the structure (the electron spin $s=\pm 1/2$ and the hole angular momentum $j=\pm 3/2$). Exchange interaction splits this state into a radiation doublet $|\pm 1\rangle$ and two closely lying optically inactive singlets, which are a superposition of the $|\pm 2\rangle$ states. When the exciton becomes localized at an anisotropic island, the system symmetry is lowered, and the radiation doublet splits into two sublevels, which are linearly polarized in two orthogonal directions.[1] In this case, when excitons are excited by circularly polarized light, photoluminescence (PL) spectra obtained in a zero magnetic field do not contain a circularly polarized component because of the anisotropic exchange interaction, which mixes the $|+1\rangle$ and $|-1\rangle$ radiative states. If observed in Faraday geometry in a magnetic field ($\mathbf{B}\|z$), the Zeeman effect decouples the latter to make the PL circularly polarized, i.e. the magnetic field restores the orientation of the optically active excitons.[2] Similarly, magnetic field restores the spin polarization of the optically inactive excitons as well (the $|\pm 2\rangle$ states). Their polarization becomes manifest in the PL of n-type InP islands in the InP/InGaP system due to the formation of a complex of an exciton bound to a neutral donor, D^0X (or the trion, a charged exciton).[3] Here the degree of PL circular polarization of the D^0X complex is determined by the polarization of both the excitons and of the donor-bound electrons before its creation.

Hyperfine interaction between the electrons and the lattice nuclei affects substantially the spin splitting of the excitonic levels and the degree of the exciton circular polarization. The optically oriented electrons in excitons impart their angular momentum to the nuclear spin system (the Overhauser effect). The polarized nuclei, in their turn, generate an effective magnetic field, which changes the spin splitting of the levels and, hence, the orientation of the excitons and the polarization of their recombination radiation. The dynamic polarization of nuclei in GaAs/AlGaAs quantum wells was reported in Ref. 4, which showed that the nuclear polarization is due to the electrons and excitons localized at donors or well thickness fluctuations. This conclusion was subsequently confirmed by near-field spectroscopy experiments,[5] in which one succeeded in directly measuring the level splittings of the excitons localized at single-island fluctuations of the quantum-well thickness. The nuclei in a self-organized ensemble of size-quantized InP islands in an InGaP matrix were found to be dynamically polarized.[6]

This paper reports on the effect of spin-polarized nuclei on the optical orientation of both active and inactive excitons in a self-organized ensemble of size-quantized InP islands in an InGaP matrix, which was studied in a magnetic field in Faraday geometry. The effective magnetic fields of polarized nuclei are different for the active and inactive excitons because of the difference between the excitonic g factors. The nuclear fields, as well as the heavy-hole g factor, have been determined.

1. EXPERIMENTAL

The structures were grown by MOCVD epitaxy on GaAs substrates and were made up of a 500-nm-thick $In_{0.5}Ga_{0.5}P$ buffer layer lattice-matched to the substrate, a layer of nanosized InP islands with a nominal thickness of three (sample ISL1) or five (sample ISL2) monolayers, and a 50-nm-thick $In_{0.5}Ga_{0.5}P$ cap layer. The layers contained donor impurities at a level of 10^{15} cm^{-3}.

The samples to be studied, immersed in liquid helium in a cryostat, were placed at the center of a coil. The excitation was provided by a He–Ne laser beam ($h\nu=1.96$ eV) of intensity ~ 10 W/cm^2 directed along the structure growth axis, $z\|[001]$. The photoluminescence polarization was measured in Faraday geometry in a magnetic field near the maxi-

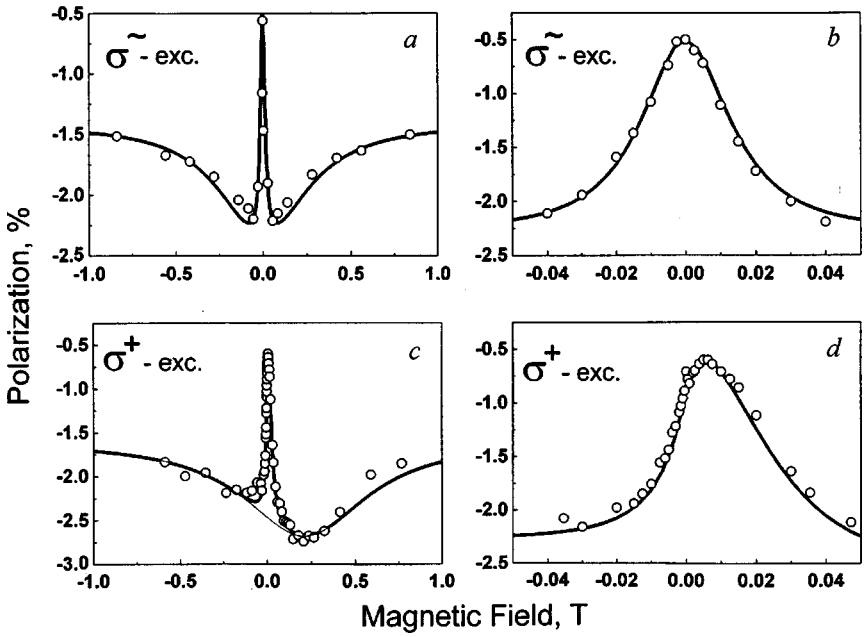

FIG. 1. Degree of circular polarization of the luminescence $\rho_c(B)$ vs external magnetic field obtained in Faraday geometry on the ISL1 sample. The experimental points were measured under (a,b) alternating circular polarization ($\sigma^{\sim}$ excitation) and (c,d) constant polarization (σ^+ polarization). The solid curves were constructed using Eqs. (1)–(5), as described in text.

mum of the InP-island ($\lambda = 723$ nm) recombination-radiation band. The optical orientation and measurement of the degree of circular polarization of the recombination radiation were performed in two ways. By the first method, the sign of the circular polarization of the exciting light was varied with a photoelastic polarization modulator at a high frequency (with a modulation period of 33 μs), and the luminescence polarization was analyzed with a fixed quarter-wave phase plate and a linear polarizer. In this case the nuclear spin cannot follow the variation of the polarization of the photoexcited electrons, so that there is no dynamic polarization of the nuclei (the nuclear spin-relaxation time $T_1 \sim 0.1-1$ s, Ref. 7). One measures the effective degree of circular polarization $\rho_c = (I_+^+ - I_+^-)/(I_+^+ + I_+^-)$, where I_+^+ and I_+^- are the intensities of the σ^+ luminescence component under σ^+ and σ^- excitation, respectively.

The Overhauser effect becomes manifest when one employs the second technique, namely, excitation with light whose circular polarization does not vary in time. The luminescence polarization is analyzed with a quartz modulator and a linear polarizer. One measures the degree of circular polarization $\rho_c = (I_+^+ - I_-^+)/(I_+^+ + I_-^+)$. The samples we used practically did not exhibit circular dichroism, so that the ρ_c parameters are the same in both geometries and may be considered as the conventional Stokes parameter characterizing the circular polarization of luminescence caused by that of the excitation.

2. OPTICAL ORIENTATION OF ELECTRONS AND EXCITONS IN THE ABSENCE OF NUCLEAR POLARIZATION

The $\rho_c(B)$ relation corresponding to the recombination of the D^0X complex and measured on the ISL1 sample under alternating excitation ($\sigma^{\sim}$) is shown in Fig. 1a and 1b with circles. The $\rho_c(B)$ relation is invariant under magnetic field reversal and reflects the recovery of the spin orientation of excitons as the Zeeman splitting becomes larger than their exchange splitting. For $B=0$, the excitons are unpolarized, and the nonvanishing polarization $\rho_c(B=0) \approx -0.5\%$ is due to the field-independent spin polarization of the donor-bound electrons. The relation shown graphically in Fig. 1a and 1b was studied comprehensively,[3] and the nonmonotonic variation of ρ_c with magnetic field was interpreted as follows. When circularly polarized light is used for excitation, the circular polarization of the recombination radiation of the D^0X complexes formed by neutral donors trapping optically inactive excitons has the sign opposite to that of the excitation. If, however, the complex is due to optically active excitons becoming trapped by a neutral donor, the PL polarization coincides in sign with the exciting polarization. Because the orientation recovery of the active and inactive excitons occurs at different magnetic fields, the resultant $\rho_c(B)$ relation should be nonmonotonic. This can be illustrated with a simple example. Light with σ^+ polarization creates active excitons with a momentum projection $M=+1$. If the hole relaxes in spin before the exciton has become bound to a neutral donor, one will have in a steady state one half of the $M=+1$ excitons and one half of the optically inactive excitons with $M=-2$. When trapped by a donor, the active excitons create a complex with a total-momentum projection $M_T=+3/2$ (because of the electron spins being antiparallel). Recombination of such a complex gives rise to σ^+ luminescence. Similarly, optically inactive excitons make up a complex with $M_T=-3/2$, whose recombination is accompanied by emission of a σ^- photon. In a zero field, the excitons are depolarized because of the anisotropic exchange interaction mixing the $|+1\rangle$ and $|-1\rangle$ states of the optically active excitons, and the $|+2\rangle$ and $|-2\rangle$ states of the optically inactive excitons. Magnetic field decouples them and restores the optical orientation of the excitons. Incidentally, as the field increases, the first to recover is the orientation of the optically inactive excitons (their exchange splitting is less than that of the active states), thus making ρ_c more negative (Fig. 1a and

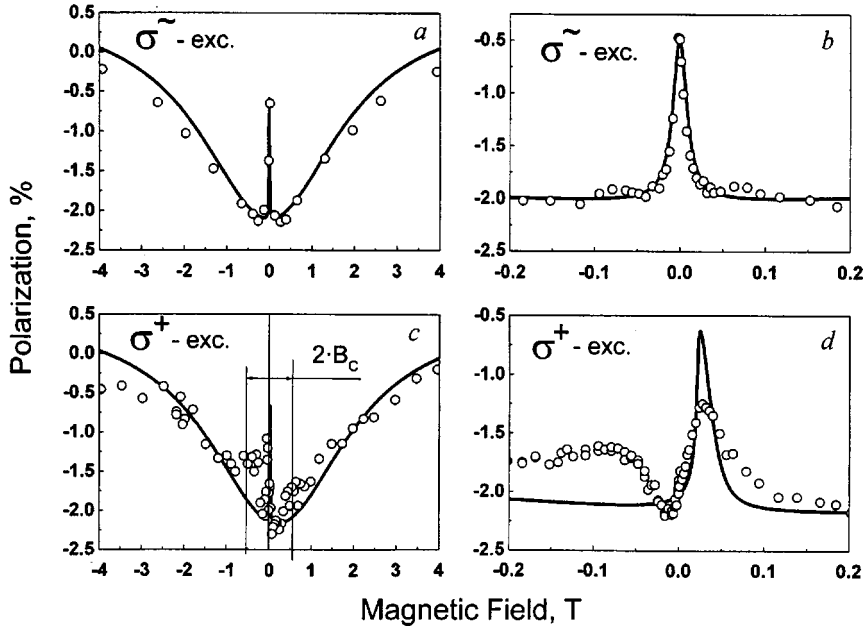

FIG. 2. Same as in Fig. 1, but for the ISL2 sample. Note the two additional maxima (c) at $B \sim 0.5$ T, which is interpreted as a manifestation of cross relaxation.

1b). Strong fields restore the orientation of the active excitons, and the decrease of ρ_c is replaced by its growth (Fig. 1a). Thus the $\rho_c(B)$ relation is nonmonotonic because of the active and inactive excitons being polarized in opposite directions. Their orientation is restored in substantially different magnetic fields, which makes possible an analysis of the behavior of both exciton species by measuring only one $\rho_c(B)$ relation.

3. OPTICAL ORIENTATION OF EXCITONS IN THE PRESENCE OF NUCLEAR POLARIZATION

Consider now exciton polarization under excitation by light with a constant circular polarization (in this case, the nuclei are polarized). The circles in Fig. 1c and 1d identify the $\rho_c(B)$ relation measured in the ISL1 sample under σ^+ excitation. This relation exhibits a narrow maximum (with a halfwidth ≈ 150 G), which is reached in a field $B \approx 54$ G (Fig. 1d), rather than at $B=0$, as was the case with excitation by light with an alternating polarization. This indicates the existence of a field generated by dynamically polarized nuclei. The optically inactive excitons are acted upon by a field equal to the difference between the external field B and the effective nuclear field B_{N2}. Similarly, the optically active excitons feel, besides the external field, also the nuclear field B_{N1}. Their polarization reaches a minimum (shown in Fig. 1c with a thin solid line) at a field $B=B_{N1}=0.2$ T, where the external field compensates the nuclear one. If the nuclear field did not depend on the external field B, nuclear polarization would have resulted only in a shift of the $\rho_c(B)$ relation in weak and strong fields along the horizontal axis by the magnitude of the nuclear fields B_{N2} and B_{N1}, respectively. Moreover, on finding B_{N2} and B_{N1} from an experiment one can determine the magnitude and sign of the hole g factor, because the different nuclear fields are due in this case only to the difference between the active, g_1, and inactive, g_2, excitons: $B_{N1}/B_{N2}=-g_2/g_1=-(g_h+g_e)/(g_h-g_e)$, ($g_2=g_h+g_e$ and $g_1=g_h-g_e$, see Sec. 4). The electronic g factor g_e in these samples coincides with the g factor of bulk $In_{0.5}Ga_{0.5}P$, $g_e=1.6$.[8] Because $B_{N1}/B_{N2} \approx 35$, the hole g factor can be estimated as $g_h=1.5$. However Fig. 1d shows clearly that the recovery of the inactive-exciton orientation is asymmetric with respect to the maximum. This means that the nuclear field acting on the inactive excitons depends itself on the external magnetic field. This finds an explanation in the fact that nuclei are polarized not only by the donor-bound electrons, whose average spin (and, hence, the contribution to nuclear polarization) is independent of magnetic field, but also by the exciton electrons with field-dependent polarization.[6] As a result, the system becomes substantially nonlinear; indeed, the oriented electrons at the donors and in excitons polarize the nuclei, which, in their turn, generate an effective magnetic field influencing the exciton orientation. The recovery of the orientation of the optically active excitons is symmetric relative to the minimum ($B_{\min} \approx 0.2$ T, see Fig. 1c). The absence of asymmetry implies that the nonlinear coupling of nuclei with active excitons is weaker than that with inactive ones. The fact is that nuclear fields give rise to an asymmetry in the dependence of exciton orientation on the external field, provided the characteristic exciton-level splitting in the nuclear field AIP_N (A is the hfs constant, I is the nuclear spin, and P_N is the degree of nuclear polarization) exceeds the anisotropic splitting δ_2 (δ_1) of the active (inactive) states. Because $\delta_2 > \delta_1$,[9] in weak fields (inactive excitons) the asymmetry of the $\rho_c(B)$ curve is more strongly pronounced than that in the strong-field domain (active excitons). As we shall see in Sec. V, in the given sample $\delta_2 \approx 4\ \mu\text{eV} > AIP_N \approx \delta_1 \approx 2.7\ \mu\text{eV}$, in accordance with the above qualitative consideration. Moreover, the polarization of the inactive excitons [governed by the $\rho_c(B)$ dependence in weak fields $B<0.1$ T, see Fig. 1a and 1c] is $\approx 1.8\%$, whereas that of the active excitons (the region of strong fields $B>0.1$ T) is $\approx 0.7\%$, i.e., almost three times smaller. Because the polarization of the nuclei is proportional to that of the electron in the exciton (i.e., to that of the active and

inactive excitons), the contribution of the active excitons to nuclear polarization in the given sample may be neglected. Thus the nuclei in sample ISL1 are polarized both by donor-bound electrons and by the optically inactive excitons.

The $\rho_c(B)$ dependence of sample ISL2 obtained in the absence of nuclear polarization behaves similarly to that of the ISL1 sample (Fig. 2a and 2b). The situation changes substantially, however, when one applies σ^+ excitation, i.e., in the presence of nuclear polarization (Fig. 2c and 2d). Besides the main maximum, the $\rho_c(B)$ curve exhibits now two additional diffuse maxima at $B=\pm B_c$, where $B_c \approx 0.5$ T. This means that at the fields $B=\pm B_c$ the inactive excitons undergo additional depolarization. We associate this with cross-relaxation effects, i.e., transitions occurring in the case of equal splittings of the active and inactive states (see Sec. 5).

4. THEORETICAL MODEL

We assume the nuclei in InP islands to be polarized through contact interaction with electrons and neglect, as in the case of bulk semiconductors,[7] the magnetic interaction of the nuclei with the holes. Polarized nuclei generate an effective magnetic field, which splits the electronic spin levels by AIP_N. In the presence of nuclear polarization, the Zeeman splitting of the electronic spin levels is $\mu g_e B + AIP_N$, whereas for holes it is $\mu g_h B$. Now one readily obtains for the Zeeman splittings of the optically active $|\pm 1\rangle$ states, ΔE_1, and of the optically inactive $|\pm 2\rangle$ ones, ΔE_2,

$$\Delta E_1 = \mu(g_h - g_e)B - AIP_N \equiv \mu g_1 (B - B_{N1}),$$
$$\Delta E_2 = \mu(g_h + g_e)B + AIP_N \equiv \mu g_2 (B - B_{N2}), \qquad (1)$$

where $B_{N1} = AIP_N/\mu g_1$ and $B_{N2} = -AIP_N/\mu g_2$ are the effective magnetic fields created by the nuclei at the optically active and inactive excitons, respectively. Note that the total splittings of the radiative, ΔE_r, and nonradiative, ΔE_{nr}, states are determined not only by their Zeeman but the anisotropic exchange splittings δ_2 and δ_1, respectively, and can be written

$$\Delta E_r = \sqrt{\Delta E_1^2 + \delta_2^2} \quad \text{and} \quad \Delta E_{nr} = \sqrt{\Delta E_2^2 + \delta_1^2}. \qquad (1a)$$

Dynamic polarization of nuclei appears as a result of their hyperfine interaction with electrons.[7] Optically oriented electrons impart the angular momentum to the nuclear spin system. Because the samples studied contain donor impurities, the nuclei can be polarized not only by the exciton electrons but by donor-bound electrons as well. It appears therefore reasonable to assume that the hyperfine splitting of electronic levels

$$AIP_N = \alpha P_d + \beta P_2(B) + \gamma P_1(B) \qquad (2)$$

includes the contribution to nuclear polarization due to donor-bound optically oriented electrons with polarization P_d (the first term), as well as contributions of the optically oriented electrons in the inactive and active excitons [the second and third terms, respectively; in the final count, the polarization of electrons in excitons is determined by that of the excitons themselves, $P_1(B)$ and $P_2(B)$]. The phenomenological parameters α, β, and γ are assumed to be independent of magnetic field, and they characterize the efficiency of nuclear polarization by donor-bound electrons and electrons in the optically inactive and active excitons, respectively. The degree of orientation of the optically active excitons $P_1(B)$, determined by the competition between the Zeeman splitting ΔE_1 [see (1)] and the anisotropic exchange splitting δ_2 of optically inactive states,[1] can be written

$$P_1(B) = P_1^0 \frac{\Delta E_1^2}{\Delta E_1^2 + \delta_2^2} = P_1^0 \frac{(B - B_{N1})^2}{(B - B_{N1})^2 + B_1^2}, \qquad (3)$$

where $B_1 = \delta_2/\mu g_1$, and P_1^0 is the initial degree of polarization of the excitons at the instant of their formation. Similarly, the degree of polarization of the inactive excitons

$$P_2(B) = P_2^0 \frac{\Delta E_2^2}{\Delta E_2^2 + \delta_2^2} = P_2^0 \frac{(B - B_{N2})^2}{(B - B_{N2})^2 + B_2^2}. \qquad (4)$$

Here the anisotropic exchange splitting of the inactive states δ_1 determines the characteristic field $B_2 = \delta_1/\mu g_2$, and P_2^0 is the initial degree of polarization of the inactive excitons. Equations (1)–(5) describe the behavior of the nonlinear exciton-nuclear spin-system of nanosized InP islands, in which the nuclear spin affects the exciton polarization (through the nuclear field) and, in its turn, depends on the latter (through the Overhauser effect). In an experiment one measures the degree of circular polarization of the luminescence produced by recombination of the D^0X complex (exciton bound to a neutral donor) or of the trion.[3] The ground state of the D^0X complex is made up of two electrons with antiparallel spins and a hole. Therefore the hole in an optically pumped complex is oriented. However the hole orientation is determined by the polarization of excitons (both active and inactive) and of the donor-bound electrons before the D^0X formation. Then the degree ρ_c of circular polarization of the D^0X luminescence should contain information on the electron and exciton polarizations[3]

$$\rho_c(B) = (2W - 1)P_d + (1 - W)P_2(B) + WP_1(B). \qquad (5)$$

Here the numbers of the active and inactive excitons relate to one another as W to $(1-W)$. The magnetic-field dependence of ρ_c comes only from the field dependence of the exciton polarization, because the polarization of donor-bound electrons does not depend on the field in Faraday geometry.[3] Equations (1)–(4) describe the steady-states of the exciton-nuclear spin system in quantum dots, which can be detected by studying the PL polarization given by Eq. (5).

5. DISCUSSION

We are turning now to a quantitative comparison of theory with experiment for the ISL1 sample (Fig. 1), where, as we have seen, the cross-relaxation effects may be neglected. The simplest way consists in starting the treatment with the case of alternating excitation (Fig. 1a and 1b), where the nuclear polarization is zero. Then we can set $P_N = 0$, $B_{N1} = B_{N2} = 0$ in Eqs. (1)–(4). In this case there are five fitting parameters. Three of them, $(2W-1)P_d = -0.5\%$, $(1-W)P_2^0 = -1.86\%$, and $WP_1^0 = 0.95\%$, characterize the contributions to the polarized PL of the D^0X complex due to

electrons bound to donors and those present in the optically inactive and active excitons, respectively. Their magnitude can be readily estimated from the characteristic points in the $\rho_c(B)$ relation. For instance, the maximum in the $\rho_c(B)$ relation corresponds to the case where the excitons are unpolarized, and therefore $(2W-1)P_d \equiv \rho_c(B=0) = -0.5\%$. Since the optical orientation of inactive excitons is restored in weaker fields than that of the active states, one can readily estimate the contributions due to the inactive and active excitons [the $(1-W)P_2^0$ and WP_1^0 parameters]. The two remaining parameters, $B_1 = \delta_2/\mu g_1$ and $B_2 = \delta_1/\mu g_2$, determine the characteristic magnetic fields restoring the optical orientation of the active and inactive excitons, accordingly. They were chosen so as to fit the theoretical plots (solid curves in Fig. 1a and 1b) to the experiment. Incidentally, the best fit is obtained for $B_1 = 0.3$ T and $B_2 = 0.016$ T. These values will be used in the treatment of the experimental results obtained in the presence of nuclear polarization, i.e., under σ^+ excitation (the circles in Fig. 1c and 1d). In this case, the excitons feel, besides the external field, the effective nuclear magnetic field as well. The optically active excitons are acted upon by the nuclear field $B_{N1} = AIP_N/\mu g_1 = [\alpha P_d + \beta P_2(B)]/\mu g_1$, and the inactive ones, by the field $B_{N2} = -AIP_N/\mu g_2 = -[\alpha P_d + \beta P_2(B)]/\mu g_2$. We have neglected here the contribution to the nuclear polarization due to the optically active excitons (see Sec. 3), i.e., the γ parameter in Eq. (2) is zero. Thus four new, unknown parameters appear in the problem, namely, $\alpha P_d/\mu g_1$, $\beta P_2^0/\mu g_1$, $\alpha P_d/\mu g_2$, and $\beta P_2^0/\mu g_2$. The key factor making possible determination of all these parameters is that the polarization of the active and inactive excitons is restored in essentially different fields, and therefore when treating the $\rho_c(B)$ dependence in fields $B < 1$ kG one can neglect the contribution of the optically active excitons to the variation of the PL polarization. The maximum in the $\rho_c(B)$ dependence at $B = 54$ G (Fig. 1d) corresponds to the case where the inactive excitons are depolarized, i.e., where $B \approx B_{N2}$, and the nuclear field $B_{N2} = B_{Nd} = -\alpha P_d/\mu g_2 = 54$ G is determined by the polarization of the donor-bound electrons only. The $B_{NX} = -\beta P_2^0/\mu g_2$ parameter describes the contribution to the nuclear field due to the optically oriented inactive excitons, where the degree of their orientation P_2 is equal to its extreme value P_2^0. Because the P_2 orientation recovers in the total (external plus nuclear) field, and the latter depends, in its turn, on $P_2(B)$, the B_{NX} parameter determines the nonlinear coupling between the exciton and nuclear spins. The nonlinear coupling manifests itself in the asymmetry of the $\rho_c(B)$ dependence relative to the maximum (Fig. 1d). The solid curve in Fig. 1d was constructed using Eqs. (1)–(5) and the above parameters $B_2 = 160$ G and $B_{Nd} = 54$ G, and the B_{NX} parameter was chosen so as to fit the theoretical curve to the experiment. The best fit is obtained at $B_{NX} = -\beta P_2^0/\mu g_2 = 100$ G.

Let us turn now to the strong-field region, $|B| > 1$ kG (Fig. 1a), where the active-exciton orientation is restored. In these fields, the orientation of the inactive excitons is restored too, so that the degree $P_2 = P_2^0$ and does not depend on magnetic field any longer. In these conditions, an optically active exciton is acted upon, besides the external field, by the nuclear field $B_{N1} = (\alpha P_d + \beta P_2^0)/\mu g_1$, which does not depend on B. Now the minimum in the $\rho_c(B)$ dependence (the thin solid line) is reached at $B = B_{N1} = 0.2$ T. The solid line in Fig. 1c was plotted using Eqs. (1)–(5) for the above parameters $\alpha P_d/\mu g_2 = 54$ G, $\beta P_2^0/\mu g_2 = 100$ G, and $B_{N1} = (\alpha P_d + \beta P_2^0)/\mu g_2 = 0.2$ T. Using these values, one can readily determine the g-factor ratio for the active and inactive excitons $g_1/g_2 = (g_h - g_e)/(g_h + g_e) = (B_{Nd} + B_{NX})/B_{N1} = -0.08$. One finds from this the hole g factor $g_h = 1.4$, which is in accord with the estimate obtained in Sec. 3. Note that in contrast to the electronic g factor, the hole g factor is very sensitive to the parameters of a given sample (residual strains, size quantization etc.). Therefore the hole g factor can vary strongly from one sample to another. Knowing the g factors, one can determine the hyperfine splitting of the electronic spin levels in the nuclear field created by the donor-bound electrons, $\alpha P_d = -0.9\,\mu$eV, and by the optically inactive excitons, $\beta P_d^0 = -1.8\,\mu$eV. The anisotropic exchange-coupling parameters for an electron and a hole in an exciton $\delta_1 = 2.7\,\mu$eV and $\delta_2 = 4\,\mu$eV. Note that $\delta_2 > \delta_1$. This is due to the fact that the exchange splitting of exciton levels in a quantum dot is dominated by the long-range part of the exchange interaction,[10] which is actually the result of interaction of the dipole moment of the exciton with the electric field of the medium polarized by the latter. For the optically inactive states, this contribution is zero. Thus our model is in a satisfactory agreement with experiment, which permits one to determine all the main parameters characterizing the exciton-nuclear spin system in a quantum dot.

We are turning now to the results obtained on the ISL2 sample. The $\rho_c(B)$ relation obtained in the absence of nuclear polarization does not differ in shape from the one measured on the ISL1 (Fig. 2a and 2b). The solid curves were constructed using Eqs. (1)–(5) for $P_N = 0$, $(2W-1)P_d = -0.5\%$, $(1-W)P_2^0 = -1.6\%$, $WP_1^0 = 2.7\%$, $B_1 = 2$ T, and $B_2 = 100$ G. The fitting parameters were chosen by the procedure outlined above. In the presence of nuclear polarization (σ^+ excitation), the main maximum in the $\rho_c(B)$ dependence is reached at $B \approx 250$ G. There are also two additional maxima (the cross-relaxation effect), which cannot be accounted for within the model used, which predicts only stabilization of the exciton optical orientation by an external longitudinal magnetic field. Therefore we shall first attempt to treat the plots in Fig. 2c and 2d in the way this was done for the ISL1 sample, i.e., using Eqs. (1)–(5) and neglecting cross-relaxation. The solid curves were drawn for the g factors $g_e = 1.6$, $g_h = 1.1$ and the hyperfine interaction parameters $\alpha P_d = -3.9\,\mu$eV, $\beta P_2^0 = -1.6\,\mu$eV. The exchange splitting of the active states in this sample, $\delta_2 = 55\,\mu$eV, is also larger than that of the inactive ones, $\delta_1 = 1.6\,\mu$eV. One readily sees that theory predicts a qualitatively correct behavior, but the numerical values of the parameters should be considered in this case as not more than estimates. Indeed, first, the main maximum in the weak-field domain (Fig. 2d) is broadened and lower than predicted by theory. This may be due to the nuclear polarization being distributed nonuniformly over an InP island, whereas the model used here assumes that it is uniform over the whole of an island. Second, at intermediate fields, $B \approx \pm 0.5$ T, there

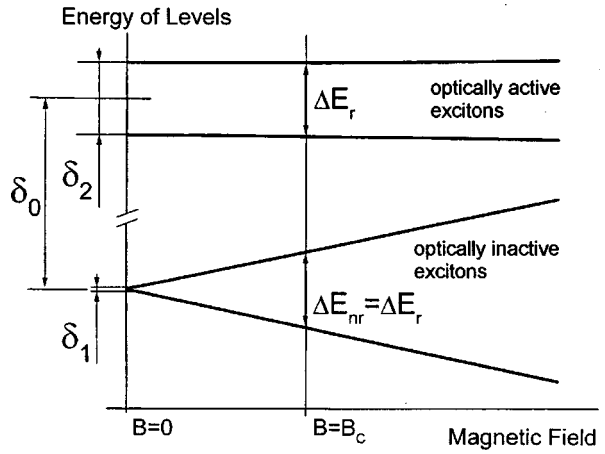

FIG. 3. The exciton fine structure obtained in a magnetic field in Faraday geometry. The energy levels were calculated using Eqs. (1) and (1a) with the parameters $\delta_2=55\,\mu$eV, $g_1=0.5$, $g_2=2.7$, and $\delta_1=1.6\,\mu$eV, which were derived from the plots in Fig. 2 neglecting the cross relaxation. The cross-relaxation field B_c at which the active and inactive states have the same splittings is identified.

are two additional maxima interpreted, as pointed out before, as due to cross-relaxation effects, where the splitting of the active states, ΔE_r, is equal to that of the inactive ones, ΔE_{nr} (Fig. 3). In this case the mixing of active and inactive states may give rise to transitions involving simultaneous spin flip of the active excitons (the $+1\rightarrow-1$ transition) and inactive ones (the $-2\rightarrow+2$ transition). Active excitons are unpolarized in weak fields and, hence, such mixing will depolarize the excitons in inactive states, thus resulting in the appearance of an additional maximum. Because in this sample $\delta_2\gg\delta_1$, for the splitting of the active states in a field $B\sim0.5$ T we have $\Delta E_r\approx\delta_2$, while for the inactive states it is determined by the Zeeman splitting in an external field, $\Delta E_{nr}\approx\mu g_2 B_c$. Equating these splittings and using the above values for the parameters $\delta_2=55\,\mu$eV and $g_2=g_h+g_e=2.7$, we find for the cross-relaxation field $B_c=0.3$ T. This agrees in order of magnitude with the experimental value $B_c\approx0.5$ T (Fig. 2c). Thus the hypothesis of cross-relaxation does not contradict experiment. A question may now arise as to the nature of the mixing, and why it is not observed in the ISL1 sample. For the above cross-relaxation to occur, the island symmetry must be low enough. Because the anisotropic exchange splitting in the ISL2 sample ($\delta_2=55\,\mu$eV) is substantially larger than that in the ISL1 ($\delta_2=4\,\mu$eV), the island symmetry in ISL2 is lower than that in ISL1. Therefore cross-relaxation in the ISL1 sample is suppressed. Also, active and inactive states can be mixed by a magnetic field directed across the size-quantization axis *z*. In this experiment, the external field is parallel to the *z* axis. Besides the external field, however, there is the nuclear field, which may not coincide in direction with the former. In InP islands, the states of In nuclei (spin 9/2) can undergo quadrupole splitting; note that the principal axis of quadrupole interaction between In nuclei may not coincide with the *z* axis. This implies that it is the nuclear field that can mix the active and inactive states. This conclusion is supported also by the fact that in the case of alternating excitation (no nuclear field present) the cross-relaxation effect is suppressed. Thus the cross relaxation is apparently accounted for by the effective nuclear magnetic field and the low symmetry of the quantum dots (the large anisotropic exchange splitting δ_2).

The authors express their sincere gratitude to I. A. Merkulov for fruitful discussions.

Partial support of the Russian Fund for Fundamental Research (Grant 98-02-18213), Scientific-School Support Grant 96-15-96393, and the Physics of Solid-State Nanostructures Project (Grant 99-1108) is gratefully acknowledged.

[1] E. L. Ivchenko and G. E. Pikus, *Superlattices and Other Heterostructures. Symmetry and Optical Phenomena* (Springer, Berlin, 1995).
[2] R. I. Dzhioev, H. M. Gibbs, E. L. Ivchenko, G. Khitrova, V. L. Korenev, M. N. Tkachuk, and B. P. Zakharchenya, Phys. Rev. B **56**, 13405 (1997); R. I. Dzhioev, B. P. Zakharchenya, E. L. Ivchenko, V. L. Korenev, Yu. G. Kusraev, N. N. Ledentsov, V. M. Ustinov, A. E. Zhukov, and A. F. Tsatsul'nikov, JETP Lett. **65**, 804 (1997).
[3] R. I. Dzhioev, B. P. Zakharchenya, V. L. Korenev, P. E. Pak, D. A. Vinokurov, O. V. Kovalenkov, and I. S. Tarasov, Fiz. Tverd. Tela (St. Petersburg) **40**, 1745 (1998) [Phys. Solid State **40**, 1587 (1998)].
[4] V. K. Kalevich, V. L. Korenev, and O. M. Fedorova, JETP Lett. **52**, 349 (1990).
[5] S. W. Brown, T. A. Kennedy, D. Gammon, and E. S. Snow, Phys. Rev. B **54**, R17339 (1996); D. Gammon, S. W. Brown, E. S. Snow, T. A. Kennedy, D. S. Katzer, and D. Park, Science **277**, 85 (1997).
[6] R. I. Dzhioev, B. P. Zakharchenya, V. L. Korenev, P. E. Pak, M. N. Tkachuk, D. A. Vinokurov, and I. S. Tarasov, JETP Lett. **68**, 745 (1998).
[7] *Optical Orientation*, Modern Problems in Condensed Matter Sciences, vol. 8, ed. by F. Meier and B. Zakharchenya (North-Holland, Amsterdam, 1984; Nauka, Leningrad, 1989).
[8] A. A. Sirenko, T. Ruf, A. Kurfenbach, and K. Eberl, *Proceedings of the 23rd International Conference on the Physics Semiconductors (Berlin, 1996)* (World Scientific, Singapore), p. 1385.
[9] H. W. van Kesteren, E. C. Cosman, W. A. J. A. van der Poel, and C. T. Foxon, Phys. Rev. B **41**, 5283 (1990).
[10] S. V. Goupalov, E. L. Ivchenko, and A. V. Kavokin, Superlattices Microstruct. **23**, 1209 (1998).

Translated by G. Skrebtsov